Atomistic simulation study on silicon carbide precipitation in silicon

Zur Erlangung des akademischen Grades eines
Doktors der Naturwissenschaften
der Mathematisch-Naturwissenschaftlichen Fakultät
der Universität Augsburg vorgelegte

Dissertation

von
Frank Zirkelbach
aus
Berlin

Augsburg, September 2011

Erstgutachter:	Prof. Dr. Bernd Stritzker
Zweitgutachter:	Priv.-Doz. Dr. habil. Volker Eyert
Drittgutachter:	Prof. Dr. Kai Nordlund
Tag der mündlichen Prüfung:	10. Januar 2012

Contents

List of Figures

List of Tables

Chapter 1

Introduction

Silicon carbide (SiC) has a number of remarkable physical and chemical properties that make it a promising new material in various fields of applications. The high electron mobility and saturation drift velocity as well as the high band gap and breakdown field in conjunction with its unique thermal stability and conductivity unveil SiC as the ideal candidate for high-power, high-frequency and high-temperature electronic and optoelectronic devices exceeding conventional silicon based solutions [1–5]. Due to the large Si-C bonding energy, SiC is a hard and chemical inert material suitable for applications under extreme conditions and capable for microelectromechanical systems, both as structural material and as a coating layer [6, 7]. Its radiation hardness allows the operation as a first wall material in nuclear reactors [8] and as electronic devices in space [4].

The realization of silicon carbide based applications demands for reasonable sized wafers of high crystalline quality. Despite the tremendous progress achieved in the fabrication of high purity SiC employing techniques like the modified Lely process for bulk crystal growth [9, 10] or chemical vapor deposition (CVD) and molecular beam epitaxy (MBE) for homo- and heteroepitaxial growth [11–13], available wafer dimensions and crystal qualities are not yet sufficient.

Another promising alternative to fabricate SiC is ion beam synthesis (IBS). High-dose carbon implantation at elevated temperatures into silicon with subsequent annealing results in the formation of buried SiC layers [14, 15]. A two-temperature implantation technique was proposed to achieve single crystalline, epitaxial SiC layers and a sharp SiC/Si interface [16–19].

Although high-quality SiC can be achieved by means of IBS, the precipitation mechanism is not yet fully understood. High resolution transmission electron microscopy studies indicate the formation of C-Si interstitial complexes sharing conventional silicon lattice sites (C-Si dumbbells) during the implantation of carbon in silicon. These C-Si dumbbells agglomerate and once a critical radius is reached, the topotactic transformation into a SiC precipitate occurs [18, 20]. In contrast, investigations of strained $\text{Si}_{1-y}\text{C}_y$/Si heterostructures formed by MBE [21, 22], which incidentally involve the formation of SiC nanocrystallites, suggest an initial coherent precipitation by agglomeration of substitutional instead of interstitial C. Coherency is lost once the increasing strain energy of the stretched SiC structure surpasses the interfacial energy of the incoherent 3C-SiC precipitate and the Si substrate. These two different mechanisms of precipitation might be attributed to the respective method of fabrication. While in CVD and MBE surface effects need to be taken into account, SiC formation during IBS takes place in the bulk of the Si crystal. However, in another IBS study [23], a topotactic transformation is proposed that is likewise based on the formation of substitutional C, which is accompanied by the emission of Si self-interstitial atoms that previously occupied the lattice sites and a compensating reduction of volume due to the lower lattice constant of SiC compared to Si. The atomic migration involved in such a transformation is not clear.

For several reasons, solving the controversial view of SiC precipitation in Si is of fundamental interest. A better understanding of the supposed SiC conversion mechanism and related carbon-mediated effects in silicon will enable significant technological progress in SiC thin film formation on the one hand and likewise offer perspectives for processes which rely upon prevention of precipitation events for improved silicon based devices on the other hand. Implanted carbon is known to suppress transient enhanced diffusion of dopant species like boron or phosphorus in the annealing step [24], which can be exploited to create shallow p-n junctions in submicron technologies. Si self-interstitials ($\mathrm{Si_i}$), known as the transport vehicles for dopants [25, 26], get trapped by reacting with the carbon atoms [27]. Furthermore, carbon incorporated in silicon is being used to fabricate strained silicon [21, 28, 29] utilized in semiconductor industry for increased charge carrier mobilities in silicon [30, 31] as well as to adjust its band gap [32, 33].

Thus, the understanding of carbon in silicon either as an isovalent impurity as well as at concentrations exceeding the solid solubility limit up to the stoichiometric ratio to form silicon carbide is of fundamental interest. Due to the impressive growth in computer power on the one hand and outstanding progress in the development of new theoretical concepts, algorithms and computational methods on the other hand, computer simulations enable the modeling of increasingly complex systems. Atomistic simulations offer a powerful tool to study materials and molecular systems on a microscopic level providing detailed insight not accessible by experiment.

The intention of this work is to contribute to the understanding of C in Si by means of atomistic simulations targeted on the task to elucidate the SiC conversion mechanism in silicon. The outline of this work is as follows: In chapter 2, a review of the Si/C compound is given, including the very central discussion on two controversial precipitation mechanisms present in literature in section 2.4. Chapter 3 introduces some basics and internals of the utilized atomistic simulations as well as special methods of application. Details of the simulation and associated test calculations are presented in chapter 4. In chapter 5, results of investigations of single defect configurations, structures of combinations of two individual defects as well as some selected diffusion pathways in silicon are shown. These allow to draw conclusions with respect to the SiC precipitation mechanism in Si. More complex systems aiming to model the transformation of C incorporated in bulk Si into a SiC nucleus are examined in chapter 6. Finally, a summary and concluding remarks are given in chapter 7.

Chapter 2

Review of the silicon carbon compound

2.1 Structure, properties and applications of silicon carbide

The phase diagram of the C/Si system is shown in Fig. 2.1. In the solid state the stoichiometric composition of silicon and carbon termed silicon carbide (SiC) is the only chemical stable compound in the C/Si system [34]. SiC was first discovered by Henri Moissan in 1893 when he observed brilliant sparkling crystals while examining rock samples from a meteor crater in Arizona. He mistakenly identified these crystals as diamond. Although they might have been considered „diamonds from space“, Moissan identified them as SiC in 1904 [35]. In mineralogy SiC is still referred to as moissanite in honor of its discoverer. It is extremely rare and almost impossible to find in nature.

SiC is a mainly covalent material in which both, Si and C atoms are sp^3 hybridized. Each of the four sp^3 hybridized orbitals of a Si atom overlaps with one of the four sp^3 hybridized orbitals of the four surrounding C atoms and vice versa. This results in fourfold coordinated, mostly covalent σ bonds of equal length and strength for each atom with its neighbors. Although the local order of Si and C next neighbor atoms characterized by the tetrahedral bonding is the same, more than 250 different types of structures called polytypes of SiC exist [36]. The polytypes differ in the one-dimensional stacking sequence of identical, close-packed SiC bilayers. Each SiC bilayer can be situated in one of three possible positions (abbreviated a, b or c) with respect to the lattice while maintaining the tetrahedral bonding scheme of the crystal. Fig. 2.2 shows the stacking sequence of the most common and technologically most important SiC polytypes, which are the cubic (3C) and hexagonal (2H, 4H and 6H) polytypes.

Different polytypes of SiC exhibit different properties. Some of the key properties are listed in Table 2.1 and compared to other technologically relevant semiconductor materials. Despite the lower charge carrier mobilities for low electric fields, SiC outperforms Si concerning all other properties. The wide band gap, large breakdown field and high saturation drift velocity make SiC an ideal candidate for high-temperature, high-power and high-frequency electronic devices exhibiting high efficiency [1–5, 7, 37]. In addition, the high thermal conductivity enables the implementation of small-sized electronic devices enduring increased power densities. Its formidable mechanical stability, heat resistance, radiation hardness and low neutron capture cross section allow operation in harsh and radiation-hard environments [4].

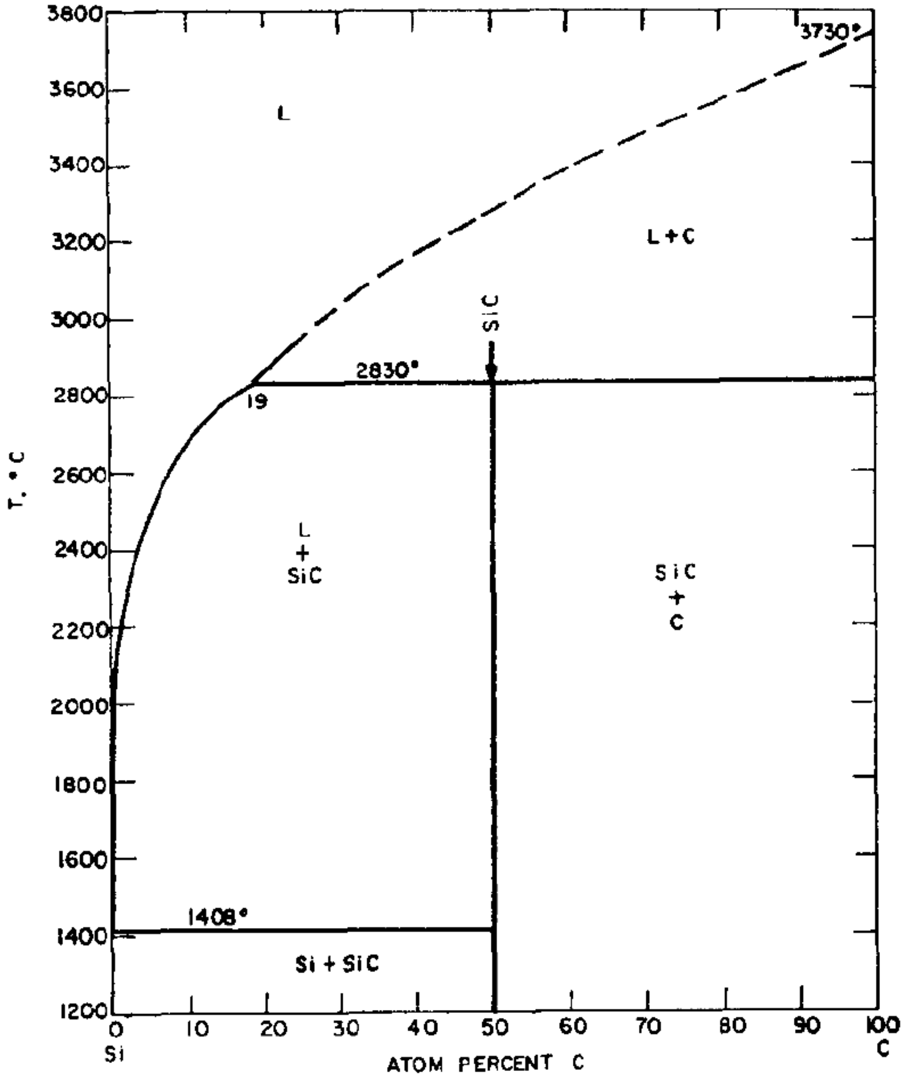

Figure 2.1: Phase diagram of the C/Si system [34].

In addition to high-temperature operations, the wide band gap also allows the use of SiC in optoelectronic devices. Indeed, a forgotten figure, Oleg V. Losev discovered what we know as the light emitting diode (LED) today in the mid 1920s by observing light emission from SiC crystal rectifier diodes used in radio receivers when a current was passed through them [38]. Apparently not known to Losev, Henry J. Round published a small note [39] reporting a bright glow from a SiC diode already in 1907. However, it was Losev who continued his studies providing comprehensive knowledge on light emission of SiC (entitled luminous carborundum) and its relation to diode action [40–43] constituting the birth of solid-state optoelectronics. And indeed, the first significant blue LEDs reinvented at the start of the 1990s were based on SiC. Due to the indirect band gap and, thus, low light emitting efficiency, however, it is nowadays replaced by GaN and InGaN based diodes. However, even for GaN based diodes SiC turns out to be of great importance since it constitutes an ideal substrate material for GaN epitaxial layer growth [44]. As such, SiC will continue to play a major role in the

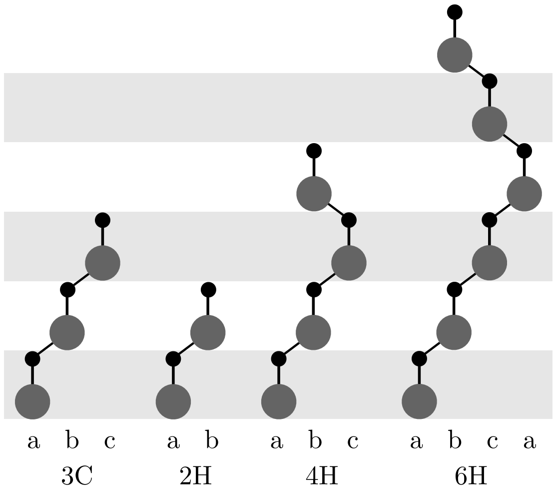

Figure 2.2: Stacking sequence of SiC bilayers of the most common polytypes of SiC (from left to right): 3C, 2H, 4H and 6H.

	3C-SiC	4H-SiC	6H-SiC	Si	GaN	Diamond
Hardness [Mohs]		—— 9.6 ——		6.5	-	10
Band gap [eV]	2.36	3.23	3.03	1.12	3.39	5.5
Break down field^{A} [10^6 V/cm]	4	3	3.2	0.6	5	10
Saturation drift velocity^{A} [10^7 cm/s]	2.5	2.0	2.0	1	2.7	2.7
Electron mobility^{B} [cm^2/Vs]	800	900	400	1100	900	2200
Hole mobility^{B} [cm^2/Vs]	320	120	90	420	150	1600
Thermal conductivity [W/cmK]	5.0	4.9	4.9	1.5	1.3	22

Table 2.1: Properties of SiC polytypes and other semiconductor materials. Doping concentrations are 10^{16} cm^{-3} (A) and 10^{17} cm^{-3} (B) respectively. References: 1, 3, 7.

production of future super-bright visible emitters. Especially substrates of the 3C polytype promise good quality, single crystalline GaN films [45–48].

The focus of SiC based applications, however, is in the area of solid state electronics experiencing revolutionary performance improvements enabled by its capabilities [1–5, 7, 37]. These devices include ultraviolet (UV) detectors [49, 50], high power radio frequency (RF) amplifiers, rectifiers and switching transistors [51–57] as well as microelectromechanical system (MEMS) applications [6]. For UV detectors the wide band gap is useful for realizing low photodiode dark currents as well as sensors that are blind to undesired near-infrared wavelengths produced by heat and solar radiation. These photodiodes serve as excellent sensors applicable in the monitoring and control of turbine engine combustion. The low dark currents enable the use in x-ray, heavy ion and neutron detection in nuclear reactor monitoring and enhanced scientific studies of high-energy particle collisions as well as cosmic radiation. The low neutron capture cross section and radiation hardness favors its use in detector applications. The high breakdown field and carrier saturation velocity coupled with the high thermal conductivity allow SiC RF transistors to handle much higher power densities and frequencies in stable operation at high temperatures. Smaller transistor sizes and less

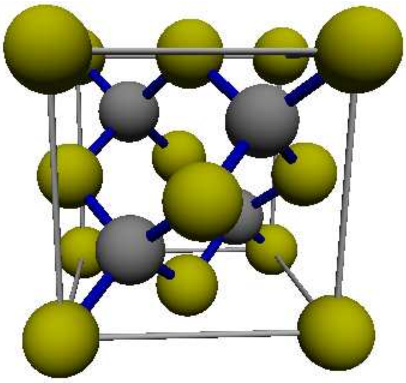

Figure 2.3: 3C-SiC unit cell. Yellow and gray spheres correspond to Si and C atoms respectively. Covalent bonds are illustrated by blue lines.

cooling requirements lead to a reduced overall size and cost of these systems. For instance, SiC based solid state transmitters hold great promise for High Definition Television (HDTV) broadcast stations [51, 58] abandoning the reliance on tube-based technology for high-power transmitters significantly reducing the size of such transmitters and long-term maintenance costs. The high breakdown field of SiC compared to Si allows the blocking voltage region of a device to be designed roughly 10 times thinner and 10 times heavier doped, resulting in a decrease of the blocking region resistance by a factor of 100 and a much faster switching behavior. Thus, rectifier diodes and switching transistors with higher switching frequencies and much greater efficiencies can be realized and exploited in highly efficient power converters. Therefore, SiC constitutes a promising candidate to become the key technology towards an extensive development and use of regenerative energies and electromobility. Beside the mentioned electrical capabilities, the mechanical stability, which is almost as hard as diamond, and chemical inertness almost suggest SiC to be used in MEMS designs.

Among the different polytypes of SiC, the cubic phase shows a high electron mobility and the highest break down field as well as saturation drift velocity [1, 59]. In contrast to its hexagonal counterparts, 3C-SiC exhibits isotropic mechanical and electronic properties. Additionally, the smaller band gap is expected to be favorable concerning the interface state density in MOSFET devices fabricated on 3C-SiC [60]. Thus, the cubic phase is most effective for highly efficient high-performance electronic devices. Its unit cell is shown in Fig. 2.3. 3C-SiC grows in zincblende structure, i.e. it is composed of two face-centered cubic (fcc) lattices, which are displaced by one quarter of the volume diagonal as in Si. However, in 3C-SiC, one of the fcc lattices is occupied by Si atoms while the other one is occupied by C atoms. Its lattice constant of 0.436 nm compared to 0.543 nm from that of Si results in a lattice mismatch of almost 20 %, i.e. four lattice constants of Si approximately match five SiC lattice constants. Thus, the Si density of SiC is only slightly lower, i.e. 97 % of plain Si.

2.2 Fabrication of silicon carbide

Although the constituents of SiC are abundant and the compound is chemically and thermally stable, large deposits of SiC have never been found. Due to the rarity, SiC is typically man-made. The development of several methods was necessary to synthetically produce SiC crystals matching the needs of a respective application. The fact that natural SiC is almost only observed as individual presolar SiC stardust grains near craters of primitive meteorite impacts already indicates the complexity involved in the synthesis process.

The attractive properties and wide range of applications, however, have triggered extensive efforts to grow this material as a bulk crystal and as an epitaxial surface thin film. In the following, the principal difficulties involved in the formation of crystalline SiC and the most recent achievements will be summarized.

Though possible, melt growth processes [61] are complicated due to the small C solubility in Si at temperatures below 2000 °C and its small change with temperature [34]. High process temperatures are necessary and the evaporation of Si must be suppressed by a high-pressure inert atmosphere. Crystals grown by this method are not adequate for practical applications with respect to their size as well as quality and purity. The presented methods, thus, focus on vapor transport growth processes such as chemical vapor deposition (CVD) or molecular beam epitaxy (MBE) and the sublimation technique. Excellent reviews of the different SiC growth methods have been published by Wesch [1] and Davis et al. [62].

2.2.1 SiC bulk crystal growth

The industrial Acheson process [63] is utilized to produce SiC on a large scale by thermal reaction of silicon dioxide (silica sand) and carbon (coal). The heating is accomplished by a core of graphite centrally placed in a furnace, which is heated up to a maximum temperature of 2700 °C, after which the temperature is gradually lowered. Due to the insufficient and uncontrollable purity, material produced by this method, originally termed carborundum by Acheson, can hardly be used for device applications. However, it is often used as an abrasive material and as seed crystals for subsequent vapor phase growth and sublimation processes.

In the van Arkel apparatus [64], Si and C containing gases like methylchlorosilanes [65] and silicon tetrachloride [66] are pyrolitically decomposed and SiC is deposited on heated carbon rods in a vapor growth process. Typical deposition temperatures are in the range between 1400 °C and 1600 °C while studies up to 2500 °C have been performed. The obtained polycrystalline material consists of small crystal grains with a size of several hundred microns stated to be mainly of the cubic polytype.

A significant breakthrough was made in 1955 by Lely, who proposed a sublimation process for growing higher purity bulk SiC single crystals [67]. In the so called Lely process, a tube of porous graphite is surrounded by polycrystalline SiC as gained by previously described processes. Heating the hollow carbon cylinder to 2500 °C leads to sublimation of the material at the hot outer wall and diffusion through the porous graphite tube followed by an uncontrolled crystallization on the slightly cooler parts of the inner graphite cavity resulting in the formation of randomly sized, hexagonally shaped platelets, which exhibit a layered structure of various alpha (non-cubic) polytypes with equal $\{0\,0\,0\,1\}$ orientation.

Subsequent research [9, 68] resulted in the implementation of a seeded growth sublimation process wherein only one large crystal of a single polytype is grown. In the so called modified Lely or modified sublimation process, nucleation occurs on a SiC seed crystal located at the top or bottom of a cylindrical growth cavity. As in the Lely process, SiC sublimes at a temperature of 2400 °C from a polycrystalline source diffusing through a porous graphite retainer along carefully adjusted thermal and pressure gradients. Controlled nucleation occurs on the SiC seed, which is held at approximately 2200 °C. The growth process is commonly done in a high-purity argon atmosphere. The method was successfully applied to grow 6H and 4H boules with diameters up to 60 mm [68–71]. This refined versions of the physical vapor transport (PVT) technique enabled the reproducible boule growth of device quality SiC crystals, which were for instance used to fabricate blue light emitting diodes with increased quantum efficiencies [72].

Although significant advances have been achieved in the field of SiC bulk crystal growth, a variety of problems remain. The high temperatures required in PVT growth processes limit the range of materials used in the hot zones of the reactors, for which mainly graphite is used. The porous material constitutes a severe source of contamination, e.g. with the dopants N, B and Al, which is particularly effective at low temperatures due to the low growth rate. Since the vapor pressure of Si is much higher than that of C, a careful manipulation of the Si vapor content above the seed crystal is required. Additionally, to preserve epitaxial growth conditions, graphitization of the seed crystal has to be avoided. Avoiding defects constitutes a major difficulty. These defects include growth spirals (stepped screw dislocations), subgrain boundaries and twins as well as micropipes (micron sized voids extending along the core of screw dislocations) [73, 74] and 3C inclusions at the seed crystal in hexagonal growth systems. Micropipe-free growth of 6H-SiC has been realized by a reduction of the temperature gradient in the sublimation furnace resulting in near-equilibrium growth conditions in order to avoid stresses, which is, however, accompanied by a reduction of the growth rate [75]. Further efforts have to be expended to find relations between the growth parameters, the kind of polytype and the occurrence and concentration of defects, which are of fundamental interest and might help to improve the purity of the bulk materials.

2.2.2 SiC epitaxial thin film growth

Crystalline SiC layers have been grown by a large number of techniques on the surfaces of different substrates. Most of the crystal growth processes are based on CVD, solid-source MBE (SSMBE) and gas-source MBE (GSMBE) on Si as well as SiC substrates. In CVD as well as GSMBE, C and Si atoms are supplied by C containing gases like CH_4, C_3H_8, C_2H_2 or C_2H_4 and Si containing gases like SiH_4, Si_2H_6, SiH_2Cl_2, $SiHCl_3$ or $SiCl_4$ respectively. In the case of SSMBE, atoms are provided by electron beam evaporation of graphite and solid Si or thermal evaporation of fullerenes. The following review will exclusively focus on CVD and MBE techniques.

The availability and reproducibility of Si substrates of controlled purity made it the first choice for SiC epitaxy. The heteroepitaxial growth of SiC on Si substrates has been stimulated for a long time due to a lack of suitable large substrates that could be adopted for homoepitaxial growth. Furthermore, heteroepitaxy on Si substrates enables the fabrication of the advantageous 3C polytype, which constitutes a metastable phase and, thus, can be grown as a bulk crystal only with small sizes of a few mm. The main difficulties in SiC heteroepitaxy on Si arise due to the lattice mismatch of Si and SiC by 20 % and the difference in the thermal expansion coefficient of 8 %. Thus, in most of the applied CVD and MBE processes, the SiC layer formation process is split into two steps, the surface carbonization and the growth step, as proposed by Nishino et al. [76]. Cleaning of the substrate surface with HCl is required prior to carbonization. During carbonization the Si surface is chemically converted into a SiC film with a thickness of a few nm by exposing it to a flux of C atoms and concurrent heating up to temperatures of about 1400 °C. In a next step, the epitaxial deposition of SiC is realized by an additional supply of Si atoms at similar temperatures. Low defect densities in the buffer layer are a prerequisite for obtaining good quality SiC layers during growth, although defect densities decrease with increasing distance to the SiC/Si interface [77]. Next to surface morphology defects such as pits and islands, the main defects in 3C-SiC heteroepitaxial layers are twins, stacking faults (SF) and antiphase boundaries (APB) [77, 78]. APB defects, which constitute the primary residual defects in thick layers, are formed near surface terraces that differ in a single-atom-height step resulting in domains of SiC separated by a boundary, which consists of either Si-Si or C-C bonds due to missing or disturbed sublattice information [79, 80]. However, the number of such defects can be reduced by off-axis growth on a Si (0 0 1) substrate miscut towards [1 1 0] by 2 °-4 ° [77, 81]. This results in the thermodynamically favored growth of a single phase due to the uni-directional contraction of Si-C-Si bond chains perpendicular to the terrace steps edges during carbonization and the fast growth parallel to the terrace edges during growth under Si rich conditions [80]. A reduction of the SF in addition to the APB defects was recently achieved by growing 3C-SiC on undulant Si [82], i.e. a Si (0 0 1) substrate covered with continuous slopes oriented in the [1 1 0] and $[\bar{1}\,\bar{1}\,0]$ directions. In this way, APB defects are eliminated by a mechanism similar to that in the off-axis growth process while, at the same time, SFs are aligned in the (1 1 1) or $(\bar{1}\,\bar{1}\,1)$ planes and, thus, terminate as they connect with each other during the growth process. By MBE, lower process temperatures than these typically employed in CVD have been realized [83–86], which is essential for limiting thermal stresses and to avoid resulting substrate bending, a key issue in obtaining large area 3C-SiC surfaces. In summary, the almost universal use of Si has allowed significant progress in the understanding of heteroepitaxial growth of SiC on Si. However, mismatches in the thermal expansion coefficient and the lattice parameter cause a considerably high concentration of various defects, which is responsible for structural and electrical qualities that are not yet satisfactory.

The alternative attempt to grow SiC on SiC substrates has shown to drastically reduce the concentration of defects in deposited layers. By CVD, both, the 3C [12, 87] as well as the 6H [88, 89] polytype could be successfully grown. In order to obtain the homoepitaxially grown 6H polytype, off-axis 6H-SiC wafers are required as a substrate [11]. Investigations indicate that in the so-called step-controlled epitaxy, crystal growth proceeds through the adsorption of Si species at atomic steps and their carbonization by hydrocarbon molecules. This growth mechanism does not require two-dimensional nucleation. Instead, crystal growth is governed by mass transport, i.e. the diffusion of reactants in a stagnant layer. In contrast, layers of the 3C polytype are formed on exactly oriented (0 0 0 1) 6H-SiC substrates by two-dimensional nucleation on terraces. These films show a high density of double positioning boundary (DPB) defects, which is a special type of twin boundary arising at the interface of regions that occupy one of the two possible orientations of the hexagonal stacking sequence, which are rotated by 60 ° relative to each other. However, lateral 3C-SiC growth was also observed on low tilt angle off-axis substrates originating from intentionally induced dislocations [90]. Additionally, 6H-SiC was observed on clean substrates even for a tilt angle as low as 0.1 ° due to low surface mobilities that facilitate arriving molecules to reach surface steps. Thus, 3C nucleation is assumed as a result of migrating Si and C containing molecules interacting with surface disturbances, in contrast to a model [91], in which the competing 6H versus 3C growth depends on the density of surface steps. Combining the fact of a well defined 3C lateral growth direction, i.e. the tilt direction, and an intentionally induced dislocation, enables the controlled growth of a 3C-SiC film mostly free of DPBs [90].

Lower growth temperatures, a clean growth ambient, in situ control of the growth process, layer-by-layer deposition and the possibility to achieve dopant profiles within atomic dimensions due to the reduced diffusion at low growth temperatures reveal MBE as a promising technique to produce SiC epitaxial layers. Using alternating supply of the gas beams Si_2H_6 and C_2H_2 in GSMBE, 3C-SiC epilayers were obtained on 6H-SiC substrates at temperatures between 850 °C and 1000 °C [92]. On $(0\,0\,0\,\bar{1})$ substrates twinned $(\bar{1}\,\bar{1}\,\bar{1})$ oriented 3C-SiC domains are observed, which suggest a nucleation driven rather than step-flow growth mechanism. On $(0\,\bar{1}\,1\,\bar{4})$ substrates, however, single crystalline $(0\,0\,1)$ oriented 3C-SiC grows with the c axes of substrate and film being equal. The beneficial epitaxial relation of substrate and film limits the structural difference between the two polytypes in two out of six layers with respect to the stacking sequence along the c axis. Homoepitaxial growth of 3C-SiC by GSMBE was realized for the first time by atomic layer epitaxy (ALE) utilizing the periodical change in the surface superstructure by the alternating supply of the source gases, which determines the growth rate giving atomic level control in the growth process [93]. The cleaned substrate surface shows a C terminated (2×2) pattern at 1000 °C, which turns into a (3×2) pattern when Si_2H_6 is introduced and it is maintained after the supply is stopped. A more detailed investigation showed the formation of a preceding (2×1) and (5×2) pattern within the exposure to the Si containing gas [94, 95]. The (3×2) superstructure contains approximately 1.7 monolayers of Si atoms, crystallizing into 3C-SiC with a smooth and mirror-like surface after C_2H_6 is inserted accompanied by a reconstruction of the surface into the initial C terminated (2×2) pattern. A minimal growth rate of 2.3 monolayers per cycle exceeding the value of 1.7 is due to physically adsorbed Si atoms not contributing to the superstructure. To realize single monolayer growth, precise control of the gas supply to form the (2×1) structure is required. However, accurate layer-by-layer growth is achieved under certain conditions, which facilitate the spontaneous desorption of an additional layer of one atom species by supply of the other species [96]. Homoepitaxial growth of the 6H polytype has been realized on off-oriented substrates utilizing simultaneous supply of the source gases [97]. Depending on the gas flow ratio either 3C island formation or step flow growth of the 6H polytype occurs, which is explained by a model including aspects of enhanced surface mobilities of adatoms on a (3×3) reconstructed surface. Due to the strong adsorption of atomic hydrogen [98] decomposed of the gas phase reactants at low temperatures, however, there seems to be no benefit of GSMBE compared to CVD. Next to lattice imperfections, incorporated hydrogen effects the surface mobility of the adsorbed species [99] setting a minimum limit for the growth temperature, which would preferably be further decreased in order to obtain sharp doping profiles. Thus, growth rates must be adjusted to be lower than the desorption rate of hydrogen, which leads to very low deposition rates at low temperatures. SSMBE, by supplying the atomic species to be deposited by evaporation of a solid, presumably constitutes the preferred method in order to avoid the problems mentioned above. Although, in the first experiments, temperatures still above 1100 °C were necessary to epitaxially grow 3C-SiC films on 6H-SiC substrates [100], subsequent attempts succeeded in growing mixtures of twinned 3C-SiC and 6H-SiC films on off-axis $(0\,0\,0\,1)$ 6H-SiC wafers at temperatures between 800 °C and 1000 °C [13, 101]. In the latter approach, as in GSMBE, excess Si atoms, which are controlled by the Si/C flux ratio, result in the formation of a Si adlayer and the formation of a non-stoichiometric, reconstructed surface superstructure, which influences the mobility of adatoms and, thus, has a decisive influence on the growth mode, polytype and crystallinity [13, 102, 103]. Therefore, carefully controlling the Si/C ratio could be exploited to obtain definite heterostructures of different SiC polytypes providing the possibility for band gap engineering in SiC materials.

To summarize, much progress has been achieved in SiC thin film growth during the last few years. However, the frequent occurrence of defects such as dislocations, twins and double positioning boundaries limit the structural and electrical quality of large SiC films. Solving this issue remains a challenging problem necessary to drive SiC for potential applications in high-performance electronic device production [1].

2.2.3 Ion beam synthesis of cubic silicon carbide

Although tremendous progress has been achieved in the above-mentioned growth methods during the last decades, available wafer dimensions and crystal qualities are not yet satisfactory. Thus, alternative approaches to fabricate SiC have been explored. The ion beam synthesis (IBS) technique, i.e. high-dose ion implantation followed by a high-temperature annealing step, turned out to constitute a promising method to directly form compound layers of high purity and accurately controllable depth and stoichiometry. A short chronological summary of the IBS of SiC and its origins is presented in the following.

High-dose carbon implantation into crystalline silicon (c-Si) with subsequent or in situ annealing was found to result in SiC microcrystallites in Si [14]. Rutherford backscattering spectrometry (RBS) and infrared (IR) spectroscopy investigations indicate a 10 at.% C concentration peak and the occurrence of disordered C-Si bonds after implantation at room temperature (RT) followed by crystallization into SiC precipitates upon annealing. This is demonstrated by a shift in the IR absorption band and the disappearance of the C profile peak in RBS. Implantations at different temperatures revealed a strong influence of the implantation temperature on the compound structure [104]. Temperatures below 500 °C result in amorphous layers, which are transformed into polycrystalline 3C-SiC after annealing at 850 °C. Otherwise, single crystalline 3C-SiC is observed for temperatures above 600 °C. Annealing temperatures necessary for the onset of the amorphous to crystalline transition have been confirmed by further studies [105, 106]. Overstoichiometric doses result in the formation of clusters of C, which do not contribute to SiC formation during annealing up to 1200 °C [106]. The amount of formed SiC, however, increases with increasing implantation temperature. The authors, thus, concluded that implantations at elevated temperatures lead to a reduction in the annealing temperatures required for the synthesis of homogeneous layers of SiC. In a comparative study of O, N and C implantation into Si, the absence of the formation of a stoichiometric SiC compound layer involving the transition of a Gaussian into a box-like C depth profile with respect to the implantation depth for the superstoichiometric C implantation and an annealing temperature of 1200 °C in contrast to the O and N implantations, which successfully form homogeneous layers, has been observed [107]. This was attributed to the difference in the enthalpy of formation of the respective compound and the different mobility of the respective impurity in bulk Si. Thus, higher annealing temperatures and longer annealing times were considered necessary for the formation of homogeneous SiC layers. Indeed, for the first time, buried homogeneous and stoichiometric epitaxial 3C-SiC layers embedded in single crystalline Si were obtained by the same group consequently applying annealing temperatures of 1405 °C for 90 min and implantation temperatures of approximately 550 °C [15]. The necessity of the applied extreme temperature (a few degrees below the Si melting point) and time scale is attributed to the stability of substitutional C within the Si matrix being responsible for high activation energies necessary to dissolve such precipitates and, thus, allow for redistribution of the implanted C atoms. In order to avoid extreme annealing temperatures close to the melting temperature of Si, triple-energy implantations in the range from 180–190 keV with stoichiometric doses at a constant target temperature of 860 °C achieved by external substrate heating were performed [108]. It was shown that a thick buried layer of SiC is directly formed during implantation, which consists of small, only slightly misorientated but severely twinned 3C-SiC crystallites. The authors assumed that due to the auxiliary heating rather than ion beam heating as employed in all the preceding studies, the complexity of the remaining defects in the synthesized structure is fairly reduced. Even better qualities by direct synthesis were obtained for implantations at 950 °C [23]. Since no amorphous or polycrystalline regions have been identified, twinning is considered to constitute the main limiting factor in the IBS of SiC. Layers obtained by direct synthesis are characterized by rough surfaces of the buried layer and the substrate originating from the dendritic growth of SiC crystals at these temperatures [109].

Further studies revealed the possibility to form buried layers of SiC by IBS at moderate substrate and anneal temperatures [110, 111]. Different doses of C ions with an energy of 180 keV were implanted at 330–440 °C and annealed at 1200 °C or 1250 °C for 5–10 h. For a critical dose, which was found to depend on the Si substrate orientation, the formation of a stoichiometric buried layer of SiC exhibiting a well-defined interface to the Si host matrix was observed. In case of overstoichiometric C concentrations, the excess C is not redistributed. These investigations demonstrate the presence of an upper dose limit, which corresponds to a 53 at.% C concentration at the implantation peak, for the thermally induced redistribution of the C atoms from a Gaussian to a box-shaped depth profile upon annealing. This is explained by the formation of strong graphitic C-C bonds for higher C concentrations [112]. Increased temperatures exceeding the Si melting point are expected to be necessary for the dissociation of these C clusters. Furthermore, higher implantation energies were found to result in layers of variable composition exhibiting randomly distributed SiC precipitates. In another study [113] high dose C implantations were performed at room temperature and 500 °C respectively. Implantations at room temperature lead to the formation of a buried amorphous carbide layer in addition to a thin C-rich film at the surface, which is attributed to the migration of C atoms towards the surface. In contrast, implantations at elevated temperatures result in the exclusive formation of a buried layer consisting of 3C-SiC precipitates epitaxially aligned to the Si host, which obviously is more favorable than the C migration towards the surface. Annealing at temperatures up to 1150 °C does not alter the C profile. Instead, defect annihilation is observed and the C-rich surface layer of the room temperature implant turns into a layer consisting of SiC precipitates, which, however, are not aligned with the Si matrix indicating a mechanism different to the one of the direct formation for the high-temperature implantation.

Based on these findings, a recipe was developed to form buried layers of single-crystalline SiC featuring an improved interface and crystallinity [16, 18, 19]. Therefor, the dose must not exceed the stoichiometry dose, i.e. the dose corresponding to 50 at.% C concentration at the implantation peak. Otherwise, clusters of C are formed, which cannot be dissolved during post-implantation annealing at moderate temperatures below the Si melting point [111, 112]. Annealing should be performed for 5–10 h at 1250 °C to enable the redistribution from the as-implanted Gaussian into a box-like C depth profile [110]. The implantation temperature constitutes the most critical parameter, which is responsible for the structure after implantation and, thus, the starting point for subsequent annealing steps. Implantations at 400 °C resulted in buried layers of SiC subdivided into a polycrystalline upper and an epitaxial lower part. This corresponds to the region of randomly oriented SiC crystallites and epitaxially aligned precipitates surrounded by thin amorphous layers without crystalline SiC inclusions in the as-implanted state. However, an abrupt interface to the Si host is observed after an-

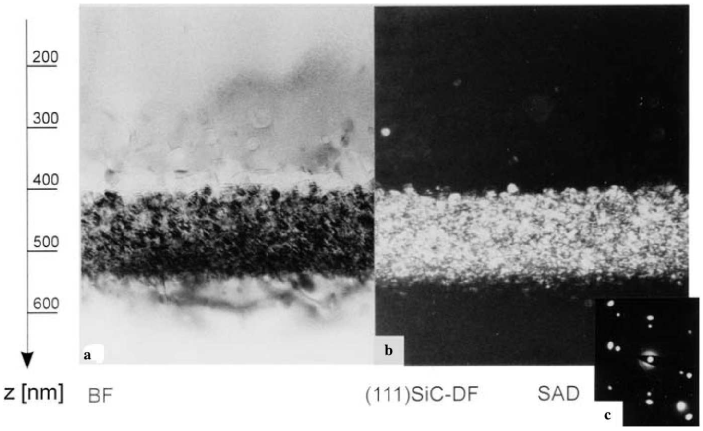

Figure 2.4: Bright field (a) and (1 1 1) SiC dark field (b) cross-sectional TEM micrographs of the buried SiC layer in Si created by the two-temperature implantation technique and subsequent annealing as explained in the text [17]. The inset shows a selected area diffraction pattern of the buried layer.

nealing. As expected, single-crystalline layers were achieved for an increased temperature of 600 °C. However, these layers show an extremely poor interface to the Si top layer governed by a high density of SiC precipitates, which are not affected in the C redistribution during annealing and, thus, responsible for the rough interface. Hence, to obtain sharp interfaces and single-crystalline SiC layers temperatures between 400 °C and 600 °C have to be used. Indeed, reasonable results were obtained at 500 °C [114] and even better interfaces were observed for 450 °C [17]. To further improve the interface quality and crystallinity, a two-temperature implantation technique was developed [16]. To form a narrow, box-like density profile of oriented SiC nanocrystals, 93 % of the total dose of $8.5 \cdot 10^{17}\,\text{cm}^{-2}$ is implanted at 500 °C. The remaining dose is implanted at 250 °C, which leads to the formation of amorphous zones above and below the SiC precipitate layer and the destruction of SiC nanocrystals within these zones. After annealing for 10 h at 1250 °C, a homogeneous, stoichiometric SiC layer with sharp interfaces is formed. Fig. 2.4 shows the respective high resolution transmission electron microscopy micrographs.

To summarize, by understanding some basic processes, IBS nowadays has become a promising method to form thin SiC layers of high quality exclusively of the 3C polytype embedded in and epitaxially aligned to the Si host featuring a sharp interface. Due to the high areal homogeneity achieved in IBS, the size of the layers is only limited by the width of the beam-scanning equipment used in the implantation system. Buried layers can be revealed at the surface by additional implantation and etching steps [115]. They do not exhibit surface bending effects in contrast to these formed by the MBE or CVD technique. This enables the synthesis of large area SiC films.

2.3 Substoichiometric concentrations of carbon in crystalline silicon

In the following, some basic properties of C in crystalline Si are reviewed. A lot of work has been done contributing to the understanding of C in Si either as an isovalent impurity as well as at concentrations exceeding the solid solubility limit. A comprehensive survey on C-mediated effects in Si has been published by Skorupa and Yankov [116].

2.3.1 Carbon as an impurity in silicon

Below the solid solubility, C impurities mainly occupy substitutionally Si lattice sites in Si [117]. Due to the much smaller covalent radius of C compared to Si, every incorporated C atom leads to a decrease in the lattice constant corresponding to a lattice contraction of about one atomic volume [118]. The induced strain is assumed to be responsible for the low solid solubility of C in Si, which was determined [119] to be

$$c_{\mathrm{s}} = 4 \times 10^{24}\,\mathrm{cm}^{-3} \cdot \exp(-2.3\,\mathrm{eV}/k_{\mathrm{B}}T) \ . \tag{2.1}$$

The barrier of diffusion of substitutional C has been determined to be around 3 eV [120]. However, as suspected due to the substitutional position, the diffusion of C requires intrinsic point defects, i.e. Si self-interstitials and vacancies. Similar to phosphorous and boron, which exclusively use self-interstitials as a diffusion vehicle, the diffusion of C atoms is expected to obey the same mechanism. Indeed, enhanced C diffusion was observed in the presence of self-interstitial supersaturation [121] indicating an appreciable diffusion component involving self-interstitials and only a negligible contribution by vacancies. Substitutional C and interstitial Si react into a C-Si complex forming a dumbbell structure oriented along a crystallographic $\langle 1\,0\,0\rangle$ direction on a regular Si lattice site. This structure, the so called C-Si $\langle 1\,0\,0\rangle$ dumbbell structure, was initially suspected by local vibrational mode absorption [122] and finally verified by electron paramagnetic resonance [123] studies on irradiated Si substrates at low temperatures. Measuring the annealing rate of the defect as a function of temperature reveals barriers for migration of 0.70 eV [109], 0.73 eV [124] and 0.87 eV [125], which is highly mobile compared to substitutional C.

2.3.2 Suppression of transient enhanced diffusion of dopant species

The predominant diffusion mechanism of most dopants in Si based on native self-interstitials [25] has a large impact on the diffusion behavior of dopants that have been implanted in Si. The excess population of Si self-interstitials created by low-energy implantations of dopants for shallow junction formation in submicron technologies may enhance the diffusion of the respective dopant during annealing by more than one order of magnitude compared to normal diffusion. This kind of diffusion, labeled transient enhanced diffusion (TED), which is driven by the presence of non-equilibrium concentrations of point defects, was first discovered for implantations of boron in Si [126] and is well understood today [26, 27, 127, 128]. The TED of B was found to be inhibited in the presence of a sufficient amount of incorporated C [24]. This is due to the reduction of the excess Si self-interstitials with substitutional C atoms forming the C-Si interstitial complex [27, 129]. Therefore, incorporation of C provides a promising method for suppressing TED enabling an improved shallow junction formation in future Si devices.

2.3.3 Strained silicon and silicon heterostructures

Radiation damage introduced during implantation and a high concentration of the implanted species, which results in the reduction of the topological constraint of the host lattice imposed on the implanted species, can affect the manner of impurity incorporation. The probability of finding C, which will be most stable at sites for which the number of neighbors equals the natural valence, i.e. substitutionally on a regular Si site of a perfect lattice, is, thus, reduced at substitutional lattice sites and likewise increased at interstitial sites. Indeed, x-ray rocking curves reveal a positive lattice strain, which is decreased but still remains with increasing annealing temperature, indicating the location of the majority of implanted C atoms at interstitial sites [130]. Due to the absence of dislocations in the implanted region, interstitial C is assumed to prevent clustering of implantation-induced Si self-interstitials by agglomeration of C-Si interstitials or the formation of SiC precipitates accompanied by a relaxation of the lattice strain.

However, there is great interest to incorporate C onto substitutional lattice sites, which results in a contraction of the Si lattice due to the smaller covalent radius of C compared to Si [118], causing tensile strain, which is applied to the Si lattice. Thus, substitutional C enables strain engineering of Si and $\text{Si}/\text{Si}_{1-x}\text{Ge}_x$ heterostructures [30, 31, 131, 132], which is used to increase charge carrier mobilities in Si as well as to adjust its band structure [32, 33]. Epitaxial layers with 1.4 at.% of substitutional C have been successfully synthesized in preamorphized $\text{Si}_{0.86}\text{Ge}_{0.14}$ layers, which were grown by CVD on Si substrates, using multiple-energy C implantation followed by solid-phase epitaxial regrowth at 700 °C [133]. The tensile strain induced by the C atoms is found to compensate the compressive strain present due to the Ge atoms. Studies on the thermal stability of $\text{Si}_{1-y}\text{C}_y/\text{Si}$ heterostructures formed in the same way and equal C concentrations showed a loss of substitutional C accompanied by strain relaxation for temperatures ranging from 810–925 °C and the formation of spherical 3C-SiC precipitates with diameters of 2–4 nm, which are incoherent but aligned to the Si host [21]. During the initial stages of precipitation C-rich clusters are assumed, which maintain coherency with the Si matrix and the associated biaxial strain. Using this technique, a metastable solubility limit was achieved, which corresponds to a C concentration exceeding the solid solubility limit at the Si melting point by nearly three orders of magnitude and, furthermore, a reduction of the defect density near the metastable solubility limit is assumed if the regrowth temperature is increased by rapid thermal annealing [28]. Since high temperatures used in the solid-phase epitaxial regrowth method promotes SiC precipitation, other groups realized substitutional C incorporation for strained $\text{Si}_{1-y}\text{C}_y/\text{Si}$ heterostructures [29, 134–138] or partially to fully strain-compensated (even inversely distorted [139]) $\text{Si}_{1-x-y}\text{Ge}_x\text{C}_y$ layers on Si [140–143] by MBE. Investigations reveal a strong temperature-dependence of the amount of substitutionally incorporated C, which is increased for decreasing temperature accompanied by deterioration of the crystal quality [29, 137]. While not being compatible to very-large-scale integration technology, C concentrations of 2 % and more have been realized [138].

2.4 Assumed silicon carbide conversion mechanisms

Although high-quality films of single-crystalline 3C-SiC can be produced by means of IBS, the precipitation mechanism in bulk Si is not yet fully understood. Indeed, closely investigating the large amount of literature pulled up in the last two sections and a cautious combination of some of the findings reveals controversial ideas of SiC formation, which are reviewed in more detail in the following.

High resolution transmission electron microscopy (HREM) investigations of C-implanted Si at room temperature followed by rapid thermal annealing (RTA) indicate the formation

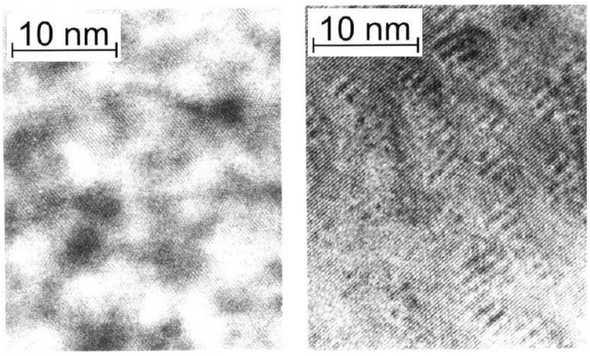

(a) (b)

Figure 2.5: High resolution transmission electron microscopy (HREM) micrographs [17] of agglomerates of C-Si dimers showing dark contrasts and otherwise undisturbed Si lattice fringes (a) and equally sized Moiré patterns indicating 3C-SiC precipitates (b).

of C-Si dumbbell agglomerates, which are stable up to annealing temperatures of about 700–800 °C, and a transformation into 3C-SiC precipitates at higher temperatures [20, 144]. The precipitates with diameters between 2 nm and 5 nm are incorporated in the Si matrix without any remarkable strain fields, which is explained by the nearly equal atomic density of C-Si agglomerates and the SiC unit cell. Implantations at 500 °C likewise suggest an initial formation of C-Si dumbbells on regular Si lattice sites, which agglomerate into large clusters [17]. The agglomerates of such dimers, which do not generate lattice strain but lead to a local increase of the lattice potential [20, 144], are indicated by dark contrasts and otherwise undisturbed Si lattice fringes in HREM, as can be seen in Fig. 2.5(a). A topotactic transformation into a 3C-SiC precipitate occurs once a critical radius of 2 nm to 4 nm is reached. The precipitation is manifested by the disappearance of the dark contrasts in favor of Moiré patterns (Fig. 2.5(b)) due to the lattice mismatch of 20 % of the 3C-SiC precipitate and the Si host. The insignificantly lower Si density of SiC of approximately 3 % compared to c-Si results in the emission of only a few excess Si atoms. The same mechanism was identified by high resolution x-ray diffraction [145]. For implantation temperatures of 500 °C, C-Si dumbbells agglomerate in an initial stage followed by the additional appearance of aligned SiC precipitates in a slightly expanded Si region with increasing dose. The precipitation mechanism based on a preceding dumbbell agglomeration as indicated by the above-mentioned experiments is schematically displayed in Fig. 2.6. The incorporated C atoms form C-Si dumbbells on regular Si lattice sites. With increasing dose and proceeding time, the highly mobile dumbbells agglomerate into large clusters. Finally, when the cluster size reaches a critical radius, the high interfacial energy due to the 3C-SiC/c-Si lattice misfit is overcome and precipitation occurs. Due to the slightly lower silicon density of 3C-SiC, excessive silicon atoms exist, which will most probably end up as self-interstitials in the c-Si matrix since there is more space than in 3C-SiC.

In contrast, IR spectroscopy and HREM investigations on the thermal stability of strained $Si_{1-y}C_y$/Si heterostructures formed by solid-phase epitaxy (SPE) [21] and MBE [22], which finally involve the incidental formation of SiC nanocrystallites, suggest a coherent initiation of precipitation by agglomeration of substitutional instead of interstitial C. These experiments

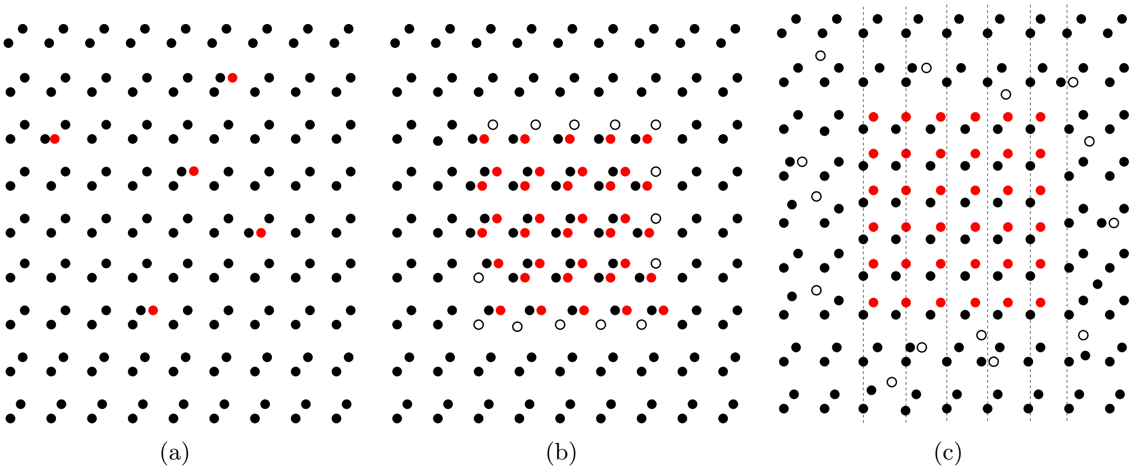

Figure 2.6: Two dimensional schematic of the assumed SiC precipitation mechanism based on an initial C-Si dumbbell agglomeration. C atoms (red dots) incorporated into the Si (black dots) host form C-Si dumbbells (a), which agglomerate into clusters (b) followed by precipitation of SiC and the emission of a few excess Si atoms (black circles), which are located in the interstitial Si lattice (c). The dotted lines mark the atomic spacing of c-Si in [1 0 0] direction indicating the 4/5 ratio of the lattice constants of c-Si and 3C-SiC.

show that the C atoms, which are initially incorporated substitutionally at regular lattice sites, form C-rich clusters maintaining coherency with the Si lattice during annealing above a critical temperature prior to the transition into incoherent 3C-SiC precipitates. Increased temperatures in the annealing process enable the diffusion and agglomeration of C atoms. Coherency is lost once the increasing strain energy of the stretched SiC structure surpasses the interfacial energy of the incoherent 3C-SiC precipitate and the Si substrate. Estimates of the SiC/Si interfacial energy [146] and the consequent critical size correspond well with the experimentally observed precipitate radii within these studies.

This different mechanism of precipitation might be attributed to the respective method of fabrication. While in CVD and MBE surface effects need to be taken into account, SiC formation during IBS takes place in the bulk of the Si crystal. However, in another IBS study Nejim et al. [23] propose a transformation that is likewise based on substitutional C, which replaces four of the eight Si atoms in the Si unit cell accompanied by the generation of four Si interstitials. The replacement of a Si unit cell by a 3C-SiC unit cell is accompanied by a volume reduction of 48 % due to the 20 % lower lattice constant. Since the emerging strain caused by the expected volume reduction would result in the formation of dislocations, which, however, are not observed, the interstitial Si is assumed to react with further implanted C atoms in the released volume. The resulting strain due to the slightly lower Si density of SiC compared to Si of about 3 % is sufficiently small to legitimate the absence of dislocations. However, the exact atomic rearrangement involved within this topotactic transformation is not identified. Furthermore, IBS studies of Reeson et al. [15], in which implantation temperatures of 500 °C were employed, revealed the necessity of extreme annealing temperatures for C redistribution, which is assumed to result from the stability of substitutional C and consequently high activation energies required for precipitate dissolution. The results support a mechanism of an initial coherent precipitation based on substitutional C that is likewise valid for the IBS of 3C-SiC by C implantation into Si at elevated temperatures. The fact that the metastable cubic phase instead of the thermodynamically more favorable hexagonal α-SiC structure is formed and the alignment of these cubic precipitates within the Si matrix, which can be explained straightforward by considering a topotactic transformation by C atoms occupying substitutionally Si lattice sites of one of the two fcc lattices that make up the Si crystal, reinforce the proposed mechanism.

To conclude, a controversy with respect to the precipitation model of SiC in Si exists in literature. Next to the pure scientific interest, solving this controversy and gaining new insight in the SiC conversion mechanism might enable significant progress in the heteroepitaxial growth of thin films featuring non-coherent interfaces in the C/Si system. On the other hand, processes relying upon prevention of precipitation in order to produce strained heterostructures will likewise benefit.

Chapter 3

Basic principles of utilized simulation techniques

In the following, the simulation methods used within the scope of this study are introduced. Enabling the investigation of the evolution of structure on the atomic scale, molecular dynamics (MD) simulations are chosen for modeling the behavior and precipitation of C introduced into an initially crystalline Si environment. To be able to model systems with a large amount of atoms, computational efficient classical potentials to describe the interaction of the atoms are most often used in MD studies. For reasons of flexibility in executing this non-standard task and in order to be able to use a novel interaction potential [147], an appropriate MD code called POSIC[1] including a library collecting respective MD subroutines was developed from scratch[2]. The basic ideas of MD in general and the adopted techniques as implemented in POSIC in particular are outlined in section 3.1 while the functional form and derivative of the employed classical potential is presented in appendix A. An overview of the most important tools within the MD package is given in appendix C. Although classical potentials are often most successful and at the same time computationally efficient in calculating some physical properties of a particular system, not all of its properties might be described correctly due to the lack of quantum-mechanical effects. Thus, in order to obtain more accurate results, quantum-mechanical calculations from first principles based on density functional theory (DFT) were performed. The Vienna *ab initio* simulation package (VASP) [148] is used for this purpose. The relevant basics of DFT are described in section 3.2 while an overview of utilities mainly used to create input or parse output data of VASP is given in appendix C. The gain in accuracy achieved by this method, however, is accompanied by an increase in computational effort constraining the simulated system to be much smaller in size. Thus, investigations based on DFT are restricted to single defects or combinations of two defects in a rather small Si supercell, their structural relaxation as well as some selected diffusion processes. Next to the structure, defects can be characterized by the defect formation energy, a scalar indicating the costs necessary for the formation of the defect, which is explained in section 3.3. The method used to investigate migration pathways to identify the prevalent diffusion mechanism is introduced in section 3.4 and modifications to the VASP code implementing this method are presented in appendix B.

---

[1] POSIC is an abbreviation for **p**recipitation **o**f **SiC**

[2] Source code: http://www.physik.uni-augsburg.de/~zirkelfr/posic

3.1 Molecular dynamics simulations

> ”We may regard the present state of the universe as the effect of the past and the cause of the future. An intellect which at any given moment knew all of the forces that animate nature and the mutual positions of the beings that compose it, if this intellect were vast enough to submit the data to analysis, could condense into a single formula the movement of the greatest bodies of the universe and that of the lightest atom; for such an intellect nothing could be uncertain and the future just like the past would be present before its eyes.”
>
> *Marquis Pierre Simon de Laplace, 1814.* [149]

Pierre Simon de Laplace phrased this vision in terms of a controlling, omniscient instance — the *Laplace demon* — which would be able to look into the future as well as into the past due to the deterministic nature of processes, which is governed by the solution of differential equations. Although Laplace’s vision is nowadays corrected by chaos theory and quantum mechanics, it expresses two main features of classical mechanics, i.e. the determinism of processes and time reversibility of the fundamental equations. This understanding may be regarded as the basic principle of molecular dynamics, considering an isolated system of particles, the behavior of which is fully determined by the solution of the classical equations of motion.

3.1.1 Introduction to molecular dynamics simulations

Molecular dynamics (MD) simulation is a technique to compute a system of particles, referred to as molecules, with their positions, velocities and forces among each other evolving in time. The MD method was first introduced by Alder and Wainwright in 1957 [150, 151] to study the interactions of hard spheres. The basis of the approach are Newton’s equations of motion to describe classically the many-body system. MD is the numerical way of solving the N-body problem which cannot be solved analytically for $N > 3$. A potential is necessary to describe the interaction of the particles. By MD, a complete description of the system in the sense of classical mechanics on the microscopic level is obtained. The microscopic information can then be translated to macroscopic observables by means of statistical mechanics.

The basic idea is to assume that the particles can be described classically by Newton’s equations of motion, which are integrated numerically. A system of N particles of masses m_i $(i = 1, \ldots, N)$ at positions $\mathbf{r}_i$ and velocities $\dot{\mathbf{r}}_i$ is given by

$$m_i \ddot{\mathbf{r}}_i = \mathbf{F}_i \Leftrightarrow m_i \dot{\mathbf{r}}_i = \mathbf{p}_i,\ \dot{\mathbf{p}}_i = \mathbf{F}_i\ . \tag{3.1}$$

The forces $\mathbf{F}_i$ are obtained from the potential energy $U(\{\mathbf{r}\})$:

$$\mathbf{F}_i = -\nabla_{\mathbf{r}_i} U(\{\mathbf{r}\})\,. \tag{3.2}$$

Given the initial conditions $\mathbf{r}_i(t_0)$ and $\dot{\mathbf{r}}_i(t_0)$, the equations can be integrated by a certain integration algorithm. The solution of these equations provides the complete information of a system evolving in time. The following sections cover the tools of the trade necessary for the MD simulation technique. Three ingredients are required for a MD simulation:

1. A model for the interaction between system constituents is needed. Interaction potentials and their accuracy for describing certain systems of elements will be outlined in section 3.1.2.
2. An integrator is needed, which propagates the particle positions and velocities from time t to $t+\delta t$, realized by a finite difference scheme which moves trajectories discretely in time. This is explained in section 3.1.3.
3. A statistical ensemble has to be chosen, which allows certain thermodynamic quantities to be controlled or to stay constant. This is discussed in section 3.1.4.

These ingredients will be outlined in the following. The discussion is restricted to methods employed within this study.

3.1.2 Interaction potentials for silicon and carbon

The potential energy of N interacting atoms can be written in the form

$$U(\{\mathbf{r}\}) = \sum_i U_1(\mathbf{r}_i) + \sum_i \sum_{j>i} U_2(\mathbf{r}_i, \mathbf{r}_j) + \sum_i \sum_{j>i} \sum_{k>j>i} U_3(\mathbf{r}_i, \mathbf{r}_j, \mathbf{r}_k) \ldots \tag{3.3}$$

where U is the total potential energy. U_1 is a single particle potential describing external forces. Examples of single particle potentials are the gravitational force or an electric field. U_2 is a two body pair potential which only depends on the distance r_{ij} between the two atoms i and j. If not only pair potentials are considered, three body potentials U_3 or many body potentials U_n can be included. Usually these higher order terms are avoided since they are not easy to model and it is rather time consuming to evaluate potentials and forces originating from these many body terms. Ordinary pair potentials have a close-packed structure like face-centered cubic (fcc) or hexagonal close-packed (hcp) as a ground state. A pair potential is, thus, unable to describe properly elements with other structures than fcc or hcp. Silicon and carbon for instance, have a diamond and zincblende structure with four covalently bonded neighbors, which is far from a close-packed structure. A three body potential has to be included for these types of elements.

The Tersoff bond order potential

Tersoff proposed an empirical interatomic potential for covalent systems [152, 153]. The Tersoff potential explicitly incorporates the dependence of bond order on local environments, permitting an improved description of covalent materials. Due to the covalent character, Tersoff restricted the interaction to nearest neighbor atoms accompanied by an increase in computational efficiency for the evaluation of forces and energy based on the short-range potential. Tersoff applied the potential to silicon [152–154], carbon [155] and also to multicomponent systems like silicon carbide [156]. The basic idea is that, in real systems, the bond order, i.e. the strength of the bond, depends upon the local environment [157]. Atoms with many neighbors form weaker bonds than atoms with only a few neighbors. Although the bond strength intricately depends on geometry, the focus on coordination, i.e. the number of neighbors forming bonds, is well motivated qualitatively from basic chemistry since for every additional formed bond the amount of electron pairs per bond and, thus, the strength of the bonds is decreased. If the energy per bond decreases rapidly enough with increasing coordination, the most stable structure will be the dimer. In the other extreme, if the dependence is weak, the material system will end up in a close-packed structure in order to maximize the number of bonds and likewise minimize the cohesive energy. This suggests the bond order to be a monotonously decreasing function with respect to coordination and the equilibrium coordination being determined by the balance of bond strength and number of bonds. Based on pseudopotential theory, the bond order term b_{ijk} limiting the attractive pair interaction is of the form $b_{ijk} \propto Z^{-\delta}$ where Z is the coordination number and δ a constant [157], which is $\frac{1}{2}$ in the second-moment approximation within the tight binding scheme [158].

Tersoff incorporated the concept of bond order in a three-body potential formalism. The interatomic potential is taken to have the form

$$\begin{aligned} E &= \sum_i E_i = \frac{1}{2} \sum_{i \neq j} V_{ij} \;, && (3.4)\\ V_{ij} &= f_C(r_{ij}) [f_R(r_{ij}) + b_{ij} f_A(r_{ij})] \;. && (3.5) \end{aligned}$$

E is the total energy of the system, constituted either by the sum over the site energies E_i or by the bond energies V_{ij}. The indices i and j correspond to the atoms of the system with r_{ij} being the distance from atom i to atom j. The functions f_R and f_A represent a repulsive and an attractive pair potential. The repulsive part is due to the orthogonalization energy of overlapped atomic wave functions. The attractive part is associated with the bonding.

$$\begin{aligned} f_R(r_{ij}) &= A_{ij} \exp(-\lambda_{ij} r_{ij}) && (3.6)\\ f_A(r_{ij}) &= -B_{ij} \exp(-\mu_{ij} r_{ij}) && (3.7) \end{aligned}$$

The function f_C is a cut-off function to limit the range of interaction to nearest neighbors. It is designed to have a smooth transition of the potential at distances R_{ij} and S_{ij}.

$$f_C(r_{ij}) = \begin{cases} 1, & r_{ij} < R_{ij} \\ \frac{1}{2} + \frac{1}{2} \cos\Big[\pi (r_{ij} - R_{ij})/(S_{ij} - R_{ij})\Big], & R_{ij} < r_{ij} < S_{ij} \\ 0, & r_{ij} > S_{ij} \end{cases} \qquad (3.8)$$

As discussed above, b_{ij} represents a measure of the bond order, monotonously decreasing with the coordination of atoms i and j. It is of the form

$$\begin{aligned} b_{ij} &= \chi_{ij} (1 + \beta_i^{n_i} \zeta_{ij}^{n_i})^{-1/2n_i} && (3.9)\\ \zeta_{ij} &= \sum_{k \neq i,j} f_C(r_{ik}) \omega_{ik} g(\theta_{ijk}) && (3.10)\\ g(\theta_{ijk}) &= 1 + c_i^2/d_i^2 - c_i^2/[d_i^2 + (h_i - \cos\theta_{ijk})^2] && (3.11) \end{aligned}$$

where θ_{ijk} is the bond angle between bonds ij and ik. This is illustrated in Fig. 3.1. The angular dependence does not give a fixed minimum angle between bonds since the expression is embedded inside the bond order term. The relation to the above discussed bond order potential becomes obvious if $\chi = 1, \beta = 1, n = 1, \omega = 1$ and $c = 0$. Parameters with a single subscript correspond to the parameters of the elemental system [154, 155] while the mixed parameters are obtained by interpolation from the elemental parameters by the arithmetic or geometric mean. The elemental parameters were obtained by a fit with respect to the cohesive

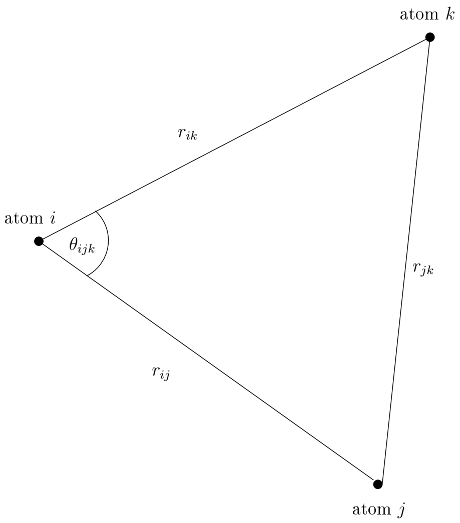

Figure 3.1: Angle between bonds of atoms i, j and i, k.

energies of real and hypothetical bulk structures and the bulk modulus and bond length of the diamond structure. New parameters for the mixed system are χ, which is used to finetune the strength of heteropolar bonds, and ω, which is set to one for the C-Si interaction but is available as a feature to permit the application of the potential to more drastically different types of atoms in the future.

The force acting on atom i is given by the derivative of the potential energy. For a three body potential ($V_{ij} \neq Vji$) the derivation is of the form

$$\nabla_{\mathbf{r}_i} E = \frac{1}{2} \big[\sum_j (\nabla_{\mathbf{r}_i} V_{ij} + \nabla_{\mathbf{r}_i} V_{ji}) + \sum_k \sum_j \nabla_{\mathbf{r}_i} V_{jk} \big] \ . \tag{3.12}$$

The force is then given by

$$F^i = -\nabla_{\mathbf{r}_i} E \ . \tag{3.13}$$

Details of the Tersoff potential derivative are presented in appendix A.

Improved analytical bond order potential

Although the Tersoff potential is one of the most widely used potentials, there are some shortcomings. Describing the Si-Si interaction, Tersoff was unable to find a single parameter set to describe well both, bulk and surface properties. Due to this, and since the first approach labeled T1 [152] turned out to be unstable [159], two further parametrizations exist, T2 [153] and T3 [154]. While T2 describes well surface properties, T3 yields improved elastic constants and should be used for describing bulk properties. However, T3, which is used in the Si/C potential, suffers from an underestimation of the dimer binding energy. Similar behavior is found for the C-C interaction.

For this reason, Erhart and Albe provide a reparametrization of the Tersoff potential based on three independently fitted parameter sets for the Si-Si, C-C and Si-C interaction [147]. The functional form is similar to the one proposed by Tersoff. Differences in the energy functional and the force evaluation routine are pointed out in appendix A. Concerning Si, the elastic properties of the diamond phase as well as the structure and energetics of the dimer are reproduced very well. The new parameter set for the C-C interaction yields improved dimer properties while at the same time delivers a description of the bulk phase similar to the Tersoff potential. The potential succeeds in the description of the low as well as high coordinated structures. The description of elastic properties of SiC is improved with respect to the potentials available in literature. Defect properties are only fairly reproduced but the description is comparable to previously published potentials. It is claimed that the potential enables modeling of widely different configurations and transitions among these and has recently been used to simulate the inert gas condensation of Si-C nanoparticles [160]. Therefore, the Erhart/Albe (EA) potential is considered the superior analytical bond order potential to study the SiC precipitation and associated processes in Si.

3.1.3 Verlet integration

A numerical method to integrate Newton's equations of motion was presented by Verlet in 1967 [161]. The idea of the so-called Verlet and a variant, the velocity Verlet algorithm, which additionally generates directly the velocities, is explained in the following. Starting point is the Taylor series for the particle positions at time $t+\delta t$ and $t-\delta t$

$$\mathbf{r}_i(t+\delta t)=\mathbf{r}_i(t)+\delta t\mathbf{v}_i(t)+\frac{\delta t^2}{2m_i}\mathbf{f}_i(t)+\frac{\delta t^3}{6}\mathbf{b}_i(t)+\mathcal{O}(\delta t^4) \tag{3.14}$$

$$\mathbf{r}_i(t-\delta t)=\mathbf{r}_i(t)-\delta t\mathbf{v}_i(t)+\frac{\delta t^2}{2m_i}\mathbf{f}_i(t)-\frac{\delta t^3}{6}\mathbf{b}_i(t)+\mathcal{O}(\delta t^4) \tag{3.15}$$

where $\mathbf{v}_i=\frac{d}{dt}\mathbf{r}_i$ are the velocities, $\mathbf{f}_i=m\frac{d^2}{dt^2}\mathbf{r}_i$ are the forces and $\mathbf{b}_i=\frac{d^3}{dt^3}\mathbf{r}_i$ are the third derivatives of the particle positions with respect to time. The Verlet algorithm is obtained by summarizing and subtracting equations (3.14) and (3.15)

$$\mathbf{r}_i(t+\delta t)=2\mathbf{r}_i(t)-\mathbf{r}_i(t-\delta t)+\frac{\delta t^2}{m_i}\mathbf{f}_i(t)+\mathcal{O}(\delta t^4) \tag{3.16}$$

$$\mathbf{v}_i(t)=\frac{1}{2\delta t}[\mathbf{r}_i(t+\delta t)-\mathbf{r}_i(t-\delta t)]+\mathcal{O}(\delta t^3) \tag{3.17}$$

the truncation error of which is of order δt^4 for the positions and δt^3 for the velocities. The velocities, although not used to update the particle positions, are not synchronously determined with the positions but drag behind one step of discretization. The Verlet algorithm can be rewritten into an equivalent form, which updates the velocities and positions in the same step. The so-called velocity Verlet algorithm is obtained by combining equation (3.14) with equation (3.15) displaced in time by $+\delta t$

$$\mathbf{v}_i(t+\delta t)=\mathbf{v}_i(t)+\frac{\delta t}{2m_i}[\mathbf{f}_i(t)+\mathbf{f}_i(t+\delta t)]+\mathcal{O}(\delta t^3) \tag{3.18}$$

$$\mathbf{r}_i(t+\delta t)=\mathbf{r}_i(t)+\delta t\mathbf{v}_i(t)+\frac{\delta t^2}{2m_i}\mathbf{f}_i(t)+\mathcal{O}(\delta t^3)\ . \tag{3.19}$$

Since the forces for the new positions are required to update the velocity, the determination of the forces has to be carried out within the integration algorithm.

3.1.4 Statistical ensembles

Using the above mentioned algorithms, the most basic type of MD is realized by simply integrating the equations of motion of a fixed number of particles (N) in a closed volume V realized by periodic boundary conditions (PBC). Providing a stable integration algorithm, the total energy E, i.e. the kinetic and configurational energy of the particles, is conserved. This is known as the NVE or microcanonical ensemble, describing an isolated system composed of microstates, among which the number of particles, volume and energy are held constant.

However, the successful formation of SiC dictates precise control of temperature by external heating. While the temperature of such a system is well defined, the energy is no longer conserved. The microscopic states of a system, which is in thermal equilibrium with an external thermal heat bath, are represented by the NVT ensemble. In the so-called canonical ensemble the temperature T is related to the expectation value of the kinetic energy of the particles, i.e.

$$\langle E_{\text{kin}}\rangle = \frac{3}{2}Nk_{\text{B}}T,\ E_{\text{kin}} = \sum_i \frac{\mathbf{p}_i^2}{2m_i}\ . \tag{3.20}$$

The volume of the synthesized material can hardly be controlled in experiment. Instead the pressure can be adjusted. Holding constant the pressure in addition to the temperature of the system, its states are represented by the isothermal-isobaric NpT ensemble. The expression for the pressure of a system derived from the equipartition theorem is given by

$$pV = Nk_{\text{B}}T + \langle W\rangle,\ W = -\frac{1}{3}\sum_i \mathbf{r}_i\nabla_{\mathbf{r}_i}U, \tag{3.21}$$

where W is the virial and U is the configurational energy.

Berendsen et al. proposed a method [162], which is easy to implement, to couple the system to an external bath with constant temperature T_0 or pressure p_0 with adjustable time constants τ_T and τ_p determining the strength of the coupling. Control of the respective variable is based on the relations given in equations (3.20) and (3.21). The thermostat is achieved by scaling the velocities of all atoms in every time step δt from $\mathbf{v}_i$ to $\lambda\mathbf{v}_i$, with

$$\lambda = \left[1 + \frac{\delta t}{\tau_T}(\frac{T_0}{T} - 1)\right]^{\frac{1}{2}}\ , \tag{3.22}$$

where T is the current temperature according to equation (3.20). The barostat adjusts the pressure by changing the virial through scaling of the particle positions $\mathbf{r}_i$ to $\mu\mathbf{r}_i$ and the volume V to μ^3V, with

$$\mu = \left[1 - \frac{\beta\delta t}{\tau_p}(p_0 - p)\right]^{\frac{1}{3}}\ , \tag{3.23}$$

where β is the isothermal compressibility and p corresponds to the current pressure, which is determined by equation (3.21).

Using this method, the system does not behave like a true NpT ensemble. On average, T and p correspond to the expected values. For large enough time constants, i.e. $\tau > 100\delta t$, the method shows realistic fluctuations in T and p. The advantage of the approach is that the coupling can be decreased to minimize the disturbance of the system and likewise be adjusted to suit the needs of a given application. It provides a stable algorithm that allows smooth changes of the system to new values of temperature or pressure, which is ideal for the investigated problem.

3.2 Density functional theory

Dirac declared that chemistry has come to an end, its content being entirely contained in the powerful equation published by Schrödinger in 1926 [163] marking the beginning of wave mechanics. Following the path of Schrödinger, the problem in quantum-mechanical modeling of describing the many-body problem, i.e. a system of a large amount of interacting particles, is manifested in the high-dimensional Schrödinger equation for the wave function $\Psi(\mathbf{R}, \mathbf{r})$ that depends on the coordinates of all nuclei and electrons. The Schrödinger equation contains the kinetic energy of the ions and electrons as well as the electron-ion, ion-ion and electron-electron interaction. This cannot be solved exactly and finding approximate solutions requires several layers of simplification in order to reduce the number of free parameters. Approximations that consider a truncated Hilbert space of single-particle orbitals yield promising results, however, with increasing complexity and demand for high accuracy, the amount of Slater determinants to be evaluated massively increases.

In contrast, instead of using the description by the many-body wave function, the key point in density functional theory (DFT) is to recast the problem to a description utilizing the charge density $n(\mathbf{r})$, which constitutes a quantity in real space depending only on the three spatial coordinates. In the following sections, the basic idea of DFT will be outlined. As will be shown, DFT can formally be regarded as an exactification of the Thomas Fermi theory [164, 165] and the self-consistent Hartree equations [166]. A nice review is given in the Nobel lecture of Kohn [167], one of the inventors of DFT.

3.2.1 Born-Oppenheimer approximation

Born and Oppenheimer proposed a simplification enabling the effective decoupling of the electronic and ionic degrees of freedom [168]. Within the Born-Oppenheimer (BO) approximation, the light electrons are assumed to move much faster and, thus, follow adiabatically to the motion of the heavy nuclei, if the latter are only slightly deflected from their equilibrium positions. Thus, on the timescale of electronic motion, the ions appear at fixed positions. On the other way round, on the timescale of nuclear motion, the electrons appear blurred in space adding an extra term to the ion-ion potential. The simplified Schrödinger equation no longer contains the kinetic energy of the ions. The momentary positions of the ions enter as fixed parameters and, therefore, the ion-ion interaction may be regarded as a constant added to the electronic energies. The Schrödinger equation describing the remaining electronic problem reads

$$\left[-\frac{\hbar^2}{2m}\sum_j \nabla_j^2 - \sum_{j,l} \frac{Z_l e^2}{|\mathbf{r}_j - \mathbf{R}_l|} + \frac{1}{2}\sum_{j\neq j'} \frac{e^2}{|\mathbf{r}_j - \mathbf{r}_{j'}|}\right]\Psi = E\Psi \ , \tag{3.24}$$

where Z_l are the atomic numbers of the nuclei and Ψ is the many-electron wave function, which depends on the positions and spins of the electrons. Accordingly, there is only a parametric dependence on the ionic coordinates $\mathbf{R}_l$. However, the remaining number of free parameters is still too high and needs to be further decreased.

3.2.2 Hohenberg-Kohn theorem and variational principle

Investigating the energetics of $\mathrm{Cu}_x\mathrm{Zn}_{1-x}$ alloys, which for different compositions exhibit different transfers of charge between the Cu and Zn unit cells due to their chemical difference and, thus, varying electrostatic interactions contributing to the total energy, the work of Hohenberg and Kohn had a natural focus on the distribution of charge. Although it was clear that the Thomas Fermi (TF) theory only provides a rough approximation to the exact solution of the many-electron Schrödinger equation, the theory was of high interest since it provides an implicit relation of the potential and the electron density distribution. This raised the question how to establish a connection between TF expressed in terms of $n(\mathbf{r})$ and the exact Schrödinger equation expressed in terms of the many-electron wave function $\Psi(\mathbf{r})$ and whether a complete description in terms of the charge density is possible in principle. The answer to this question, whether the charge density completely characterizes a system, became the starting point of modern DFT.

Considering a system with a nondegenerate ground state, there is obviously only one ground-state charge density $n_0(\mathbf{r})$ that corresponds to a given potential $V(\mathbf{r})$. In 1964, Hohenberg and Kohn showed the opposite and far less obvious result [169]. Employing no more than the Rayleigh-Ritz minimal principle, it is concluded by *reductio ad absurdum* that for a nondegenerate ground state the same charge density cannot be generated by different potentials. Thus, the charge density of the ground state $n_0(\mathbf{r})$ uniquely determines the potential $V(\mathbf{r})$ and, consequently, the full Hamiltonian and ground-state energy E_0. In mathematical terms, the full many-electron ground state is a unique functional of the charge density. In particular, E is a functional $E[n(\mathbf{r})]$ of $n(\mathbf{r})$.

The ground-state charge density $n_0(\mathbf{r})$ minimizes the energy functional $E[n(\mathbf{r})]$, its value corresponding to the ground-state energy E_0, which enables the formulation of a minimal principle in terms of the charge density [169, 170]

$$E_0 = \min_{n(\mathbf{r})} \left\{ F[n(\mathbf{r})] + \int n(\mathbf{r}) V(\mathbf{r}) d\mathbf{r} \right\} \ , \tag{3.25}$$

where $F[n(\mathbf{r})]$ is a universal functional of the charge density $n(\mathbf{r})$, which is composed of the kinetic energy functional $T[n(\mathbf{r})]$ and the interaction energy functional $U[n(\mathbf{r})]$. The challenging problem of determining the exact ground-state is now formally reduced to the determination of the 3-dimensional function $n(\mathbf{r})$, which minimizes the energy functional. However, the complexity associated with the many-electron problem is now relocated in the task of finding the well-defined but, in contrast to the potential energy, not explicitly known functional $F[n(\mathbf{r})]$.

It is worth to note that this minimal principle may be regarded as exactification of the TF theory, which is rederived by the approximations

$$T = \int n(\mathbf{r}) \frac{3}{10} k_\mathrm{F}^2(n(\mathbf{r})) d\mathbf{r} \ , \tag{3.26}$$

$$U = \frac{1}{2} \int \frac{n(\mathbf{r}) n(\mathbf{r}')}{|\mathbf{r} - \mathbf{r}'|} d\mathbf{r} d\mathbf{r}' \ . \tag{3.27}$$

3.2.3 Kohn-Sham system

Inspired by the Hartree equations, i.e. a set of self-consistent single-particle equations for the approximate solution of the many-electron problem [166], which describe atomic ground states much better than the TF theory, Kohn and Sham presented a Hartree-like formulation of the Hohenberg and Kohn minimal principle (3.25) [171]. However, due to a more general approach, the new formulation is formally exact by introducing the energy functional $E_{\mathrm{xc}}[n(\mathbf{r})]$, which accounts for the exchange and correlation energy of the electron interaction U and possible corrections due to electron interaction to the kinetic energy T. The respective Kohn-Sham equations for the effective single-particle wave functions $\Phi_i(\mathbf{r})$ take the form

$$\left[-\frac{\hbar^2}{2m}\nabla^2 + V_{\mathrm{eff}}(\mathbf{r})\right]\Phi_i(\mathbf{r}) = \epsilon_i\Phi_i(\mathbf{r}) \ , \tag{3.28}$$

$$V_{\mathrm{eff}}(\mathbf{r}) = V(\mathbf{r}) + \int \frac{e^2 n(\mathbf{r}')}{|\mathbf{r}-\mathbf{r}'|}d\mathbf{r}' + V_{\mathrm{xc}}(\mathbf{r}) \ , \tag{3.29}$$

$$n(\mathbf{r}) = \sum_{i=1}^{N} |\Phi_i(\mathbf{r})|^2 \ , \tag{3.30}$$

where the local exchange-correlation potential $V_{\mathrm{xc}}(\mathbf{r})$ is the partial derivative of the exchange-correlation functional $E_{\mathrm{xc}}[n(\mathbf{r})]$ with respect to the charge density $n(\mathbf{r})$ for the ground-state $n_0(\mathbf{r})$. The first term in equation (3.28) corresponds to the kinetic energy of non-interacting electrons and the second term of equation (3.29) is just the Hartree contribution $V_{\mathrm{H}}(\mathbf{r})$ to the interaction energy.

The system of interacting electrons is mapped to an auxiliary system, the Kohn-Sham (KS) system, of non-interacting electrons in an effective potential. The exact effective potential $V_{\mathrm{eff}}(\mathbf{r})$ may be regarded as a fictitious external potential yielding a ground-state density for non-interacting electrons, which is equal to that for interacting electrons in the external potential $V(\mathbf{r})$. The one-electron KS orbitals $\Phi_i(\mathbf{r})$ as well as the respective KS energies ϵ_i are not directly attached to any physical observable except for the ground-state density, which is determined by equation (3.30) and the ionization energy, which is equal to the highest occupied relative to the vacuum level. The KS equations may be considered the formal exactification of the Hartree theory, which it is reduced to if the exchange-correlation potential and functional are neglected. In addition to the Hartree-Fock (HF) method, KS theory includes the difference of the kinetic energy of interacting and non-interacting electrons as well as the remaining contributions to the correlation energy that are not part of the HF correlation.

The self-consistent KS equations (3.28), (3.29) and (3.30) are non-linear partial differential equations, which may be solved numerically by an iterative process. Starting from a first approximation for $n(\mathbf{r})$, the effective potential $V_{\mathrm{eff}}(\mathbf{r})$ can be constructed followed by determining the one-electron orbitals $\Phi_i(\mathbf{r})$, which solve the single-particle Schrödinger equation for the respective potential. The $\Phi_i(\mathbf{r})$ are used to obtain a new expression for $n(\mathbf{r})$. These steps are repeated until the initial and new density are equal or reasonably converged.

Again, it is worth to note that the KS equations are formally exact. Assuming exact functionals $E_{\mathrm{xc}}[n(\mathbf{r})]$ and potentials $V_{\mathrm{xc}}(\mathbf{r})$, all many-body effects are included. Clearly, this directs attention to the functional, which now contains the costs involved with the many-electron problem.

3.2.4 Approximations for exchange and correlation

As discussed above, the HK and KS formulations are exact and so far no approximations except the adiabatic approximation entered the theory. However, to make concrete use of the theory, effective approximations for the exchange and correlation energy functional $E_{\mathrm{xc}}[n(\mathbf{r})]$ are required.

Most simple and at the same time remarkably useful, is the approximation of $E_{\mathrm{xc}}[n(\mathbf{r})]$ by a function of the local density [171],

$$E_{\mathrm{xc}}^{\mathrm{LDA}}[n(\mathbf{r})] = \int \epsilon_{\mathrm{xc}}(n(\mathbf{r}))n(\mathbf{r})d\mathbf{r} \ , \tag{3.31}$$

which is, thus, called local density approximation (LDA). Here, the exchange-correlation energy per particle of the uniform electron gas of constant density n is used for $\epsilon_{\mathrm{xc}}(n(\mathbf{r}))$. Although, even in such a simple case, no exact form of the correlation part of $\epsilon_{\mathrm{xc}}(n)$ is known, highly accurate numerical estimates using Monte Carlo methods [172] and corresponding parametrizations exist [173]. Obviously exact for the homogeneous electron gas, the LDA was *a priori* expected to be useful only for densities varying slowly on scales of the local Fermi or TF wavelength. Nevertheless, LDA turned out to be extremely successful in describing some properties of highly inhomogeneous systems accurately within a few percent. Although LDA is known to overestimate the cohesive energy in solids by 10–20 %, the lattice parameters are typically determined with an astonishing accuracy of about 1 %.

More accurate approximations of the exchange-correlation functional are realized by the introduction of gradient corrections with respect to the density [171]. Respective considerations are based on the concept of an exchange-correlation hole density describing the depletion of the electron density in the vicinity of an electron. The averaged hole density can be used to give a formally exact expression for $E_{\mathrm{xc}}[n(\mathbf{r})]$ and an equivalent expression [174, 175], which makes use of the electron density distribution $n(\tilde{\mathbf{r}})$ at positions $\tilde{\mathbf{r}}$ near $\mathbf{r}$, yielding the form

$$E_{\mathrm{xc}}[n(\mathbf{r})] = \int \epsilon_{\mathrm{xc}}(\mathbf{r}; [n(\tilde{\mathbf{r}})])n(\mathbf{r})d\mathbf{r} \tag{3.32}$$

for the exchange-correlation energy, where $\epsilon_{\mathrm{xc}}(\mathbf{r}; [n(\tilde{\mathbf{r}})])$ becomes a nearsighted functional of $n(\tilde{\mathbf{r}})$. Expressing $n(\tilde{\mathbf{r}})$ in a Taylor series, ϵ_{xc} can be thought of as a function of coefficients, which correspond to the respective terms of the expansion. Neglecting all terms of order $\mathcal{O}(\nabla n(\mathbf{r}))$ results in the functional equal to LDA, which requires the function of variable n. Including the next element of the Taylor series introduces the gradient correction to the functional, which requires the function of variables n and $|\nabla n|$. This is called the generalized-gradient approximation (GGA), which expresses the exchange-correlation energy density as a function of the local density and the local gradient of the density

$$E_{\mathrm{xc}}^{\mathrm{GGA}}[n(\mathbf{r})] = \int \epsilon_{\mathrm{xc}}(n(\mathbf{r}), |\nabla n(\mathbf{r})|)n(\mathbf{r})d\mathbf{r} \ . \tag{3.33}$$

This functional constitutes the simplest extension of the LDA for inhomogeneous systems. At modest computational costs, gradient-corrected functionals very often yield much better results than the LDA with respect to cohesive and binding energies.

3.2.5 Plane-wave basis set

Finally, a set of basis functions is required to represent the one-electron KS wave functions. With respect to the numerical treatment, it is favorable to approximate the wave functions by linear combinations of a finite number of such basis functions. Convergence of the basis set, i.e. convergence of the wave functions with respect to the amount of basis functions, is most crucial for the accuracy of the numerical calculations. Two classes of basis sets, the plane-wave and local basis sets, exist.

Local basis set functions usually are atomic orbitals, i.e. mathematical functions that describe the wave-like behavior of electrons, which are localized, i.e. centered on atoms or bonds. Molecular orbitals can be represented by linear combinations of atomic orbitals (LCAO). By construction, only a small number of basis functions is required to represent all of the electrons of each atom within reasonable accuracy. Thus, local basis sets enable the implementation of methods that scale linearly with the number of atoms. However, these methods rely on the fact that the wave functions are localized and exhibit an exponential decay resulting in a sparse Hamiltonian.

Another approach is to represent the KS wave functions by plane waves. In fact, the employed VASP software is solving the KS equations within a plane-wave (PW) basis set. The idea is based on the Bloch theorem [176], which states that in a periodic crystal each electronic wave function $\Phi_i(\mathbf{r})$ can be written as the product of a wave-like envelope function $\exp(i\mathbf{kr})$ and a function that has the same periodicity as the lattice. The latter one can be expressed by a Fourier series, i.e. a discrete set of plane waves whose wave vectors just correspond to reciprocal lattice vectors $\mathbf{G}$ of the crystal. Thus, the one-electron wave function $\Phi_i(\mathbf{r})$ associated with the wave vector $\mathbf{k}$ can be expanded in terms of a discrete PW basis set:

$$\Phi_i(\mathbf{r}) = \sum_{\mathbf{G}} c_{i,\mathbf{k}+\mathbf{G}} \exp\left(i(\mathbf{k}+\mathbf{G})\mathbf{r}\right) \ . \tag{3.34}$$

The basis set, which in principle should be infinite, can be truncated to include only plane waves that have kinetic energies $\hbar^2|\mathbf{k}+\mathbf{G}|^2/2m$ less than a particular cut-off energy E_{cut}. Although coefficients $c_{i,\mathbf{k}+\mathbf{G}}$ corresponding to small kinetic energies are typically more important, convergence with respect to the cut-off energy is crucial for the accuracy of the calculations. Convergence with respect to the basis set, however, is easily achieved by increasing E_{cut} until the respective differences in total energy approximate zero.

Next to their simplicity, plane waves have several advantages. The basis set is orthonormal by construction and, as mentioned above, it is simple to check for convergence. The biggest advantage, however, is the ability to perform exact calculations by a discrete sum over a numerical grid. This is due to the related construction of the grid and the PW basis. Of course, exactness is restricted by the fact that the PW basis set is finite. The simple form of the PW representation of the KS equations

$$\sum_{\mathbf{G}'} \left[\frac{\hbar^2}{2m} |\mathbf{k}+\mathbf{G}|^2 \delta_{\mathbf{G}\mathbf{G}'} + \tilde{V}(\mathbf{G}-\mathbf{G}') + \tilde{V}_{\text{H}}(\mathbf{G}-\mathbf{G}') + \tilde{V}_{\text{xc}}(\mathbf{G}-\mathbf{G}') \right] c_{i,\mathbf{k}+\mathbf{G}} = \epsilon_i c_{i,\mathbf{k}+\mathbf{G}} \tag{3.35}$$

reveals further advantages. The various potentials are described in terms of their Fourier transforms. Equation (3.35) is solved by diagonalization of the Hamiltonian matrix $H_{\mathbf{k}+\mathbf{G},\mathbf{k}+\mathbf{G}'}$ given by the terms in the brackets. The gradient operator is diagonal in reciprocal space whereas the exchange-correlation potential has a diagonal representation in real space. This suggests to carry out different operations in real and reciprocal space, which requires frequent Fourier transformations. These, however, can be efficiently achieved by the fast Fourier transformation (FFT) algorithm.

There are likewise disadvantages associated with the PW representation. By construction, PW calculations require a periodic system. This does not pose a severe problem since nonperiodic systems can still be described by a suitable choice of the simulation cell. Describing a defect, for instance, requires the inclusion of enough bulk material in the simulation to prevent or reduce the interaction with its periodic, artificial images. As a consequence, the number of atoms involved in the calculations are increased. To describe surfaces, sufficiently thick vacuum layers need to be included to avoid interaction of adjacent crystal slabs. Clearly, to appropriately approximate the wave functions and the respective charge density of a system composed of vacuum in addition to the solid in a PW basis, an increase of the cut-off energy is required. According to equation (3.35), the size of the Hamiltonian depends on the cut-off energy and, therefore, the computational effort is likewise increased. For the same reason, the description of tightly bound core electrons and the respective, highly localized charge density is hindered. However, a much more profound problem exists whenever wave functions for the core as well as the valence electrons need to be calculated within a PW basis set. Wave functions of the valence electrons exhibit rapid oscillations in the region occupied by the core electrons near the nuclei. The oscillations maintain the orthogonality between the wave functions of the core and valence electrons, which is compulsory due to the exclusion principle. Accurately approximating these oscillations demands for an extremely large PW basis set, which is too large for practical use. Fortunately, the impossibility to model the core in addition to the valence electrons is eliminated in the pseudopotential approach discussed in the next section.

3.2.6 Pseudopotentials

As discussed in the last part of the previous section, an extremely large basis set of plane waves would be required to perform an all-electron calculation and a vast amount of computational time would be required to calculate the electronic wave functions. It is worth to stress out one more time that this is mainly due to the orthogonalization wiggles of the wave functions of valence electrons near the nuclei. Thus, existing core states practically prevent the use of a PW basis set. However, the core electrons, which are tightly bound to the nuclei, do not contribute significantly to chemical bonding or other physical properties of the solid. This fact is exploited in the pseudopotential (PP) approach [177] by removing the core electrons and replacing the atom and the associated strong ionic potential by a pseudoatom and a weaker PP that acts on a set of pseudo wave functions rather than the true valance wave functions. This way, the pseudo wave functions become smooth near the nuclei.

Most PPs satisfy four general conditions. The pseudo wave functions generated by the PP should not contain nodes, i.e. the pseudo wave functions should be smooth and free of wiggles in the core region. Outside the core region, the pseudo and real valence wave functions as well as the generated charge densities need to be identical. The charge enclosed within the core region must be equal for both wave functions. Last, almost redundantly, the valence all-electron and pseudopotential eigenvalues must be equal. Pseudopotentials that meet the conditions outlined above are referred to as norm-conserving pseudopotentials [178].

In order to achieve these properties, different PPs are required for the different shapes of the orbitals, which are determined by their angular momentum. Mathematically, a non-local PP, which depends on the angular momentum, has the form

$$V_{\mathrm{nl}}(\mathbf{r}) = \sum_{lm} |lm\rangle V_l(\mathbf{r}) \langle lm| \ . \tag{3.36}$$

Applying the operator $V_{\mathrm{nl}}(\mathbf{r})$ decomposes the electronic wave functions into spherical harmonics $|lm\rangle$, i.e. the orbitals with azimuthal angular momentum l and magnetic number m, which are then multiplied by the respective pseudopotential $V_l(\mathbf{r})$ for angular momentum l. The standard generation procedure of pseudopotentials proceeds by varying its parameters until the pseudo eigenvalues are equal to the all-electron valence eigenvalues and the pseudo wave functions match the all-electron valence wave functions beyond a certain cut-off radius determining the core region. Modified methods to generate ultra-soft pseudopotentials were proposed, which address the rapid convergence with respect to the size of the plane wave basis set [179, 180].

Using PPs, the rapid oscillations of the wave functions near the core of the atoms are removed considerably reducing the number of plane waves necessary to appropriately expand the wave functions. More importantly, less accuracy is required compared to all-electron calculations to determine energy differences among ionic configurations, which almost totally appear in the energy of the valence electrons that are typically a factor 10^3 smaller than the energy of the core electrons.

3.2.7 Brillouin zone sampling

Following Bloch's theorem, only a finite number of electronic wave functions need to be calculated for a periodic system. However, to calculate quantities like the total energy or charge density, these have to be evaluated in a sum over an infinite number of **k** points. Since the values of the wave function within a small interval around **k** are almost identical, it is possible to approximate the infinite sum by a sum over an affordable number of **k** points, each representing the respective region of the wave function in **k** space. Methods have been derived for obtaining very accurate approximations by a summation over special sets of **k** points with distinct, associated weights [181–183]. If present, symmetries in reciprocal space may further reduce the number of calculations. For supercells, i.e. repeating unit cells that contain several primitive cells, restricting the sampling of the Brillouin zone (BZ) to the Γ point can yield quite accurate results. In fact, with respect to BZ sampling, calculating wave functions of a supercell containing n primitive cells for only one **k** point is equivalent to the scenario of a single primitive cell and the summation over n points in **k** space. In general, finer **k**-point meshes better account for the periodicity of a system, which in some cases, however, might be fictitious anyway.

3.2.8 Structural relaxation and Hellmann-Feynman theorem

Up to this point, the system is in the ground state with respect to the electronic subsystem while the positions of the ions as well as size and shape of the supercell are fixed. To investigate equilibrium structures, however, the ionic subsystem must also be allowed to relax into a minimum energy configuration. Local minimum configurations can be easily obtained in a MD-like way by moving the nuclei over small distances along the directions of the forces, as discussed in the MD chapter above. Clearly, the conjugate gradient method constitutes a more sophisticated scheme, which will locate the equilibrium positions of the ions more rapidly. To find the global minimum, i.e. the absolute ground state, methods like simulated annealing or the Monte Carlo technique, which allow the system to escape local minima, have to be used for the search.

The force on an ion is given by the negative derivative of the total energy with respect to the position of the ion. However, moving an ion, i.e. altering its position, changes the wave functions to the KS eigenstates corresponding to the new ionic configuration. Writing down the derivative of the total energy E with respect to the position $\mathbf{R}_i$ of ion i

$$\frac{dE}{d\mathbf{R_i}} = \sum_j \langle \Phi_j | \frac{\partial H}{\partial \mathbf{R}_i} | \Phi_j \rangle + \sum_j \langle \frac{\partial \Phi_j}{\partial \mathbf{R}_i} | H \Phi_j \rangle + \sum_j \langle \Phi_j H | \frac{\partial \Phi_j}{\partial \mathbf{R}_i} \rangle \ , \tag{3.37}$$

indeed reveals a contribution to the change in total energy due to the change of the wave functions Φ_j. However, provided that the Φ_j are eigenstates of H, it is easy to show that the last two terms cancel each other and in the special case of $H = T + V$ the force is given by

$$\mathbf{F}_i = - \sum_j \langle \Phi_j | \frac{\partial V}{\partial \mathbf{R}_i} \Phi_j \rangle \ . \tag{3.38}$$

This is called the Hellmann-Feynman theorem [184], which enables the calculation of forces, called the Hellmann-Feynman forces, acting on the nuclei for a given configuration, without the need for evaluating computationally costly energy maps.

3.3 Modeling of point defects

Point defects are defects that affect a single lattice site. At this site, the crystalline periodicity is interrupted. An empty lattice site, which would be occupied in the perfect crystal structure, is called a vacancy defect. If an additional atom is incorporated into the perfect crystal, this is called interstitial defect. A substitutional defect exists, if an atom belonging to the perfect crystal is replaced with an atom of another species. The disturbance caused by these defects may result in the distortion of the surrounding atomic structure and is accompanied by an increase in configurational energy. Thus, next to the structure of the defect, the energy needed to create such a defect, i.e. the defect formation energy, is an important value characterizing the defect and likewise determining its relative stability.

The formation energy of a defect is defined by

$$E_{\text{f}} = E - \sum_i N_i \mu_i \ , \tag{3.39}$$

where E is the total energy of the interstitial structure involving N_i atoms of type i with chemical potential μ_i. Here, the chemical potentials are determined by the chemical potential of the respective equilibrium bulk structure, i.e. the cohesive energy per atom for the fully relaxed structure at zero temperature and pressure. Considering C interstitial defects in Si, the chemical potential for C could also be determined by the cohesive energies of Si and SiC according to the relation $\mu_{\text{C}} = \mu_{\text{SiC}} - \mu_{\text{Si}}$ of the chemical potentials. In this way, SiC is chosen as a reservoir for the C impurity. For defect configurations consisting of a single atom species the formation energy reduces to

$$E_{\text{f}} = \left(E_{\text{coh}}^{\text{defect}} - E_{\text{coh}}^{\text{defect-free}} \right) N \ , \tag{3.40}$$

where N and $E_{\text{coh}}^{\text{defect}}$ are the number of atoms and the cohesive energy per atom in the defect configuration and $E_{\text{coh}}^{\text{defect-free}}$ is the cohesive energy per atom of the defect-free structure. Clearly, for a single atom species equation (3.39) is equivalent to equation (3.40) since $NE_{\text{coh}}^{\text{defect}}$

is equal to the total energy of the defect structure and $NE_{\text{coh}}^{\text{defect-free}}$ corresponds to $N\mu$, provided the structure is fully relaxed at zero temperature.

However, there is hardly ever only one defect in a crystal, not even only one kind of defect. Again, energetic considerations can be used to investigate the existing interaction of two defects. The binding energy E_{b} of a defect pair is given by the difference of the formation energy of the defect combination $E_{\text{f}}^{\text{comb}}$ and the sum of the two separated defect configurations $E_{\text{f}}^{1^{\text{st}}}$ and $E_{\text{f}}^{2^{\text{nd}}}$. This can be expressed by

$$E_{\text{b}} = E_{\text{f}}^{\text{comb}} - E_{\text{f}}^{1^{\text{st}}} - E_{\text{f}}^{2^{\text{nd}}} \tag{3.41}$$

where the formation energies $E_{\text{f}}^{\text{comb}}$, $E_{\text{f}}^{1^{\text{st}}}$ and $E_{\text{f}}^{2^{\text{nd}}}$ are determined as discussed above. Accordingly, energetically favorable configurations result in binding energies below zero while unfavorable configurations show positive values for the binding energy. The interaction strength, i.e. the absolute value of the binding energy, approaches zero for increasingly non-interacting isolated defects. Thus, E_{b} indeed can be best thought of a binding energy, which is required to bring the defects to infinite separation.

The methods presented in the last two chapters can be used to investigate defect structures and energetics. Therefor, a supercell containing the perfect crystal is generated in an initial process. If not by construction, the system should be fully relaxed. The substitutional or vacancy defect is realized by replacing or removing one atom contained in the supercell. Interstitial defects are created by adding an atom at positions located in the space between regular lattice sites. Once the intuitively created defect structure is generated, structural relaxation methods will yield the respective local minimum configuration. Since the supercell approach applies periodic boundary conditions, enough bulk material surrounding the defect is required to exclude possible interaction of the defect with its periodic image.

The respective estimated interstitial insertion positions for various interstitial structures in a diamond lattice are displayed in Fig. 3.2. The labels of the interstitial types indicate their positions in the interstitial lattice. In a dumbbell (DB) configuration two atoms share a single lattice site along a certain direction that is also comprehended in the label of the defect. For the DB configurations the nearest atom of the bulk lattice is slightly displaced by $(0, 0, -1/8)$ and $(-1/8, -1/8, 0)$ of the unit cell length respectively. This is indicated by the dashed, unfilled circles. By this, high forces, which might enable the system to overcome barriers of the local minimum configuration and, thus, result in a different structure, are avoided.

3.4 Migration paths and diffusion barriers

Investigating diffusion mechanisms is based on determining migration paths in between two local minimum configurations of an atom at different locations in the lattice. During migration, the total energy of the system increases, traverses at least one maximum of the configurational energy and finally decreases to a local minimum value. The maximum difference in energy is the barrier necessary for the respective migration process. The path exhibiting the minimal energy difference determines the diffusion path and associated diffusion barrier and the maximum configuration turns into a saddle point configuration.

One possibility to compute the migration path from one stable configuration into another one is provided by the constrained relaxation technique (CRT) [185]. The atoms involving great structural changes in the diffusion process are moved stepwise from the starting to the

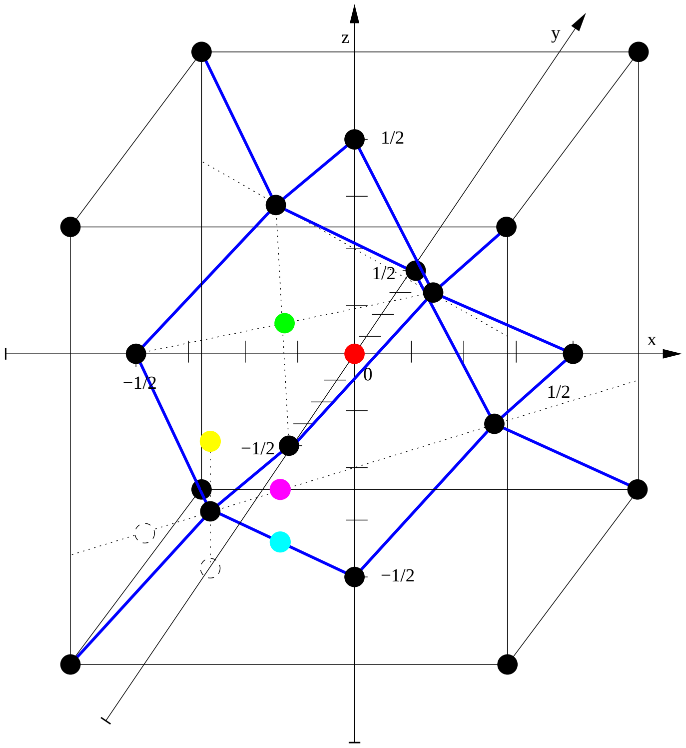

Figure 3.2: Insertion positions for the tetrahedral (●), hexagonal (●), ⟨1 0 0⟩ dumbbell (●), ⟨1 1 0⟩ dumbbell (●) and bond-centered (●) interstitial defect atom in the diamond lattice. The black dots correspond to the lattice atoms and the blue lines indicate the covalent bonds of the perfect diamond structure.

final position and relaxation after each step is only allowed in the plane perpendicular to the direction of the vector connecting its starting and final position. This is illustrated in Fig. 3.3(a). The number of steps required for smooth transitions depends on the shape of the potential energy surface. No constraints are applied to the remaining atoms to allow for the relaxation of the surrounding lattice. To prevent the remaining lattice to shift according to the displacement of the defect, however, some atoms far away from the defect region should be fixed in all three coordinate directions. However, for the present study, the method tremendously failed. Abrupt changes in structure and configurational energy occurred among relaxed structures of two successive displacement steps. For some structures even the expected final configurations are not obtained. Thus, the method mentioned above is adjusted adding further constraints in order to obtain smooth transitions with respect to energy and structure. In the modified method all atoms are stepwise displaced towards their final positions. In addition to this, relaxation of each individual atom is only allowed in the plane perpendicular to the last individual displacement vector, as displayed in Fig. 3.3(b). In the modified version respective energies could be higher than the real ones due to the additional constraints that prevent a more adequate relaxation until the final configuration is reached.

Structures of maximum configurational energy do not necessarily constitute saddle point configurations, i.e. the method does not guarantee to find the true minimum energy path. Whether a saddle point configuration and, thus, the minimum energy path is obtained by the

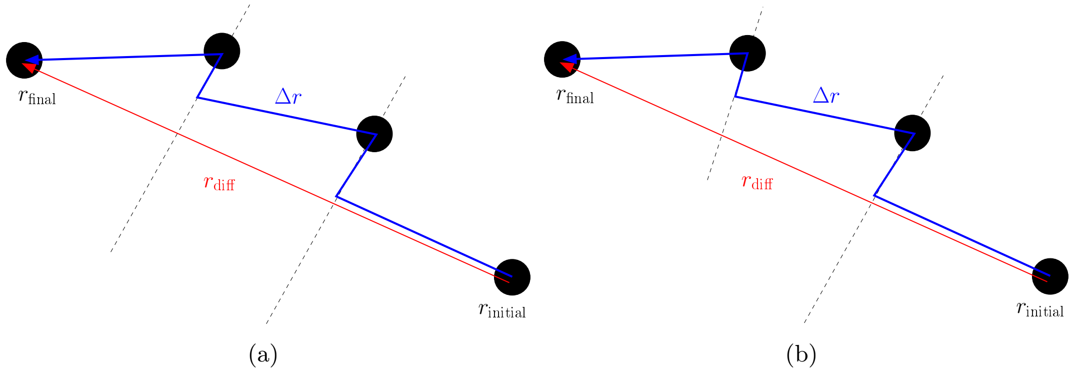

(a) (b)

Figure 3.3: Schematic of the constrained relaxation technique (a) and of a modified version (b) used to obtain migration pathways and corresponding configurational energies.

CRT method, needs to be verified by calculating the respective vibrational modes. Modifications used to add the CRT feature to the VASP code and a short instruction on how to use it can be found in appendix B.

Chapter 4

Details of simulation parameters and test calculations

All calculations are carried out utilizing the supercell approach, which means that the simulation cell contains a multiple of unit cells and periodic boundary conditions are imposed on the boundaries of that simulation cell. Strictly, these supercells become the unit cells, which, by a periodic sequence, compose the bulk material that is actually investigated by this approach. Thus, importance need to be attached to the construction of the supercell. Three basic types of supercells to compose the initial Si bulk lattice, which can be scaled by integers in the different directions, are considered. The basis vectors of the supercells are shown in Fig. 4.1. Type 1 (Fig. 4.1(a)) constitutes the primitive cell. The basis is face-centered cubic and is given by $x_1 = (0.5, 0.5, 0)$, $x_2 = (0, 0.5, 0.5)$ and $x_3 = (0.5, 0, 0.5)$. Two atoms, one at $(0, 0, 0)$ and the other at $(0.25, 0.25, 0.25)$ with respect to the basis, generate the Si diamond primitive cell. Type 2 (Fig. 4.1(b)) covers two primitive cells with 4 atoms. The basis is given by $x_1 = (0.5, -0.5, 0)$, $x_2 = (0.5, 0.5, 0)$ and $x_3 = (0, 0, 1)$. Type 3 (Fig. 4.1(c)) contains 4 primitive cells with 8 atoms and corresponds to the unit cell shown in Fig. 2.3. The basis is simple cubic.

In the following, an overview of the different simulation procedures and respective parameters is presented. These procedures and parameters differ depending on whether classical potentials or *ab initio* methods are used as well as on the object of investigation.

4.1 DFT calculations

The first-principles DFT calculations are performed with the plane-wave-based Vienna *ab initio* simulation package (VASP) [148]. The Kohn-Sham equations are solved using the GGA utilizing the exchange-correlation functional proposed by Perdew and Wang (GGA-PW91) [186, 187]. The electron-ion interaction is described by norm-conserving ultra-soft pseudopotentials as implemented in VASP [179]. An energy cut-off of 300 eV is used to expand the wave functions into the plane-wave basis. Sampling of the Brillouin zone is restricted to the Γ point. Spin polarization has been fully accounted for. The electronic ground state is calculated by an iterative Davidson scheme [188] until the difference in total energy of two subsequent iterations is below 10^{-4} eV.

Defect structures and the migration paths have been modeled in cubic supercells of type 3 containing 216 Si atoms. The conjugate gradient algorithm is used for ionic relaxation.

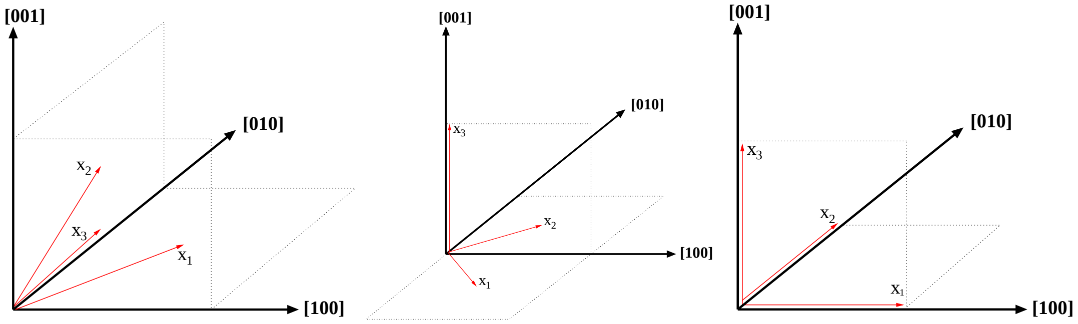

(a) (b) (c)

Figure 4.1: Basis vectors of three basic types of supercells used to create the initial Si bulk lattice.

Migration paths are determined by the modified version of the CRT method as explained in section 3.4. The cell volume and shape is allowed to change using the pressure control algorithm of Parrinello and Rahman [189] in order to realize constant pressure simulations. Due to restrictions by the VASP code, *ab initio* MD could only be performed at constant volume. In MD simulations the equations of motion are integrated by a fourth order predictor corrector algorithm for a time step of 1 fs.

Most of the parameter settings, as determined above, constitute a tradeoff regarding the tasks that need to be addressed. These parameters include the size of the supercell, cut-off energy and **k**-point mesh. The choice of these parameters is considered to reflect a reasonable treatment with respect to both, computational efficiency and accuracy, as will be shown in the next sections. Furthermore, criteria concerning the choice of the potential and the exchange-correlation (XC) functional are being outlined. Finally, the utilized parameter set is tested by comparing the calculated values of the cohesive energy and the lattice constant to experimental data.

4.1.1 Supercell

Describing defects within the supercell approach runs the risk of a possible interaction of the defect with its periodic, artificial images. Obviously, the interaction reduces with increasing system size and will be negligible from a certain size on. To estimate a critical size, the formation energies of several intrinsic defects in Si with respect to the system size are calculated. An energy cut-off of 250 eV and a $4 \times 4 \times 4$ Monkhorst-Pack **k**-point mesh [183] is used. The results are displayed in Fig. 4.2. The formation energies converge fast with respect to the system size. Thus, investigating supercells containing more than 56 primitive cells or 112 ± 1 atoms should be reasonably accurate.

4.1.2 Brillouin zone sampling

Throughout this work sampling of the BZ is restricted to the Γ point. The calculation is usually two times faster and half of the storage needed for the wave functions can be saved since $c_{i,q} = c^*_{i,-q}$, where the $c_{i,q}$ are the Fourier coefficients of the wave function. As discussed in section 3.2.7, this does not pose a severe limitation if the supercell is large enough. Indeed, it was shown [190] that already for calculations involving only 32 atoms,

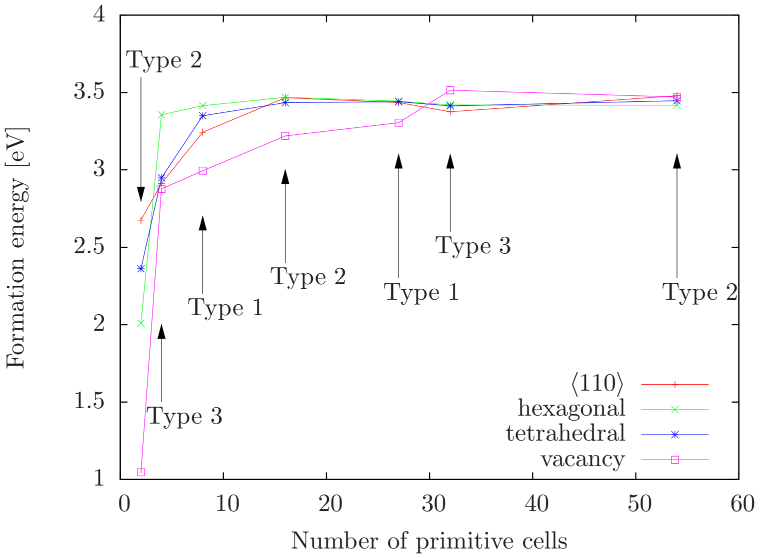

Figure 4.2: Defect formation energies of several defects in c-Si with respect to the size of the supercell.

energy values obtained by sampling the Γ point differ by less than 0.02 eV from calculations using the Baldereschi point [181], which constitutes a mean-value point in the BZ. Thus, the calculations of the present study on supercells containing 108 primitive cells can be considered sufficiently converged with respect to the **k**-point mesh.

4.1.3 Energy cut-off

To determine an appropriate cut-off energy of the plane-wave basis set, a $2 \times 2 \times 2$ supercell of type 3 containing 32 Si and 32 C atoms in the 3C-SiC structure is equilibrated for different cut-off energies in the LDA. Fig. 4.3 shows the respective lattice constants of the relaxed 3C-SiC structure with respect to the cut-off energy. As can be seen, convergence is reached already for low energies. Obviously, an energy cut-off of 300 eV, although the minimum acceptable, is sufficient for the plane-wave expansion.

4.1.4 Potential and exchange-correlation functional

To find the most suitable combination of potential and XC functional for the C/Si system, a $2 \times 2 \times 2$ supercell of type 3 of Si and C, both in the diamond structure, as well as 3C-SiC is equilibrated for different combinations of the available potentials and XC functionals. To exclude a possibly corrupting influence of the other parameters, highly accurate calculations are performed, i.e. an energy cut-off of 650 eV and a $6 \times 6 \times 6$ Monkhorst-Pack **k**-point mesh is used. Next to the ultra-soft pseudopotentials [179], VASP offers the projector augmented-wave method (PAW) [191] to describe the ion-electron interaction. The two XC functionals included in the test are of the LDA [172, 173] and GGA [186, 187] type as implemented in VASP.

Table 4.1 shows the lattice constants and cohesive energies obtained for the fully relaxed structures with respect to the utilized potential and XC functional. As expected, cohesive

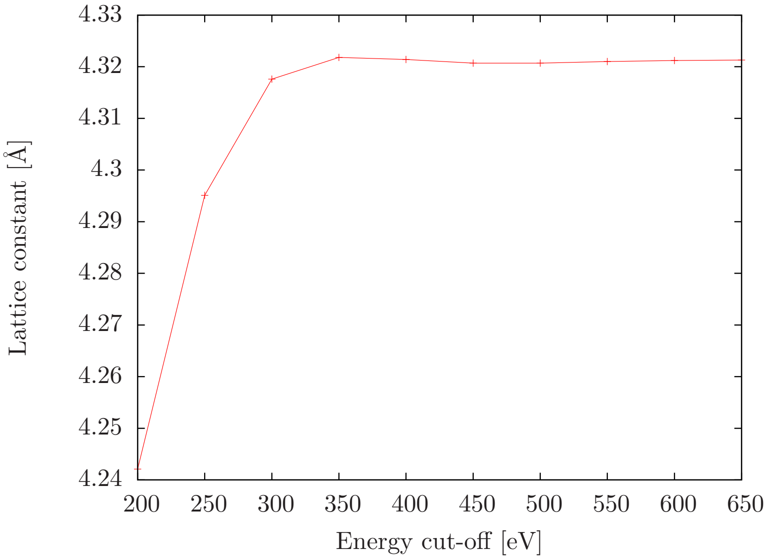

Figure 4.3: Lattice constants of 3C-SiC with respect to the cut-off energy used for the plane-wave basis set.

energies are poorly reproduced by the LDA whereas the equilibrium lattice constants are in good agreement. Using GGA together with the ultra-soft pseudopotential yields improved lattice constants and, more importantly, a very nice agreement of the cohesive energies to the experimental data. The 3C-SiC calculations employing the PAW method in conjunction with the LDA suffers from the general problem inherent to LDA, i.e. overestimated binding energies. Thus, the PAW & LDA combination is not pursued. Since the lattice constant and cohesive energy of 3C-SiC calculated by the PAW method using the GGA are not improved compared to the ultra-soft pseudopotential calculations using the same XC functional, this concept is likewise stopped. To conclude, the combination of ultra-soft pseudopotentials and the GGA XC functional are considered the optimal choice for the present study.

4.1.5 Lattice constants and cohesive energies

As a last test, the equilibrium lattice parameters and cohesive energies of Si, C (diamond) and 3C-SiC are again compared to experimental data. However, in the current calculations, the entire parameter set as determined in the beginning of this section is applied. Table 4.2 shows the respective results and deviations from experiment. A nice agreement with experimental results is achieved. Clearly, a competent parameter set is found, which is capable of describing the C/Si system by *ab initio* calculations.

4.2 Classical potential MD

The classical potential MD method is much less computationally costly compared to the highly accurate quantum-mechanical method. Thus, the method is capable of performing structural optimizations on large systems and MD calculations may be used to model a system over long time scales. Defect structures are modeled in a cubic supercell (type 3) of nine Si lattice

		USPP, LDA	USPP, GGA	PAW, LDA	PAW, GGA	Exp.
Si (dia)	a [Å]	5.389	5.455	-	-	5.429
	Δ_a [%]	0.7 %	0.5 %	-	-	-
	E_{coh} [eV]	-5.277	-4.591	-	-	-4.63
	Δ_E [%]	14.0 %	0.8 %	-	-	-
C (dia)	a [Å]	3.527	3.567	-	-	3.567
	Δ_a [%]	1.1 %	0.01 %	-	-	-
	E_{coh} [eV]	-8.812	-7.703	-	-	-7.374
	Δ_E [%]	19.5 %	4.5 %	-	-	-
3C-SiC	a [Å]	4.319	4.370	4.330	4.379	4.359
	Δ_a [%]	0.9 %	0.3 %	0.7 %	0.5 %	-
	E_{coh} [eV]	-7.318	-6.426	-7.371	-6.491	-6.340
	Δ_E [%]	15.4 %	1.4 %	16.3 %	2.4 %	-

Table 4.1: Equilibrium lattice constants and cohesive energies of fully relaxed structures of Si, C (diamond) and 3C-SiC for different potentials (ultra-soft PP and PAW) and XC functionals (LDA and GGA). Deviations of the respective values from experimental values are given. Values are in good (green), fair (orange) and poor (red) agreement.

	Si (dia)	C (dia)	3C-SiC
a [Å]	5.458	3.562	4.365
Δ_a [%]	0.5	0.1	0.1
E_{coh} [eV]	-4.577	-7.695	-6.419
Δ_E [%]	1.1	4.4	1.2

Table 4.2: Equilibrium lattice constants and cohesive energies of Si, C (diamond) and 3C-SiC using the entire parameter set as determined in the beginning of this section.

constants in each direction containing 5832 Si atoms. Reproducing the SiC precipitation was attempted in cubic c-Si supercells, which have a size up to 31 Si unit cells in each direction consisting of 238328 Si atoms. A Tersoff-like bond order potential by Erhart and Albe (EA) [147] is used to describe the atomic interaction. Constant pressure simulations are realized by the Berendsen barostat [162] using a time constant of 100 fs and a bulk modulus of 100 GPa for Si. The temperature is controlled by the Berendsen thermostat [162] with a time constant of 100 fs. Integration of the equations of motion is realized by the velocity Verlet algorithm [161] using a fixed time step of 1 fs. For structural relaxation of defect structures, the same algorithm is utilized with the temperature set to zero Kelvin. This also applies for the relaxation of structures within the CRT calculations to find migration pathways. In the latter case the time constant of the Berendsen thermostat is set to 1 fs in order to achieve direct velocity scaling, which corresponds to a steepest descent minimization driving the system into a local minimum, if the temperature is set to zero Kelvin. However, in some cases a time constant of 100 fs turned out to result in lower barriers. Defect structures as well as the simulations modeling the SiC precipitation are performed in the isothermal-isobaric NpT ensemble.

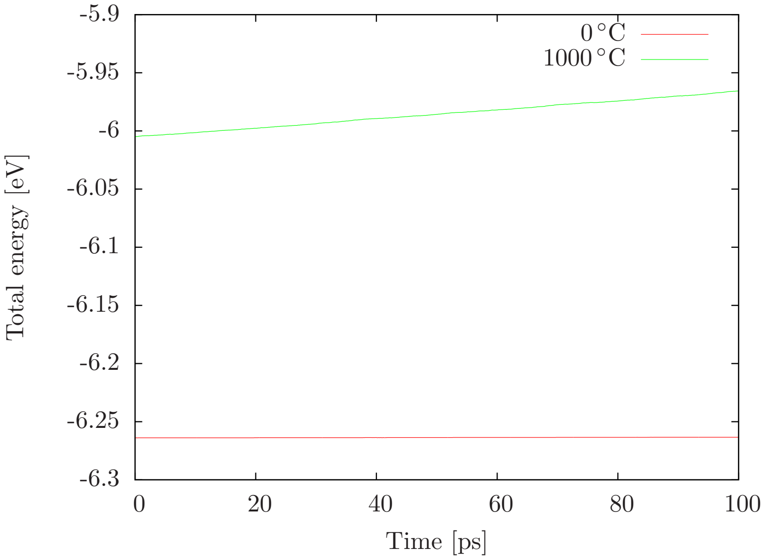

Figure 4.4: Evolution of the total energy of 3C-SiC in the *NVE* ensemble for two different initial temperatures.

In addition to the bond order formalism, the EA potential provides a set of parameters to describe the interaction in the C/Si system, as discussed in section 3.1.2. There are basically no free parameters, which could be set by the user, and the properties of the potential and its parameters are well known and have been extensively tested by the authors [147]. Therefore, test calculations are restricted to the time step used in the Verlet algorithm to integrate the equations of motion. Nevertheless, a further and rather uncommon test is carried out to roughly estimate the capabilities of the EA potential regarding the description of 3C-SiC precipitation in c-Si.

4.2.1 Time step

The quality of the integration algorithm and the occupied time step of 1 fs is determined by the ability to conserve the total energy. Therefor, simulations of a $9 \times 9 \times 9$ 3C-SiC unit cell containing 5832 atoms in total are carried out in the *NVE* ensemble. The calculations are performed for 100 ps corresponding to 10^5 integration steps and two different initial temperatures are considered, i.e. 0 °C and 1000 °C. The evolution of the total energy is displayed in Fig. 4.4. Almost no shift in energy is observable for the simulation at 0 °C. Even for 1000 °C the shift is as small as 0.04 eV, which is a quite acceptable error for 10^5 integration steps. Thus, using a time step of 1 fs is considered small enough.

4.2.2 3C-SiC precipitate in c-Si

Below, a spherical 3C-SiC precipitate enclosed in a c-Si surrounding is investigated by means of MD. On the one hand, these investigations are meant to draw conclusions on the capabilities of the potential for modeling the respective tasks in the C/Si system. Since, on the other hand, properties of the 3C-SiC precipitate, its surrounding as well as the interface can be

	C in 3C-SiC	Si in 3C-SiC	Si in c-Si surrounding	total amount of Si
Obtained	5495	5486	68591	74077
Expected	5500	5500	68588	74088
Difference	-5	-14	3	-11
Notation	$N_{\text{C}}^{\text{3C-SiC}}$	$N_{\text{Si}}^{\text{3C-SiC}}$	$N_{\text{Si}}^{\text{c-Si}}$	$N_{\text{Si}}^{\text{total}}$

Table 4.3: Comparison of the expected and obtained amounts of Si and C atoms by applying the values from equations (4.2) and (4.3) in the 3C-SiC precipitate construction approach.

obtained, the calculations could be considered to constitute a first investigation rather than a test of the capabilities of the potential.

Interfacial energy

To construct a spherical and topotactically aligned 3C-SiC precipitate in c-Si, the approach illustrated in the following is applied. A total simulation volume V consisting of 21 unit cells of c-Si in each direction is created. To obtain a minimal and stable precipitate, 5500 carbon atoms are considered necessary according to experimental results as discussed in section 2.2.3 and 2.4. This corresponds to a spherical 3C-SiC precipitate with a radius of approximately 3 nm. The initial precipitate configuration is constructed in two steps. In the first step, the surrounding Si matrix is created. This is realized by just skipping the generation of Si atoms inside a sphere of radius x, which is the first unknown variable. The Si lattice constant a_{Si} of the surrounding c-Si matrix is assumed to not alter dramatically and, thus, is used for the initial lattice creation. In a second step 3C-SiC is created inside the empty sphere of radius x. The lattice constant y, the second unknown variable, is chosen in such a way that the necessary amount of carbon is generated and that the total amount of silicon atoms corresponds to the usual amount contained in the simulation volume. This is entirely described by the equation

$$\frac{8}{a_{\text{Si}}^3}(V-\frac{4}{3}\pi x^3)+\frac{4}{y^3}\frac{4}{3}\pi x^3=21^3\cdot 8\ , \tag{4.1}$$

where the volume is given by $V=21^3 a_{\text{Si}}^3$ and the the additional condition $\frac{4}{y^3}\frac{4}{3}\pi x^3=5500$. This can be simplified to read

$$\frac{8}{a_{\text{Si}}^3}\frac{4}{3}\pi x^3=5500\Rightarrow x=\left(\frac{5500\cdot 3}{32\pi}\right)^{1/3}a_{\text{Si}} \tag{4.2}$$

and

$$y=\left(\frac{1}{2}\right)^{1/3}a_{\text{Si}}\ . \tag{4.3}$$

By this means, values of 2.973 nm and 4.309 Å are obtained for the initial precipitate radius and lattice constant of 3C-SiC. Since the generation of atoms is a discrete process with regard to the size of the volume, the expected amounts of atoms are not obtained. However, by applying these values, the final configuration varies only slightly from the expected one by five carbon and eleven silicon atoms, as can be seen in Table 4.3.

After the initial configuration is constructed, some of the atoms located at the 3C-SiC/c-Si interface show small distances, which results in high repulsive forces acting on the atoms.

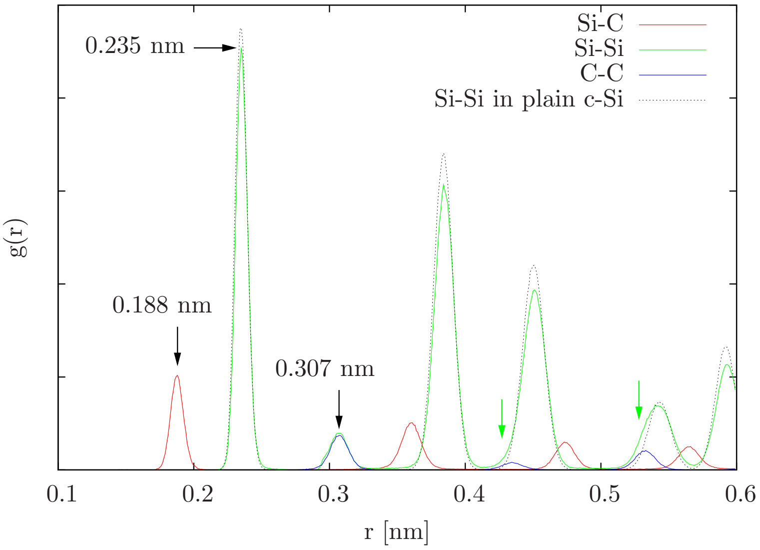

Figure 4.5: Radial distribution of a 3C-SiC precipitate embedded in c-Si at 20 °C. The Si-Si radial distribution of plain c-Si is plotted for comparison. Green arrows mark bumps in the Si-Si distribution of the precipitate configuration, which do not exist in plain c-Si.

Thus, the system is equilibrated using strong coupling to the heat bath, which is set to be 20 °C. Once the main part of the excess energy is carried out, previous settings for the Berendsen thermostat are restored and the system is relaxed for another 10 ps.

Fig. 4.5 shows the radial distribution of the obtained precipitate configuration. The Si-Si radial distribution for both, plain c-Si and the precipitate configuration show a maximum at a distance of 0.235 nm, which is the distance of next neighbored Si atoms in c-Si. Although no significant change of the lattice constant of the surrounding c-Si matrix was assumed, surprisingly, there is no change at all within observational accuracy. Looking closer at higher order Si-Si peaks might even allow the guess of a slight increase of the lattice constant compared to the plain c-Si structure. A new Si-Si peak arises at 0.307 nm, which is identical to the peak of the C-C distribution around that value. It corresponds to second next neighbors in 3C-SiC, which applies for Si as well as C pairs. The bumps of the Si-Si distribution at higher distances marked by the green arrows can be explained in the same manner. They correspond to the fourth and sixth next neighbor distance in 3C-SiC. It is easily identifiable how these C-C peaks, which imply Si pairs at same distances inside the precipitate, contribute to the bumps observed in the Si-Si distribution. The Si-Si and C-C peak at 0.307 nm enables the determination of the lattice constant of the embedded 3C-SiC precipitate. A lattice constant of 4.34 Å compared to 4.36 Å for bulk 3C-SiC is obtained. This is in accordance with the peak of Si-C pairs at a distance of 0.188 nm. Thus, the precipitate structure is slightly compressed compared to the bulk phase. This is a quite surprising result since due to the finite size of the c-Si surrounding, a non-negligible impact of the precipitate on the materializing c-Si lattice constant especially near the precipitate could be assumed. However, it seems that the size of the c-Si host matrix is chosen large enough to even find the precipitate in a compressed state.

The absence of a compression of the c-Si surrounding is due to the possibility of the system to change its volume. Otherwise, the increase of the lattice constant of the precipitate of roughly 4.31 Å in the beginning up to 4.34 Å in the relaxed precipitate configuration could not take place without an accompanying reduction of the lattice constant of the c-Si surrounding. If the total volume is assumed to be the sum of the volumes that are composed of Si atoms forming the c-Si surrounding and Si atoms involved forming the precipitate, the expected increase can be calculated by

$$\frac{V}{V_0} = \frac{\frac{N^{\text{c-Si}}_{\text{Si}}}{8/a_{\text{c-Si prec}}} + \frac{N^{\text{3C-SiC}}_{\text{Si}}}{4/a_{\text{3C-SiC prec}}}}{\frac{N^{\text{total}}_{\text{Si}}}{8/a_{\text{plain c-Si}}}} \tag{4.4}$$

with the notation used in Table 4.3. Here, $a_{\text{c-Si prec}}$ denotes the lattice constant of the surrounding crystalline Si and $a_{\text{3C-SiC prec}}$ is the lattice constant of the precipitate. The lattice constant of plain c-Si at 20 °C can be determined more accurately by the side lengths of the simulation box of an equilibrated structure instead of using the radial distribution data. By this, a value of $a_{\text{plain c-Si}} = 5.439$ Å is obtained. The same lattice constant is assumed for the c-Si surrounding in the precipitate configuration $a_{\text{c-Si prec}}$ since peaks in the radial distribution match the ones of plain c-Si. Using $a_{\text{3C-SiC prec}} = 4.34$ Å as observed from the radial distribution finally results in an increase of the initial volume by 0.12 %. However, each side length and the total volume of the simulation box is increased by 0.20 % and 0.61 % respectively compared to plain c-Si at 20 °C. Since the c-Si surrounding resides in an uncompressed state, the excess increase must be attributed to relaxation of strain with the strain resulting from either the compressed precipitate or the 3C-SiC/c-Si interface region. This also explains the possibly identified slight increase of the c-Si lattice constant in the surrounding as mentioned earlier. As the pressure is set to zero, the free energy is minimized with respect to the volume enabled by the Berendsen barostat algorithm. Apparently, the minimized structure with respect to the volume is a configuration of a small compressively stressed precipitate and a large amount of slightly stretched c-Si in the surrounding.

To finally draw some conclusions concerning the capabilities of the potential, the 3C-SiC/c-Si interface is now addressed. One important size analyzing the interface is the interfacial energy. A good estimate of the interfacial energy should be obtained by utilizing the formula for determining the defect formation energy as described in equation (3.39). Using the notation of Table 4.3 and assuming that the system is composed out of $N^{\text{3C-SiC}}_{\text{C}}$ C atoms forming the SiC compound plus the remaining Si atoms, the energy is given by

$$E_{\text{f}} = E - N^{\text{3C-SiC}}_{\text{C}} E^{\text{SiC}}_{\text{coh}} - \left(N^{\text{total}}_{\text{Si}} - N^{\text{3C-SiC}}_{\text{C}} \right) \mu^{\text{Si}}_{\text{coh}} \ , \tag{4.5}$$

where E is the total energy of the precipitate configuration at zero temperature. An interfacial energy of 2267.28 eV is obtained. The amount of C atoms together with the observed lattice constant of the precipitate leads to a precipitate radius of 29.93 Å. Thus, the interface tension, given by the energy of the interface divided by the surface area of the precipitate is 20.15 eV/nm^2 or 3.23×10^{-4} J/cm^2. This value perfectly fits within the experimentally estimated range of 2–8$\times 10^{-4}$ J/cm^2 [146]. Thus, the EA potential is considered an appropriate choice for the current study concerning the accurate description of the energetics of interfaces. Furthermore, since the calculated interfacial energy is located in the lower part of the experimental range, the obtained interface structure might resemble an authentic configuration of an energetically favorable interface structure of a 3C-SiC precipitate in c-Si.

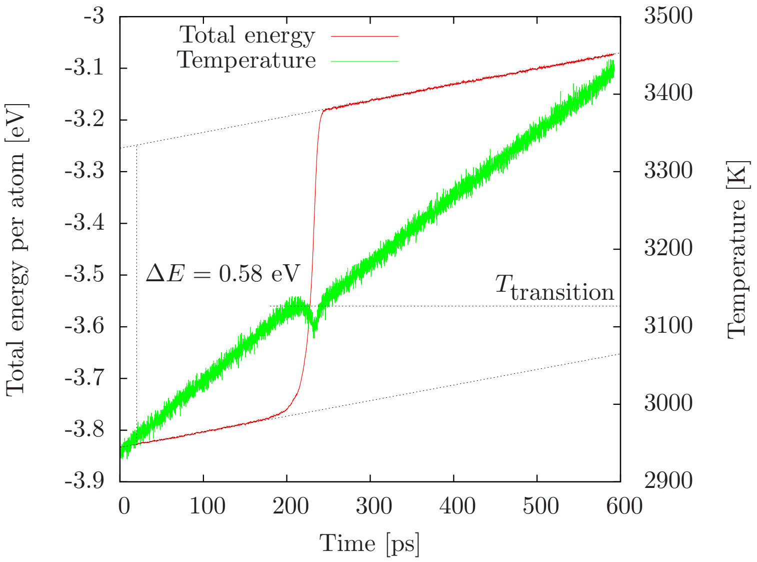

Figure 4.6: Total energy and temperature evolution of c-Si at temperatures in the region around the melting transition.

Stability of the precipitate

To investigate the stability of the precipitate, which is assumed to be stable even at temperatures above the Si melting temperature, the configuration is heated up beyond the critical point, at which the Si melting transition occurs. For this, the transition point of c-Si needs to be evaluated first. According to the authors of the potential, the Si melting point is 2450 K. However, melting is not predicted to occur instantly after exceeding the melting point due to the additionally required transition enthalpy and hysteresis behavior. To determine the transition point, c-Si is heated up using a heating rate of 1 °C/ps. Fig. 4.6 shows the total energy and temperature evolution in the region around the transition temperature. Indeed, a transition and the accompanied critical behavior of the total energy is first observed at approximately 3125 K, which corresponds to 128 % of the Si melting temperature. The difference in total energy is 0.58 eV per atom corresponding to 55.7 kJ/mole, which compares quite well to the Si enthalpy of melting of 50.2 kJ/mole.

The precipitate structure is heated up using the same heating rate. As can be seen in Fig. 4.7, which shows a cross-sectional image of the configuration at different temperatures, the precipitate is stable whereas melting of the surrounding Si host matrix starting at the interface region is observed. This is verified by the radial distribution function shown in Fig. 4.8, which displays configurations before and after the Si transition occurs. The precipitate itself is not involved in the transition, as indicated by the Si-C and C-C distribution, which essentially stays the same. It is only the c-Si surrounding undergoing a structural phase transition, which is very well reflected by the difference observed for the respective Si-Si distributions. The temperature of transition is determined to be around 2840 K. This is surprising since the melting transition of c-Si for the same heating conditions is expected at temperatures around 3125 K as discussed above. Obviously, the precipitate lowers the transition point of the surrounding c-Si matrix. This is indeed verified by the cross-sectional

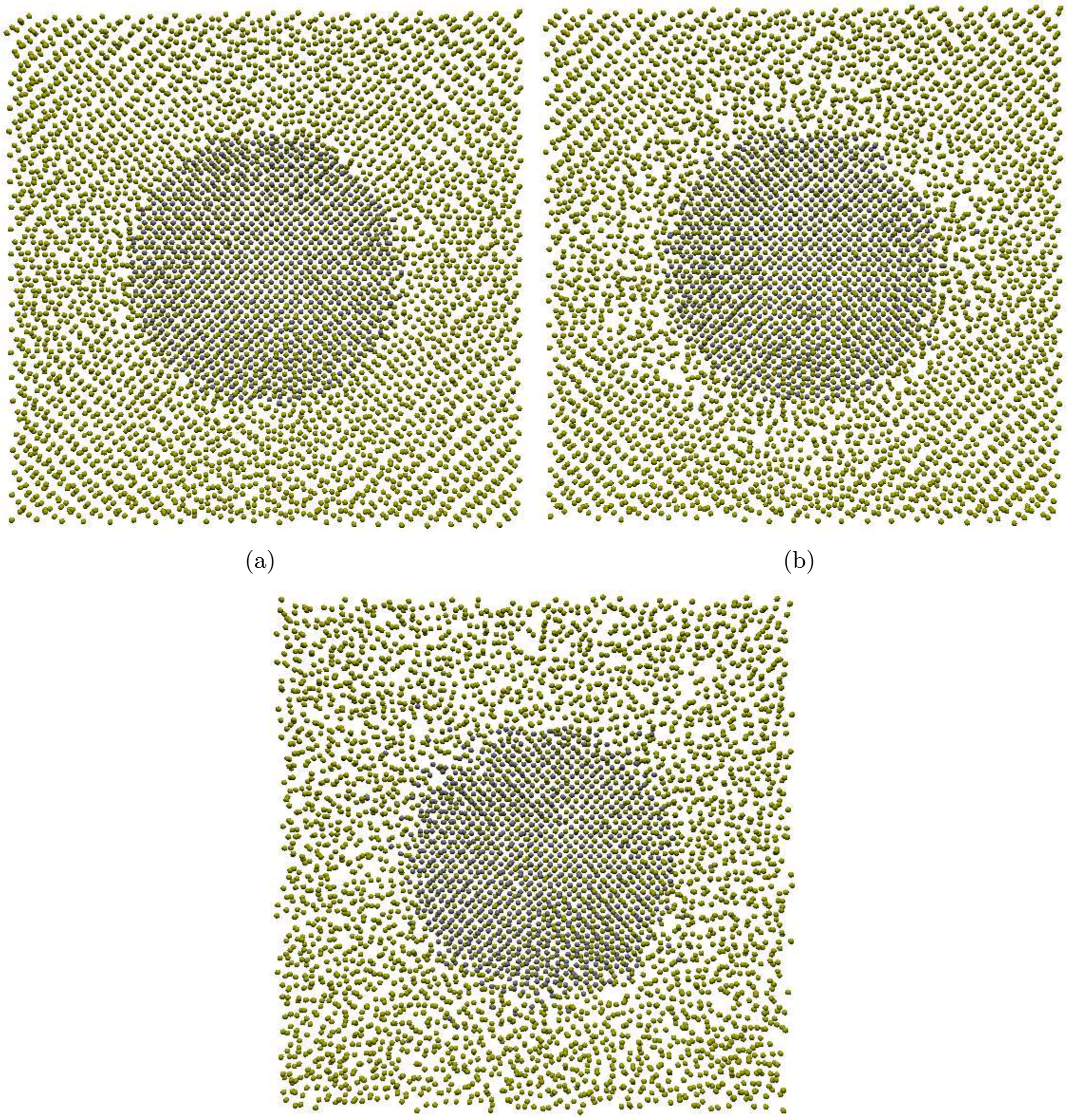

(a) (b)

(c)

Figure 4.7: Cross section image of the 3C-SiC precipitate in c-Si at temperatures before (a), at the onset of (b) and after (c) the Si melting transition.

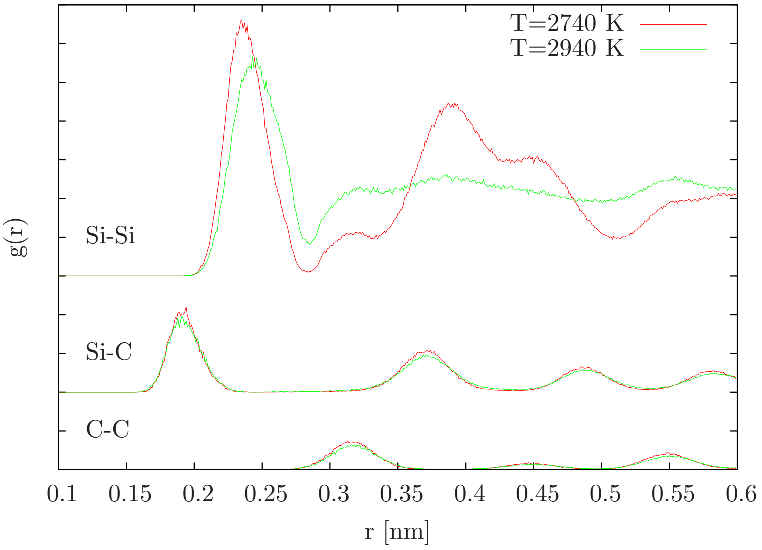

Figure 4.8: Radial distribution of a 3C-SiC precipitate embedded in c-Si at temperatures below and above the Si melting transition point.

images of the configurations shown in Fig. 4.7. Melting of the Si surrounding in fact starts in the defective interface region of the 3C-SiC precipitate and the c-Si surrounding propagating outwards until the whole Si matrix is affected.

Concluding remarks

To conclude, the obtained results, particularly the accurate value of the interface energy, the Si enthalpy of melting as well as the stability of the 3C-SiC structure give quite a good feeling concerning the applicability of the potential.

Chapter 5

Point defects in silicon

Regarding the supposed conversion mechanisms of SiC in c-Si as introduced in section 2.4, the understanding of C and Si interstitial point defects in c-Si is of fundamental interest. During implantation, defects such as vacancies (V), substitutional C (C_s), interstitial C (C_i) and Si self-interstitials (Si_i) are created, which are believed to play a decisive role in the precipitation process. In the following, these defects are systematically examined by computationally efficient classical potential as well as highly accurate DFT calculations with the parameters and simulation conditions that are defined in chapter 4. Both methods are used to investigate selected diffusion processes of some of the defect configurations. While the quantum-mechanical description yields results that excellently compare to experimental findings, shortcomings of the classical potential approach are identified. These shortcomings are further investigated and the basis for a workaround, as proposed later on in the classical MD simulation chapter, is discussed.

However, the implantation of highly energetic C atoms results in a multiplicity of possible defect configurations. Next to individual Si_i, C_i, V and C_s defects, combinations of these defects and their interaction are considered important for the problem under study. Thus, investigations proceed examining pairs of most probable defect configurations and related diffusion processes exclusively by first-principles methods. These systems can still be described by the highly accurate but computationally costly method. Respective results allow to draw conclusions concerning the SiC precipitation in Si.

5.1 Silicon self-interstitials

For investigating the Si_i structures, a Si atom is inserted or removed according to Fig. 3.2 of section 3.3. The formation energies of Si_i configurations are listed in Table 5.1 for both methods used in this work as well as results obtained by other *ab initio* studies [192, 193]. The final configurations obtained after relaxation are presented in Fig. 5.1. The displayed structures are the results of the classical potential simulations.

There are differences between the various results of the quantum-mechanical calculations but the consensus view is that the $\langle 1\,1\,0\rangle$ dumbbell (DB) followed by the hexagonal and tetrahedral defect is the lowest in energy. This is nicely reproduced by the DFT calculations performed in this work.

It has turned out to be very difficult to capture the results of quantum-mechanical calculations in analytical potential models. Among the established analytical potentials only the

	$\langle 1\,1\,0\rangle$ DB	H	T	$\langle 1\,0\,0\rangle$ DB	V
	Present study				
VASP	3.39	3.42	3.77	4.41	3.63
POSIC	4.39	4.48*	3.40	5.42	3.13
	Other *ab initio* studies				
Ref. 192	3.40	3.45	-	-	3.53
Ref. 193	3.31	3.31	3.43	-	-

Table 5.1: Formation energies of Si self-interstitials in crystalline Si determined by classical potential MD and DFT calculations. The formation energies are given in eV. T denotes the tetrahedral and H the hexagonal interstitial configuration. V corresponds to the vacancy configuration. Dumbbell configurations are abbreviated by DB. Formation energies for unstable configurations are marked by an asterisk and determined by using the low kinetic energy configuration shortly before the relaxation into the more favorable configuration starts.

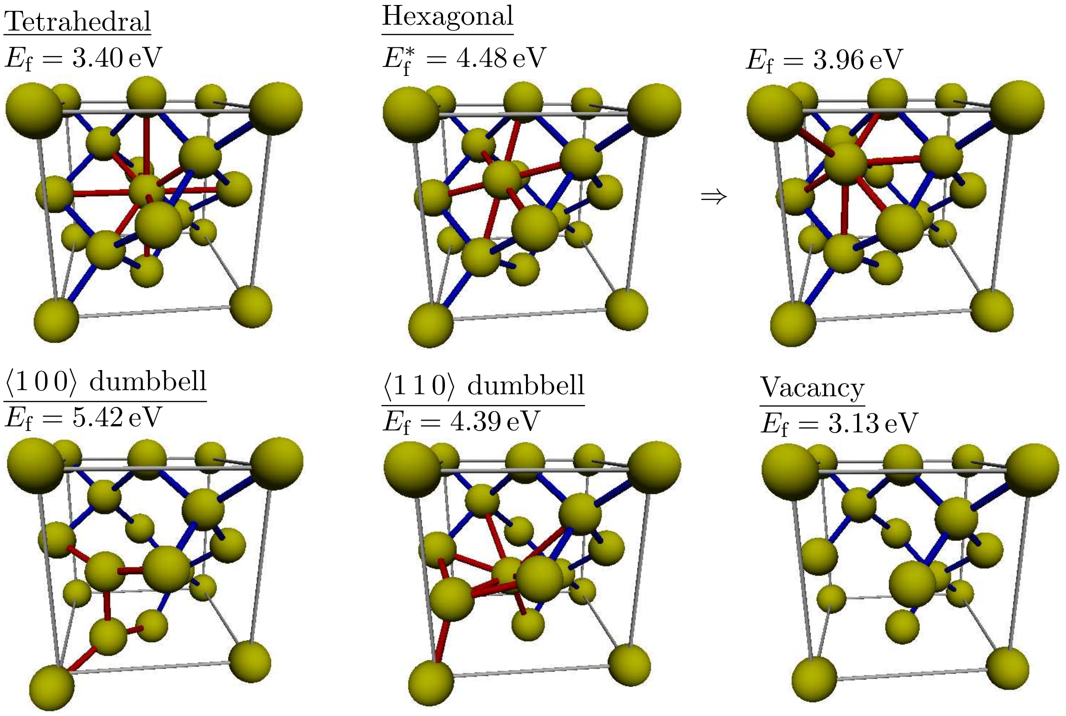
Tetrahedral
$E_\text{f} = 3.40\,\text{eV}$

Hexagonal
$E_\text{f}^* = 4.48\,\text{eV}$ $\Rightarrow$ $E_\text{f} = 3.96\,\text{eV}$

$\langle 1\,0\,0\rangle$ dumbbell
$E_\text{f} = 5.42\,\text{eV}$

$\langle 1\,1\,0\rangle$ dumbbell
$E_\text{f} = 4.39\,\text{eV}$

Vacancy
$E_\text{f} = 3.13\,\text{eV}$

Figure 5.1: Relaxed Si self-interstitial defect configurations obtained by classical potential calculations. Si atoms and bonds are illustrated by yellow spheres and blue lines. Bonds of the defect atoms are drawn in red color.

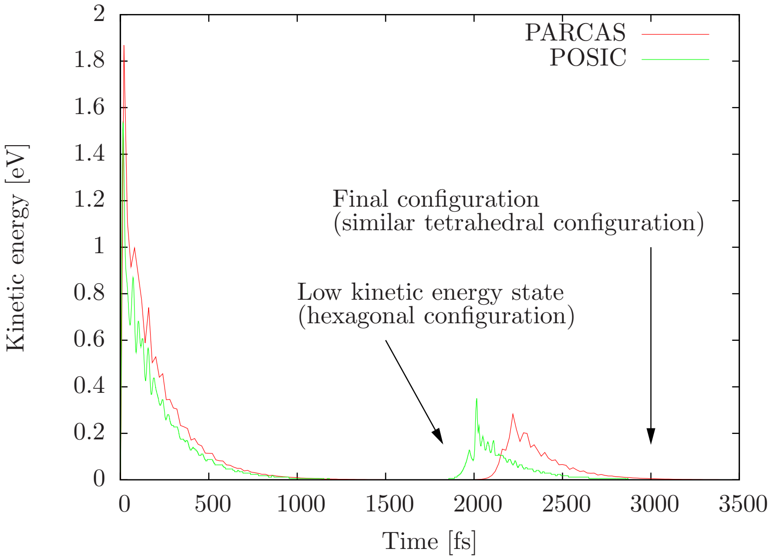

Figure 5.2: Kinetic energy plot of the relaxation process of the hexagonal silicon self-interstitial defect simulation using the EA potential.

environment-dependent interatomic potential (EDIP) [194, 195] and Stillinger-Weber [196] potential reproduce the correct order in energy of the defects. However, these potentials show shortcomings concerning the description of other physical properties and are unable to describe the C-C and C-Si interaction. In fact, the EA potential calculations favor the tetrahedral defect configuration. This limitation is assumed to arise due to the cut-off. In the tetrahedral configuration the second neighbors are only slightly more distant than the first neighbors, which creates the particular problem. Indeed, an increase of the cut-off results in increased values of the formation energies [147], which is most significant for the tetrahedral configuration. The same issue has already been discussed by Tersoff [197] with regard to the description of the tetrahedral C defect using his potential. While not completely rendering impossible further, more challenging empirical potential studies on large systems, the artifact has to be taken into account in the investigations of defect combinations later on in this chapter.

The hexagonal configuration is not stable opposed to results of the authors of the potential [147]. In the first two picoseconds, while kinetic energy is decoupled from the system, the Si_i seems to condense at the hexagonal site. The formation energy of 4.48 eV is determined by this low kinetic energy configuration shortly before the relaxation process starts. The Si_i atom then begins to slowly move towards an energetically more favorable position very close to the tetrahedral one but slightly displaced along the three coordinate axes. The formation energy of 3.96 eV for this type of interstitial is equal to the result for the hexagonal one in the original work [147]. Obviously, the authors did not carefully check the relaxed results assuming a hexagonal configuration. In Fig. 5.2 the relaxation process is shown on the basis of the kinetic energy plot. To exclude failures in the implementation of the potential or the MD code itself, the hexagonal defect structure was double-checked with the PARCAS MD code [198]. The respective relaxation energetics are likewise plotted and look similar to the energetics obtained by POSIC. In fact, the same type of interstitial arises using random

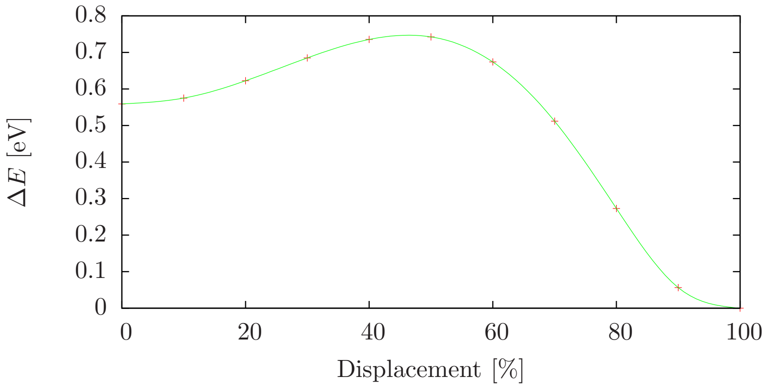

Figure 5.3: Migration barrier of the tetrahedral Si self-interstitial slightly displaced along all three coordinate axes into the exact tetrahedral configuration using classical potential calculations.

insertions. In addition, variations exist, in which the displacement is only along two $\langle 1\,0\,0\rangle$ axes ($E_{\mathrm{f}} = 3.8\,\mathrm{eV}$) or along a single $\langle 1\,0\,0\rangle$ axis ($E_{\mathrm{f}} = 3.6\,\mathrm{eV}$) successively approximating the tetrahedral configuration and formation energy. The existence of these local minima located near the tetrahedral configuration seems to be an artifact of the analytical potential without physical authenticity revealing fundamental problems of analytical potential models for describing defect structures. However, the energy barrier required for a transition into the tetrahedral configuration is small. This is exemplified in Fig. 5.3, which shows the change in configurational energy during the migration of the interstitial displaced along all three coordinate axes into the tetrahedral configuration. The barrier is smaller than $0.2\,\mathrm{eV}$. Hence, these artifacts have a negligible influence in finite temperature simulations.

The bond-centered (BC) configuration is unstable and, thus, is not listed. The $\mathrm{Si_i}$ $\langle 1\,0\,0\rangle$ DB constitutes the most unfavorable configuration for both, the EA and VASP calculations. The quantum-mechanical treatment of the $\mathrm{Si_i}$ $\langle 1\,0\,0\rangle$ DB demands for spin polarized calculations. The same applies for the vacancy. In the $\mathrm{Si_i}$ $\langle 1\,0\,0\rangle$ DB configuration, the net spin up density is localized in two caps at each of the two DB atoms perpendicularly aligned to the bonds to the other two Si atoms respectively. For the vacancy, the net spin up electron density is localized in caps at the four surrounding Si atoms directed towards the vacant site. No other intrinsic defect configuration, within the ones that are mentioned, is affected by spin polarization.

In the case of the classical potential simulations, bonds between atoms are displayed if there is an interaction according to the potential model, i.e. if the distance of two atoms is within the cut-off radius S_{ij} introduced in equation (3.8). For the tetrahedral and the slightly displaced configurations four bonds to the atoms located in the center of the planes of the unit cell exist in addition to the four tetrahedral bonds. The length of these bonds are, however, close to the cut-off range and, thus, are weak interactions not constituting actual chemical bonds. The same applies to the bonds between the interstitial and the upper two atoms in the $\mathrm{Si_i}$ $\langle 1\,1\,0\rangle$ DB configuration. A more detailed description of the chemical bonding is achieved through quantum-mechanical calculations by investigating the accumulation of negative charge between the nuclei.

	T	H	$\langle 1\,0\,0\rangle$ DB	$\langle 1\,1\,0\rangle$ DB	S	BC
Present study						
POSIC	6.09	9.05*	3.88	5.18	0.75	5.59*
VASP	Unstable	Unstable	3.72	4.16	1.95	4.66
Other studies						
Tersoff [197]	3.8	6.7	4.6	5.9	1.6	5.3
Ab initio [190, 199]	-	-	x	-	1.89	x+2.1

Table 5.2: Formation energies of C point defects in c-Si determined by classical potential MD and DFT calculations. The formation energies are given in eV. T denotes the tetrahedral, H the hexagonal and BC the bond-centered interstitial configuration. S corresponds to the substitutional interstitial configuration. The dumbbell configurations are abbreviated by DB. Formation energies for unstable configurations are marked by an asterisk and are determined by using the low kinetic energy configuration shortly before the relaxation into the more favorable configuration starts.

5.2 Carbon point defects in silicon

5.2.1 Defect structures in a nutshell

For investigating the C_i structures, a C atom is inserted or removed according to Fig. 3.2 of section 3.3. Formation energies of the most common C point defects in crystalline Si are summarized in Table 5.2. The relaxed configurations are visualized in Fig. 5.4. Again, the displayed structures are the results obtained by the classical potential calculations. The type of reservoir of the C impurity to determine the formation energy of the defect is chosen to be SiC. This is consistent with the methods used in the articles [190, 197], which the results are compared to in the following. Hence, the chemical potential of Si and C is determined by the cohesive energy of Si and SiC as discussed in section 3.3.

C_s occupying an already vacant Si lattice site, which is in fact not an interstitial defect, is found to be the lowest configuration in energy for all potential models. An experimental value of the formation energy of C_s was determined by a fit to solubility data yielding a concentration of $3.5 \times 10^{24} \exp(-2.3\,\text{eV}/k_{\text{B}}T)$ cm^{-3} [119]. However, there is no particular reason for treating the prefactor as a free parameter in the fit to the experimental data. It is simply given by the atomic density of pure silicon, which is 5×10^{22} cm^{-3}. Tersoff [197] and Dal Pino et al. [190] pointed out that by combining this prefactor with the calculated values for the energy of formation ranging from 1.6–1.89 eV, an excellent agreement with the experimental solubility data within the entire temperature range of the experiment is obtained. This reinterpretation of the solubility data, first proposed by Tersoff and later on reinforced by Dal Pino et al. is in good agreement with the results of the quantum-mechanical calculations performed in this work. Unfortunately, the EA potential undervalues the formation energy roughly by a factor of two, which is a definite drawback of the potential.

Except for Tersoff's results for the tetrahedral configuration, the C_i $\langle 1\,0\,0\rangle$ DB is the energetically most favorable interstitial configuration. As mentioned above, the low energy of formation for the tetrahedral interstitial in the case of the Tersoff potential is believed to be an artifact of the abrupt cut-off set to 2.5 Å (see Ref. 11 and 13 in [197]) and the real formation energy is, thus, supposed to be located between 3–10 eV. Keeping these considerations in mind, the C_i $\langle 1\,0\,0\rangle$ DB is the most favorable interstitial configuration for all interaction models. This

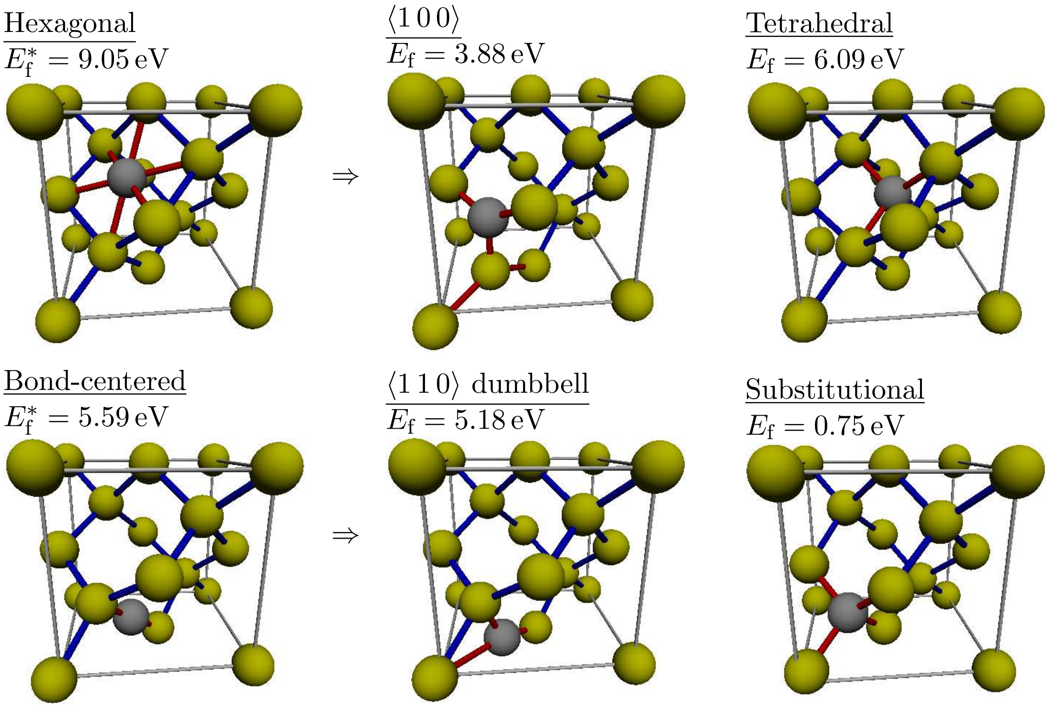

Hexagonal
$E_f^* = 9.05\,\mathrm{eV}$

⇒

$\langle 1\,0\,0 \rangle$
$E_f = 3.88\,\mathrm{eV}$

Tetrahedral
$E_f = 6.09\,\mathrm{eV}$

Bond-centered
$E_f^* = 5.59\,\mathrm{eV}$

⇒

$\langle 1\,1\,0 \rangle$ dumbbell
$E_f = 5.18\,\mathrm{eV}$

Substitutional
$E_f = 0.75\,\mathrm{eV}$

Figure 5.4: Relaxed C point defect configurations obtained by classical potential calculations. Si/C atoms and bonds are illustrated by yellow/gray spheres and blue lines. Bonds of the defect atoms are drawn in red color.

finding is in agreement with several theoretical [190, 199–202] and experimental [123, 124] investigations, which all predict this configuration to be the ground state. However, no energy of formation for this type of defect based on first-principles calculations has yet been explicitly stated in literature. The defect is frequently generated in the classical potential simulation runs, in which C is inserted at random positions in the c-Si matrix. In quantum-mechanical simulations the unstable tetrahedral and hexagonal configurations undergo a relaxation into the $\mathrm{C_i}$ $\langle 1\,0\,0\rangle$ DB configuration. Thus, this configuration is of great importance and discussed in more detail in section 5.2.2. It should be noted that EA and DFT predict almost equal formation energies.

The highest energy is observed for the hexagonal interstitial configuration using classical potentials. Quantum-mechanical calculations reveal this configuration to be unstable, which is also reproduced by the EA potential. In both cases, a relaxation towards the $\mathrm{C_i}$ $\langle 1\,0\,0\rangle$ DB configuration is observed. Opposed to results of the first-principles calculations, Tersoff finds this configuration to be stable [197]. In fact, the stability of the hexagonal interstitial could not be reproduced in simulations performed in this work using the unmodified Tersoff potential parameters. Unfortunately, apart from the modified parameters, no more conditions specifying the relaxation process are given in Tersoff's study on C point defects in Si.

The tetrahedral is the second most unfavorable interstitial configuration using classical potentials if the abrupt cut-off effect of the Tersoff potential is taken into account. Again, quantum-mechanical results reveal this configuration to be unstable. The fact that the tetrahedral and hexagonal configurations are the two most unstable configurations in classical potential calculations and, thus, are less likely to arise in MD simulations, acts in concert with the fact that these configurations are found to be unstable in the more accurate quantum-mechanical description.

Just as for $\mathrm{Si_i}$, a $\mathrm{C_i}$ $\langle 1\,1\,0\rangle$ DB configuration exists. It constitutes the second most favorable configuration, which is reproduced by both methods. Similar structures arise in both types of simulations. The Si and C atom share a regular Si lattice site aligned along the $\langle 1\,1\,0\rangle$ direction. The C atom is slightly displaced towards the next nearest Si atom located in the opposite direction with respect to the site-sharing Si atom and even forms a bond with this atom.

The $\mathrm{C_i}$ $\langle 1\,1\,0\rangle$ DB structure is energetically followed by the BC configuration. However, even though EA based results yield the same difference in energy with respect to the $\langle 1\,1\,0\rangle$ defect as DFT does, the BC configuration is found to be unstable within the EA description. The BC configuration descends into the $\mathrm{C_i}$ $\langle 1\,1\,0\rangle$ DB configuration. Due to the high formation energy of the BC defect resulting in a low probability of occurrence of this defect, the wrong description is not posing a serious limitation of the EA potential. Tersoff indeed predicts a metastable BC configuration. However, it is not in the correct order and lower in energy than the $\mathrm{C_i}$ $\langle 1\,1\,0\rangle$ DB. Quantum-mechanical results of this configuration are discussed in more detail in section 5.2.3. In another *ab initio* study, Capaz et al. [199] in turn found the BC configuration to be an intermediate saddle point structure of a possible migration path, which is 2.1 eV higher than the $\mathrm{C_i}$ $\langle 1\,0\,0\rangle$ DB structure. This is assumed to be due to the neglecting of the electron spin in these calculations. Another VASP calculation without fully accounting for the electron spin results in the smearing of a single electron over two non-degenerate states for the BC configuration. This problem is resolved by spin polarized calculations resulting in a net spin of one accompanied by a reduction of the total energy by 0.3 eV and the transformation into a metastable local minimum configuration. It is worth to

Displacements

				Atom 2			Atom 3		
	a	b	$\|a\|+\|b\|$	Δx	Δy	Δz	Δx	Δy	Δz
POSIC	0.084	-0.091	0.175	-0.015	-0.015	-0.031	-0.014	0.014	0.020
VASP	0.109	-0.065	0.174	-0.011	-0.011	-0.024	-0.014	0.014	0.025

Distances

	$r(1C)$	$r(2C)$	$r(3C)$	$r(12)$	$r(13)$	$r(34)$	$r(23)$	$r(25)$	$a_{\text{Si}}^{\text{equi}}$
POSIC	0.175	0.329	0.186	0.226	0.300	0.343	0.423	0.425	0.543
VASP	0.174	0.341	0.182	0.229	0.286	0.347	0.422	0.417	0.548

Angles

	θ_1	θ_2	θ_3	θ_4
POSIC	140.2	109.9	134.4	112.8
VASP	130.7	114.4	146.0	107.0

Table 5.3: Atomic displacements, distances and bond angles of the C$_\text{i}$ $\langle 1\,0\,0\rangle$ DB structure obtained by POSIC and VASP calculations. The displacements and distances are given in nm and the angles are given in degrees. Displacements, distances and angles are schematically displayed in Fig. 5.5. In addition, the equilibrium lattice constant for crystalline Si is listed.

note that all other listed configurations are not affected by spin polarization. However, in calculations performed in this work, which fully account for the spin of the electrons, the BC configuration in fact is a real local minimum and an energy barrier is needed to reach this configuration starting from the C$_\text{i}$ $\langle 1\,0\,0\rangle$ DB configuration. This is discussed in more detail in section 5.3.

To conclude, discrepancies between the results from classical potential calculations and those obtained from first principles are observed. Within the classical potentials, EA outperforms Tersoff and is, therefore, used for further studies. Both methods (EA and DFT) predict the C$_\text{i}$ $\langle 1\,0\,0\rangle$ DB configuration to be most stable. Also the remaining defects and their energetic order are described fairly well. It is thus concluded that, so far, modeling of the SiC precipitation by the EA potential might lead to trustable results.

5.2.2 C $\langle 1\,0\,0\rangle$ dumbbell interstitial configuration

As the C$_\text{i}$ $\langle 1\,0\,0\rangle$ DB constitutes the ground-state configuration of a C atom incorporated into otherwise perfect c-Si, it is the most probable and, hence, one of the most important interstitial configurations of C in Si. The structure was initially suspected by IR local vibrational mode absorption [122] and finally verified by electron paramagnetic resonance (EPR) [123] studies on irradiated Si substrates at low temperatures.

Fig. 5.5 schematically shows the C$_\text{i}$ $\langle 1\,0\,0\rangle$ DB structure and Table 5.3 lists the details of the atomic displacements, distances and bond angles obtained by classical potential and quantum-mechanical calculations. For comparison, the obtained structures for both methods are visualized in Fig. 5.6. The Si atom labeled '1' and the C atom compose the DB structure. They share the lattice site which is indicated by the dashed red circle. They are displaced

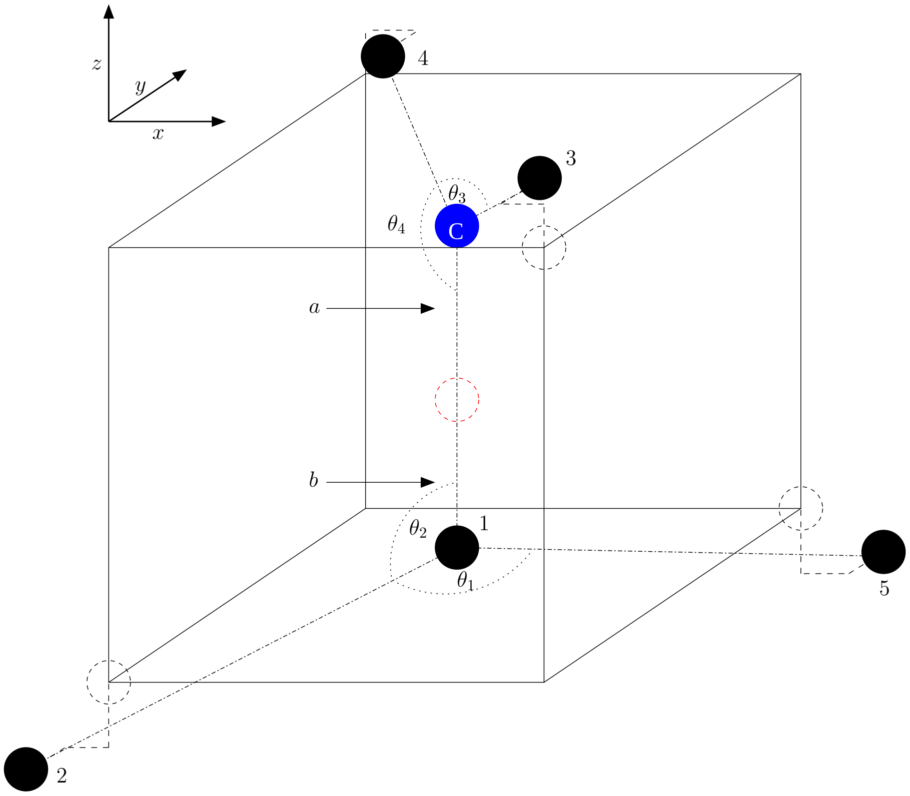

Figure 5.5: Sketch of the C_i $\langle 1\,0\,0\rangle$ dumbbell structure. Atomic displacements, distances and bond angles are listed in Table 5.3.

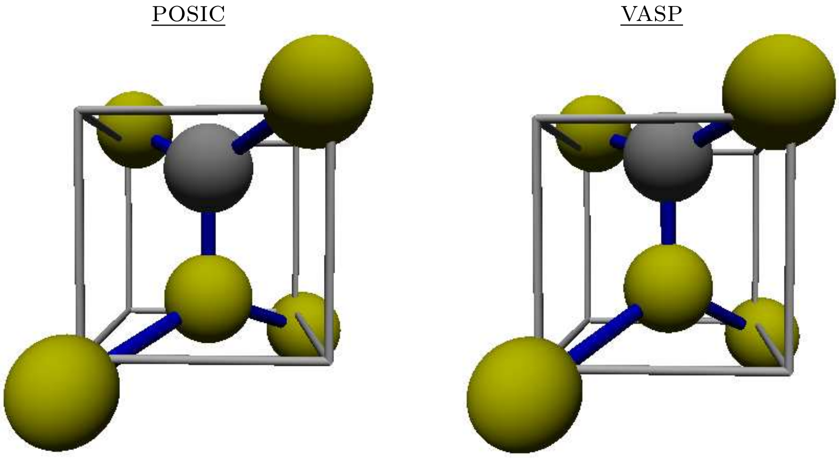

Figure 5.6: Comparison of the C_i $\langle 1\,0\,0\rangle$ DB structures obtained by POSIC and VASP calculations.

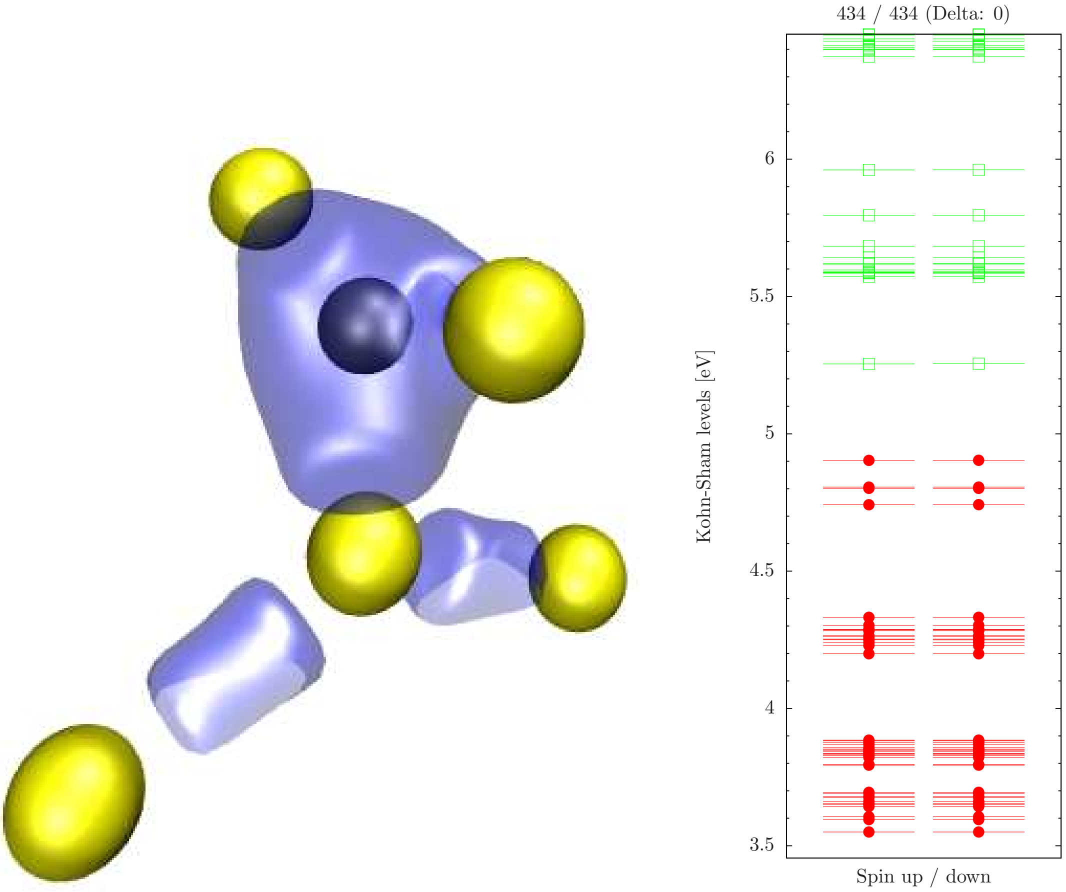

Figure 5.7: Charge density isosurface and Kohn-Sham levels of the C_i $\langle 1\,0\,0\rangle$ DB structure obtained by VASP calculations. Yellow and gray spheres correspond to Si and C atoms. The blue surface is the charge density isosurface. In the energy level diagram red and green lines and dots mark occupied and unoccupied states.

from the regular lattice site by length a and b respectively. The atoms no longer have four tetrahedral bonds to the Si atoms located on the alternating opposite edges of the cube. Instead, each of the DB atoms forms threefold coordinated bonds, which are located in a plane. One bond is formed to the other DB atom. The other two bonds are bonds to the two Si edge atoms located in the opposite direction of the DB atom. The distance of the two DB atoms is almost the same for both types of calculations. However, in the case of the VASP calculation, the DB structure is pushed upwards compared to the results using the EA potential. This is easily identified by comparing the values for a and b and the two structures in Fig. 5.6. Thus, the angles of bonds of the Si DB atom (θ_1 and θ_2) are closer to 120° signifying the predominance of sp^2 hybridization. On the other hand, the C atom forms an almost collinear bond (θ_3) with the two Si edge atoms implying the predominance of *sp* bonding. This is supported by the image of the charge density isosurface in Fig. 5.7. The two lower Si atoms are sp^3 hybridized and form σ bonds to the Si DB atom. The same is true for the upper two Si atoms and the C DB atom. In addition, the DB atoms form π bonds. However, due to the increased electronegativity of the C atom, the electron density is attracted by and, thus, localized around the C atom. In the same figure the Kohn-Sham levels are shown. There is no magnetization density. An acceptor level arises at approximately $E_v + 0.35\,\text{eV}$ while a band gap of about $0.75\,\text{eV}$ can be estimated from the Kohn-Sham level diagram for plain Si. However, strictly speaking, the Kohn-Sham levels and orbitals do not have a direct physical meaning and, thus, these values have to be taken with care.

5.2.3 Bond-centered interstitial configuration

In the BC interstitial configuration the interstitial atom is located in between two next neighbored Si atoms forming linear bonds. In a previous study this configuration was found to constitute an intermediate saddle point configuration determining the migration barrier of one possible migration path of a C_i $\langle 1\,0\,0\rangle$ DB configuration into an equivalent one [199]. This is in agreement with results of the EA potential simulations, which reveal this configuration to be unstable relaxing into the C_i $\langle 1\,1\,0\rangle$ configuration. However, this fact could not be reproduced by spin polarized VASP calculations performed in this work. Present results suggest this configuration to correspond to a real local minimum. In fact, an additional barrier has to be passed to reach this configuration starting from the C_i $\langle 1\,0\,0\rangle$ interstitial configuration, which is investigated in section 5.3. After slightly displacing the C atom along the $[1\,0\,0]$ (equivalent to a displacement along $[0\,1\,0]$), $[0\,0\,1]$, $[0\,0\,\overline{1}]$ and $[1\,\overline{1}\,0]$ direction, the distorted structures relax back into the BC configuration. As will be shown in subsequent migration simulations, the same would happen to structures where the C atom is displaced along the migration direction, which approximately is the $[1\,1\,0]$ direction. These relaxations indicate that the BC configuration is a real local minimum instead of an assumed saddle point configuration. Fig. 5.8 shows the structure, charge density isosurface and Kohn-Sham levels of the BC configuration. In fact, the net magnetization of two electrons is already suggested by simple molecular orbital theory considerations with respect to the bonding of the C atom. The linear bonds of the C atom to the two Si atoms indicate the *sp* hybridization of the C atom. Two electrons participate to the linear σ bonds with the Si neighbors. The other two electrons constitute the $2p^2$ orbitals resulting in a net magnetization. This is supported by the charge density isosurface and the Kohn-Sham levels in Fig. 5.8. The blue torus, which reinforces the assumption of the p orbital, illustrates the resulting spin up electron density. In addition, the energy level diagram shows a net amount of two spin up electrons.

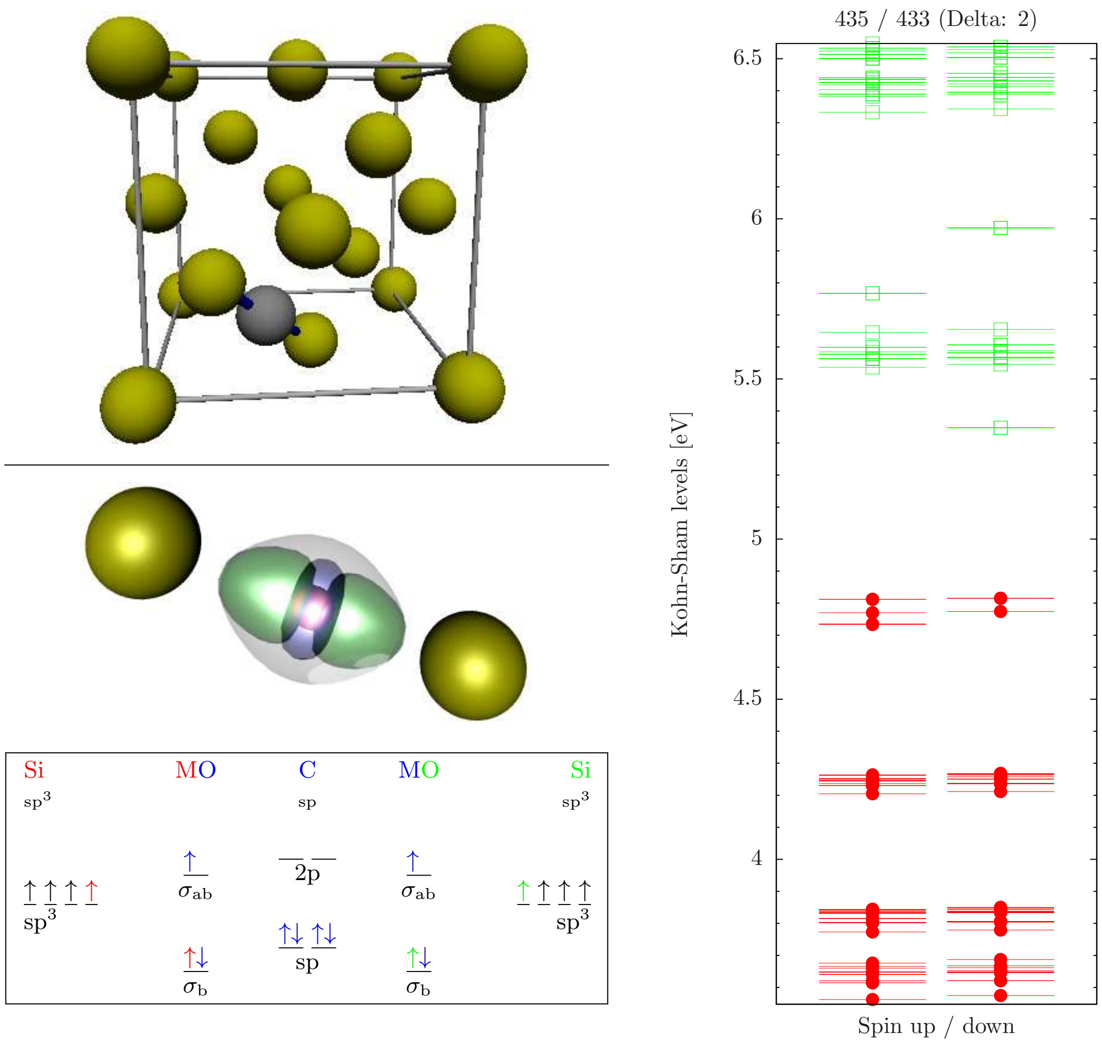

Figure 5.8: Structure, charge density isosurface, molecular orbital diagram and Kohn-Sham level diagram of the bond-centered interstitial configuration. Gray, green and blue surfaces mark the charge density of spin up, spin down and the resulting spin up electrons in the charge density isosurface, in which the carbon atom is represented by a red sphere. In the energy level diagram red and green lines mark occupied and unoccupied states.

5.3 Migration of the carbon interstitial

A measure for the mobility of interstitial C is the activation energy necessary for the migration from one stable position to another. The stable defect geometries have been discussed in the previous subsection. In the following, the problem of interstitial C migration in Si is considered. Since the $\mathrm{C_i}$ $\langle 1\,0\,0\rangle$ DB is the most probable, hence, most important configuration, the migration of this defect atom from one site of the Si host lattice to a neighboring site is in the focus of investigation. Three different migration paths are accounted in this work, which are displayed in Fig. 5.9. The first investigated migration is a transition of a $[0\,0\,\bar{1}]$ into a $[0\,0\,1]$ DB interstitial configuration. During this migration the C atom is changing its Si DB partner. The new partner is the one located at $a_{\mathrm{Si}}/4[1\,1\,\bar{1}]$ relative to the initial one, where a_{Si} is the Si lattice constant. Two of the three bonds to the next neighbored Si atoms are preserved while the breaking of the third bond and the accompanying formation of a new bond is observed. The C atom resides in the $(\bar{1}\,1\,0)$ plane. This transition involves the intermediate BC configuration. However, results discussed in the previous section indicate that the BC configuration is a real local minimum. Thus, the $[0\,0\,\bar{1}]$ to $[0\,0\,1]$ migration can be thought of a two-step mechanism, in which the intermediate BC configuration constitutes a metastable configuration. Due to symmetry, it is enough to consider the transition from the BC to a $\langle 1\,0\,0\rangle$ configuration or vice versa. In the second path, the C atom is changing its Si partner atom as in path one. However, the trajectory of the C atom is no longer proceeding in the $(\bar{1}\,1\,0)$ plane. The orientation of the new DB configuration is transformed from $[0\,0\,\bar{1}]$ to $[0\,\bar{1}\,0]$. Again, one bond is broken while another one is formed. As a last migration path, the defect is only changing its orientation. Thus, this path is not responsible for long-range migration. The Si DB partner remains the same. The bond to the face-centered Si atom at the bottom of the unit cell breaks and a new one is formed to the face-centered atom at the forefront of the unit cell.

5.3.1 Migration paths obtained by first-principles calculations

In Fig. 5.10 results of the $[0\,0\,\bar{1}]$ to $[0\,0\,1]$ migration fully described by the migration of the $[0\,0\,\bar{1}]$ to the BC configuration is displayed. To reach the BC configuration, which is 0.94 eV higher in energy than the $[0\,0\,\bar{1}]$ DB configuration, an energy barrier of approximately 1.2 eV given by the saddle point structure at a displacement of 60 % has to be passed. This amount of energy is needed to break the bond of the C atom to the Si atom at the bottom left. In a second process 0.25 eV of energy are needed for the system to revert into a $\langle 1\,0\,0\rangle$ configuration.

Fig. 5.11 shows the migration barrier and structures of the $\mathrm{C_i}$ $[0\,0\,\bar{1}]$ to $[0\,\bar{1}\,0]$ DB transition. The resulting migration barrier of approximately 0.9 eV is very close to the experimentally obtained values of 0.70 eV [109], 0.73 eV [124] and 0.87 eV [125].

The third migration path, in which the DB is changing its orientation, is shown in Fig. 5.12. An energy barrier of roughly 1.2 eV is observed. Experimentally measured activation energies for reorientation range from 0.77 eV to 0.88 eV [123, 124]. Thus, this pathway is more likely to be composed of two consecutive steps of the second path.

Since the activation energy of the first and last migration path is much greater than the experimental value, the second path is identified to be responsible as a migration path for the most likely C interstitial in Si explaining both, annealing and reorientation experiments. The activation energy of roughly 0.9 eV nicely compares to experimental values reinforcing the correct identification of the C-Si DB diffusion mechanism. Slightly increased values compared to

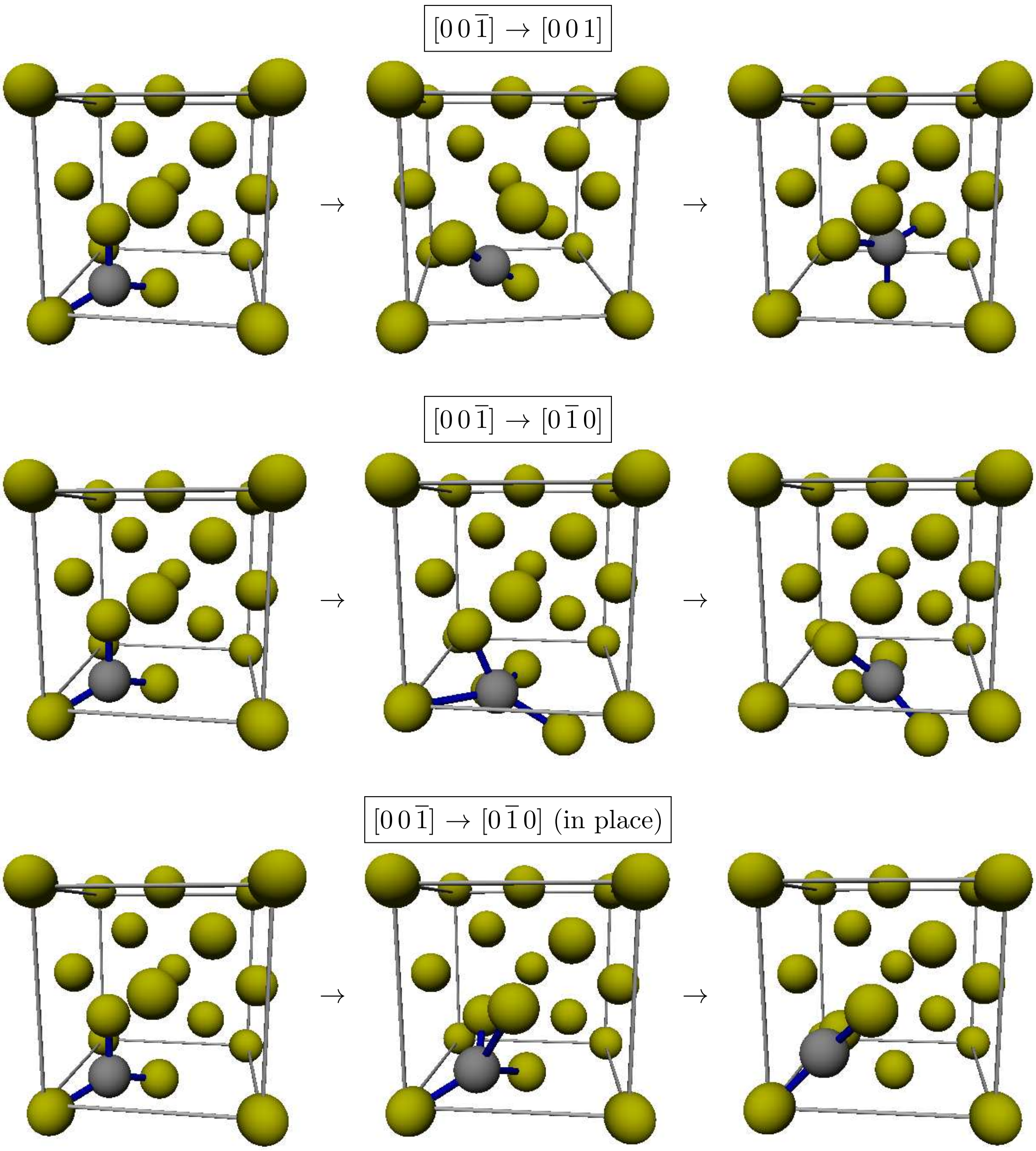

Figure 5.9: Conceivable migration pathways among two $\mathrm{C_i}$ $\langle 1\,0\,0 \rangle$ DB configurations.

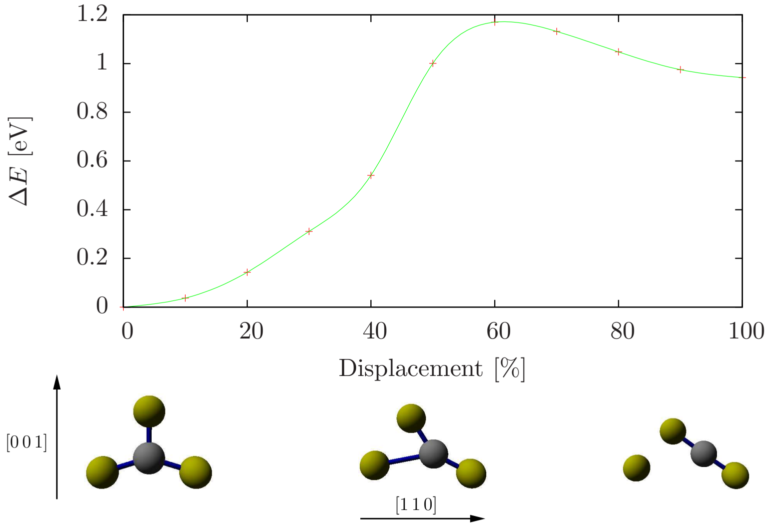

Figure 5.10: Migration barrier and structures of the $[0\,0\,\overline{1}]$ DB (left) to BC (right) transition. Bonds of the C atom are illustrated by blue lines.

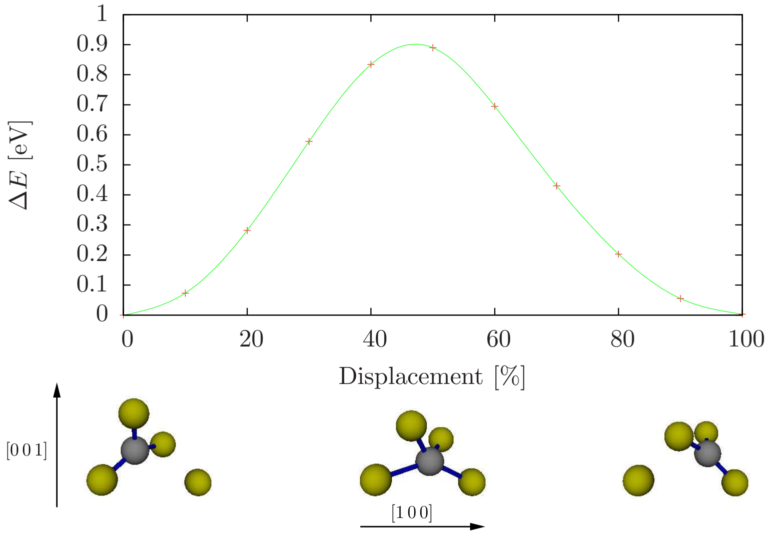

Figure 5.11: Migration barrier and structures of the $[0\,0\,\overline{1}]$ DB (left) to the $[0\,\overline{1}\,0]$ DB (right) transition. Bonds of the C atom are illustrated by blue lines.

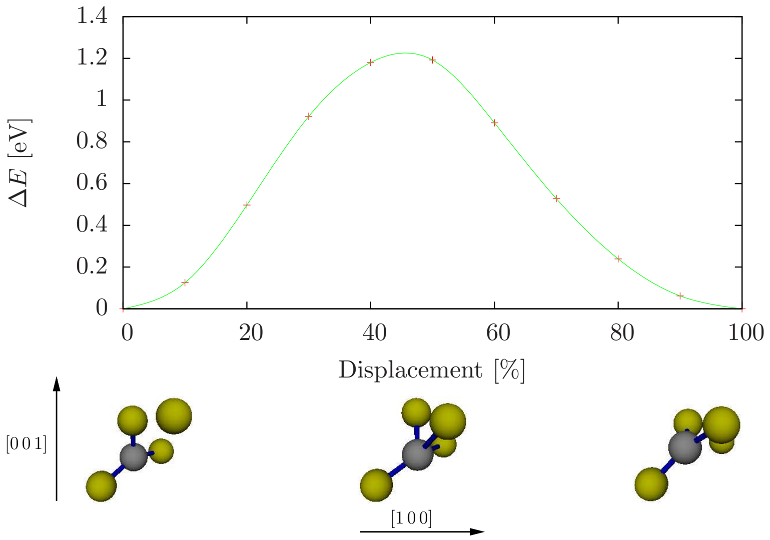

Figure 5.12: Reorientation barrier and structures of the $[0\,0\,\bar{1}]$ DB (left) to the $[0\,\bar{1}\,0]$ DB (right) transition in place. Bonds of the carbon atoms are illustrated by blue lines.

experiment might be due to the tightened constraints applied in the modified CRT approach. Nevertheless, the theoretical description performed in this work is improved compared to a former study [199], which underestimates the experimental value by 35 %. In addition, it is finally shown that the BC configuration, for which spin polarized calculations are necessary, constitutes a real local minimum instead of a saddle point configuration due to the presence of restoring forces for displacements in migration direction.

Further migration pathways, in particular those occupying other defect configurations than the $\langle 1\,0\,0\rangle$-type either as a transition state or a final or starting configuration, are totally conceivable. This is investigated in the following in order to find possible migration pathways that have an activation energy lower than the ones found up to now. The next energetically favorable defect configuration is the $\langle 1\,1\,0\rangle$ C-Si DB interstitial. Fig. 5.13 shows the migration barrier of the $[1\,1\,0]$ C-Si DB to the BC, $[0\,0\,\bar{1}]$ and $[0\,\bar{1}\,0]$ (in place) transition. Indeed less than 0.7 eV are necessary to turn the $[0\,\bar{1}\,0]$ to the $[1\,1\,0]$ C-Si DB interstitial. This transition is carried out in place, i.e. the Si DB pair is not changed and both, the Si and C atom share the initial lattice site. Thus, this transition does not contribute to long-range diffusion. Once the C atom resides in the $[1\,1\,0]$ DB interstitial configuration, it can migrate into the BC configuration requiring approximately 0.95 eV of activation energy, which is only slightly higher than the activation energy needed for the $[0\,0\,\bar{1}]$ to $[0\,\bar{1}\,0]$ pathway as shown in Fig. 5.11. As already known from the migration of the $[0\,0\,\bar{1}]$ to the BC configuration discussed in Fig. 5.10, another 0.25 eV are needed to turn back from the BC to a $\langle 1\,0\,0\rangle$-type interstitial. However, due to the fact that this migration consists of three single transitions with the second one having an activation energy slightly higher than observed for the direct transition, this sequence of paths is considered very unlikely to occur. The migration barrier of the $[1\,1\,0]$ to $[0\,0\,\bar{1}]$ transition, in which the C atom is changing its Si partner and, thus, moving to the neighbored lattice site, corresponds to approximately 1.35 eV. During this transition the C atom is escaping the $(\bar{1}\,1\,0)$ plane approaching the final configuration on a

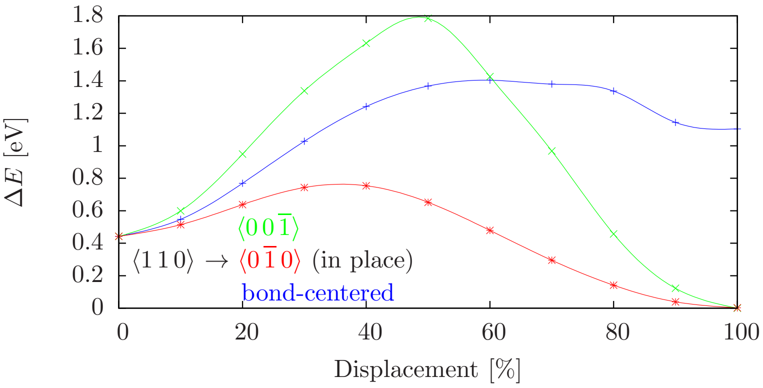

Figure 5.13: Migration barriers of the $[1\,1\,0]$ DB to BC (blue), $[0\,0\,\bar{1}]$ (green) and $[0\,\bar{1}\,0]$ (in place, red) C-Si DB transition.

curved path. This barrier is much higher than the ones found previously, which again make this transition very unlikely to occur. For this reason, the assumption that C diffusion and reorientation is achieved by transitions of the type presented in Fig. 5.11 is reinforced.

5.3.2 Migration described by classical potential calculations

Fig. 5.14 shows the evolution of structure and energy along the $\mathrm{C_i}$ BC to $[0\,0\,\bar{1}]$ DB transition. Since the $\mathrm{C_i}$ BC configuration is unstable relaxing into the $[1\,1\,0]$ DB configuration within this potential, the low kinetic energy state is used as a starting configuration. Two different pathways are obtained for different time constants of the Berendsen thermostat. With a time constant of 1 fs, the C atom resides in the $(\bar{1}\,1\,0)$ plane resulting in a migration barrier of 2.4 eV. However, weaker coupling to the heat bath realized by an increase of the time constant to 100 fs enables the C atom to move out of the $(\bar{1}\,1\,0)$ plane already at the beginning, which is accompanied by a reduction in energy, approaching the final configuration on a curved path. The energy barrier of this path is 0.2 eV lower in energy than the direct migration within the $(\bar{1}\,1\,0)$ plane. However, the investigated pathways cover an activation energy approximately twice as high as the one obtained by quantum-mechanical calculations. If the entire transition of the $[0\,0\,\bar{1}]$ into the $[0\,0\,1]$ configuration is considered a two step process passing the intermediate BC configuration, an additional activation energy of 0.5 eV is necessary to escape the BC towards the $[0\,0\,1]$ configuration. Assuming equal preexponential factors for both diffusion steps, the total probability of diffusion is given by $\exp\left((2.2\,\text{eV} + 0.5\,\text{eV})/k_{\text{B}}T\right)$. Thus, the activation energy should be located within the range of 2.2–2.7 eV.

Figures 5.15 and 5.16 show the migration barriers of the $\mathrm{C_i}$ $[0\,0\,\bar{1}]$ to $[0\,\bar{1}\,0]$ DB transition. In the first case, the transition involves a change in the lattice site of the C atom whereas in the second case, a reorientation at the same lattice site takes place. In the first case, the pathways for the two different time constants look similar. A local minimum exists in between the two peaks of the graph. The corresponding configuration, which is illustrated for the results obtained for a time constant of 1 fs, looks similar to the $\mathrm{C_i}$ $[1\,1\,0]$ configuration. Indeed, this configuration is obtained by relaxation simulations without constraints of configurations near this local minimum. Activation energies of roughly 2.8 eV and 2.7 eV are needed for migration.

The $\mathrm{C_i}$ $[1\,1\,0]$ configuration seems to play a decisive role in all migration pathways in

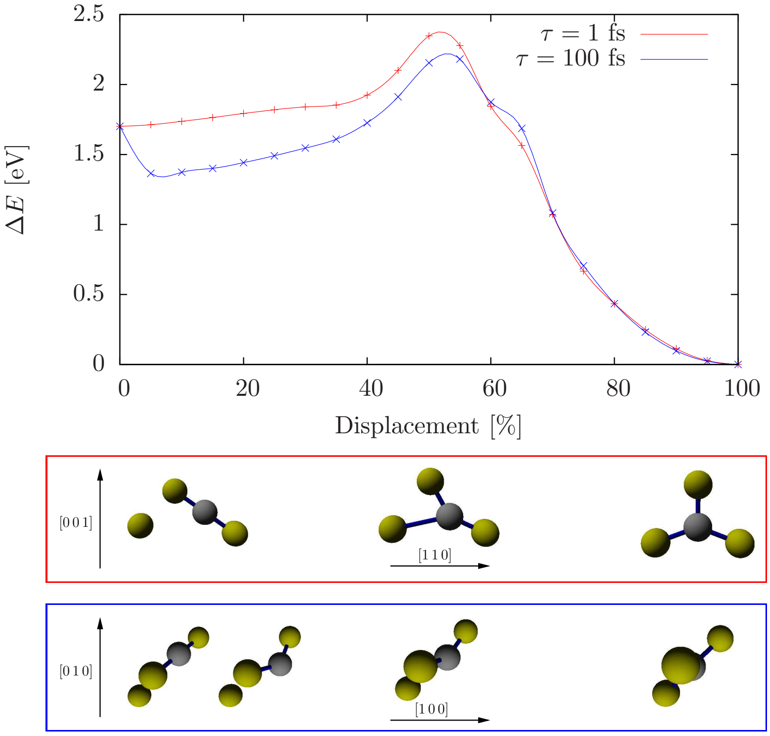

Figure 5.14: Migration barrier and structures of the C_i BC to $[0\,0\,\bar{1}]$ DB transition using the classical EA potential. Two migration pathways are obtained for different time constants of the Berendsen thermostat. The lowest activation energy is 2.2 eV.

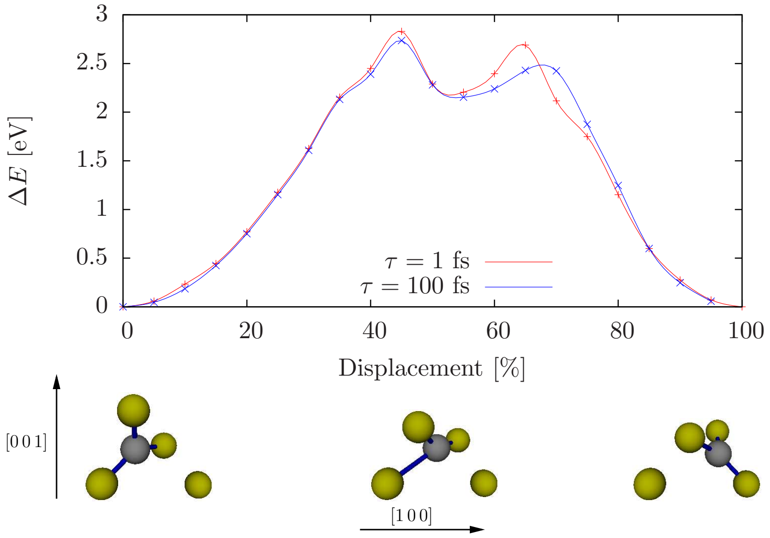

Figure 5.15: Migration barrier and structures of the C_i $[0\,0\,\bar{1}]$ to $[0\,\bar{1}\,0]$ DB transition using the classical EA potential.

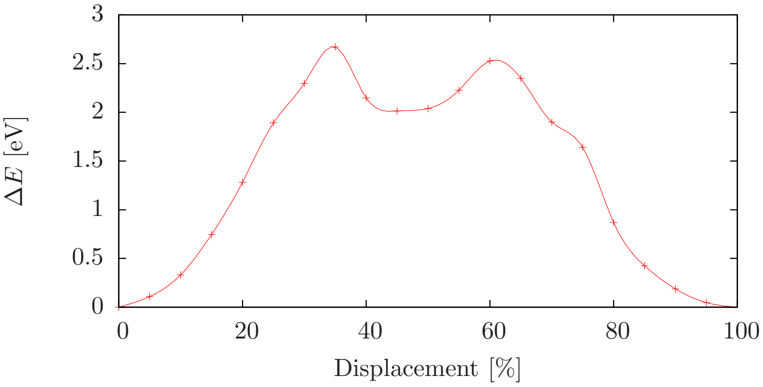

Figure 5.16: Reorientation barrier of the C_i $[0\,0\,\overline{1}]$ to $[0\,\overline{1}\,0]$ DB transition in place using the classical EA potential.

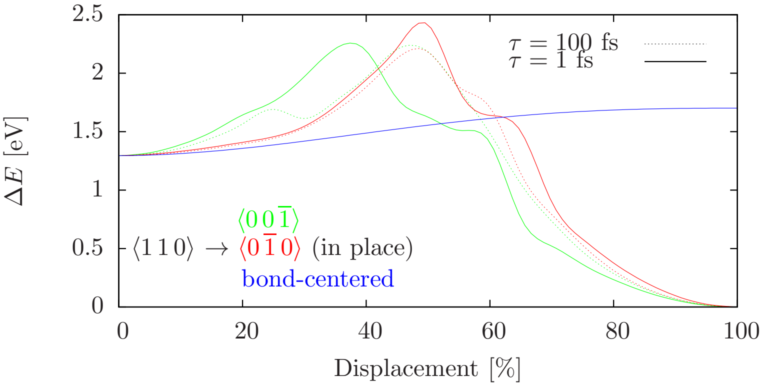

Figure 5.17: Migration barriers of the C_i $[1\,1\,0]$ DB to BC (blue), $[0\,0\,\overline{1}]$ (green) and $[0\,\overline{1}\,0]$ (in place, red) transition. Solid lines show results for a time constant of 1 fs and dashed lines correspond to simulations employing a time constant of 100 fs.

the classical potential calculations. As mentioned above, the starting configuration of the first migration path, i.e. the BC configuration, is fixed to be a transition point but in fact is unstable. Further relaxation of the BC configuration results in the C_i $[1\,1\,0]$ configuration. Even the last two pathways show configurations almost identical to the C_i $[1\,1\,0]$ configuration, which constitute local minima within the pathways. Thus, migration pathways involving the C_i $[1\,1\,0]$ DB configuration as a starting or final configuration are further investigated. Fig. 5.17 shows migration barriers of the C_i $[1\,1\,0]$ DB to $[0\,0\,\overline{1}]$, $[0\,\overline{1}\,0]$ (in place) and BC configuration. As expected, there is no maximum for the transition into the BC configuration. As mentioned earlier, the BC configuration itself constitutes a saddle point configuration relaxing into the energetically more favorable $[1\,1\,0]$ DB configuration. An activation energy of 2.2 eV is necessary to reorientate the $[0\,0\,\overline{1}]$ into the $[1\,1\,0]$ DB configuration, which is 1.3 eV higher in energy. Residing in this state, another 0.90 eV is enough to make the C atom form a $[0\,0\,\overline{1}]$ DB configuration with the Si atom of the neighbored lattice site. In contrast to quantum-mechanical calculations, in which the direct transition is the energetically most

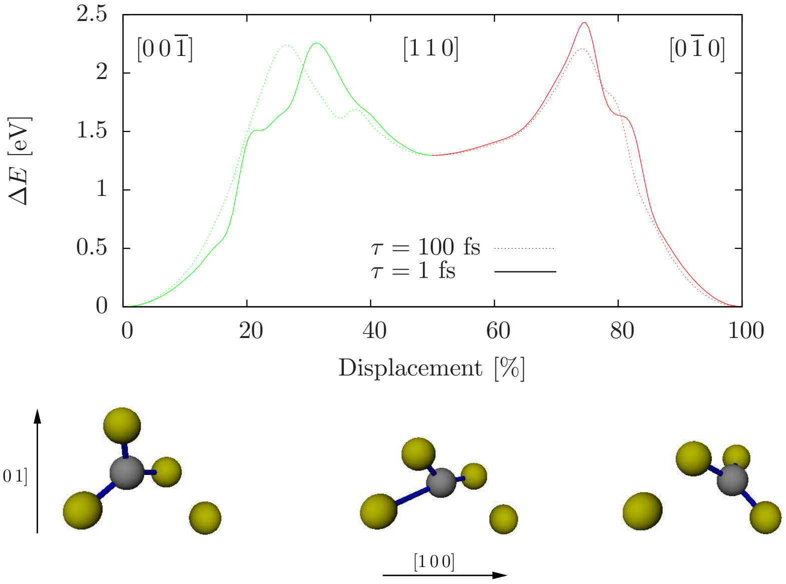

Figure 5.18: Migration barrier and structures of the C_i $[0\,0\,\bar{1}]$ (left) to the $[0\,\bar{1}\,0]$ DB (right) transition involving the $[1\,1\,0]$ DB (center) configuration. Migration simulations are performed utilizing time constants of 1 fs (solid line) and 100 fs (dashed line) for the Berendsen thermostat.

favorable transition and the transition composed of the intermediate migration steps is very unlikely to occur, the just presented pathway is much more conceivable in classical potential simulations since the energetically most favorable transition found so far is likewise composed of two migration steps with activation energies of 2.2 eV and 0.5 eV, for which the intermediate state is the BC configuration, which is unstable. Thus, the just proposed migration path, which involves the $[1\,1\,0]$ interstitial configuration, becomes even more probable than the initially proposed path involving the BC configuration. Due to these findings, the respective path is proposed to constitute the diffusion-describing path. The evolution of structure and configurational energy is displayed again in Fig. 5.18. Approximately 2.2 eV are needed to turn the C_i $[0\,0\,\bar{1}]$ into the $[1\,1\,0]$ DB located at the neighbored lattice site in $[1\,1\,\bar{1}]$ direction. Another barrier of 0.90 eV exists for the rotation into the C_i $[0\,\bar{1}\,0]$ DB configuration for the path obtained with a time constant of 100 fs for the Berendsen thermostat. Roughly the same amount would be necessary to excite the C_i $[1\,1\,0]$ DB to the BC configuration (0.40 eV) and a successive migration into the $[0\,0\,1]$ DB configuration (0.50 eV) as displayed in Fig. 5.17 and Fig. 5.14. The former diffusion process, however, would more nicely agree with the *ab initio* path since the migration is accompanied by a rotation of the DB orientation. By considering a two step process and assuming equal preexponential factors for both diffusion steps, the probability of the total diffusion event is given by $\exp(\frac{2.24\,\text{eV}+0.90\,\text{eV}}{k_B T})$, which corresponds to a single diffusion barrier that is 3.5 times higher than the barrier obtained by *ab initio* calculations.

5.3.3 Conclusions

Although classical potential simulations reproduce the same order in energy of the C_i $\langle 1\,0\,0\rangle$ and $\langle 1\,1\,0\rangle$ DB interstitial configurations as obtained by more accurate quantum-mechanical calculations, the obtained migration pathways and resulting activation energies differ to a great extent. On the one hand, the most favorable pathways differ. However, the pathway, which is considered most probable in the classical potential treatment, exhibits the same starting and final configuration of the DB structure as well as the change in orientation during migration as obtained by quantum-mechanical calculations. On the other hand, the activation energy obtained by classical potential simulations is tremendously overestimated by a factor of 2.4 to 3.5. The overestimated barrier is due to the short range character of the potential, which drops the interaction to zero within the first and next neighbor distance. Since the total binding energy is accommodated within a short distance, which according to the universal energy relation would usually correspond to a much larger distance, unphysical high forces between two neighbored atoms arise. This is explained in more detail in a previous study [203]. Thus, atomic diffusion is wrongly described in the classical potential approach. The probability of already rare diffusion events is further decreased for this reason. However, agglomeration of C and diffusion of Si self-interstitials are an important part of the proposed SiC precipitation mechanism. Thus, a serious limitation that has to be taken into account for appropriately modeling the C/Si system using the otherwise quite promising EA potential is revealed. Possible workarounds are discussed in more detail in section 6.2.

5.4 Combination of point defects and related diffusion processes

The study proceeds with a structural and energetic investigation of pairs of the ground-state and, thus, most probable defect configurations that are believed to be fundamental in the Si to SiC conversion. Investigations are restricted to quantum-mechanical calculations. Fig. 5.19 schematically displays the initial C_i $[0\,0\,\overline{1}]$ DB structure (Fig. 5.19(a)) as well as the lattice site chosen for the initial Si_i $\langle 1\,1\,0\rangle$ DB (Fig. 5.19(b)) and various positions for the second defect (1–5) that are used for investigating defect pairs. The color of the number denotes the amount of possible atoms for the second defect resulting in equivalent configurations. Binding energies of the defect pair are determined by equation 3.41. Next to formation and binding energies, migration barriers are investigated, which allow to draw conclusions on the probability of the formation of such defect complexes by thermally activated diffusion processes.

5.4.1 Pairs of C_i $\langle 1\,0\,0\rangle$-type interstitials

C_i pairs of the $\langle 1\,0\,0\rangle$-type are investigated in the first part. Table 5.4 summarizes resulting binding energies for the combination with a second C_i $\langle 1\,0\,0\rangle$ DB obtained for different orientations at positions 1 to 5 after structural relaxation. Most of the obtained configurations result in binding energies well below zero indicating a preferable agglomeration of this type of defects. For increasing distances of the defect pair, the binding energy approaches to zero as it is expected for non-interacting, isolated defects. In fact, a C_i $[0\,0\,\overline{1}]$ DB interstitial created at position R separated by a distance of $\frac{a_{\text{Si}}}{2}\langle 3\,2\,3\rangle$ ($\approx$12.8 Å) from the initial one results in an energy as low as -0.19 eV. There is still a low interaction remaining, which is due to the equal orientation of the defects. By changing the orientation of the second DB interstitial

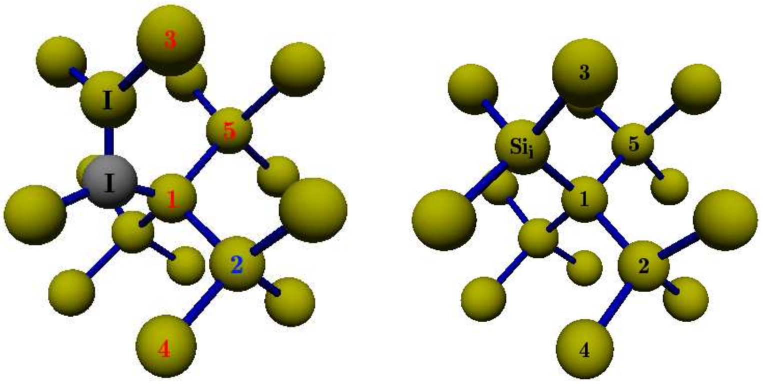

(a) (b)

Figure 5.19: Position of the initial C$_\text{i}$ $[0\,0\,\bar{1}]$ DB (I) (a) and of the lattice site chosen for the initial Si$_\text{i}$ $\langle 1\,1\,0\rangle$ DB (Si$_\text{i}$) (b). Lattice sites for the second defect used for investigating defect pairs are numbered from 1 to 5. For black/red/blue numbers, one/two/four possible atom(s) exist for the second defect to create equivalent defect combinations.

	1	2	3	4	5	R
$[0\,0\,\bar{1}]$	-0.08	-1.15	-0.08	0.04	-1.66	-0.19
$[0\,0\,1]$	0.34	0.004	-2.05	0.26	-1.53	-0.19
$[0\,\bar{1}\,0]$	-2.39	-0.17	-0.10	-0.27	-1.88	-0.05
$[0\,1\,0]$	-2.25	-1.90	-2.25	-0.12	-1.38	-0.06
$[\bar{1}\,0\,0]$	-2.39	-0.36	-2.25	-0.12	-1.88	-0.05
$[1\,0\,0]$	-2.25	-2.16	-0.10	-0.27	-1.38	-0.06

Table 5.4: Binding energies in eV of C$_\text{i}$ $\langle 1\,0\,0\rangle$-type defect pairs. The given energies in eV are defined by equation (3.41). Equivalent configurations are marked by identical colors. The first column lists the types of the second defect combined with the initial C$_\text{i}$$[0\,0\,\bar{1}]$ DB interstitial. The position index of the second defect is given in the first row according to Fig. 5.19(a). R is the position located at $\frac{a_{\text{Si}}}{2}[3\,2\,3]$ relative to the initial defect, which is the maximum realizable distance due to periodic boundary conditions.

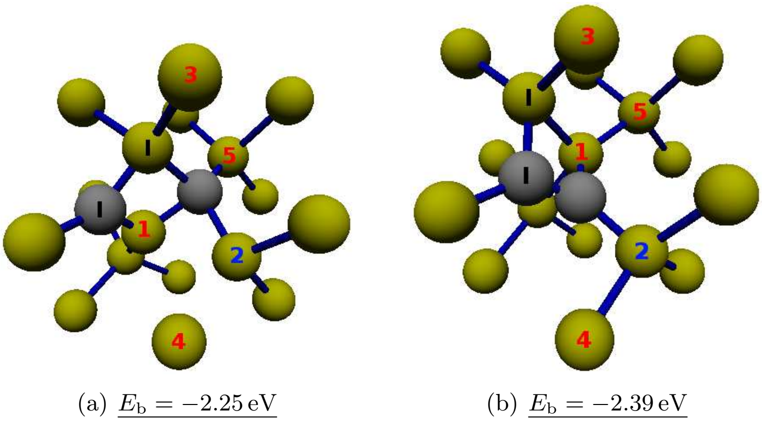

(a) $\underline{E_\mathrm{b} = -2.25\,\mathrm{eV}}$ (b) $\underline{E_\mathrm{b} = -2.39\,\mathrm{eV}}$

Figure 5.20: Relaxed structures of defect combinations obtained by creating [1 0 0] (a) and [0 $\bar{1}$ 0] (b) DBs at position 1.

to the [0 $\bar{1}$ 0]-type, the interaction is even more reduced resulting in an energy of -0.05 eV for a distance, which is the maximum that can be realized due to periodic boundary conditions. Energetically favorable and unfavorable configurations can be explained by stress compensation and increase respectively based on the resulting net strain of the respective configuration of the defect combination. Antiparallel orientations of the second defect, i.e. [0 0 1] for positions located below the (0 0 1) plane with respect to the initial one (positions 1, 2 and 4) form the energetically most unfavorable configurations. In contrast, the parallel and particularly the twisted orientations constitute energetically favorable configurations, in which a vast reduction of strain is enabled by combination of these defects.

Mattoni et al. [204] predict the ground-state configuration of $\mathrm{C_i}$ $\langle 1\,0\,0\rangle$-type defect pairs for a [1 0 0] or equivalently a [0 1 0] defect created at position 1 with both defects basically maintaining the as-isolated DB structure resulting in a binding energy of -2.1 eV. In the present study, a further relaxation of this defect structure is observed. The C atom of the second and the Si atom of the initial DB move towards each other forming a bond, which results in a somewhat lower binding energy of -2.25 eV. The corresponding defect structure is displayed in Fig. 5.20(a). In this configuration the initial Si and C DB atoms are displaced along [1 0 0] and [$\bar{1}$ 0 0] in such a way that the Si atom is forming tetrahedral bonds with two Si and two C atoms. The C and Si atom constituting the second defect are as well displaced in such a way that the C atom forms tetrahedral bonds with four Si neighbors, a configuration expected in SiC. The two carbon atoms, which are spaced by 2.70 Å, do not form a bond but anyhow reside in a shorter distance than expected in SiC. Si atom number 2 is pushed towards the C atom, which results in the breaking of the bond to Si atom number 4. Breaking of the σ bond is indeed confirmed by investigating the charge density isosurface of this configuration.

Apart from that, a more favorable configuration is found for the combination with a [0 $\bar{1}$ 0] and [$\bar{1}$ 0 0] DB respectively, which is assumed to constitute the actual ground-state configuration of two $\mathrm{C_i}$ DBs in Si. The atomic arrangement is shown in Fig. 5.20(b). The initial configuration is still evident in the relaxed configuration. The two $\mathrm{C_i}$ atoms form a strong C-C bond, which is responsible for the large gain in energy resulting in a binding energy of -2.39 eV. This bond has a length of 1.38 Å close to the next neighbor distance in diamond or graphite, which is approximately 1.54 Å. The minimum of the binding energy observed for this

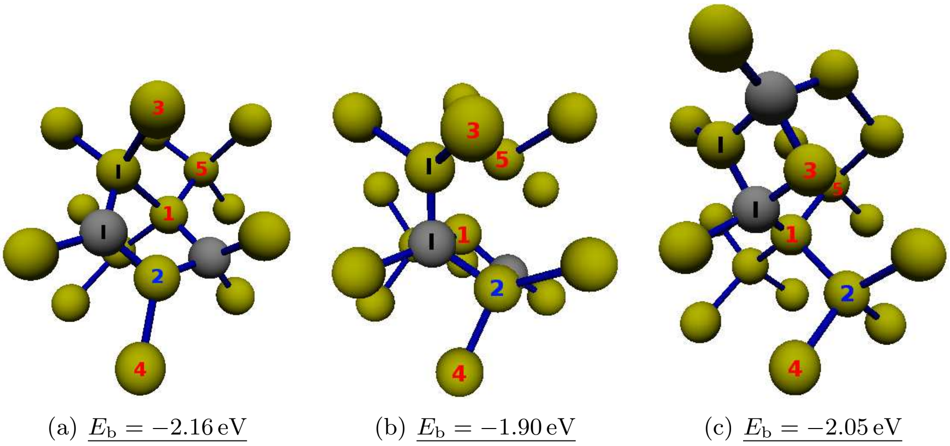

(a) $E_{\mathrm{b}} = -2.16\,\mathrm{eV}$ (b) $E_{\mathrm{b}} = -1.90\,\mathrm{eV}$ (c) $E_{\mathrm{b}} = -2.05\,\mathrm{eV}$

Figure 5.21: Relaxed structures of defect combinations obtained by creating [1 0 0] (a) and [0 1 0] (b) DBs at position 2 and a [0 0 1] (c) DB at position 3.

configuration suggests preferred C clustering as a competing mechanism to the $\mathrm{C_i}$ DB interstitial agglomeration inevitable for the SiC precipitation. However, the second most favorable configuration ($E_{\mathrm{f}} = -2.25\,\mathrm{eV}$) is represented four times, i.e. two times more often than the ground-state configuration, within the systematically investigated configuration space. Thus, particularly at high temperatures that cause an increase of the entropic contribution, this structure constitutes a serious opponent to the ground state. In fact, following results on migration simulations will reinforce the assumption of a low probability for C clustering by thermally activated processes.

Fig. 5.21 shows the three next energetically favorable configurations. The relaxed configuration obtained by creating a [1 0 0] DB at position 2 is shown in Fig. 5.21(a). A binding energy of -2.16 eV is observed. After relaxation, the second DB is aligned along [1 1 0]. The bond of Si atoms 1 and 2 does not persist. Instead, the Si atom forms a bond with the initial $\mathrm{C_i}$ and the second C atom forms a bond with Si atom 1 forming four bonds in total. The C atoms are spaced by 3.14 Å, which is very close to the expected C-C next neighbor distance of 3.08 Å in SiC. Figure 5.21(c) displays the results of a [0 0 1] DB inserted at position 3. The binding energy is -2.05 eV. Both DBs are tilted along the same direction remaining aligned in parallel and the second DB is pushed downwards in such a way that the four DB atoms form a rhomboid. Both C atoms form tetrahedral bonds to four Si atoms. However, Si atom number 1 and number 3, which are bound to the second $\mathrm{C_i}$ atom are also bound to the initial C atom. These four atoms of the rhomboid reside in a plane and, thus, do not match the situation in SiC. The C atoms have a distance of 2.75 Å. In Fig. 5.21(b) the relaxed structure of a [0 1 0] DB constructed at position 2 is displayed. An energy of -1.90 eV is observed. The initial DB and especially the C atom is pushed towards the Si atom of the second DB forming an additional fourth bond. Si atom number 1 is pulled towards the C atoms of the DBs accompanied by the disappearance of its bond to Si number 5 as well as the bond of Si number 5 to its neighbored Si atom in $[1\,1\,\overline{1}]$ direction. The C atom of the second DB forms threefold coordinated bonds to its Si neighbors. A distance of 2.80 Å is observed for the two C atoms. Again, the two C atoms and its two interconnecting Si atoms form a rhomboid. C-C distances of 2.70–2.80 Å seem to be characteristic for such configurations, in which the

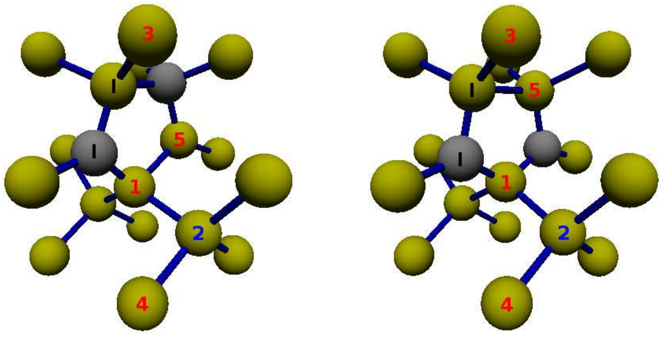

(a) $E_\mathrm{b} = -1.53\,\mathrm{eV}$ (b) $E_\mathrm{b} = -1.66\,\mathrm{eV}$

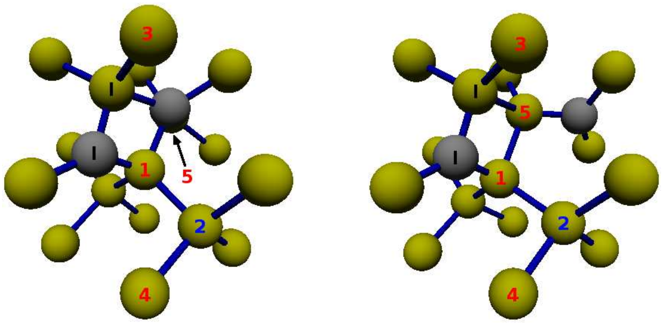

(c) $E_\mathrm{b} = -1.88\,\mathrm{eV}$ (d) $E_\mathrm{b} = -1.38\,\mathrm{eV}$

Figure 5.22: Relaxed structures of defect combinations obtained by creating $[0\,0\,1]$ (a), $[0\,0\,\bar{1}]$ (b), $[0\,\bar{1}\,0]$ (c) and $[1\,0\,0]$ (d) DBs at position 5.

C atoms and the two interconnecting Si atoms reside in a plane.

Configurations obtained by adding a $\mathrm{C_i}$ $\langle 1\,0\,0\rangle$ DB at position 4 are characterized by minimal changes from their initial creation condition during relaxation. There is a low interaction of the DBs, which seem to exist independent of each other. This, on the one hand, becomes evident by investigating the final structure, in which both of the DBs essentially retain the structure expected for a single DB and, on the other hand, is supported by the observed binding energies, which vary only slightly around zero. This low interaction is due to the large distance and a missing direct connection by bonds along a chain in the crystallographic $\langle 1\,1\,0\rangle$ direction. Both, C and Si atoms of the DBs form threefold coordinated bonds to their neighbors. The energetically most unfavorable configuration ($E_\mathrm{b} = 0.26\,\mathrm{eV}$) is obtained for the $\mathrm{C_i}$ $[0\,0\,1]$ DB, which is oppositely orientated with respect to the initial one. A DB taking the same orientation as the initial one is less unfavorable ($E_\mathrm{b} = 0.04\,\mathrm{eV}$). Both configurations are unfavorable compared to far-off, isolated DBs. Nonparallel orientations, i.e. the $[0\,1\,0]$, $[0\,\bar{1}\,0]$ and its equivalents, result in binding energies of -0.12 eV and -0.27 eV, thus, constituting energetically favorable configurations. The reduction of strain energy is higher in the second case, where the C atom of the second DB is placed in the direction pointing away from the initial C atom.

Energetically beneficial configurations of defect combinations are observed for interstitials of all orientations placed at position 5, a position two bonds away from the initial interstitial along the $[1\,1\,0]$ direction. Relaxed structures of these combinations are displayed in Fig. 5.22.

	1	2	3	4	5	6
E_{b} [eV]	-2.39	-1.88	-0.59	-0.31	-0.24	-0.21
C-C distance [Å]	1.4	4.6	6.5	8.6	10.5	10.8
Type	$[\bar{1}\,0\,0]$	$[1\,0\,0]$	$[1\,0\,0]$	$[1\,0\,0]$	$[1\,0\,0]$	$[1\,0\,0]$, $[0\,\bar{1}\,0]$

Table 5.5: Binding energies E_{b}, C-C distance and types of energetically most favorable $\mathrm{C_i}$ $\langle 1\,0\,0\rangle$-type defect pairs separated along the $[1\,1\,0]$ bond chain.

Fig. 5.22(a) and 5.22(b) show the relaxed structures of $[0\,0\,1]$ and $[0\,0\,\bar{1}]$ DBs. The upper DB atoms are pushed towards each other forming fourfold coordinated bonds. While the displacements of the Si atoms in case (b) are symmetric to the $(1\,1\,0)$ plane, in case (a), the Si atom of the initial DB is pushed a little further in the direction of the C atom of the second DB than the C atom is pushed towards the Si atom. The bottom atoms of the DBs remain in threefold coordination. The symmetric configuration is energetically more favorable ($E_{\mathrm{b}} = -1.66\,\mathrm{eV}$) since the displacements of the atoms is less than in the antiparallel case ($E_{\mathrm{b}} = -1.53\,\mathrm{eV}$). In Fig. 5.22(c) and 5.22(d) the non-parallel orientations, namely the $[0\,\bar{1}\,0]$ and $[1\,0\,0]$ DBs, are shown. Binding energies of -1.88 eV and -1.38 eV are obtained for the relaxed structures. In both cases, the Si atom of the initial interstitial is pulled towards the near by atom of the second DB. Both atoms form fourfold coordinated bonds to their neighbors. In case (c), it is the C and in case (d) the Si atom of the second interstitial, which forms the additional bond with the Si atom of the initial interstitial. The respective atom of the second DB, the $\mathrm{C_i}$ atom of the initial DB and the two interconnecting Si atoms again reside in a plane. As observed before, a typical C-C distance of 2.79 Å is, thus, observed for case (c). In both configurations, the far-off atom of the second DB resides in threefold coordination.

The interaction of $\mathrm{C_i}$ $\langle 1\,0\,0\rangle$ DBs is investigated along the $[1\,1\,0]$ bond chain assuming a possible reorientation of the DB atom at each position to minimize its configurational energy. Therefor, the binding energies of the energetically most favorable configurations with the second DB located along the $[1\,1\,0]$ direction and resulting C-C distances of the relaxed structures are summarized in Table 5.5. The binding energy of these configurations with respect to the C-C distance is plotted in Fig. 5.23. The interaction is found to be proportional to the reciprocal cube of the C-C distance for extended separations of the $\mathrm{C_i}$ DBs and saturates for the smallest possible separation, i.e. the ground-state configuration. The ground-state configuration was ignored in the fitting process. Not considering the previously mentioned elevated barriers for migration, an attractive interaction between the $\mathrm{C_i}$ $\langle 1\,0\,0\rangle$ DB defects indeed is detected with a capture radius that clearly exceeds 1 nm. The interpolated graph suggests the disappearance of attractive interaction forces, which are proportional to the slope of the graph, in between the two lowest separation distances of the defects. This finding, in turn, supports the previously established assumption of C agglomeration and absence of C clustering.

To draw further conclusions on the probability of C clustering, transitions into the ground-state configuration are investigated. Based on the lowest energy migration path of a single $\mathrm{C_i}$ $\langle 1\,0\,0\rangle$ DB, the configuration, in which the second $\mathrm{C_i}$ DB is oriented along $[0\,1\,0]$ at position 2, is assumed to constitute an ideal starting point for a transition into the ground state. In addition, the starting configuration exhibits a low binding energy (-1.90 eV) and is, thus, very

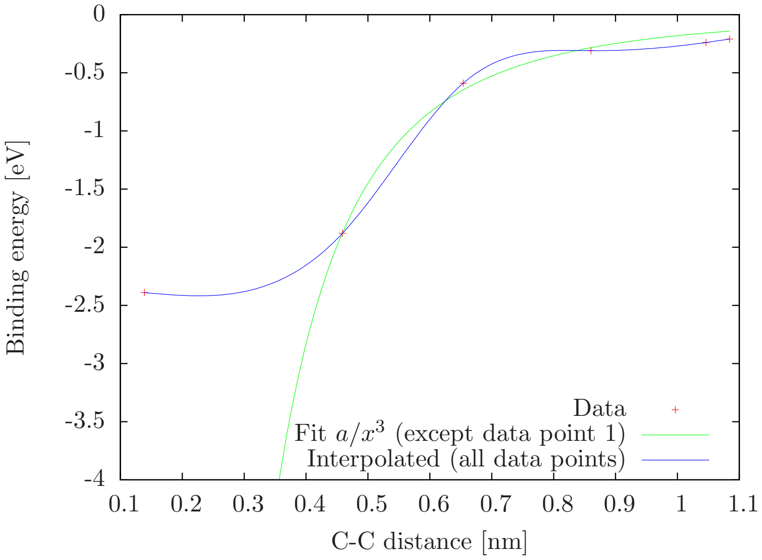

Figure 5.23: Minimum binding energy of dumbbell combinations separated along [1 1 0] with respect to the C-C distance. The blue line is a guide for the eye and the green curve corresponds to the most suitable fit function consisting of all but the first data point.

likely to occur. However, a smooth transition path is not found. Intermediate configurations within the investigated turbulent pathway identify barrier heights of more than 4 eV resulting in a low probability for the transition. The high activation energy is attributed to the stability of such a low energy configuration, in which the C atom of the second DB is located close to the initial DB. Due to an effective stress compensation realized in the respective low energy configuration, which will necessarily be lost during migration, a high energy configuration needs to get passed, which is responsible for the high barrier. Low barriers are only identified for transitions starting from energetically less favorable configurations, e.g. the configuration of a $[\bar{1}\,0\,0]$ DB located at position 2 (-0.36 eV). Starting from this configuration, an activation energy of only 1.2 eV is necessary for the transition into the ground state configuration. The corresponding migration energies and atomic configurations are displayed in Fig. 5.24. Since thermally activated C clustering is, thus, only possible by traversing energetically unfavored configurations, extensive C clustering is not expected. Furthermore, the migration barrier of 1.2 eV is still higher than the activation energy of 0.9 eV observed for a single $\mathrm{C_i}$ $\langle 1\,0\,0\rangle$ DB in c-Si. The migration barrier of a $\mathrm{C_i}$ DB in a complex system is assumed to approximate the barrier of a DB in a separated system with increasing defect separation. Accordingly, lower migration barriers are expected for pathways resulting in larger separations of the $\mathrm{C_i}$ DBs. However, if the increase of separation is accompanied by an increase in binding energy, this difference is needed in addition to the activation energy for the respective migration process. Configurations, which exhibit both, a low binding energy as well as afferent transitions with low activation energies are, thus, most probable $\mathrm{C_i}$ complex structures. On the other hand, if elevated temperatures enable migrations with huge activation energies, comparably small differences in configurational energy can be neglected resulting in an almost equal occupation of such configurations. In both cases, the configuration yielding a binding energy of -2.25 eV is promising. First of all, it constitutes the second most energetically favorable structure.

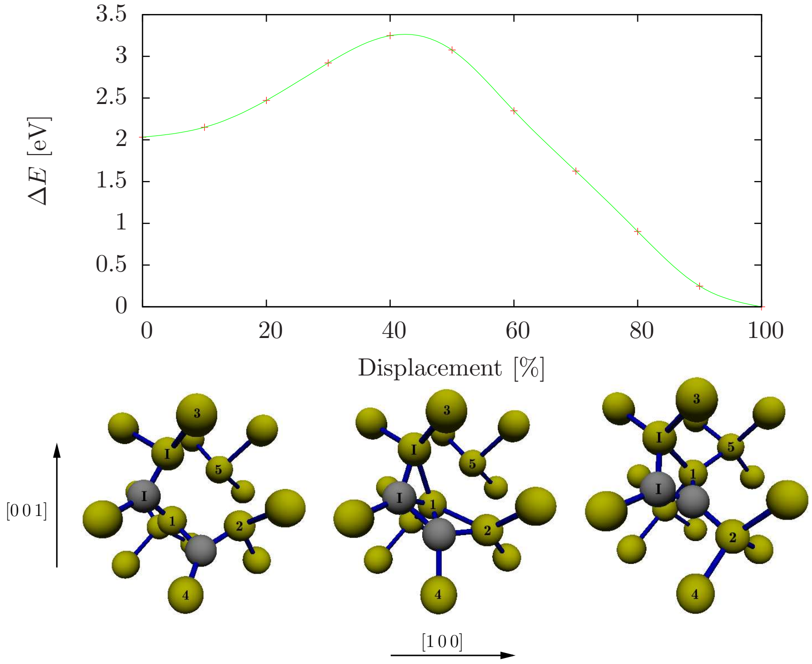

Figure 5.24: Migration barrier and structures of the transition of a C_i $[\bar{1}\,0\,0]$ DB at position 2 (left) into a C_i $[0\,\bar{1}\,0]$ DB at position 1 (right). An activation energy of 1.2 eV is observed.

1	2	3	4	5	R
0.26^a/-1.28^b	-0.51	-0.93^A/-0.95^B	-0.15	0.49	-0.05

Table 5.6: Binding energies of combinations of the C_i $[0\,0\,\bar{1}]$ defect with a C_s atom located at positions 1 to 5 according to Fig. 5.19(a). R corresponds to the position located at $\frac{a_{\text{Si}}}{2}[3\,2\,3]$ relative to the initial defect position, which is the maximum realizable distance due to periodic boundary conditions.

Secondly, a migration path with a barrier as low as 0.47 eV exists starting from a configuration of largely separated defects exhibiting a low binding energy (-1.88 eV). The migration barrier and corresponding structures are shown in Fig. 5.25. Finally, as already mentioned above, this type of defect pair is represented two times more often than the ground-state configuration. The latter is considered very important at high temperatures, accompanied by an increase in the entropic contribution to structure formation. As a result, C defect agglomeration indeed is expected, but only a low probability is assumed for C-C clustering by thermally activated processes with regard to the considered process time in IBS.

5.4.2 Combinations of the C_i $\langle 1\,0\,0\rangle$ and C_s type

Table 5.6 lists the energetic results of C_s combinations with the initial C_i $[0\,0\,\bar{1}]$ DB. For C_s located at position 1 and 3, the configurations α and A correspond to the naive relaxation of the structure by substituting the Si atom by a C atom in the initial C_i $[0\,0\,\bar{1}]$ DB structure at positions 1 and 3 respectively. However, small displacements of the involved atoms near the

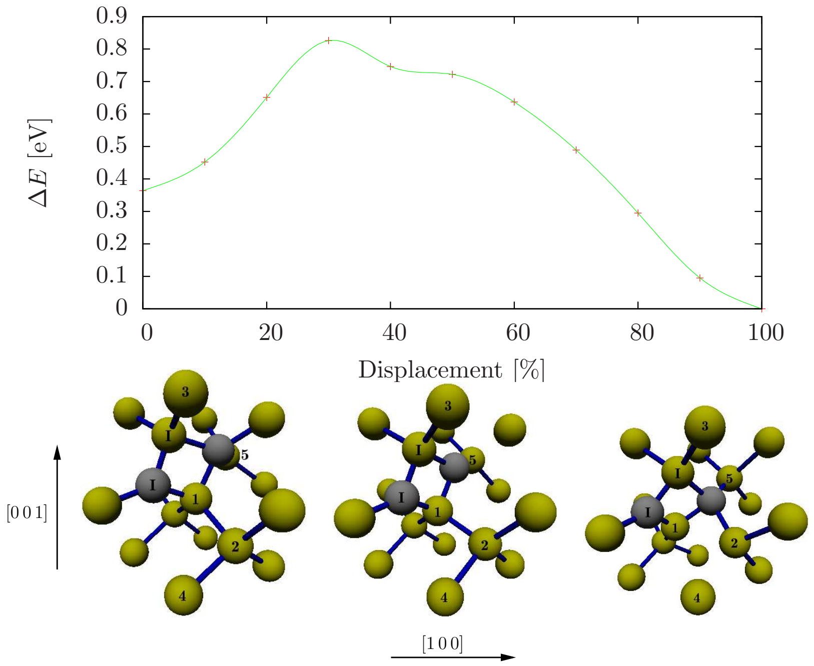

Figure 5.25: Migration barrier and structures of the transition of a $\mathrm{C_i}$ $[0\,\bar{1}\,0]$ DB at position 5 (left) into a $\mathrm{C_i}$ $[1\,0\,0]$ DB at position 1 (right). An activation energy of 0.47 eV is observed.

defect result in different stable structures labeled β and B respectively. Fig. 5.26 and 5.27 show structures A, B and α, β together with the barrier of migration for the A to B and α to β transition respectively.

Configuration A consists of a $\mathrm{C_i}$ $[0\,0\,\bar{1}]$ DB with threefold coordinated Si and C DB atoms slightly disturbed by the $\mathrm{C_s}$ at position 3, facing the Si DB atom as a neighbor. By a single bond switch, i.e. the breaking of a Si-Si in favor of a Si-C bond, configuration B is obtained, which shows a twofold coordinated Si atom located in between two substitutional C atoms residing on regular Si lattice sites. This configuration has been identified and described by spectroscopic experimental techniques [205] as well as theoretical studies [201, 206]. Configuration B is found to constitute the energetically slightly more favorable configuration. However, the gain in energy due to the significantly lower energy of a Si-C compared to a Si-Si bond turns out to be smaller than expected due to a large compensation by introduced strain as a result of the Si interstitial structure. Present results show a difference in energy of states A and B, which exactly matches the experimental value of 0.02 eV [205], reinforcing qualitatively correct results of previous theoretical studies on these structures. The migration barrier is identified to be 0.44 eV, almost three times higher than the experimental value of 0.16 eV [205] estimated for the neutral charge state transition in p- and n-type Si. Keeping in mind the formidable agreement of the energy difference with experiment, the overestimated activation energy is quite unexpected. Obviously, either the CRT algorithm fails to seize the actual saddle point structure or the influence of dopants has exceptional effect in the experimentally covered diffusion process being responsible for the low migration barrier.

Configuration α is similar to configuration A, except that the $\mathrm{C_s}$ atom at position 1 is facing the C DB atom as a neighbor resulting in the formation of a strong C-C bond and

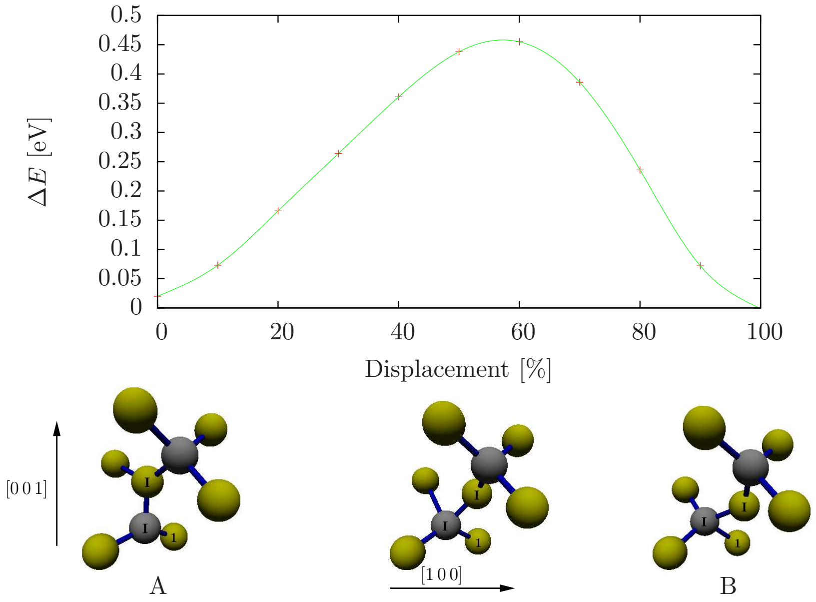

Figure 5.26: Migration barrier and structures of the transition of the initial C_i $[0\,0\,\overline{1}]$ DB and C_s at position 3 (left) into a configuration of a twofold coordinated Si_i located in between two C_s atoms occupying the lattice sites of the initial DB and position 3 (right). An activation energy of 0.44 eV is observed.

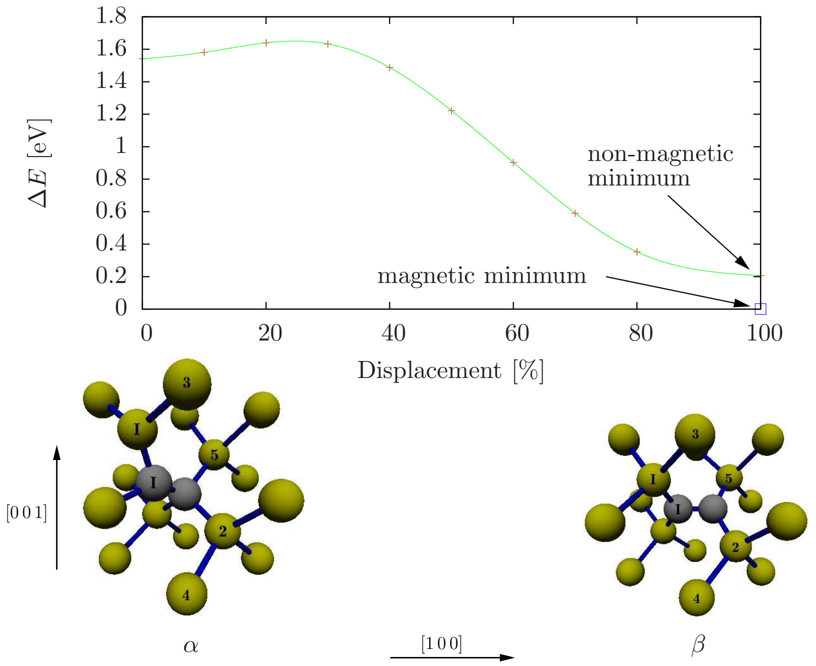

Figure 5.27: Migration barrier and structures of the transition of the initial C_i $[0\,0\,\overline{1}]$ DB and C_s at position 1 (left) into a C-C $[1\,0\,0]$ DB occupying the lattice site at position 1 (right). An activation energy of 0.1 eV is observed.

a much more noticeable perturbation of the DB structure. Nevertheless, the C and Si DB atoms remain threefold coordinated. Although the C-C bond exhibiting a distance of 0.15 nm close to the distance expected in diamond or graphite should lead to a huge gain in energy, a repulsive interaction with a binding energy of 0.26 eV is observed due to compressive strain of the Si DB atom and its top neighbors (0.230 nm/0.236 nm) along with additional tensile strain of the C_s and its three neighboring Si atoms (0.198–0.209 nm/0.189 nm). Again, a single bond switch, i.e. the breaking of the bond of the Si atom bound to the fourfold coordinated C_s atom and the formation of a double bond between the two C atoms, results in configuration b. The two C atoms form a [1 0 0] DB sharing the initial C_s lattice site while the initial Si DB atom occupies its previously regular lattice site. The transition is accompanied by a large gain in energy as can be seen in Fig. 5.27 making it the ground-state configuration of a C_s and C_i DB in Si yet 0.33 eV lower in energy than configuration B. This finding is in good agreement with a combined *ab initio* and experimental study of Liu et al. [207], who first proposed this structure as the ground state identifying an energy difference compared to configuration B of 0.2 eV. A net magnetization of two spin up electrons, which are equally localized as in the Si_i $\langle 1 0 0\rangle$ DB structure is observed. In fact, these two configurations are very similar and are qualitatively different from the C_i $\langle 1 0 0\rangle$ DB that does not show magnetization but a nearly collinear bond of the C DB atom to its two neighbored Si atoms while the Si DB atom approximates 120 ° angles in between its bonds. Configurations α, A and B are not affected by spin polarization and show zero magnetization. Mattoni et al. [204], in contrast, find configuration β less favorable than configuration A by 0.2 eV. Next to differences in the XC functional and plane-wave energy cut-off, this discrepancy might be attributed to the neglect of spin polarization in their calculations, which – as has been shown for the C_i BC configuration – results in an increase of configurational energy. Indeed, investigating the migration path from configurations α to β and, in doing so, reusing the wave functions of the previous migration step, the final structure, i.e. configuration β, is obtained with zero magnetization and an increase in configurational energy by 0.2 eV. Obviously, a different energy minimum of the electronic system is obtained indicating hysteresis behavior. However, since the total energy is lower for the magnetic result, it is believed to constitute the real, i.e. global, minimum with respect to electronic minimization. A low activation energy of 0.1 eV is observed for the a→b transition. Thus, configuration a is very unlikely to occur in favor of configuration b.

A repulsive interaction is observed for C_s at lattice sites along [1 1 0], i.e. positions 1 (configuration a) and 5. This is due to tensile strain originating from both, the C_i DB and the C_s atom residing within the [1 1 0] bond chain. This finding agrees well with results by Mattoni et al. [204]. In contrast, all other investigated configurations show attractive interactions. The most favorable configuration is found for C_s at position 3, which corresponds to the lattice site of one of the upper neighbored Si atoms of the DB structure that is compressively strained along $[1 \bar{1} 0]$ and [0 0 1] by the C-Si DB. The substitution with C allows for most effective compensation of strain. This structure is followed by C_s located at position 2, the lattice site of one of the neighbor atoms below the two Si atoms that are bound to the C_i DB atom. As mentioned earlier, these two lower Si atoms indeed experience tensile strain along the [1 1 0] bond chain, however, additional compressive strain along [0 0 1] exists. The latter is partially compensated by the C_s atom. Yet less of compensation is realized if C_s is located at position 4 due to a larger separation although both bottom Si atoms of the DB structure are indirectly affected, i.e. each of them is connected by another Si atom to the C atom enabling

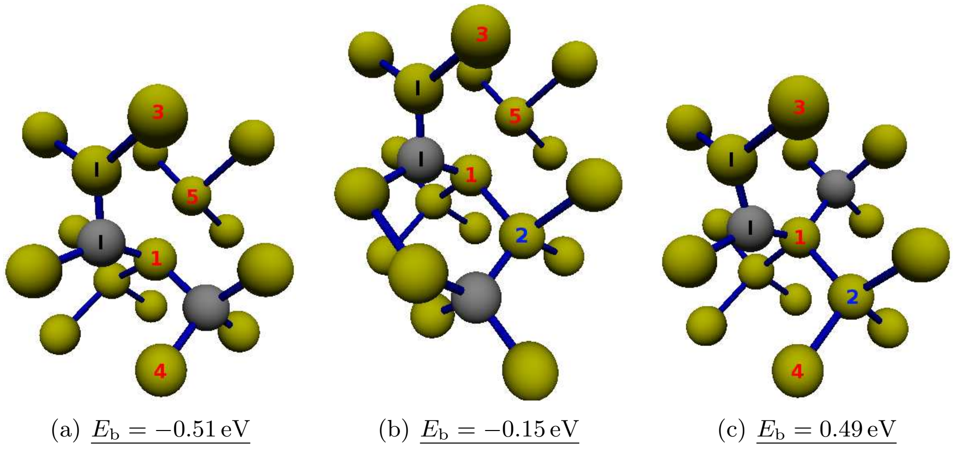

(a) $E_{\mathrm{b}} = -0.51\,\mathrm{eV}$ (b) $E_{\mathrm{b}} = -0.15\,\mathrm{eV}$ (c) $E_{\mathrm{b}} = 0.49\,\mathrm{eV}$

Figure 5.28: Relaxed structures of defect combinations obtained by creating $\mathrm{C_s}$ at positions 2 (a), 4 (b) and 5 (c) in the $\mathrm{C_i}$ $[0\,0\,\bar{1}]$ DB configuration.

the reduction of strain along $[0\,0\,1]$. Fig. 5.28 lists the remaining configurations and binding energies of the relaxed structures obtained by creating a $\mathrm{C_s}$ at positions 2, 4 and 5 in the $\mathrm{C_i}$ $[0\,0\,\bar{1}]$ DB configuration.

Obviously, agglomeration of $\mathrm{C_i}$ and $\mathrm{C_s}$ is energetically favorable except for separations along one of the $\langle 1\,1\,0\rangle$ directions. The energetically most favorable configuration (configuration β) forms a strong but compressively strained C-C bond with a separation distance of 0.142 nm sharing a Si lattice site. Again, conclusions concerning the probability of formation are drawn by investigating respective migration paths. Since $\mathrm{C_s}$ is unlikely to exhibit a low activation energy for migration, the focus is on $\mathrm{C_i}$. Pathways starting from the next most favored configuration, i.e. $\mathrm{C_s}$ located at position 2, into configuration α and β are investigated, which show activation energies above 2.2 eV and 2.5 eV. The respective barriers and structures are displayed in Fig. 5.29. For the transition into configuration β, as before, the non-magnetic configuration is obtained. If not forced by the CRT algorithm, the structures beyond 50 % and below 90 % displacement of the transition approaching configuration α would settle into configuration β. Although lower than the barriers for obtaining the ground state of two $\mathrm{C_i}$ defects, the activation energies are yet considered too high. For the same reasons as in the last subsection, structures other than the ground-state configuration are, thus, assumed to arise more likely due to much lower activation energies necessary for their formation and still comparatively low binding energies.

5.4.3 Combinations of a $\mathrm{C_i}$ $\langle 1\,0\,0\rangle$ DB and a vacancy

In the last section, configurations of a $\mathrm{C_i}$ DB with $\mathrm{C_s}$ occupying a vacant site have been investigated. Additionally, configurations might arise in IBS, in which the impinging C atom creates a vacant site near a $\mathrm{C_i}$ DB, but does not occupy it. These structures are investigated in the following.

Resulting binding energies of a $\mathrm{C_i}$ DB and a nearby vacancy are listed in the second row of Table 5.7. Figure 5.30 shows the associated configurations. All investigated structures are preferred compared to isolated, largely separated defects. In contrast to $\mathrm{C_s}$, this is also

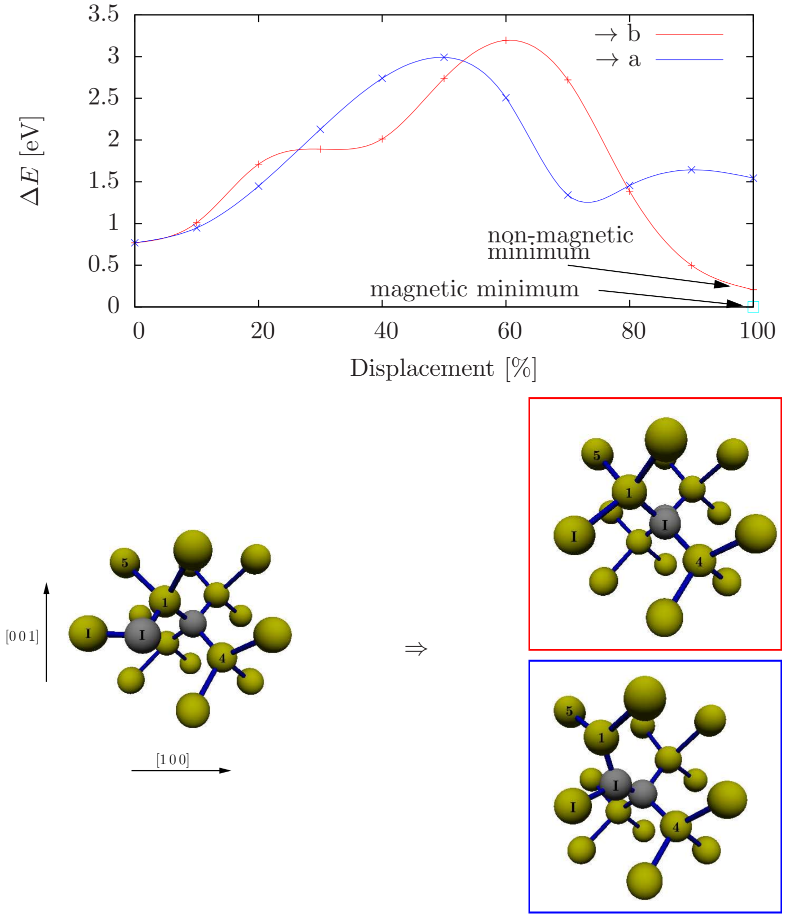

Figure 5.29: Migration barrier and structures of the transition of a configuration equivalent to the one of the initial $\langle 0\,0\,\bar{1}\rangle$ C_i DB with C_s located at position 2 into the α and β configurations.

1	2	3	4	5	R
-5.39 (→ C_S)	-0.59	-3.14	-0.54	-0.50	-0.31

Table 5.7: Binding energies of combinations of the C_i $[0\,0\,\bar{1}]$ defect with a vacancy located at positions 1 to 5 according to Fig. 5.19(a). R corresponds to the position located at $\frac{a_{Si}}{2}[3\,2\,3]$ relative to the initial defect position, which is the maximum realizable distance due to periodic boundary conditions.

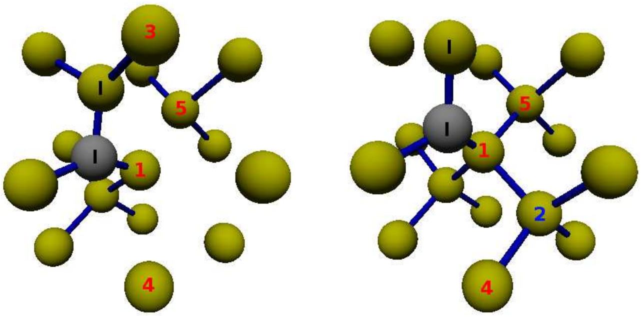

(a) $\underline{E_{\mathrm{b}} = -0.59\,\mathrm{eV}}$ (b) $\underline{E_{\mathrm{b}} = -3.14\,\mathrm{eV}}$

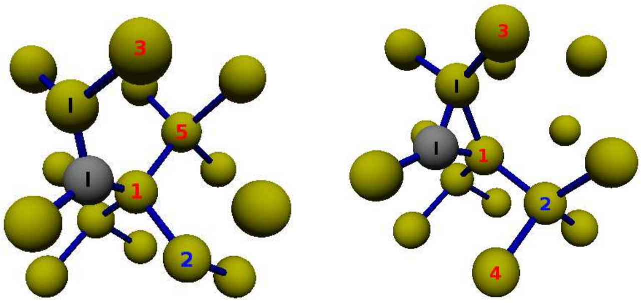

(c) $\underline{E_{\mathrm{b}} = -0.54\,\mathrm{eV}}$ (d) $\underline{E_{\mathrm{b}} = -0.50\,\mathrm{eV}}$

Figure 5.30: Relaxed structures of defect combinations obtained by creating a vacancy at positions 2 (a), 3 (b), 4 (c) and 5 (d).

valid for positions along [1 1 0] resulting in an entirely attractive interaction between defects of these types. Even for the largest possible distance (R) achieved in the calculations of the periodic supercell a binding energy as low as -0.31 eV is observed. The creation of a vacancy at position 1 results in a configuration of substitutional C on a Si lattice site and no other remaining defects. The C_i DB atom moves to position 1 where the vacancy is created and the Si_i DB atom recaptures the DB lattice site. With a binding energy of -5.39 eV, this is the energetically most favorable configuration observed. A great amount of strain energy is reduced by removing the Si atom at position 3, which is illustrated in Fig. 5.30(b). The DB structure shifts towards the position of the vacancy, which replaces the Si atom usually bound to and at the same time strained by the Si_i DB atom. Due to the displacement into the $[1\,\bar{1}\,0]$ direction, the bond of the DB Si atom to the Si atom on the top left breaks and instead forms a bond to the Si atom located in $[1\,\bar{1}\,1]$ direction, which is not shown in Fig. 5.30(b). A binding energy of -3.14 eV is obtained for this structure composing another energetically favorable configuration. A vacancy created at position 2 enables the relaxation of Si atom number 1 mainly in $[0\,0\,\bar{1}]$ direction. The bond to Si atom number 5 breaks. Hence, the Si_i DB atom is not only displaced along $[0\,0\,\bar{1}]$ but also and to a greater extent in [1 1 0] direction. The C atom is slightly displaced in $[0\,1\,\bar{1}]$ direction. A binding energy of -0.59 eV indicates the occurrence of much less strain reduction compared to that in the latter configuration. Evidently, this is due to a smaller displacement of Si atom 1, which would be directly bound to the replaced Si atom at position 2. In the case of a vacancy created at position 4, even a slightly higher binding energy of -0.54 eV is observed while the Si atom at the bottom left, which is bound to the C_i DB atom, is vastly displaced along $[1\,0\,\bar{1}]$. However, the displacement of the C atom along $[0\,0\,\bar{1}]$ is less compared to the one in the previous configuration. Although expected due to the symmetric initial configuration, Si atom number 1 is not displaced correspondingly and also the Si_i DB atom is displaced to a greater extent in $[\bar{1}\,0\,0]$ than in $[0\,\bar{1}\,0]$ direction. The symmetric configuration is, thus, assumed to constitute a local maximum, which is driven into the present state by the conjugate gradient method used for relaxation. Fig. 5.30(d) shows the relaxed structure of a vacancy created at position 5. The Si DB atom is largely displaced along [1 1 0] and somewhat less along $[0\,0\,\bar{1}]$, which corresponds to the direction towards the vacancy. The Si_i DB atom approaches Si atom number 1. Indeed, a non-zero charge density is observed in between these two atoms exhibiting a cylinder-like shape superposed with the charge density known from the DB itself. Strain reduced by this huge displacement is partially absorbed by tensile strain on Si atom number 1 originating from attractive forces of the C atom and the vacancy. A binding energy of -0.50 eV is observed.

The migration pathways of configuration 5.30(b) and 5.30(a) into the ground-state configuration, i.e. the C_s configuration, are shown in Fig. 5.31 and 5.32 respectively. Activation energies as low as 0.1 eV and 0.6 eV are observed. In the first case, the Si and C atom of the DB move towards the vacant and initial DB lattice site respectively. In total, three Si-Si and one more Si-C bond is formed during transition. The activation energy of 0.1 eV is needed to tilt the DB structure. Once this barrier is overcome, the C atom forms a bond to the top left Si atom and the Si_i atom capturing the vacant site is forming new tetrahedral bonds to its neighbored Si atoms. These new bonds and the relaxation into the C_s configuration are responsible for the gain in configurational energy. For the reverse process approximately 2.4 eV are needed, which is 24 times higher than the forward process. In the second case, the lowest barrier is found for the migration of Si number 1, which is substituted by the C_i atom, towards the vacant site. A net amount of five Si-Si bonds and one Si-C bond are

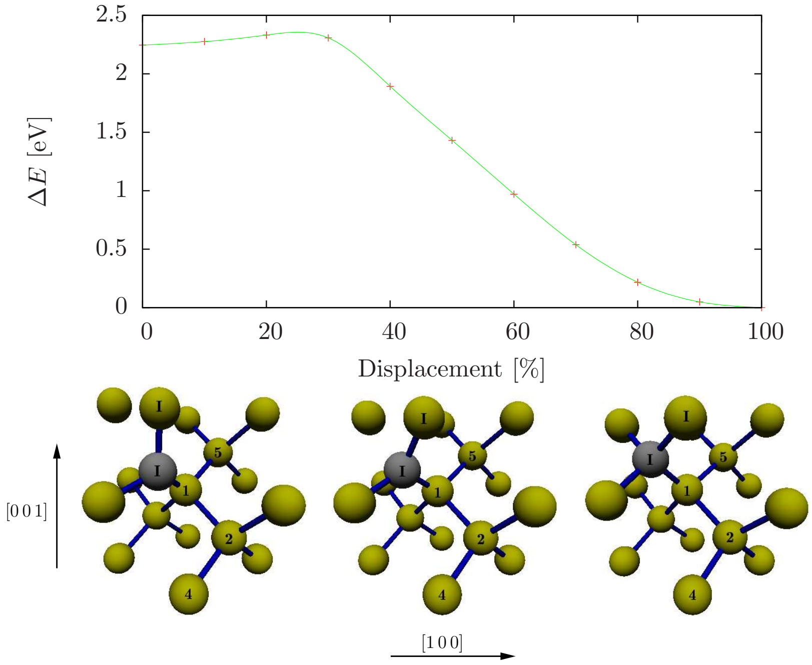

Figure 5.31: Migration barrier and structures of the transition of the initial C$_\text{i}$ $[0\,0\,\bar{1}]$ DB and a V created at position 3 (left) into a C$_\text{s}$ configuration (right). An activation energy of 0.1 eV is observed.

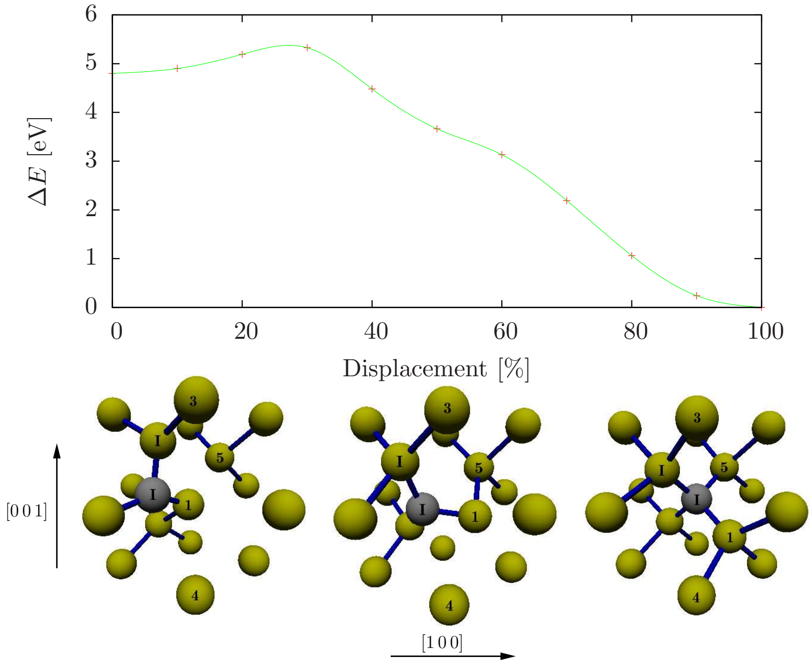

Figure 5.32: Migration barrier and structures of the transition of the initial C$_\text{i}$ $[0\,0\,\bar{1}]$ DB and a V created at position 2 (left) into a C$_\text{s}$ configuration (right). An activation energy of 0.6 eV is observed.

	$[1\,1\,0]$	$[\bar{1}\,1\,0]$	$[0\,1\,1]$	$[0\,\bar{1}\,1]$	$[1\,0\,1]$	$[\bar{1}\,0\,1]$
1	I	III	III	I	III	I
2	II	VI	VI	II	VIII	V
3	III	I	III	I	I	III
4	IV	VII	IX	X	X	IX
5	V	VIII	VI	II	VI	II

Table 5.8: Equivalent configurations labeled I-X of $\langle 1\,1\,0\rangle$-type Si_i DBs created at position I and C_s created at positions 1 to 5 according to Fig. 5.19(b). The respective orientation of the Si_i DB is given in the first row.

additionally formed during transition. An activation energy of 0.6 eV necessary to overcome the migration barrier is found. This energy is low enough to constitute a feasible mechanism in SiC precipitation. To reverse this process, 5.4 eV are needed, which make this mechanism very improbable. The migration path is best described by the reverse process. Starting at 100 %, energy is needed to break the bonds of Si atom 1 to its neighbored Si atoms as well as the bond of the C atom to Si atom number 5. At 50 % displacement, these bonds are broken. Due to this, and due to the formation of new bonds, e.g. the bond of Si atom number 1 to Si atom number 5, a less steep increase of configurational energy is observed. In a last step, the just recently formed bond of Si atom number 1 to Si atom number 5 is broken up again as well as the bond of the initial Si DB atom and its Si neighbor in $[\bar{1}\,\bar{1}\,\bar{1}]$ direction, which explains the repeated boost in energy. Finally, the system gains some configurational energy by relaxation into the configuration corresponding to 0 % displacement. The direct migration of the C_i atom onto the vacant lattice site results in a somewhat higher barrier of 1.0 eV. In both cases, the formation of additional bonds is responsible for the vast gain in energy rendering almost impossible the reverse processes.

In summary, pairs of C_i DBs and vacancies, like no other before, show highly attractive interactions for all investigated combinations independent of orientation and separation direction of the defects. Furthermore, small activation energies, even for transitions into the ground state, exist. If the vacancy is created at position 1, the system will end up in a configuration of C_s anyways. Based on these results, a high probability for the formation of C_s must be concluded.

5.4.4 Combinations of Si_i and C_s

So far, the C-Si $\langle 1\,0\,0\rangle$ DB interstitial was found to be the energetically most favorable configuration. In fact, substitutional C exhibits a configuration more than 3 eV lower with respect to the formation energy. However, the configuration does not account for the accompanying Si self-interstitial that is generated once a C atom occupies the site of a Si atom. With regard to the IBS process, in which highly energetic C atoms enter the Si target being able to kick out Si atoms from their lattice sites, such configurations are absolutely conceivable and a significant influence on the precipitation process might be attributed to them. Thus, combinations of C_s with an additional Si_i are examined in the following. The ground-state of a single Si_i was found to be the Si_i $\langle 1\,1\,0\rangle$ DB configuration. For the following study, the same type of self-interstitial is assumed to provide the energetically most favorable configuration in combination with C_s.

	I	II	III	IV	V	VI	VII	VIII	IX	X
E_f [eV]	4.37	5.26	5.57	5.37	5.12	5.10	5.32	5.28	5.39	5.32
E_b [eV]	-0.97	-0.08	0.22	-0.02	-0.23	-0.25	-0.02	-0.06	0.05	-0.03
r [nm]	0.292	0.394	0.241	0.453	0.407	0.408	0.452	0.392	0.456	0.453

Table 5.9: Formation energies E_f, binding energies E_b and C_s-Si_i separation distances of configurations combining C_s and Si_i as defined in Table 5.8.

Table 5.8 classifies equivalent configurations of $\langle 1\,1\,0\rangle$-type Si_i DBs created at position I and C_s created at positions 1 to 5 according to Fig. 5.19(b). Corresponding formation as well as binding energies and the separation distances of the C_s atom and the Si_i DB lattice site are listed in Table 5.9. In total, ten different configurations exist within the investigated range. Configuration I constitutes the energetically most favorable structure exhibiting a formation energy of 4.37 eV. Obviously, the configuration of a Si_i $[1\,1\,0]$ DB and a neighbored C_s atom along the bond chain, which has the same direction as the alignment of the DB, enables the largest possible reduction of strain. The relaxed structure is displayed in the bottom right of Fig. 5.33. Compressive strain originating from the Si_i is compensated by tensile strain inherent to the C_s configuration. The Si_i DB atoms are displaced towards the lattice site occupied by the C_s atom in such a way that the Si_i DB atom closest to the C atom does no longer form bonds to its top Si neighbors but to the next neighbored Si atom along $[1\,1\,0]$. In the same way the energetically most unfavorable configuration can be explained, which is configuration III. The C_s is located next to the lattice site shared by the Si_i $[1\,1\,0]$ DB in $[1\,\bar{1}\,1]$ direction. Thus, the compressive stress along $[1\,1\,0]$ of the Si_i $[1\,1\,0]$ DB is not compensated but intensified by the tensile stress of the C_s atom, which is no longer located along the direction of stress.

However, even configuration I is energetically less favorable than the $\langle 1\,0\,0\rangle$ C_i DB, which, thus, remains the ground state of a C atom introduced into otherwise perfect c-Si. The transition involving the latter two configurations is shown in Fig. 5.33. An activation energy as low as 0.12 eV is necessary for the migration into the ground-state configuration. Accordingly, the C_i $\langle 1\,0\,0\rangle$ DB configuration is assumed to occur more likely. However, only 0.77 eV are needed for the reverse process, i.e. the formation of C_s and a Si_i DB out of the ground state. Due to the low activation energy, this process must be considered to be activated without much effort either thermally or by introduced energy of the implantation process.

Fig. 5.34 shows the binding energies of pairs of C_s and a Si_i $\langle 1\,1\,0\rangle$ DB with respect to the separation distance. The interaction of the defects is well approximated by a Lennard-Jones (LJ) 6-12 potential, which is used for curve fitting. Unable to model possible positive values of the binding energy, i.e. unfavorable configurations, located to the right of the minimum, the LJ fit should rather be thought of as a guide for the eye describing the decrease of the interaction strength, i.e. the absolute value of the binding energy, with increasing separation distance. The binding energy quickly drops to zero. The LJ fit estimates almost zero interaction already at 0.6 nm indicating a low interaction capture radius of the defect pair. In IBS, highly energetic collisions are assumed to easily produce configurations of defects exhibiting separation distances exceeding the capture radius. For this reason, C_s without a Si_i DB located within the immediate proximity, which is, thus, unable to form the thermodynamically stable C_i $\langle 1\,0\,0\rangle$ DB, constitutes a most likely configuration to be found in IBS. Particularly in

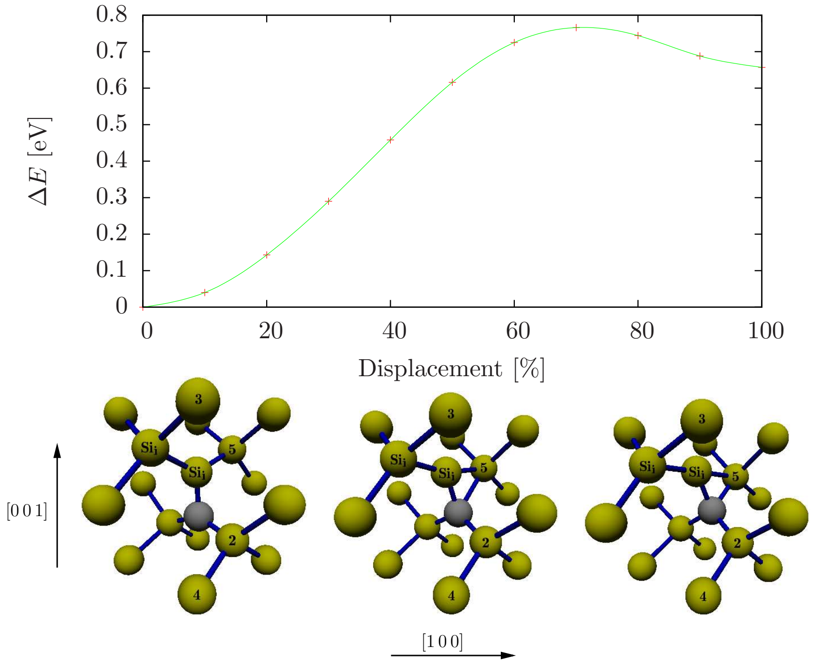

Figure 5.33: Migration barrier and structures of the transition of a [1 1 0] Si$_i$ DB next to C$_s$ (right) into the C$_i$ $[0\,0\,\bar{1}]$ DB configuration (left). An activation energy of 0.12 eV and 0.77 eV for the reverse process is observed.

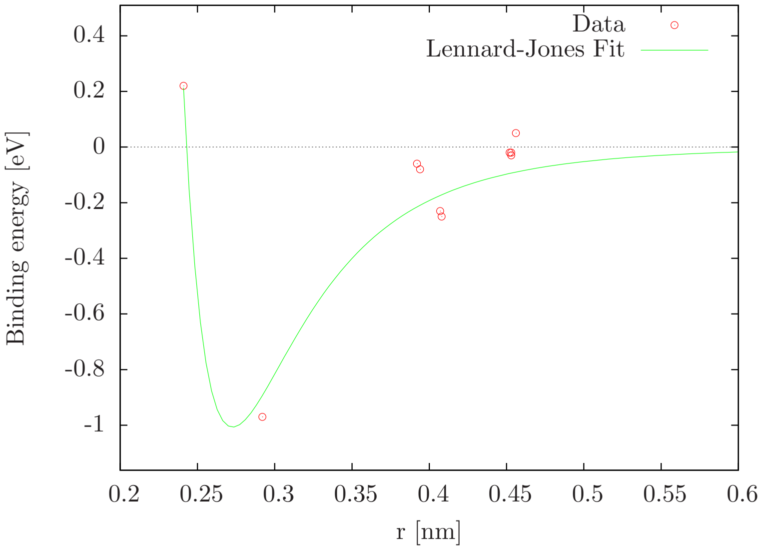

Figure 5.34: Binding energies of combinations of a C$_s$ and a Si$_i$ DB with respect to the separation distance. The interaction strength of the defect pairs are well approximated by a Lennard-Jones 6-12 potential, which is used for curve fitting.

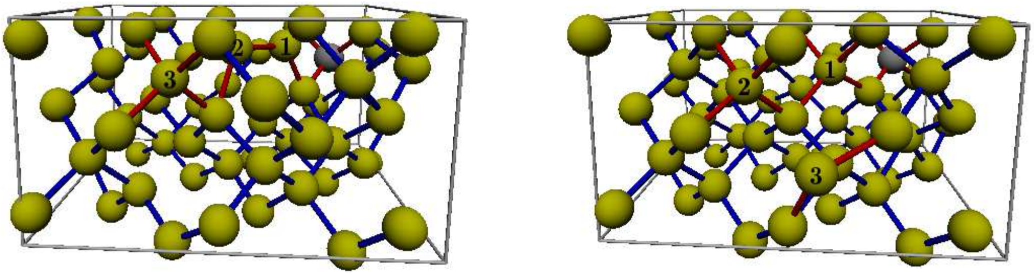

$t = 2230\,\mathrm{fs}$ $t = 2900\,\mathrm{fs}$

Figure 5.35: Atomic configurations of an *ab initio* molecular dynamics run at 900 °C starting from a configuration of $\mathrm{C_s}$ located next to a $\mathrm{Si_i}$ [1 1 0] DB (atoms 1 and 2). Equal atoms are marked by equal numbers. For substantial atoms, bonds are drawn in red color.

IBS, which constitutes a system driven far from equilibrium, respective defect configurations might exist that do not combine into the ground-state configuration. Thus, the existence of $\mathrm{C_s}$ is very likely.

Similar to what was previously mentioned, configurations of $\mathrm{C_s}$ and a $\mathrm{Si_i}$ DB might be eminently important at higher temperatures due to the low activation energy necessary for its formation. At higher temperatures, the contribution of entropy to structural formation increases, which might result in a spatial separation even for defects located within the capture radius. Indeed, an *ab initio* MD run at 900 °C starting from configuration I, which – based on the above findings – is assumed to recombine into the ground state configuration, results in a separation of the $\mathrm{C_s}$ and $\mathrm{Si_i}$ DB by more than 4 neighbor distances realized in a repeated migration mechanism of annihilating and arising $\mathrm{Si_i}$ DBs. The atomic configurations for two different points in time are shown in Fig. 5.35. Si atoms 1 and 2, which form the initial DB, occupy Si lattice sites in the final configuration while Si atom 3 is transferred from a regular lattice site into the interstitial lattice. These results support the above assumptions of an increased entropic contribution to structural formation involving $\mathrm{C_s}$ to a greater extent.

5.5 Mobility of the silicon self-interstitial

The possibility for separated configurations of $\mathrm{C_s}$ and $\mathrm{Si_i}$ becomes even more likely if one of the constituents exhibits a low barrier of migration. In this case, the $\mathrm{Si_i}$ is assumed to constitute the mobile defect compared to the stable $\mathrm{C_s}$ atom. Thus, migration paths of $\mathrm{Si_i}$ are investigated in the following excursus. According to Fig. 5.36, an activation energy of 0.67 eV is necessary for the transition of the $\mathrm{Si_i}$ $[0\,\bar{1}\,1]$ to [1 1 0] DB located at the neighbored Si lattice site in $[1\,1\,\bar{1}]$ direction. The barrier, which is even lower than the one for $\mathrm{C_i}$, indeed indicates highly mobile $\mathrm{Si_i}$. In fact, a similar transition is expected if the $\mathrm{Si_i}$ atom, which does not change the lattice site during transition, is located next to a $\mathrm{C_s}$ atom. Due to the low barrier, the initial separation of the $\mathrm{C_s}$ and $\mathrm{Si_i}$ atom are very likely to occur. Further investigations revealed transition barriers of 0.94 eV for the $\mathrm{Si_i}$ [1 1 0] DB to the hexagonal $\mathrm{Si_i}$, 0.53 eV for the $\mathrm{Si_i}$ [1 1 0] DB to the tetrahedral $\mathrm{Si_i}$ and 0.35 eV for the hexagonal $\mathrm{Si_i}$ to the tetrahedral $\mathrm{Si_i}$ configuration. The respective configurational energies are shown in Fig. 5.37. The obtained activation energies are of the same order of magnitude than values derived from other *ab initio* studies [208, 209]. The low barriers indeed enable configurations of further

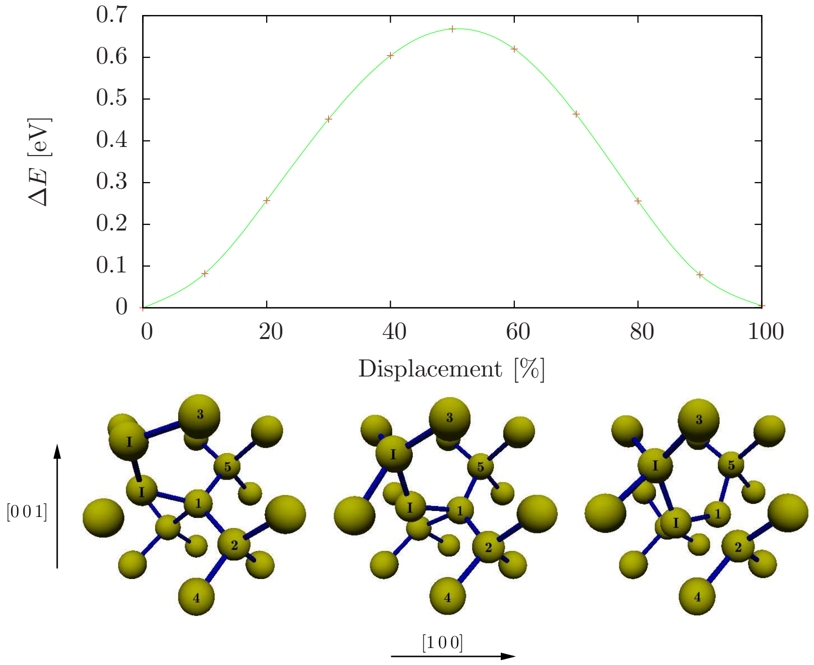

Figure 5.36: Migration barrier and structures of the Si_i $[0\,\bar{1}\,1]$ DB (left) to the $[1\,1\,0]$ DB (right) transition. Bonds are illustrated by blue lines.

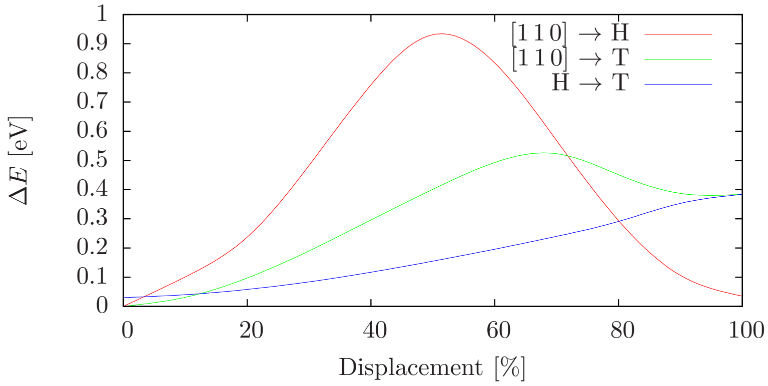

Figure 5.37: Migration barrier of the Si_i $[1\,1\,0]$ DB into the hexagonal (H) and tetrahedral (T) configuration as well as the hexagonal Si_i to tetrahedral Si_i transition.

	C_i ⟨1 0 0⟩	C_s & Si_i ⟨1 1 0⟩	C_s & Si_i T
VASP	3.72	4.37	$4.17^a/4.99^b/4.96^c$
POSIC	3.88	4.93	$5.25^a/5.08^b/4.43^c$

Table 5.10: Formation energies of defect configurations of a single C impurity in otherwise perfect c-Si determined by classical potential and *ab initio* methods. The formation energies are given in eV. T denotes the tetrahedral and the subscripts i and s indicate the interstitial and substitutional configuration. Superscripts a, b and c denote configurations of C_s located at the first, second and third nearest neighbored lattice site with respect to the Si_i atom.

separated C_s and Si_i atoms by the highly mobile Si_i atom departing from the C_s defect as observed in the previously discussed MD simulation.

5.6 Applicability: Competition of C_i and C_s-Si_i

As has been shown, the energetically most favorable configuration of C_s and Si_i is obtained for C_s located at the neighbored lattice site along the [1 1 0] bond chain of a Si_i [1 1 0] DB. However, the energy of formation is slightly higher than that of the C_i ⟨1 0 0⟩ DB, which constitutes the ground state for a C impurity introduced into otherwise perfect c-Si.

For a possible clarification of the controversial views on the participation of C_s in the precipitation mechanism by classical potential simulations, test calculations need to ensure the proper description of the relative formation energies of combined structures of C_s and Si_i compared to C_i. This is particularly important since the energy of formation of C_s is drastically underestimated by the EA potential. A possible occurrence of C_s could then be attributed to a lower energy of formation of the C_s-Si_i combination due to the low formation energy of C_s, which is obviously wrong.

Since quantum-mechanical calculations reveal the Si_i ⟨1 1 0⟩ DB as the ground-state configuration of Si_i in Si, it was assumed to provide the energetically most favorable configuration in combination with C_s in the calculations carried out in section 5.4.4. Empirical potentials, however, predict Si_i T to be the energetically most favorable configuration. Thus, investigations of the relative energies of formation of defect pairs need to include combinations of C_s with Si_i T. Results of *ab initio* and classical potential calculations are summarized in Table 5.10. Obviously, the EA potential properly describes the relative energies of formation. Combined structures of C_s and Si_i T are energetically less favorable than the ground state C_i ⟨1 0 0⟩ DB configuration. With increasing separation distance, the energies of formation decrease. However, even for non-interacting defects, the energy of formation, which is then given by the sum of the formation energies of the separated defects (4.15 eV) is still higher than that of the C_i ⟨1 0 0⟩ DB. Unexpectedly, the structure of a Si_i ⟨1 1 0⟩ DB and a neighbored C_s, which is the most favored configuration of a C_s and Si_i DB according to quantum-mechanical calculations, likewise constitutes an energetically favorable configuration within the EA description, which is even preferred over the two least separated configurations of C_s and Si_i T. This is attributed to an effective reduction in strain enabled by the respective combination. Quantum-mechanical results reveal a more favorable energy of formation for the C_s and Si_i T (a) configuration. However, this configuration is unstable involving a structural transition into the C_i ⟨1 1 0⟩ DB interstitial, thus, not maintaining the tetrahedral Si nor the C_s defect.

Thus, the underestimated energy of formation of C_s within the EA calculation does not pose a serious limitation in the present context. Since C is introduced into a perfect Si crystal and the number of particles is conserved in simulation, the creation of C_s is accompanied by the creation of Si_i, which is energetically less favorable than the ground state, i.e. the C_i $\langle 1\,0\,0\rangle$ DB configuration, for both, the EA and *ab initio* treatment. In either case, no configuration more favorable than the C_i $\langle 1\,0\,0\rangle$ DB has been found. Thus, a proper description with respect to the relative energies of formation is assumed for the EA potential.

5.7 Conclusions concerning the SiC conversion mechanism

These findings allow to draw conclusions on the mechanisms involved in the process of SiC conversion in Si. Agglomeration of C_i is energetically favored and enabled by a low activation energy for migration. Although ion implantation is a process far from thermodynamic equilibrium, which might result in phases not described by the Si/C phase diagram, i.e. a C phase in Si, high activation energies are believed to be responsible for a low probability of the formation of C-C clusters.

In the context of the initially stated controversy present in the precipitation model, these findings suggest an increased participation of C_s already in the initial stage due to its high probability of incidence. In addition, thermally activated, C_i might turn into C_s. The associated emission of Si_i serves two needs: as a vehicle for other C_s atoms and as a supply of Si atoms needed elsewhere to form the SiC structure. As for the vehicle, Si_i is believed to react with C_s turning it into highly mobile C_i again, allowing for the rearrangement of the C atom. The rearrangement is crucial to end up in a configuration of C atoms only occupying substitutionally the lattice sites of one of the two fcc lattices that build up the diamond lattice. On the other hand, the conversion of some region of Si into SiC by C_s is accompanied by a reduction of the volume since SiC exhibits a 20 % smaller lattice constant than Si. The reduction in volume is compensated by excess Si_i serving as building blocks for the surrounding Si host or a further formation of SiC.

To conclude, the available results suggest precipitation by successive agglomeration of C_s. However, the agglomeration and rearrangement of C_s is only possible by mobile C_i, which has to be present at the same time. Accordingly, the process is governed by both, C_s accompanied by Si_i as well as C_i. It is worth to mention that there is no contradiction to results of the HREM studies [17, 20, 144, 145, 210]. Regions showing dark contrasts in an otherwise undisturbed Si lattice are attributed to C atoms in the interstitial lattice. However, there is no particular reason for the C species to reside in the interstitial lattice. Contrasts are also assumed for Si_i. Once precipitation occurs, regions of dark contrasts disappear in favor of Moiré patterns indicating 3C-SiC in c-Si due to the mismatch in the lattice constant. Until then, however, these regions could either be composed of stretched coherent SiC and interstitials or of already contracted incoherent SiC surrounded by Si and interstitials, where the latter is too small to be detected in HREM. In both cases, Si_i might be attributed a third role, which is the partial compensation of tensile strain that is present either in the stretched SiC or at the interface of the contracted SiC and the Si host.

Furthermore, the experimentally observed alignment of the $(h\,k\,l)$ planes of the precipitate and the substrate is satisfied by the mechanism of successive positioning of C_s. In contrast, there is no obvious reason for the topotactic orientation of an agglomerate consisting exclusively of C-Si dimers, which would necessarily involve a much more profound change in structure for the transition into SiC.

Conclusions on the SiC precipitation mechanism in Si, which additionally include and consider results of the molecular dynamics investigations presented in the following, are elaborated in more detail within the comprehensive description in chapter 7.

Chapter 6

Silicon carbide precipitation simulations

The molecular dynamics (MD) technique is used to gain insight into the behavior of C existing in different concentrations in c-Si on the microscopic level at finite temperatures. The simulations are restricted to classical potential simulations utilizing the analytical EA bond order potential as described in section 3.1.2. Parameters are chosen according to the discussion in section 4.2.

At the beginning, simulations are performed, which try to mimic the conditions during IBS. Results reveal limitations of the employed potential and MD in general. With reference to the results of the last chapter, a workaround is discussed. The approach is followed and, finally, results gained by the MD simulations are interpreted drawing special attention to the established controversy concerning precipitation of SiC in Si.

6.1 Simulations at temperatures used in IBS

In initial simulations aiming to reproduce a precipitation process, simulation volumes of $31 \times 31 \times 31$ unit cells are utilized. Periodic boundary conditions in each direction are applied. The system temperature is set to 450 °C, the temperature for which epitaxial growth of 3C-SiC films is achieved in IBS. After equilibration of the kinetic and potential energy, C atoms are consecutively inserted. The number of C atoms N_{C} necessary to form a spherical precipitate with radius r is given by

$$N_{\text{C}} = \frac{4}{3}\pi r^3 \cdot \frac{4}{a_{\text{SiC}}^3} = \frac{16}{3}\pi \left(\frac{r}{a_{\text{SiC}}}\right)^3 \tag{6.1}$$

with a_{SiC} being the lattice constant of 3C-SiC. In IBS experiments, the smallest precipitates observed have radii starting from 2 nm up to 4 nm. For the initial simulations, a total amount of 6000 C atoms corresponding to a radius of approximately 3.1 nm is chosen. In separated simulations, the 6000 C atoms are inserted in three regions of different volume (V_1, V_2, V_3) within the simulation cell. For reasons of simplification, these regions are rectangularly shaped. V_1 is chosen to be the total simulation volume. V_2 approximately corresponds to the volume of a minimal 3C-SiC precipitate. V_3 is approximately the volume containing the amount of Si atoms necessary to form such a precipitate, which is slightly smaller than V_2 due to the slightly lower Si density of 3C-SiC compared to c-Si. The two latter insertion volumes are

	V_1	V_2	V_3
Side length [Å]	168.3	50.0	49.0
C concentration $[\frac{1}{\text{c-Si unit cell}}]$	0.20	7.68	8.16

Table 6.1: Side lengths of the insertion volumes V_1, V_2 and V_3 used for the incorporation of 6000 C atoms.

considered since no long-range diffusion of C atoms is expected within the simulated period of time at prevalent temperatures. This is due to the overestimated activation energy for the diffusion of a $\mathrm{C_i}\langle 1\,0\,0\rangle$ DB, as pointed out in section 5.3.2. For rectangularly shaped precipitates with side length L the amount of C atoms in 3C-SiC and Si atoms in c-Si is given by

$$N_{\mathrm{C}}^{\text{3C-SiC}} = 4\left(\frac{L}{a_{\mathrm{SiC}}}\right)^3 \quad \text{and} \quad N_{\mathrm{Si}}^{\text{c-Si}} = 8\left(\frac{L}{a_{\mathrm{Si}}}\right)^3 . \tag{6.2}$$

Table 6.1 summarizes the side length of each of the three different insertion volumes determined by equations (6.2) and the resulting C concentrations inside these volumes. Looking at the C concentrations, simulations can be distinguished in simulations occupying low (V_1) and high (V_2, V_3) concentrations of C.

The insertion is realized in a way to keep the system temperature constant. In each of 600 insertion steps, 10 C atoms are inserted at random positions within the respective region, which involves an increase in potential energy that is partially transformed into kinetic energy. Thus, the simulation is continued without adding more C atoms until the system temperature is equal to the chosen temperature again. This is realized by the thermostat, which decouples excessive energy. Every inserted C atom must exhibit a distance greater or equal to 1.5 Å to neighbored atoms to prevent the occurrence of too high forces. Once the total amount of C is inserted, the simulation is continued for 100 ps followed by a cooling-down process until room temperature, i.e. 20 °C, is reached. Fig. 6.1 displays a flow chart of the applied steps involved in the simulation sequence.

The radial distribution function $g(r)$ for C-C and Si-Si distances is shown in Fig. 6.2. It is easily and instantly visible that there is no significant difference among the two simulations of high C concentration. Thus, in the following, the focus can indeed be directed to low (V_1) and high (V_2, V_3) C concentration simulations. The first C-C peak appears at about 0.15 nm, which is comparable to the nearest neighbor distance of graphite or diamond. The number of C-C bonds is much smaller for V_1 than for V_2 and V_3 since C atoms are spread over the total simulation volume. On average, there are only 0.2 C atoms per Si unit cell. These C atoms are assumed to form strong bonds. This is supported by Fig. 6.3 displaying the total energy of all three simulations during the whole simulation sequence. A huge decrease of the total energy during C insertion is observed for the simulations with high C concentration in contrast to the V_1 simulation, which shows a slight increase. The difference in energy Δ growing within the C insertion process up to a value of roughly 0.06 eV per atom persists unchanged until the end of the simulation. The vast amount of strongly bonded C-C bonds in the high concentration simulations make these configurations energetically more favorable compared to the low concentration configuration. However, in the same way, a lot of energy is needed to break these bonds to get out of the local energy minimum advancing towards the global minimum configuration. Thus, such conformational changes are very unlikely to

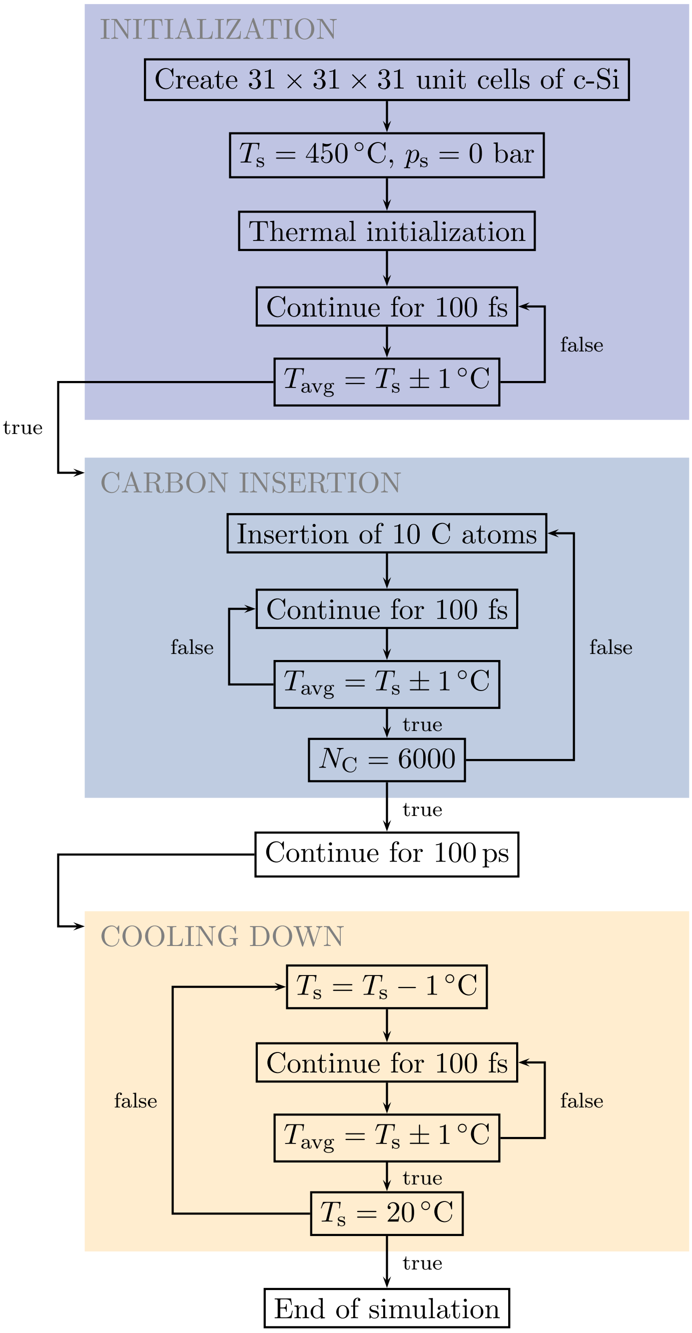

Figure 6.1: Flowchart of the simulation sequence used in MD simulations aiming to reproduce the precipitation process. T_s and p_s are the preset values for the system temperature and pressure. T_avg is the averaged actual system temperature.

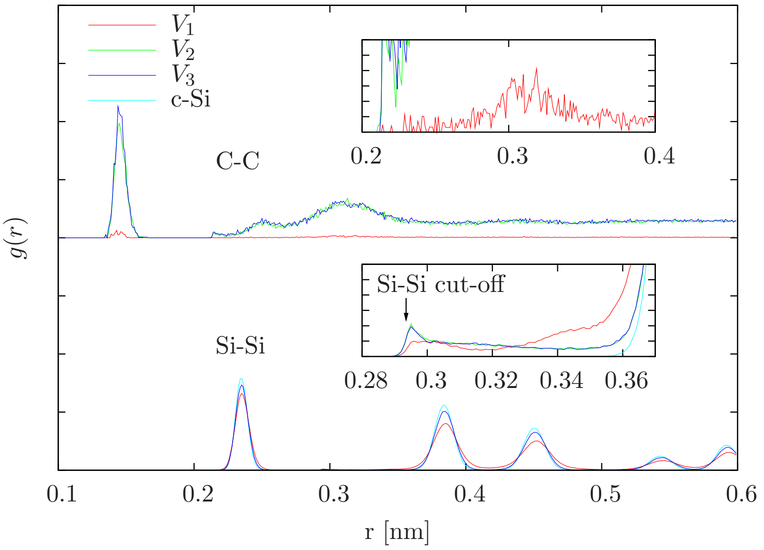

Figure 6.2: Radial distribution function of the C-C and Si-Si distances for 6000 C atoms inserted into the three different volumes V_1, V_2 and V_3 at a temperature of 450 °C and cooled down to room temperature. The bright blue graph shows the Si-Si radial distribution for pure c-Si. The insets show magnified regions of the respective type of bond.

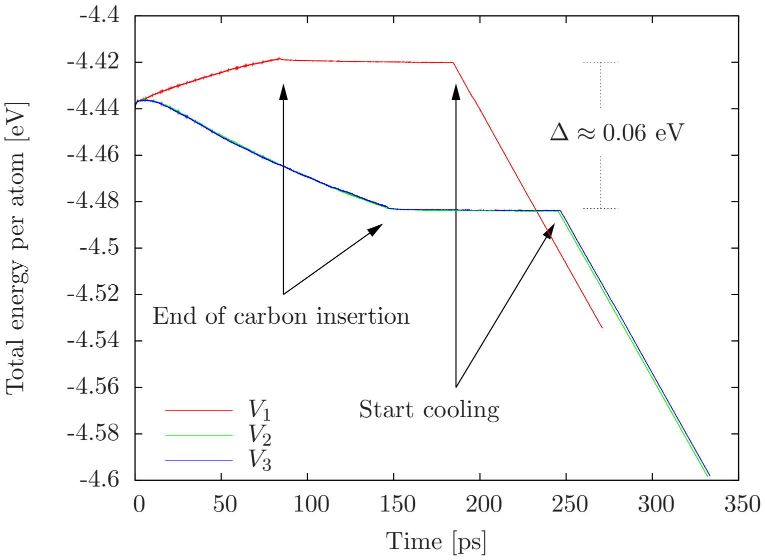

Figure 6.3: Total energy per atom as a function of time for the whole simulation sequence and for all three types of insertion volumes. Arrows mark the end of C insertion and the start of the cooling process respectively.

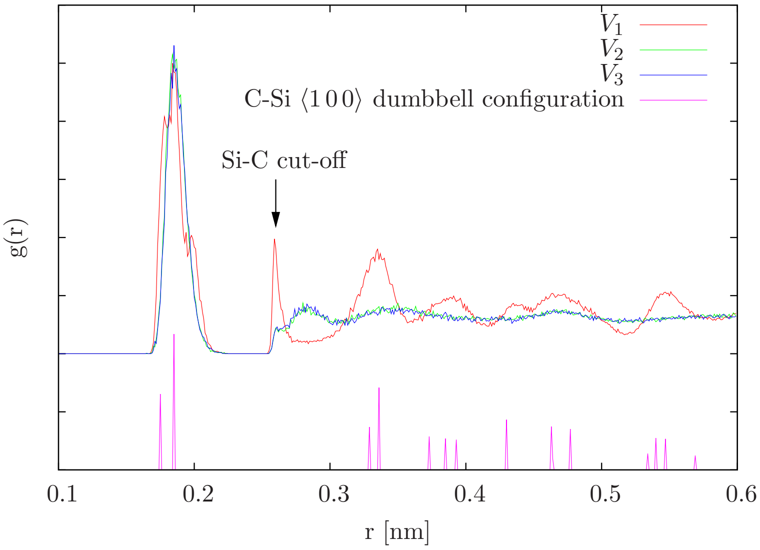

Figure 6.4: Radial distribution function of the Si-C distances for 6000 C atoms inserted into the three different volumes V_1, V_2 and V_3 at a temperature of 450 °C and cooled down to room temperature. Additionally the resulting Si-C distances of a C_i ⟨1 0 0⟩ DB configuration are given.

happen. This is in accordance with the constant total energy observed in the continuation step of 100 ps in between the end of C insertion and the cooling process. Obviously, no energetically favorable relaxation is taking place at a system temperature of 450 °C.

The C-C peak at about 0.31 nm perfectly matches the nearest neighbor distance of two C atoms in the 3C-SiC lattice. As can be seen from the inset, this peak is also observed for the V_1 simulation. Investigating the corresponding coordinates of the atoms, it turns out that concatenated and differently oriented C_i ⟨1 0 0⟩ DB interstitials constitute configurations yielding separations of C atoms by this distance. In 3C-SiC, the same distance is also expected for nearest neighbor Si atoms. The bottom of Fig. 6.2 shows the radial distribution of Si-Si bonds together with a reference graph for pure c-Si. Indeed, non-zero $g(r)$ values around 0.31 nm are observed while the amount of Si pairs at regular c-Si distances of 0.24 nm and 0.38 nm decreases. However, no clear peak is observed but the interval of enhanced $g(r)$ values corresponds to the width of the C-C $g(r)$ peak. In addition, the abrupt increase of Si pairs at 0.29 nm can be attributed to the Si-Si cut-off radius of 0.296 nm as used in the present bond order potential. The cut-off function causes artificial forces pushing the Si atoms out of the cut-off region. Without the abrupt increase, a maximum around 0.31 nm gets even more conceivable. Analyses of randomly chosen configurations, in which distances around 0.3 nm appear, identify C_i ⟨1 0 0⟩ DBs to be responsible for stretching the Si-Si next neighbor distance for low C concentrations, i.e. for the V_1 and early stages of V_2 and V_3 simulation runs. This excellently agrees with the calculated value $r(13)$ in Table 5.3 for a resulting Si-Si distance in the C_i⟨1 0 0⟩ DB configuration.

Fig. 6.4 displays the Si-C radial distribution function for all three insertion volumes together with the Si-C bonds as observed in a C_i ⟨1 0 0⟩ DB configuration. The first peak observed for all insertion volumes is at approximately 0.186 nm. This corresponds quite well to the expected next neighbor distance of 0.189 nm for Si and C atoms in 3C-SiC. By comparing the resulting Si-C bonds of a C_i $\langle 1\,0\,0\rangle$ DB with the C-Si distances of the low concentration simulation, it is evident that the resulting structure of the V_1 simulation is clearly dominated by this type of defect. This is not surprising since the C_i $\langle 1\,0\,0\rangle$ DB is found to be the ground-state defect of a C interstitial in c-Si and, for the low concentration simulations, a C interstitial is expected in every fifth Si unit cell only, thus, excluding defect superposition phenomena. The peak distance at 0.186 nm and the bump at 0.175 nm corresponds to the distance $r(3C)$ and $r(1C)$ as listed in Table 5.3 and visualized in Fig. 5.5. In addition, it can be easily identified that the C_i $\langle 1\,0\,0\rangle$ DB configuration contributes to the peaks at about 0.335 nm, 0.386 nm, 0.434 nm, 0.469 nm and 0.546 nm observed in the V_1 simulation. Not only the peak locations but also the peak widths and heights become comprehensible. The distinct peak at 0.26 nm, which exactly matches the cut-off radius of the Si-C interaction, is again a potential artifact.

For high C concentrations, i.e. the V_2 and V_3 simulation corresponding to a C density of about 8 atoms per c-Si unit cell, the defect concentration is likewise increased and a considerable amount of damage is introduced in the insertion volume. The consequential superposition of these defects and the high amounts of damage generate new displacement arrangements for the C-C as well as for the Si-C pair distances, which become hard to categorize and trace and obviously lead to a broader distribution. Short range order indeed is observed, i.e. the large amount of strong neighbored C-C bonds at 0.15 nm as expected in graphite or diamond and Si-C bonds at 0.19 nm as expected in SiC, but only hardly visible is the long range order. This indicates the formation of an amorphous SiC-like phase. In fact, the resulting Si-C and C-C radial distribution functions compare quite well with these obtained by cascade amorphized and melt-quenched amorphous SiC using a modified Tersoff potential [211].

In both cases, i.e. low and high C concentrations, the formation of 3C-SiC fails to appear. With respect to the precipitation model, the formation of C_i $\langle 1\,0\,0\rangle$ DBs indeed occurs for low C concentrations. However, sufficient defect agglomeration is not observed. For high C concentrations, a rearrangement of the amorphous SiC structure, which is not expected at prevailing temperatures, and a transition into 3C-SiC is not observed either.

6.2 Limitations of conventional MD and short range potentials

Results of the last section indicate possible limitations of the MD method regarding the task addressed in this study. Low C concentration simulations do not reproduce the agglomeration of C_i $\langle 1\,0\,0\rangle$ DBs. High concentration simulations result in the formation of an amorphous SiC-like phase, which is unexpected since IBS experiments show crystalline 3C-SiC precipitates at prevailing temperatures. On closer inspection, however, two reasons for describing this obstacle become evident, which are discussed in the following.

The first reason is a general problem of MD simulations in conjunction with limitations in computer power, which results in a slow and restricted propagation in phase space. In molecular systems, characteristic motions take place over a wide range of time scales. Vibrations of the covalent bond take place on the order of 10^{-14} s, of which the thermodynamic and kinetic properties are well described by MD simulations. To avoid discretization errors, the integration time step needs to be chosen smaller than the fastest vibrational frequency in the system. On the other hand, infrequent processes, such as conformational changes, reorganization processes during film growth, defect diffusion and phase transitions are processes undergoing long-term evolution in the range of microseconds. This is due to the existence of several local minima in the free energy surface separated by large energy barriers compared to the kinetic energy of the particles, i.e. the system temperature. Thus, the average time of a transition from one potential basin to another corresponds to a great deal of vibrational periods, which in turn determine the integration time step. Hence, time scales covering the necessary amount of infrequent events to observe long-term evolution are not accessible by traditional MD simulations, which are limited to the order of nanoseconds. New methods have been developed to bypass the time scale problem. The most famous approaches are hyperdynamics (HMD) [212, 213], parallel replica dynamics [214], temperature accelerated dynamics (TAD) [215] and self-guided dynamics (SGMD) [216], which accelerate phase space propagation while retaining proper thermodynamic sampling.

In addition to the time scale limitation, problems attributed to the short range potential exist. The sharp cut-off function, which limits the interacting ions to the next neighbored atoms by gradually pushing the interaction force and energy to zero between the first and second next neighbor distance, is responsible for overestimated and unphysical high forces of next neighbored atoms [203, 217]. This is supported by the overestimated activation energies necessary for C diffusion as investigated in section 5.3.2. Indeed, it is not only the strong C-C bond, which is hard to break, inhibiting C diffusion and further rearrangements. This is also true for the low concentration simulations dominated by the occurrence of C-Si DBs spread over the whole simulation volume. The bonds of these C-Si pairs are also affected by the cut-off artifact preventing C diffusion and agglomeration of the DBs. This can be seen from the almost horizontal progress of the total energy graph in the continuation step of Fig. 6.3, even for the low concentration simulation. These unphysical effects inherent to this type of model potentials are solely attributed to their short range character. While cohesive and formational energies are often well described, these effects increase for non-equilibrium structures and dynamics. However, since valuable insights into various physical properties can be gained using this potentials, modifications mainly affecting the cut-off were designed. One possibility is to simply skip the force contributions containing the derivatives of the cut-off function, which was successfully applied to reproduce the brittle propagation of fracture in SiC at zero temperature [203]. Another one is to use variable cut-off values scaled by the system volume, which properly describes thermomechanical properties of 3C-SiC [217] but might be rather ineffective for the challenge inherent to this study.

To conclude, the obstacle needed to get passed is twofold. The sharp cut-off of the employed bond order model potential introduces overestimated high forces between next neighbored atoms enhancing the problem of slow phase space propagation immanent to MD simulations. This obstacle could be referred to as *potential enhanced slow phase space propagation*. Due to this, pushing the time scale to the limits of computational resources or applying one of the above mentioned accelerated dynamics methods exclusively will not be sufficient enough.

Instead, the approach followed in this study, is the use of higher temperatures as exploited in TAD to find transition pathways of one local energy minimum to another one more quickly. Since merely increasing the temperature leads to different equilibrium kinetics than valid at low temperatures, TAD introduces basin-constrained MD allowing only those transitions that should occur at the original temperature and a properly advancing system clock [215]. The TAD corrections are not applied in coming up simulations. This is justified by two reasons. First of all, a compensation of the overestimated bond strengths due to the short range potential is expected. Secondly, there is no conflict applying higher temperatures without the TAD corrections since crystalline 3C-SiC is also observed for higher temperatures than 450 °C in IBS [18, 23]. It is therefore expected that the kinetics affecting the 3C-SiC precipitation are not much different at higher temperatures aside from the fact that it is occurring much more faster. Moreover, the interest of this study is focused on structural evolution of a system far from equilibrium instead of equilibrium properties which rely upon proper phase space sampling. On the other hand, during implantation, the actual temperature inside the implantation volume is definitely higher than the experimentally determined temperature tapped from the surface of the sample.

6.3 Increased temperature simulations

Due to the limitations of short range potentials and conventional MD as discussed above, elevated temperatures are used in the following. Increased temperatures are expected to compensate the overestimated diffusion barriers. These are overestimated by a factor of 2.4 to 3.5. Scaling the absolute temperatures accordingly results in maximum temperatures of 1460–2260 °C. Since melting already occurs shortly below the melting point of the potential (2450 K) [147] due to the presence of defects, temperatures ranging from 450–2050 °C are used. The simulation sequence and other parameters except for the system temperature remain unchanged as in section 6.1. Since there is no significant difference among the V_2 and V_3 simulations, only the V_1 and V_2 simulations are carried on and referred to as low C and high C concentration simulations.

A simple quality value Q is introduced, which helps to estimate the progress of structural evolution. In bulk 3C-SiC every C atom has four next neighbored Si atoms and every Si atom four next neighbored C atoms. The quality could be determined by counting the amount of atoms, which form bonds to four atoms of the other species. However, the aim of the simulation is to reproduce the formation of a 3C-SiC precipitate embedded in c-Si. The amount of Si atoms and, thus, the amount of Si atoms remaining in the c-Si diamond lattice is much higher than the amount of inserted C atoms. Thus, counting the atoms, which exhibit proper coordination, is limited to the C atoms. The quality value is defined to be

$$Q = \frac{\text{Amount of C atoms with 4 next neighbored Si atoms}}{\text{Total amount of C atoms}} \; . \tag{6.3}$$

By this, bulk 3C-SiC will still result in $Q = 1$ and precipitates will also reach values close to one. However, since the quality value does not account for bond lengths, bond angles, crystallinity or the stacking sequence, high values of Q not necessarily correspond to structures close to 3C-SiC. Structures that look promising due to high quality values need to be further investigated by other means.

6.3.1 Low C concentration simulations

Fig. 6.5 shows the radial distribution of Si-C bonds for different temperatures and the corresponding evolution of quality Q as defined above for the low concentration simulation. The first noticeable and promising change in the Si-C radial distribution is the successive decline of the artificial peak at the Si-C cut-off distance with increasing temperature up to the point of disappearance at temperatures above 1650 °C. Obviously, sufficient kinetic energy is provided

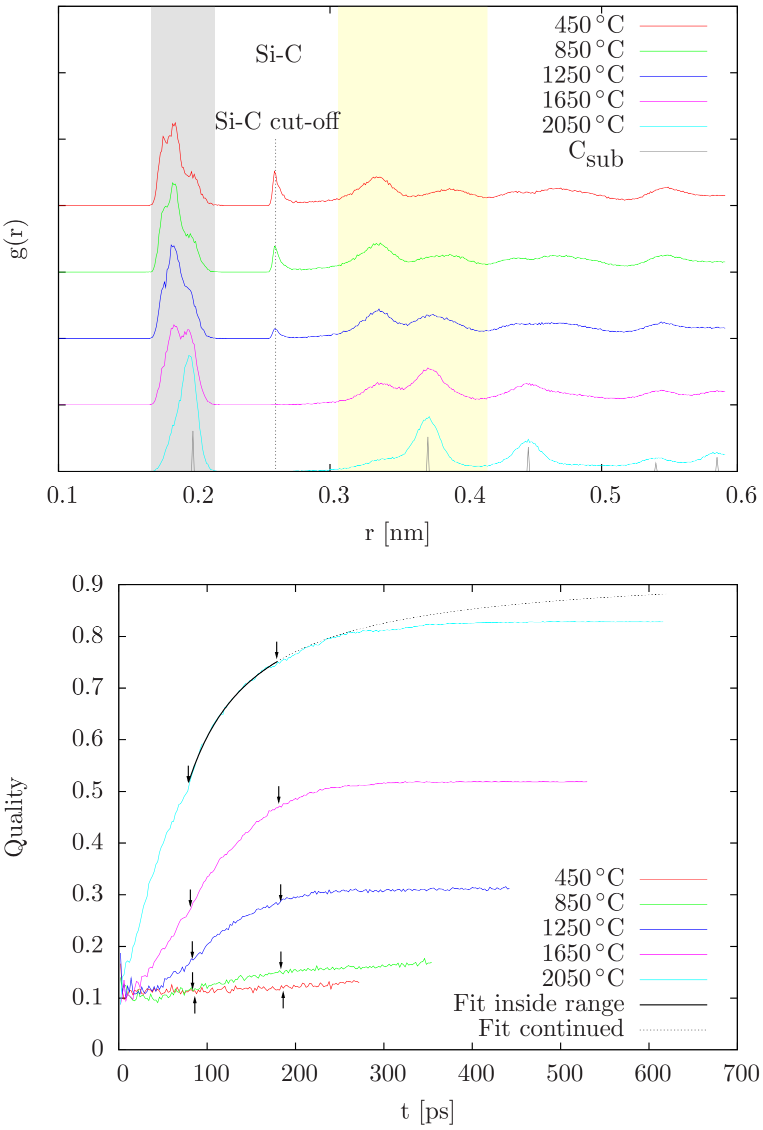

Figure 6.5: Si-C radial distribution and evolution of quality Q according to equation 6.3 for the low concentration simulations at different elevated temperatures. All structures are cooled down to 20 °C. The gray line shows resulting Si-C bonds in a configuration of C_s in c-Si (C_{sub}) at zero temperature. Arrows in the quality plot mark the end of C insertion and the start of the cooling down step. A fit function according to equation (6.4) shows the estimated evolution of quality in the absence of the cooling down sequence.

to affected atoms that are enabled to escape the cut-off region. Additionally, a more important structural change is observed, which is illustrated in the two shaded areas in Fig. 6.5. In the gray shaded region a decrease of the peak at 0.186 nm and of the bump at 0.175 nm accompanied by an increase of the peak at 0.197 nm with increasing temperature is visible. Similarly, the peaks at 0.335 nm and 0.386 nm shrink in contrast to a new peak forming at 0.372 nm as can be seen in the yellow shaded region. Obviously, the structure obtained from the 450 °C simulations, which is dominated by the existence of $\mathrm{C_i}$ $\langle 1\,0\,0\rangle$ DBs, transforms into a different structure with increasing simulation temperature. Investigations of the atomic data reveal $\mathrm{C_s}$ to be responsible for the new Si-C bonds. The peak at 0.197 nm corresponds to the distance of a $\mathrm{C_s}$ atom and its next neighbored Si atoms. The one at 0.372 nm constitutes the distance of a $\mathrm{C_s}$ atom to the second next Si neighbor along a $\langle 1\,1\,0\rangle$ direction. Comparing the radial distribution for the Si-C bonds at 2050 °C to the resulting Si-C bonds in a configuration of a $\mathrm{C_s}$ atom in c-Si excludes all possibility of doubt. The resulting bonds perfectly match and, thus, explain the peaks observed for the increased temperature simulations. To conclude, by increasing the simulation temperature, the structure characterized by the $\mathrm{C_i}$ $\langle 1\,0\,0\rangle$ DB structure transforms into a structure dominated by $\mathrm{C_s}$.

This is likewise reflected in the quality values obtained for different temperatures. While simulations at 450 °C exhibit 10 % of fourfold coordinated C, simulations at 2050 °C exceed the 80 % range. Since $\mathrm{C_s}$ has four nearest neighbored Si atoms and is the preferential type of defect in elevated temperature simulations, the increase of the quality values become evident. The quality values at a fixed temperature increase with simulation time. After the end of the insertion sequence marked by the first arrow, the quality is increasing and a saturation behavior, yet before the cooling process starts, can be expected. The evolution of the quality value of the simulation at 2050 °C inside the range, in which the simulation is continued at constant temperature for 100 fs, is well approximated by the simple fit function

$$f(t) = a - \frac{b}{t} \ , \tag{6.4}$$

which results in a saturation value of 93 %. Obviously, the decrease in temperature accelerates the saturation and inhibits further formation of $\mathrm{C_s}$. Conclusions drawn from investigations of the quality evolution correlate well with findings of the radial distribution results.

The formation of $\mathrm{C_s}$ also affects the Si-Si radial distribution displayed in the lower part of Fig. 6.6. Investigating the atomic structure indeed shows that the peak arising at 0.325 nm with increasing temperature is due to two Si atoms that form direct bonds to the $\mathrm{C_s}$ atom. The peak corresponds to the distance of next neighbored Si atoms along the $\langle 1\,1\,0\rangle$ bond chain with $\mathrm{C_s}$ in between. Since the expected distance of these Si pairs in 3C-SiC is 0.308 nm, the existing SiC structures embedded in the c-Si host are stretched.

In the upper part of Fig. 6.6 the C-C radial distribution is shown. The total amount of C-C bonds with a distance inside the displayed separation range does not change significantly. Thus, even for elevated temperatures, agglomeration of C atoms necessary to form a SiC precipitate does not take place within the simulated time scale. However, with increasing temperature, a decrease of the amount of next neighbored C pairs can be observed. This is a promising result gained by the high-temperature simulations since the breaking of these diamond and graphite like bonds is mandatory for the formation of 3C-SiC. Obviously, acceleration of the dynamics occurred by supplying additional kinetic energy. A slight shift towards higher distances can be observed for the maximum located shortly above 0.3 nm. Arrows with dashed lines mark C-C distances resulting from $\mathrm{C_i}$ $\langle 1\,0\,0\rangle$ DB combinations while arrows

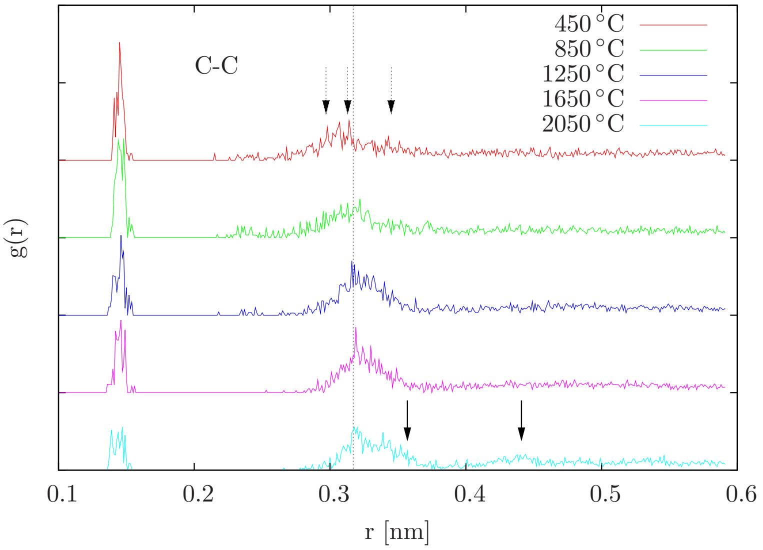

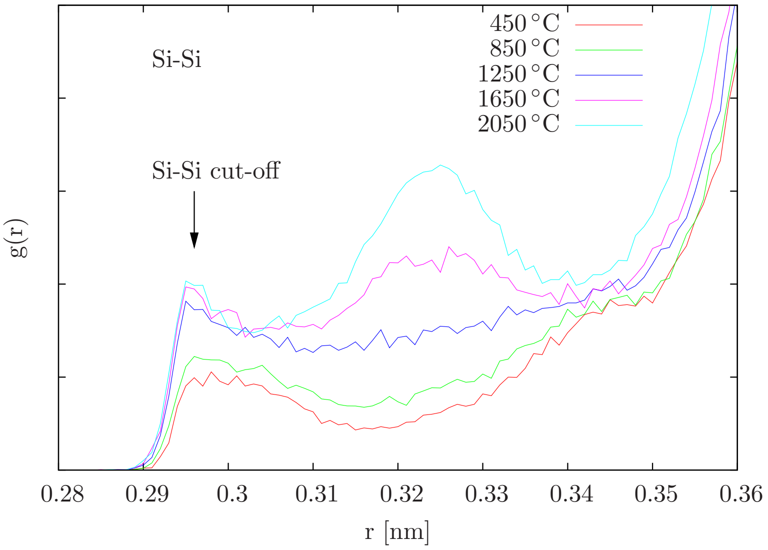

Figure 6.6: C-C and Si-Si radial distribution for the low concentration simulations at different elevated temperatures. All structures are cooled down to 20 °C. Arrows with dashed lines mark C-C distances of ⟨1 0 0⟩ DB combinations and those with solid lines mark C-C distances of combinations of substitutional C. The dashed line corresponds to the distance of a substitutional C with a next neighbored ⟨1 0 0⟩ DB.

with solid lines mark distances arising from combinations of C_s. The continuous dashed line corresponds to the distance of C_s and a next neighbored C_i $\langle 1\,0\,0\rangle$ DB. Obviously, the shift of the peak is caused by the advancing transformation of the C_i DB into the C_s defect. Next to combinations of two C_s atoms or C_i $\langle 1\,0\,0\rangle$ DBs, combinations of C_i $\langle 1\,0\,0\rangle$ DBs with a C_s atom arise. In addition, structures form that result in distances residing in between the ones obtained from combinations of mixed defect types and the ones obtained by C_s configurations, as can be seen by quite high $g(r)$ values in between the continuous dashed line and the first arrow with a solid line. For the most part, these structures can be identified as configurations of C_s with either another C atom that basically occupies a Si lattice site but is displaced by a Si_i atom residing in the very next surrounding or a C atom that nearly occupies a Si lattice site forming a defect other than the $\langle 1\,0\,0\rangle$-type with the Si atom. Again, this is a quite promising result since the C atoms are taking the appropriate coordination as expected in 3C-SiC.

To summarize, results of low concentration simulations show a phase transition in conjunction with an increase in temperature. The C_i $\langle 1\,0\,0\rangle$ DB dominated structure turns into a structure characterized by the occurrence of an increasing amount of C_s with respect to temperature. Clearly, the high-temperature results indicate the precipitation mechanism involving an increased participation of C_s. Although diamond and graphite like bonds are reduced, no agglomeration of C is observed within the simulated time. Isolated structures of stretched SiC, which are adjusted to the c-Si host with respect to the lattice constant and alignment, are formed. By agglomeration of C_s, the interfacial energy could be overcome and a transition from a coherent and stretched SiC structure into an incoherent and partially strain-compensated SiC precipitate could occur. Indeed, Si_i in the near surrounding is observed, which may initially compensate tensile strain in the stretched SiC structure or rearrange the C_s sublattice and finally serve as supply for additional C to form further SiC or compensate strain at the interface of the incoherent SiC precipitate and the Si host.

6.3.2 High C concentration simulations

Fig. 6.7 displays the radial distribution for Si-C and C-C pairs obtained from high C concentration simulations at different elevated temperatures. Again, in both cases, the cut-off artifact decreases with increasing temperature. Peaks that already exist for the low temperature simulations get slightly more distinct for elevated temperatures. This is also true for peaks located past distances of next neighbors indicating an increase in the long range order. However, this change is rather small and no significant structural change is observable. Due to the continuity of high amounts of damage, atomic configurations remain hard to identify even for the highest temperature. Other than in the low concentration simulation, analyzed defect structures are no longer necessarily aligned to the primarily existing but successively disappearing c-Si host matrix inhibiting or at least hampering their identification and classification. As for low temperatures, order in the short range exists decreasing with increasing separation. The increase of the amount of Si-C pairs at 0.186 nm could be positively interpreted since this type of bond also exists in 3C-SiC. On the other hand, the amount of next neighbored C atoms with a distance of approximately 0.15 nm, which is the distance of C in graphite or diamond, is likewise increased. Thus, higher temperatures seem to additionally enhance a conflictive process, i.e. the formation of C agglomerates, obviously inconsistent with the desired process of 3C-SiC formation. This is supported by the C-C peak at 0.252 nm, which corresponds to the second next neighbor distance in the diamond structure of elemen-

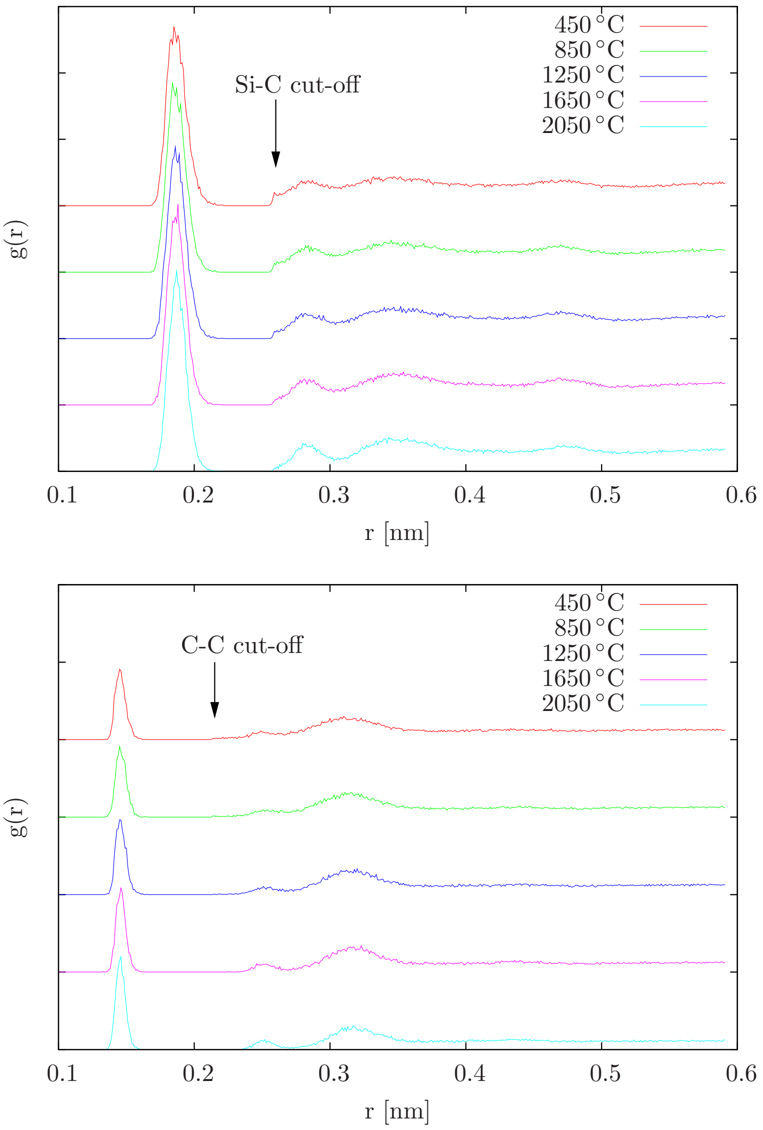

Figure 6.7: Si-C (top) and C-C (bottom) radial distribution for the high concentration simulations at different elevated temperatures. All structures are cooled down to 20 °C.

tal C. Investigating the atomic data indeed reveals two C atoms, which are bound to and interconnected by a third C atom, to be responsible for this distance. The C-C peak at about 0.31 nm, which is slightly shifted to higher distances (0.317 nm) with increasing temperature still corresponds quite well to the next neighbor distance of C in 3C-SiC as well as a-SiC and, indeed, results from C-Si-C bonds. The Si-C peak at 0.282 nm, which is pronounced with increasing temperature, is constructed out of a Si atom and a C atom, which are both bound to another central C atom. This is similar for the Si-C peak at approximately 0.35 nm. In this case, the Si and the C atom are bound to a central Si atom.

To summarize, the amorphous phase remains. Huge amounts of damage hamper identification. The alignment of the investigated structures to the c-Si host is lost in many cases, which suggests the necessity of much more time for structural evolution to maintain the topotactic orientation of the precipitate. Though, sharper peaks in the radial distributions at distances expected for a-SiC are observed indicating a slight acceleration of the dynamics due to elevated temperatures.

6.3.3 Conclusions concerning the usage of increased temperatures

Regarding the outcome of both, high and low C concentration simulations at increased temperatures, encouraging conclusions can be drawn. With the disappearance of the peaks at the respective cut-off radii, one limitation of the short range potential seems to be accomplished. In addition, sharper peaks in the radial distribution functions lead to the assumption of expeditious structural formation. The increase in temperature leads to the occupation of new defect states, which is particularly evident but not limited to the low C concentration simulations.

The question remains, whether these states are only occupied due to the additional supply of kinetic energy and, thus, have to be considered unnatural for temperatures applied in IBS or whether the increase in temperature indeed enables infrequent transitions to occur faster, thus, leading to the intended acceleration of the dynamics and weakening of the unphysical quirks inherent to the potential. As already pointed out in section 5.4.4 and section 5.7, IBS is a non-equilibrium process, which might result in the formation of the thermodynamically less stable $\mathrm{C_s}$ and $\mathrm{Si_i}$ configuration. Indeed, 3C-SiC is metastable and if not fabricated by IBS requires strong deviation from equilibrium and low temperatures to stabilize the 3C polytype. In IBS, highly energetic C atoms are able to generate vacant sites, which in turn can be occupied by highly mobile $\mathrm{C_i}$ atoms. This is in fact found to be favorable in the absence of the $\mathrm{Si_i}$, which turned out to have a low interaction capture radius with the $\mathrm{C_s}$ atom and very likely prevents the recombination into a thermodynamically stable $\mathrm{C_i}$ DB for appropriate separations of the defect pair. Results gained in this chapter show preferential occupation of Si lattice sites by $\mathrm{C_s}$ enabled by increased temperatures supporting the assumptions drawn from the defect studies of the last chapter.

Moreover, the cut-off effect as detailed in section 6.2 is particularly significant for configurations that are deviated to a great extent from their equilibrium structures. Thus, for instance, it is not surprising that short range potentials show overestimated melting temperatures while properties of structures that are only slightly deviated from equilibrium are well described. Due to this, increased temperatures are considered exceptionally necessary for modeling non-equilibrium processes and structures such as IBS and 3C-SiC.

Thus, it is concluded that increased temperatures are not exclusively useful to accelerate the dynamics approximatively describing the structural evolution. Moreover, it can be considered a necessary condition to deviate the system out of equilibrium enabling the formation of 3C-SiC, which is obviously realized by a successive agglomeration of C_s.

6.4 Conclusions concerning the SiC conversion mechanism

MD simulations at temperatures used in IBS result in structures that are dominated by the C_i $\langle 1\,0\,0\rangle$ DB and its combinations if C is inserted into the total volume. Incorporation into volumes V_2 and V_3 leads to an amorphous SiC-like structure within the respective volume. To compensate overestimated diffusion barriers, simulations at accordingly increased temperatures are performed. No significant change is observed for high C concentrations. The amorphous phase is maintained. Due to the incorporation of a huge amount of C into a small volume within a short period of time, damage is produced, which obviously decelerates structural evolution. For the low C concentrations, time scales are still too low to observe C agglomeration sufficient for SiC precipitation, which is attributed to the slow phase space propagation inherent to MD in general. However, a phase transition of the C_i-dominated into a clearly C_s-dominated structure is observed. The amount of substitutionally occupied C atoms increases with increasing temperature. Isolated structures of stretched SiC adjusted to the c-Si host with respect to the lattice constant and alignment are formed. Entropic contributions are assumed to be responsible for these structures at elevated temperatures that deviate from the ground state at 0 K.

Results of the MD simulations at different temperatures and C concentrations can be correlated to experimental findings. IBS studies revealed increased implantation temperatures to be more efficient than postannealing methods for the formation of topotactically aligned precipitates [106, 218]. In particular, the restructuring of strong C-C bonds is affected [219]. These bonds preferentially arise if additional kinetic energy provided by an increase of the implantation temperature is missing to accelerate or even enable atomic rearrangements. This is assumed to be related to the problem of slow structural evolution encountered in the high C concentration simulations. The insertion of high amounts of C into a small volume within a short period of time results in essentially no time for the system to rearrange. Furthermore, C implanted at room temperature was found to be able to migrate towards the surface and form C-rich clusters in contrast to implantations at elevated temperatures, which form stable epitaxially aligned 3C-SiC precipitates [113]. In simulation, low temperatures result in configurations of highly mobile C_i $\langle 1\,0\,0\rangle$ DBs whereas elevated temperatures show configurations of C_s, which constitute an extremely stable configuration that is unlikely to migrate. This likewise agrees to results of IBS experiments utilizing implantation temperatures of 550 °C, which require annealing temperatures as high as 1405 °C for C segregation due to the stability of C_s [15]. Indeed, in the optimized recipe to form 3C-SiC by IBS [16], elevated temperatures are used to improve the epitaxial orientation together with a low temperature implant to destroy stable SiC nanocrystals at the interface, which are unable to migrate during thermal annealing resulting in a rough surface. Furthermore, the improvement of the epitaxial orientation of the precipitate with increasing temperature in experiment perfectly conforms to the increasing occurrence of C_s in simulation. Moreover, implantations of an understoichiometric dose into preamorphized Si followed by an annealing step at 700 °C result in $Si_{1-x}C_x$ layers with C residing on substitutional Si lattice sites [133]. For implantations of an understoichiometric dose into c-Si at room temperature followed by thermal annealing below and above 700 °C, the formation of small C_i agglomerates and SiC precipitates was observed respectively [144]. However, increased implantation temperatures were found to be more efficient than postannealing methods resulting in the formation of SiC precipitates for implantations at 450 °C [16, 18]. Thus, at elevated temperatures, implanted C is expected to occupy substitutionally usual Si lattice sites right from the start. These findings, which are outlined in more detail within the comprehensive description in chapter 7, are in perfect agreement with previous results of the quantum-mechanical investigations.

Thus, elevated temperatures are considered to constitute a necessary condition to deviate the system from equilibrium, as it is the case in IBS. It is concluded that precipitation occurs by successive agglomeration of $\mathrm{C_s}$ as already proposed by Nejim et al. [23]. This agrees well with previous results of the *ab initio* study on defects in C implanted Si, which show $\mathrm{C_s}$ to occur in all probability. However, agglomeration and rearrangement is enabled by mobile $\mathrm{C_i}$, which has to be present at the same time and is formed by recombination of $\mathrm{C_s}$ and $\mathrm{Si_i}$. Indeed, $\mathrm{Si_i}$ is observed in the direct surrounding of the stretched SiC structures. Next to the rearrangement, $\mathrm{Si_i}$ is required as a supply for additional C atoms to form further SiC and to compensate strain, either within the coherent and stretched SiC structure as well as at the interface of the incoherent SiC precipitate and the Si host. In contrast to assumptions of an abrupt precipitation of an agglomerate of $\mathrm{C_i}$ [17, 20, 144, 145, 210], however, structural evolution is believed to occur by a successive occupation of usual Si lattice sites with substitutional C. This mechanism satisfies the experimentally observed alignment of the $(h\,k\,l)$ planes of the precipitate and the substrate, whereas there is no obvious reason for the topotactic orientation of an agglomerate consisting exclusively of C-Si dimers, which would necessarily involve a much more profound change in structure for the transition into SiC.

Chapter 7

Summary and conclusions

To summarize, in a short review of the C/Si compound and the fabrication of the technologically promising semiconductor SiC by IBS, two controversial assumptions of the precipitation mechanism of 3C-SiC in c-Si are elaborated. These propose precipitation of SiC by agglomeration of $\mathrm{C_i}$ DBs followed by a sudden formation of SiC and otherwise a formation by successive accumulation of $\mathrm{C_s}$ via intermediate stretched SiC structures, which are coherent to the Si lattice. To solve this controversy and contribute to the understanding of SiC precipitation in c-Si, a series of atomistic simulations is carried out. In the first part, intrinsic and C related point defects in c-Si as well as some selected diffusion processes of the C defect are investigated by means of first-principles quantum-mechanical calculations based on DFT and classical potential calculations employing a Tersoff-like analytical bond order potential. Shortcomings of the computationally efficient though less accurate classical potential approach compared to the quantum-mechanical treatment are revealed. The study proceeds investigating combinations of defect structures and related diffusion processes exclusively by the first-principles method. The applicability of the utilized bond order potential for subsequent MD simulations is discussed. Conclusions on the precipitation mechanism based on the DFT results are drawn. In the second part, classical potential MD simulations are performed, which try to directly reproduce the precipitation process. Next to the shortcomings of the potential, quirks inherent to MD are discussed and a workaround is proposed. Although direct formation of SiC fails to appear, the obtained results indicate a mechanism of precipitation, which is consistent with previous quantum-mechanical conclusions as well as experimental findings.

Quantum-mechanical results of intrinsic point defects in Si are in good agreement to previous theoretical work on this subject [192, 193]. The $\mathrm{Si_i}$ $\langle 1\,1\,0\rangle$ DB defect is reproduced as the ground-state configuration followed by the hexagonal and tetrahedral defect. Spin polarized calculations are required for the $\mathrm{Si_i}$ $\langle 1\,0\,0\rangle$ DB and vacancy whereas no other of the investigated intrinsic defects is affected. For the $\mathrm{Si_i}$ $\langle 1\,0\,0\rangle$ DB, the net spin up density is localized in two caps at each of the two DB atoms perpendicularly aligned to the bonds to the other two Si atoms. For the vacancy, the net spin up electron density is localized in caps at the four surrounding Si atoms directed towards the vacant site. Results obtained by calculations utilizing the classical EA potential yield formation energies, which are of the same order of magnitude. However, EA predicts the tetrahedral configuration to be most stable. The particular problem is due to the cut-off and the fact that the second neighbors are only slightly more distant than the first neighbors within the tetrahedral configuration. Furthermore, the hexagonal defect structure is not stable opposed to results of the authors of the potential [147]. The obtained structure after relaxation, which is similar to the tetrahedral configuration, exhibits a formation energy equal to the one given by the authors for the hexagonal one. Obviously, the authors did not check the relaxed structure still assuming a hexagonal configuration. The actual structure is equal to the tetrahedral configuration, which is slightly displaced along the three coordinate axes. Variations exist with displacements along two or a single $\langle 1\,0\,0\rangle$ direction indicating a potential artifact. However, finite temperature simulations are not affected by this artifact due to a low activation energy necessary for a transition into the energetically more favorable tetrahedral configuration. Next to the known problem of the underestimated formation energy of the tetrahedral configuration [197], the energetic sequence of the defect structures is well reproduced by the EA calculations. Migration barriers of $\mathrm{Si_i}$ investigated by quantum-mechanical calculations are found to be of the same order of magnitude than values derived in other *ab initio* studies [208, 209].

Defects of C in Si are well described by both methods. The $\mathrm{C_i}$ $\langle 1\,0\,0\rangle$ DB is found to constitute the most favorable interstitial configuration in agreement with several theoretical [190, 199–202] and experimental [123, 124] investigations. Almost equal formation energies are predicted by the EA and DFT calculations for this defect. A small discrepancy in the resulting equilibrium structure with respect to the DFT method exists due to missing quantum-mechanical effects within the classical treatment. The high formation energies of the tetrahedral and hexagonal configuration obtained by classical potentials act in concert with the fact that these configurations are found unstable by the first-principles description. The BC configuration turns out to be unstable relaxing into the $\mathrm{C_i}$ $\langle 1\,1\,0\rangle$ DB configuration within the EA approach. This is supported by another *ab initio* study [199], which in turn finds the BC configuration to be an intermediate saddle point structure of a possible migration path, which is 2.1 eV higher than the $\mathrm{C_i}$ $\langle 1\,0\,0\rangle$ DB structure. By quantum-mechanical calculations performed in this work, however, it turns out that the BC configuration constitutes a real local minimum if the electron spin is fully accounted for. Indeed, spin polarization is absolutely necessary for the BC configuration resulting in a net magnetization of two electrons accompanied by a reduction of the total energy by 0.3 eV. The resulting spin up density is localized in a torus around the C perpendicular to the linear Si-C-Si bond. No other configuration is affected by spin polarization. The underestimated formation energy of $\mathrm{C_s}$ is a definite drawback of the classical potential. However, the creation of $\mathrm{C_s}$ is necessarily accompanied by a $\mathrm{Si_i}$ in a perfect Si crystal, in which a C atom is incorporated. Fortunately, the energetics of combinations of $\mathrm{C_s}$ and $\mathrm{Si_i}$ are quite well described by the EA potential. Thus, the underestimated formation energy does not pose a serious limitation. Based on the above findings, it is concluded that modeling of the SiC precipitation by the EA potential might lead to trustable results.

Quantum-mechanical investigations of the mobility of the $\mathrm{C_i}$ $\langle 1\,0\,0\rangle$ DB yield a migration barrier of 0.9 eV, which excellently agrees to experimental values ranging from 0.70 eV to 0.87 eV [109, 124, 125]. The respective path corresponds to a $\mathrm{C_i}$ $[0\,0\,\bar{1}]$ DB migrating towards the next neighbored Si atom located in $[1\,1\,\bar{1}]$ direction forming a $\mathrm{C_i}$ $[0\,\bar{1}\,0]$ DB. The identified migration path involves a change in orientation of the DB. Thus, the same path explains the experimentally determined activation energies for reorientation of the DB ranging from 0.77 eV [123] up to 0.88 eV [124]. Investigations based on the EA bond order potential suggest a migration involving an intermediate $\mathrm{C_i}$ $\langle 1\,1\,0\rangle$ DB configuration. Although different, starting and final configuration as well as the change in orientation of the $\langle 1\,0\,0\rangle$ DB are equal to the identified pathway by the *ab initio* calculations. However, barrier heights, which are overestimated by a factor of 2.4 to 3.5 depending on the character of migration, i.e. a single step or two step process, compared to the DFT results, are obtained. Obviously, the EA potential fails to describe C_i diffusion yielding a drastically overestimated activation energy, which has to be taken into account in subsequent investigations.

A series of investigations focuses on defect combinations exclusively by the first-principles description. These configurations are constructed in such a way as to allow for a quantum-mechanical treatment.

Investigations of two C_i defects of the $\langle 1\,0\,0\rangle$-type for varying separations and orientations state a fairly attractive interaction between these interstitials. The capture radius is found to be rather large compared to other defect combinations. For the most part, energetically favorable configurations of two interstitials are found. This is due to strain compensation enabled by the combination of such defects in certain orientations. An interaction energy proportional to the reciprocal cube of the distance in the far field regime is found supporting the assumption of C_i DB agglomeration. The energetically most favorable configuration consists of a C-C bond. However, due to high activation energies of respective pathways or alternative pathways featuring less high activation energies, which, however, involve intermediate unfavorable configurations, this structure is less likely to arise than structures of C atoms that are interconnected by another Si atom. Thus, agglomeration of C_i is expected whereas the formation of C-C bonds is assumed to fail to appear by thermally activated diffusion processes.

Results of combinations of C_i and C_s revealed two additional metastable structures different to these obtained by a naive relaxation. Small displacements result in a structure of a $\langle 1\,1\,0\rangle$ C-C DB and in a structure of a twofold coordinated Si atom located in between two substitutional C atoms residing on regular Si lattice sites. Both structures are lower in energy compared to the respective counterparts. These results, for the most part, compare well with results gained in previous studies [201, 206, 207] and show an astonishingly good agreement with experiment [205]. Again, spin polarized calculations are revealed necessary. A net magnetization of two electrons is observed for the $\langle 1\,1\,0\rangle$ C-C DB configuration, which constitutes the ground state. A repulsive interaction is observed for C_s at lattice sites along $[1\,1\,0]$ due to tensile strain originating from both, the C_i DB and the C_s atom. All other investigated configurations show attractive interactions, which suggest an energetically favorable agglomeration of C_i and C_s except for separations along one of the $\langle 1\,1\,0\rangle$ directions. Although the most favorable configuration exhibits a C-C bond, migration paths show large barriers exceeding 2.2 eV for transitions into the ground state. As before, structures other than the ground-state configuration are assumed to arise more likely. Thus, agglomeration of C defects in contrast to C clustering is again reinforced by these findings.

C_i and vacancies are found to efficiently react with each other exhibiting activation energies as low as 0.1 eV and 0.6 eV resulting in stable C_s configurations. In addition, a highly attractive interaction exhibiting a large capture radius, effective independent of the orientation and the direction of separation of the defects, is observed. Accordingly, the formation of C_s is very likely to occur. Comparatively high energies necessary for the reverse process reveal this configuration to be extremely stable. Thus, C interstitials and vacancies located close together are assumed to end up in a configuration of C_s.

Investigating configurations of C_s and Si_i, formation energies higher than that of the C_i $\langle 1\,0\,0\rangle$ DB were obtained keeping up previously derived assumptions concerning the ground state of C_i in otherwise perfect Si. However, a small capture radius is identified for the respective interaction that might prevent the recombination of defects exceeding a separation of 0.6 nm into the ground-state configuration. In addition, a rather small activation energy of 0.77 eV allows for the formation of a C_s-Si_i pair originating from the C_i $\langle 1\,0\,0\rangle$ DB structure by thermally activated processes. Low diffusion barriers of Si_i enable further separation of the defect pair. Thus, elevated temperatures might lead to configurations of C_s and a remaining Si atom in the near interstitial lattice, which is likewise supported by the result of the MD run.

Classical potential MD calculations targeting the direct simulation of SiC precipitation in Si are adopted. Therefor, the necessary amount of C is gradually incorporated into a large c-Si host. Simulations at temperatures used in IBS result in structures dominated by the C_i $\langle 1\,0\,0\rangle$ DB and its combinations if C is inserted into the total volume. Incorporation into volumes V_2 and V_3, which correspond to the volume of the expected precipitate and the volume containing the necessary amount of Si, lead to an amorphous SiC-like structure within the respective volume. Both results are not expected with respect to the outcome of the IBS experiments. In the first case, i.e. the low C concentration simulations, C_i $\langle 1\,0\,0\rangle$ DBs are indeed formed. However, sufficient defect agglomeration is not observed. In the second case, i.e. the high C concentration simulations, crystallization of the amorphous structure, which is not expected at prevailing temperatures, is likewise not observed.

Limitations of the MD technique in addition to overestimated bond strengths due to the short range potential are identified to be responsible. The approach of using increased temperatures during C insertion is followed to work around this problem termed *potential enhanced slow phase space propagation*. Higher temperatures are justified for several reasons. Elevated temperatures are expected to compensate the overestimated diffusion barriers and accelerate structural evolution. In addition, formation of SiC is also observed at higher implantation temperatures [18, 23] and temperatures in the implantation region is definitely higher than the temperature determined experimentally at the surface of the sample. Furthermore, the present study focuses on structural transitions in a system far from equilibrium.

No significant change is observed for high C concentrations at increased temperatures. The amorphous phase is maintained. The huge amount of damage hampers identification of investigated structures, which in many cases lost the alignment to the c-Si host. Obviously, incorporation of a high quantity of C into a small volume within a short period of time creates damage, which decelerates structural evolution. For the low C concentrations, time scales are still too low to observe C agglomeration. However, a phase transition of the C_i-dominated into a clearly C_s-dominated structure is observed. The amount of C_s increases with increasing temperature. Diamond and graphite like bonds as well as the artificial bonds due to the cut-off are reduced. Loose structures of stretched SiC, which are adjusted to the Si lattice with respect to the lattice constant and alignment, are identified. Si_i is often found in the direct surrounding. Entropic contributions are assumed to be responsible for these structures at elevated temperatures that deviate from the ground state at 0 K. Indeed, utilizing increased temperatures is assumed to constitute a necessary condition to simulate IBS of 3C-SiC in c-Si.

Conclusions concerning the SiC conversion mechanism are derived from results of both, first-principles and classical potential calculations. Although classical potential MD calculations fail to directly simulate precipitation of SiC, obtained results, on the one hand, reinforce previous findings of the first-principles investigations and, on the other hand, allow further conclusions on the SiC precipitation in Si.

Initially, quantum-mechanical investigations suggest agglomeration of C_i defects that form energetically favorable configurations by an effective stress compensation. Low barriers of migration are found except for transitions into the ground-state configuration, which is composed of a strong C-C bond. Thus, agglomeration of C_i in the absence of C clustering is expected. These initial results suggest a conversion mechanism based on the agglomeration of C_i defects followed by a sudden precipitation once a critical size is reached. However, subsequent investigations of structures that are particularly conceivable under conditions prevalent in IBS and at elevated temperatures show C_s to occur in all probability. The transition from the ground state of a single C atom incorporated into otherwise perfect c-Si, i.e. the C_i $\langle 1\,0\,0\rangle$ DB, into a configuration of C_s next to a Si_i atom exhibits an activation energy lower than the one for the diffusion of the highly mobile C_i defect. Considering additionally the likewise lower diffusion barrier of Si_i, configurations of separated C_s and Si_i will occur in all probability. This is reinforced by the *ab initio* MD run at non-zero temperature, which shows structures of separating instead of recombining C_s and Si_i defects. This suggests increased participation of C_s already in the initial stages of the implantation process. The highly mobile Si_i is assumed to constitute a vehicle for the rearrangement of other C_s atoms onto proper lattice sites, i.e. lattice sites of one of the the two fcc lattices composing the diamond structure. This way, stretched SiC structures, which are coherently aligned to the c-Si host, are formed by agglomeration of C_s. Precipitation into an incoherent and partially strain-compensated SiC nucleus occurs once the increasing strain energy surpasses the interfacial energy of the incoherent 3C-SiC precipitate and the c-Si substrate. As already assumed by Nejim et al. [23], Si_i serves as supply for subsequently implanted C atoms to form further SiC in the resulting free space due to the accompanied volume reduction.

Several conclusions based on results obtained by classical potential MD simulations are drawn. First of all, increased temperatures are considered a necessary condition to simulate the IBS of epitaxially aligned 3C-SiC in Si, which constitutes a process far from thermodynamic equilibrium. The strong deviation from equilibrium by elevated temperatures enables the formation of C_s-Si_i structures as observed in the quantum-mechanical calculations. In contrast, structures of C_i $\langle 1\,0\,0\rangle$ DBs, which constitute the thermodynamic ground state, appear at low temperatures. Thus, the mechanism based on the agglomeration of C_s is reinforced. Secondly, in configurations of stretched SiC composed by C_s, the accompanied Si_i defect may be assigned further functionality. Next to that as a vehicle that is able to rearrange C_s and a building block for the surrounding Si host or further SiC, the analyzed configurations suggest Si_i to be required for stress compensation. As evidently observed in these structures, Si_i reduces tensile strain by capturing a position near one of the C atoms within a configuration of two C atoms that basically reside on Si lattice sites. Furthermore, Si_i might similarly compensate strain in the interface region of an incoherent, nucleated SiC precipitate and the c-Si matrix. Further conclusions are derived from results of the high C concentration simulations, in which a large amount of C atoms to obtain stoichiometry is incorporated into a small volume within a short period of time, which results in essentially no time for the system to rearrange. Due to this, the occurrence of strong C-C bonds and the production of a vast amount of damage is observed, which finally results in the formation of an amorphous phase. The strong bonds and damage obviously decelerate structural evolution. The short time, which is not sufficient for structural evolution of the strongly damaged region, can be mapped to a system of low temperature, which lacks the kinetic energy required for the restructuring process.

These findings as well as the derived conclusion on the precipitation mechanism involving an increased participation of C_s agree well with experimental results. C implanted at room temperature was found to be able to migrate towards the surface in contrast to implantations at 500 °C, which do not show redistribution of the C atoms [113]. This excellently conforms to the results of the MD simulations at different temperatures, which show the formation of highly mobile C_i $\langle 1\,0\,0\rangle$ DBs for low and much more stable C_s defects for high temperatures. This is likewise suggested by IBS experiments utilizing implantation temperatures of 550 °C followed by incoherent lamp annealing at temperatures as high as 1405 °C required for the C segregation due to the stability of C_s [15]. Furthermore, increased implantation temperatures were found to be more efficient than high temperatures in the postannealing step concerning the formation of topotactically aligned 3C-SiC precipitates [106, 218]. Particularly strong C-C bonds, which are hard to break by thermal annealing, were found to effectively aggravate the restructuring process of such configurations [219]. These bonds preferentially arise if additional kinetic energy provided by an increase of the implantation temperature is missing to accelerate or even enable atomic rearrangements in regions exhibiting a large amount of C atoms. This is assumed to be related to the problem of slow structural evolution encountered in the high C concentration simulations. More substantially, understoichiometric implantations at room temperature into preamorphized Si followed by a solid-phase epitaxial regrowth step at 700 °C result in $Si_{1-x}C_x$ layers in the diamond cubic phase with C residing on substitutional Si lattice sites [133]. The strained structure is found to be stable up to 810 °C. Coherent clustering followed by precipitation is suggested if these structures are annealed at higher temperatures. Similar, implantations of an understoichiometric dose into c-Si at room temperature followed by thermal annealing result in small spherical sized C_i agglomerates below 700 °C and SiC precipitates of the same size above 700 °C [144] annealing temperature. Since, however, the implantation temperature is considered more efficient than the postannealing temperature, SiC precipitates are expected and indeed observed for as-implanted samples [16, 18] in implantations performed at 450 °C. According to this, implanted C is likewise expected to occupy substitutionally regular Si lattice sites right from the start for implantations into c-Si at elevated temperatures. Moreover, implantations below the optimum temperature for the IBS of SiC show regions of randomly oriented SiC crystallites whereas epitaxial crystallites are found for increased temperatures [16]. The results of the MD simulations can be interpreted in terms of these experimental findings. The successive occupation of regular Si lattice sites by C_s atoms as observed in the high temperature MD simulations and assumed from results of the quantum-mechanical investigations perfectly satisfies the epitaxial relation of substrate and precipitate. In contrast, there is no obvious reason for a topotactic transition of C_i $\langle 1\,0\,0\rangle$ DB agglomerates, as observed in the low temperature MD simulations, into epitaxially aligned precipitates. The latter transition would necessarily involve a much more profound change in structure. Experimentally, randomly oriented precipitates might also be due to SiC nucleation within the arising amorphous matrix [16]. In simulation, an amorphous SiC phase is formed for high C concentrations. This is due to high amounts of introduced damage within a short period of time resulting in essentially no time for structural evolution, which is comparable to the low temperature experiments, which lack the kinetic energy necessary for recrystallization of the highly damaged region. Indeed, the complex transformation of agglomerated C_i DBs as suggested by results of the low C concentration simulations could involve an intermediate amorphous phase probably accompanied by the loss of alignment with respect to the Si host matrix. In any case, the precipitation mechanism by accumulation of C_s obviously satisfies the experimental finding of identical $(h\,k\,l)$ planes of substrate and precipitate.

Finally, it is worth to point out that the precipitation mechanism based on C_s does not necessarily contradict to results of the HREM studies [17, 20, 144], which propose precipitation by agglomeration of C_i. In these studies, regions of dark contrasts are attributed to C atoms that reside in the interstitial lattice in an otherwise undisturbed Si lattice. The C_i atoms lead to a local increase of the crystal potential, which is responsible for the dark contrast. However, there is no particular reason for the C species to reside in the interstitial lattice. Contrasts are also assumed for Si_i. Once precipitation occurs, regions of dark contrasts disappear in favor of Moiré patterns indicating 3C-SiC in c-Si due to the mismatch in the lattice constant. Until then, however, these may likewise be composed of stretched SiC structures coherently aligned to the Si host together with Si_i in the surrounding or of already contracted incoherent SiC surrounded by Si on regular lattice sites as well as in the interstitial lattice, where the latter is too small to be detected in HREM.

To conclude, results of the present study indicate a precipitation of SiC in Si by successive agglomeration of C_s. Elevated temperatures result in increased entropic contributions to structural formation. Moreover, conditions prevalent in IBS deviate the system from thermodynamic equilibrium. Thereby, C_i is enabled to turn into C_s accompanied by the emission of Si_i. Si_i, which is likewise existent, serves several needs: as a vehicle to rearrange the C_s atoms, as a building block for the surrounding Si host or further SiC and for strain compensation. The Si_i vehicle turns C_s into highly mobile C_i. This way, C can be easily rearranged in order to end up in a configuration of C atoms that occupy substitutionally the lattice sites of one of the fcc lattices of the diamond structure. Stretched SiC structures arise, which are coherently aligned to the Si matrix. Si_i is believed to likewise compensate the tensile strain within these structures. This is followed by precipitation into incoherent 3C-SiC once the strain energy of the coherent structure surpasses the interfacial energy of the incoherent precipitate and the c-Si substrate. The associated volume reduction is compensated by Si_i that may serve as a supply for further SiC or as a building block for the surrounding Si host and likewise reduce existing strain in the interface region. Results of the atomistic simulation study that indicate the respective precipitation mechanism conform well with other experimental findings. By verification, the derived conclusions with respect to the precipitation mechanism are reinforced. Furthermore, experimental results that suggest a precipitation mechanism based on the agglomeration of C_i do not conflict with the proposed model of precipitation as concluded in the present study.

Appendix A

Force evaluation for the three body Tersoff potential

A.1 Form of the Tersoff potential and its derivative

The Tersoff potential [156] is of the form

$$\begin{aligned} E &= \sum_i E_i = \frac{1}{2}\sum_{i\neq j} V_{ij} \ , && \text{(A.1)} \\ V_{ij} &= f_C(r_{ij})[f_R(r_{ij}) + b_{ij} f_A(r_{ij})] \ . && \text{(A.2)} \end{aligned}$$

The repulsive f_R and attractive f_A part is given by

$$\begin{aligned} f_R(r_{ij}) &= A_{ij}\exp(-\lambda_{ij} r_{ij}) \ , && \text{(A.3)} \\ f_A(r_{ij}) &= -B_{ij}\exp(-\mu_{ij} r_{ij}) \ . && \text{(A.4)} \end{aligned}$$

The bond order function b_{ij} is

$$b_{ij} = \chi_{ij}(1 + \beta_i^{n_i}\zeta_{ij}^{n_i})^{-1/2n_i} \tag{A.5}$$

with

$$\begin{aligned} \zeta_{ij} &= \sum_{k\neq i,j} f_C(r_{ik})\omega_{ik} g(\theta_{ijk}) \ , && \text{(A.6)} \\ g(\theta_{ijk}) &= 1 + c_i^2/d_i^2 - c_i^2/[d_i^2 + (h_i - \cos\theta_{ijk})^2] \ . && \text{(A.7)} \end{aligned}$$

The cut-off function f_C is taken to be

$$f_C(r_{ij}) = \begin{cases} 1, & r_{ij} < R_{ij} \\ \frac{1}{2} + \frac{1}{2}\cos\Big[\pi(r_{ij} - R_{ij})/(S_{ij} - R_{ij})\Big], & R_{ij} < r_{ij} < S_{ij} \\ 0, & r_{ij} > S_{ij} \end{cases} \tag{A.8}$$

with θ_{ijk} being the bond angle between bonds ij and ik as shown in Figure 3.1.

For a three body potential, if V_{ij} is not equal to V_{ji}, the derivative is of the form

$$\nabla_{\mathbf{r}_i} E = \frac{1}{2}\big[\sum_j (\nabla_{\mathbf{r}_i} V_{ij} + \nabla_{\mathbf{r}_i} V_{ji}) + \sum_k \sum_j \nabla_{\mathbf{r}_i} V_{jk}\big] \ . \tag{A.9}$$

In the following, all the necessary derivatives to calculate $\nabla_{\mathbf{r}_i} E$ are written down.

A.2 Derivative of V_{ij} with respect to $\mathbf{r}_i$

$$\begin{aligned}\nabla_{\mathbf{r}_i} V_{ij} &= \nabla_{\mathbf{r}_i} f_C(r_{ij})\big[f_R(r_{ij}) + b_{ij} f_A(r_{ij})\big] + \\ &+ f_C(r_{ij})\big[\nabla_{\mathbf{r}_i} f_R(r_{ij}) + b_{ij}\nabla_{\mathbf{r}_i} f_A(r_{ij}) + f_A(r_{ij})\nabla_{\mathbf{r}_i} b_{ij}\big] \qquad \text{(A.10)}\end{aligned}$$

$$\nabla_{\mathbf{r}_i} f_R(r_{ij}) = A_{ij}\lambda_{ij}\frac{\mathbf{r}_{ij}}{r_{ij}}\exp(-\lambda_{ij} r_{ij}) \qquad \text{(A.11)}$$

$$\nabla_{\mathbf{r}_i} f_A(r_{ij}) = -B_{ij}\mu_{ij}\frac{\mathbf{r}_{ij}}{r_{ij}}\exp(-\mu_{ij} r_{ij}) \qquad \text{(A.12)}$$

$$\nabla_{\mathbf{r}_i} f_C(r_{ij}) = \begin{cases} \frac{1}{2}\sin\left(\frac{\pi(r_{ij}-R_{ij})}{S_{ij}-R_{ij}}\right)\frac{\pi}{S_{ij}-R_{ij}}\frac{\mathbf{r}_{ij}}{r_{ij}}, & R_{ij} < r_{ij} < S_{ij} \\ 0, & \text{else.} \end{cases} \qquad \text{(A.13)}$$

$$\nabla_{\mathbf{r}_i} b_{ij} = -\frac{\chi_{ij}}{2}(1 + \beta^{n_i}\zeta_{ij}^{n_i})^{-\frac{1}{2n_i}-1}\beta^{n_i}\zeta_{ij}^{n_i-1}\nabla_{\mathbf{r}_i}\zeta_{ij} \qquad \text{(A.14)}$$

$$\nabla_{\mathbf{r}_i}\zeta_{ij} = \sum_{k\neq i,j}\big(g(\theta_{ijk})\nabla_{\mathbf{r}_i} f_C(r_{ik}) + f_C(r_{ik})\nabla_{\mathbf{r}_i} g(\theta_{ijk})\big) \qquad \text{(A.15)}$$

$$\nabla_{\mathbf{r}_i} g(\theta_{ijk}) = -\frac{2(h_i - \cos\theta_{ijk})c_i^2}{\big[d_i^2 + (h_i - \cos\theta_{ijk})^2\big]^2}\nabla_{\mathbf{r}_i}(\cos\theta_{ijk}) \qquad \text{(A.16)}$$

$$\begin{aligned}\nabla_{\mathbf{r}_i}\cos\theta_{ijk} &= \nabla_{\mathbf{r}_i}\left(\frac{\mathbf{r}_{ij}\mathbf{r}_{ik}}{r_{ij}r_{ik}}\right) \\ &= \left[\frac{\cos\theta_{ijk}}{r_{ij}^2} - \frac{1}{r_{ij}r_{ik}}\right]\mathbf{r}_{ij} + \left[\frac{\cos\theta_{ijk}}{r_{ik}^2} - \frac{1}{r_{ij}r_{ik}}\right]\mathbf{r}_{ik} \qquad \text{(A.17)}\end{aligned}$$

A.3 Derivative of V_{ji} with respect to $\mathbf{r}_i$

$$\begin{aligned}\nabla_{\mathbf{r}_i} V_{ji} &= \nabla_{\mathbf{r}_i} f_C(r_{ji})\big[f_R(r_{ji}) + b_{ji} f_A(r_{ji})\big] + \\ &+ f_C(r_{ji})\big[\nabla_{\mathbf{r}_i} f_R(r_{ji}) + b_{ji}\nabla_{\mathbf{r}_i} f_A(r_{ji}) + f_A(r_{ji})\nabla_{\mathbf{r}_i} b_{ji}\big] \qquad \text{(A.18)}\end{aligned}$$

$$\nabla_{\mathbf{r}_i} f_R(r_{ji}) = -A_{ji}\lambda_{ji}\frac{\mathbf{r}_{ji}}{r_{ji}}\exp(-\lambda_{ji} r_{ji}) = \nabla_{\mathbf{r}_i} f_R(r_{ij}) \qquad \text{(A.19)}$$

$$\nabla_{\mathbf{r}_i} f_A(r_{ji}) = +B_{ji}\mu_{ji}\frac{\mathbf{r}_{ji}}{r_{ji}}\exp(-\mu_{ji} r_{ji}) = \nabla_{\mathbf{r}_i} f_A(r_{ij}) \qquad \text{(A.20)}$$

$$\nabla_{\mathbf{r}_i} f_C(r_{ij}) = \nabla_{\mathbf{r}_i} f_C(r_{ij}) = \begin{cases} -\frac{1}{2}\sin\left(\frac{\pi(r_{ji}-R_{ji})}{S_{ji}-R_{ji}}\right)\frac{\pi}{S_{ji}-R_{ji}}\frac{\mathbf{r}_{ji}}{r_{ji}}, & R_{ji} < r_{ji} < S_{ji} \\ 0, & \text{else.} \end{cases} \qquad \text{(A.21)}$$

$$\begin{aligned}
\nabla_{\mathbf{r}_i} b_{ji} &= -\frac{\chi_{ji}}{2}\left(1+\beta^{n_j}\zeta_{ji}^{n_j}\right)^{-\frac{1}{2n_j}-1}\beta^{n_j}\zeta_{ji}^{n_j-1}\nabla_{\mathbf{r}_i}\zeta_{ji} && \text{(A.22)}\\
\nabla_{\mathbf{r}_i}\zeta_{ji} &= \sum_{k\neq j,i}\big(g(\theta_{jik})\nabla_{\mathbf{r}_i} f_C(r_{jk}) + f_C(r_{jk})\nabla_{\mathbf{r}_i} g(\theta_{jik})\big)\\
&= \sum_{k\neq j,i} f_C(r_{jk})\nabla_{\mathbf{r}_i} g(\theta_{jik}) \quad \Big(\text{Reason: } \nabla_{\mathbf{r}_i} f_C(r_{jk}) = 0\Big) && \text{(A.23)}\\
\nabla_{\mathbf{r}_i} g(\theta_{jik}) &= -\frac{2(h_j-\cos\theta_{jik})c_j^2}{\left[d_j^2+(h_j-\cos\theta_{jik})^2\right]^2}\nabla_{\mathbf{r}_i}(\cos\theta_{jik}) && \text{(A.24)}
\end{aligned}$$

$$\begin{aligned}
\nabla_{\mathbf{r}_i}\cos\theta_{jik} &= \nabla_{\mathbf{r}_i}\left(\frac{\mathbf{r}_{ji}\mathbf{r}_{jk}}{r_{ji}r_{jk}}\right)\\
&= \frac{1}{r_{ji}r_{jk}}\mathbf{r}_{jk} - \frac{\cos\theta_{jik}}{r_{ji}^2}\mathbf{r}_{ji} && \text{(A.25)}
\end{aligned}$$

A.4 Derivative of V_{jk} with respect to $\mathbf{r}_i$

$$\begin{aligned}
\nabla_{\mathbf{r}_i} V_{jk} &= f_C(r_{jk})f_A(r_{jk})\nabla_{\mathbf{r}_i} b_{jk} && \text{(A.26)}\\
\nabla_{\mathbf{r}_i} b_{jk} &= -\frac{\chi_{jk}}{2}\left(1+\beta^{n_j}\zeta_{jk}^{n_j}\right)^{-\frac{1}{2n_j}-1}\beta^{n_j}\zeta_{jk}^{n_j-1}\nabla_{\mathbf{r}_i}\zeta_{jk} && \text{(A.27)}\\
\nabla_{\mathbf{r}_i}\zeta_{jk} &= \sum_{l\neq j,k}\big(g(\theta_{jkl})\nabla_{\mathbf{r}_i} f_C(r_{jl}) + f_C(r_{jl})\nabla_{\mathbf{r}_i} g(\theta_{jkl})\big)\\
&= f_C(r_{ji})\nabla_{\mathbf{r}_i} g(\theta_{jki}) + g(\theta_{jki})\nabla_{\mathbf{r}_i} f_C(r_{ji}) && \text{(A.28)}\\
\nabla_{\mathbf{r}_i} g(\theta_{jki}) &= -\frac{2(h_j-\cos\theta_{jki})c_j^2}{\left[d_j^2+(h_j-\cos\theta_{jki})^2\right]^2}\nabla_{\mathbf{r}_i}(\cos\theta_{jki}) && \text{(A.29)}\\
\nabla_{\mathbf{r}_i}\cos\theta_{jki} &= \nabla_{\mathbf{r}_i}\left(\frac{\mathbf{r}_{jk}\mathbf{r}_{ji}}{r_{jk}r_{ji}}\right)\\
&= \frac{1}{r_{jk}r_{ji}}\mathbf{r}_{jk} - \frac{\cos\theta_{jki}}{r_{ji}^2}\mathbf{r}_{ji} && \text{(A.30)}
\end{aligned}$$

A.5 Implementation issues

As seen in the last sections, the derivatives of V_{ij}, V_{ji} and V_{jk} with respect to $\mathbf{r}_i$ are necessary to compute the forces for atom i. According to this, for every triple (ijk) the derivatives of the three potential contributions, denoted by V_{ijk}, V_{jik} and V_{jki} have to be computed. In simulation, however, it is not practical to evaluate all three potential derivatives for each (ijk) triple. The V_{jik} and V_{jki} potential and its derivatives will be calculated in subsequent loops anyways. To avoid multiple computation of the same potential derivatives, the force contributions for atom j and k due to the V_{ijk} contribution have to be considered by calculating the derivatives of V_{ijk} with respect to $\mathbf{r}_j$ and $\mathbf{r}_k$ inside the loop of the (ijk) triple in addition to the derivative with respect to $\mathbf{r}_i$. This poses a more convenient method to obtain the forces keeping in mind that all the necessary force contributions for atom i are calculated and added in subsequent loops.

A.5.1 Derivative of V_{ij} with respect to $\mathbf{r}_j$

$$\begin{aligned}\nabla_{\mathbf{r}_j} V_{ij} &= \nabla_{\mathbf{r}_j} f_C(r_{ij})\big[f_R(r_{ij}) + b_{ij} f_A(r_{ij})\big] + \\ &\quad + f_C(r_{ij})\big[\nabla_{\mathbf{r}_j} f_R(r_{ij}) + b_{ij}\nabla_{\mathbf{r}_j} f_A(r_{ij}) + f_A(r_{ij})\nabla_{\mathbf{r}_j} b_{ij}\big] \qquad \text{(A.31)}\end{aligned}$$

Using the equality $\nabla_{\mathbf{r}_i} r_{ij} = -\nabla_{\mathbf{r}_j} r_{ij}$, the following relations are valid:

$$\begin{aligned}\nabla_{\mathbf{r}_j} f_R(r_{ij}) &= -\nabla_{\mathbf{r}_i} f_R(r_{ij}) && \text{(A.32)}\\ \nabla_{\mathbf{r}_j} f_A(r_{ij}) &= -\nabla_{\mathbf{r}_i} f_A(r_{ij}) && \text{(A.33)}\\ \nabla_{\mathbf{r}_j} f_C(r_{ij}) &= -\nabla_{\mathbf{r}_i} f_C(r_{ij}) && \text{(A.34)}\end{aligned}$$

The pair contributions are, thus, easily obtained. The contribution of the bond order term is given by:

$$\begin{aligned}\nabla_{\mathbf{r}_j} \cos\theta_{ijk} &= \nabla_{\mathbf{r}_j}\left(\frac{\mathbf{r}_{ij}\mathbf{r}_{ik}}{r_{ij}r_{ik}}\right)\\ &= \frac{1}{r_{ij}r_{ik}}\mathbf{r}_{ik} - \frac{\cos\theta_{ijk}}{r_{ij}^2}\mathbf{r}_{ij} && \text{(A.35)}\end{aligned}$$

A.5.2 Derivative of V_{ij} with respect to $\mathbf{r}_k$

The derivative of V_{ij} with respect to $\mathbf{r}_k$ just consists of the single term

$$\nabla_{\mathbf{r}_k} V_{ij} = f_C(r_{ij}) f_A(r_{ij}) \nabla_{\mathbf{r}_k} b_{ij} \qquad \text{(A.36)}$$

since the derivatives of the functions only depending on atom i and j vanish.

$$\begin{aligned}\nabla_{\mathbf{r}_k} f_R(r_{ij}) &= 0 && \text{(A.37)}\\ \nabla_{\mathbf{r}_k} f_A(r_{ij}) &= 0 && \text{(A.38)}\\ \nabla_{\mathbf{r}_k} f_C(r_{ij}) &= 0 && \text{(A.39)}\end{aligned}$$

Concerning b_{ij}, in addition to the angular term, the derivative of the cut-off function has to be considered.

$$\begin{aligned}\nabla_{\mathbf{r}_k} \zeta_{ij} &= g(\theta_{ijk})\nabla_{\mathbf{r}_k} f_C(r_{ik}) + f_C(r_{ik})\nabla_{\mathbf{r}_k} g(\theta_{ijk}) && \text{(A.40)}\\ \nabla_{\mathbf{r}_k} f_C(r_{ik}) &= -\nabla_{\mathbf{r}_i} f_C(r_{ik}) && \text{(A.41)}\\ \nabla_{\mathbf{r}_k} \cos\theta_{ijk} &= \nabla_{\mathbf{r}_k}\left(\frac{\mathbf{r}_{ij}\mathbf{r}_{ik}}{r_{ij}r_{ik}}\right)\\ &= \frac{1}{r_{ij}r_{ik}}\mathbf{r}_{ij} - \frac{\cos\theta_{ijk}}{r_{ik}^2}\mathbf{r}_{ik} && \text{(A.42)}\end{aligned}$$

A.5.3 Code realization

The implementation of the force evaluation shown in the following is applied to the potential designed by Erhart and Albe [147]. There are slight differences compared to the original potential by Tersoff:

- Difference in sign of the attractive part.

- c, d and h values depend on atom k in addition to atom i.
- Difference in sign of the $\cos\theta_{ijk}$ term.
- There are no parameters β and χ.
- The exponent of the b term is constantly $-\frac{1}{2}$.

These differences actually slightly ease code realization. The respective flow chart is displayed in Fig. A.1.

```
LOOP i {
    // nop (only used in orig. Tersoff)
    LOOP j {
        // nop (only used in orig. Tersoff)
    }
    LOOP j {
        $\zeta_{ij} = 0$
        set $S_{ij}$ (cut-off)
        calculate: $r_{ij}$, $r_{ij}^2$
        IF $r_{ij} > S_{ij}$ THEN CONTINUE

        LOOP k {
            set $ik$-dependent values
            calculate: $r_{ik}$, $r_{ik}^2$
            IF $r_{ik} > S_{ik}$ THEN CONTINUE
            calculate: $\theta_{ijk}$, $\cos(\theta_{ijk})$, $dg(\theta_{ijk})$, $g(\theta)$, $f_C(r_{ik})$, $df_C(r_{ik})$
            $\zeta_{ij} = \zeta_{ij} + f_C(r_{ik})g(\theta)$
        }

        calculate: $f_C(r_{ij})$, $df_C(r_{ij})$, $f_A(r_{ij})$, $df_A(r_{ij})$, $f_R(r_{ij})$, $df_R(r_{ij})$, $b_{ij}$, $db_{ij}$
        calculate: $F = -\frac{1}{2}\big(\nabla_{\mathbf{r}_i} f_C(r_{ij})\big[f_R(r_{ij}) - b_{ij} f_A(r_{ij})\big] + f_C(r_{ij})\big[\nabla_{\mathbf{r}_i} f_R(r_{ij}) - b_{ij}\nabla_{\mathbf{r}_i} f_A(r_{ij})\big]\big)$
        $F_{Atom\,i} = F_{Atom\,i} + F$
        $F_{Atom\,j} = F_{Atom\,j} - F$
        $E = E + \frac{1}{2} f_C(r_{ij})[f_R(r_{ij}) - b_{ij} f_A(r_{ij})]$
        $d\zeta_{ij} = \frac{1}{2} f_A(r_{ij}) f_C(r_{ij}) db_{ij}$

        LOOP k {
            calculate: $\nabla_{\mathbf{r}_i}\cos\theta_{ijk}$, $\nabla_{\mathbf{r}_j}\cos\theta_{ijk}$, $\nabla_{\mathbf{r}_k}\cos\theta_{ijk}$
            $F_{Atom\,i} += d\zeta_{ij}\big(g(\theta_{ijk})\nabla_{\mathbf{r}_i} f_C(r_{ik}) + f_C(r_{ik}) dg(\theta_{ijk})\nabla_{\mathbf{r}_i}\cos\theta_{ijk}\big)$
            $F_{Atom\,j} += d\zeta_{ij} f_C(r_{ik}) dg(\theta_{ijk})\nabla_{\mathbf{r}_j}\cos\theta_{ijk}$
            $F_{Atom\,k} += d\zeta_{ij}\big(g(\theta_{ijk})\nabla_{\mathbf{r}_k} f_C(r_{ik}) + f_C(r_{ik}) dg(\theta_{ijk})\nabla_{\mathbf{r}_k}\cos\theta_{ijk}\big)$
        }
    }
}
```

Figure A.1: Flow chart of the force evaluation for Tersoff-like bond order potentials using pseudocode.

Appendix B

Modifications to the VASP code

B.1 Description

In the VASP code, the *selective dynamics* mode provides a feature to allow or constrain the change of each of the three coordinates for every single atom. By this, however, applied constraints are restricted to the chosen basis. For the investigation of migration pathways utilizing the constrained relaxation technique as detailed in section 3.4, the required constraint not necessarily corresponds to one of the coordinate axes as defined by the basis, which, in turn, is determined to enable a construction within the supercell approach.

Thus, the functionality of the *selective dynamics* mode had to be extended by modifications in the particle position evaluation routine of VASP. These modifications allow for a rotation of all atom coordinates individually before respective constraints are applied and a following, final inverse transformation. In that way, constraints for every single atom can be applied independently of the chosen basis. A patch against version 4.6 of the VASP code containing these modifications is available for download[1].

B.2 Mode of operation

The extended capabilities can only be used within the *selective dynamics* mode. It is enabled by adding the word *transformed* in front of the *selective dynamics* switch. This feature only works in *direct* mode. Two values of angles need to be added after the extra flags of each atom. The first angle corresponds to the rotation of the basis about the z-axis. The second angle determines the rotation about the transformed x-axis, x'. All values have to be supplied in degrees. The entire information is given in the POSCAR file as can be seen in the example displayed in Fig. B.1. In case of the first atom, the basis is transformed by a rotation of 45° and 30° about the z and x' axis. The basis of the fifth atom is likewise rotated by 135° and -10° respectively. Relaxation of both atoms is only allowed within the plane perpendicular to the y''-axis.

---

[1] http://www.physik.uni-augsburg.de/~zirkelfr/download/posic/sd_rot_all-atoms.patch

```
cubic diamond
 5.429
 1.00000 0.00000 0.00000
 0.00000 1.00000 0.00000
 0.00000 0.00000 1.00000
 8
transformed selective dynamics
direct
 0.00000 0.00000 0.00000 T F T 45.0 30.0
 0.50000 0.50000 0.00000 T T T 0.0 0.0
 0.50000 0.00000 0.50000 T T T 0.0 0.0
 0.00000 0.50000 0.50000 T T T 0.0 0.0
 0.25000 0.25000 0.25000 T F T 135.0 -10.0
 0.75000 0.75000 0.25000 T T T 0.0 0.0
 0.75000 0.25000 0.75000 T T T 0.0 0.0
 0.25000 0.75000 0.75000 T T T 0.0 0.0
```

Figure B.1: Example VASP input file utilizing the *transformed selective dynamics* mode of operation.

Appendix C

Description of programs and tools

Some selected programs and tools utilized within this study are introduced in the following. The source code is available for download[1]. The VASP utilities reside in the *vasp_tools* subdirectory included within the POSIC source.

C.1 Contents of the POSIC program suite

C.1.1 The molecular dynamics application

mdrun.{c,h} constitutes the actual, executable molecular dynamics application program.
config.default is a sample configuration file that is parsed by the *mdrun* application.
moldyn.{c,h} includes all the molecular dynamics routines.
potentials/albe.{c,h} implements the energy and force evaluation of the potential.
list/list.{c,h} contains code for the management of linked lists.
random/random.{c,h} deals with random numbers and distributions.
math/math.h provides inlined mathematical functions.
runmd, runmd_rx200 starts the *mdrun* application and postprocessing.

C.1.2 Postprocessing tools

calc_delta_e determines defect formation energies using SiC as a particle reservoir.
pair_correlation_calc.c computes the radial distribution function.
display_atom_data.c displays atom specific information.
bond_analyze.c counts the amount of C atoms that have four Si neighbors.
bond_analyze_script performs bond analysis on a large quantity of data.
search_bonds.c prints out pairs of atoms featuring specific bond properties.
visual_atoms.c creates a detailed atomic data file.
visualize creates images of atomic configurations.
parcasconv converts PARCAS output to POSIC format.
povconv converts POSIC output to PARCAS/RASMOL format.
s2xyz.c extracts (modified) *xyz* data from POSIC save files.
ppm2avi creates a movie out of atomic configuration images.

---

[1] http://www.physik.uni-augsburg.de/~zirkelfr/posic

C.2 VASP utilities

C.2.1 Operating VASP

create_lattice.c creates the lattice in VASP POSCAR format.
runvasp_rx200 executes VASP on the Augsburg Linux Compute Cluster.
sd_rot_all-atoms.patch enables selected dynamics in a user-defined basis for every atom.
mig_fullct.sh calculates a series of configurations within a migration path.

C.2.2 Postprocessing utilities

mig_calc prints out the configurational energies within a migration path.
e_coh calculates the cohesive energy.
e_form_tersoff calculates defect formation energies using SiC as a particle reservoir.
e_fc calculates the binding energy of a defect pair.
get_ks_levels creates the Kohn-Sham level diagram.
visualize creates images of atomic configurations.

References

[1] W. Wesch, Nucl. Instrum. Methods Phys. Res. B **116**, 305 (1996).

[2] H. Morkoç, S. Strite, G. B. Gao, M. E. Lin, B. Sverdlov, and M. Burns, J. Appl. Phys. **76**, 1363 (1994).

[3] J. B. Casady and R. W. Johnson, Solid-State Electron. **39**, 1409 (1996).

[4] M. A. Capano and R. J. Trew, MRS Bull. **22**, 19 (1997).

[5] G. Pensl and W. J. Choyke, Physica B **185**, 264 (1993).

[6] P. M. Sarro, Seonsor. Actuator. A **82**, 210 (2000).

[7] Y. S. Park, *SiC Materials and Devices* (Academic Press, San Diego, 1998).

[8] L. Giancarli, J. P. Bonal, A. Caso, G. L. Marois, N. B. Morley, and J. F. Salavy, Fusion Eng. Des. **41**, 165 (1998).

[9] Y. M. Tairov and V. F. Tsvetkov, J. Cryst. Growth **43**, 209 (1978).

[10] V. F. Tsvetkov, R. C. Glass, D. Henshall, C. H. C. Jr., and D. Asbury, Mater. Sci. Forum **264-268**, 3 (1998).

[11] T. Kimoto, H. Nishino, W. S. Yoo, and H. Matsunami, J. Appl. Phys. **73**, 726 (1993).

[12] J. A. Powell, D. J. Larkin, L. G. Matus, W. J. Choyke, J. L. Bradshaw, L. Henderson, M. Yoganathan, J. Yang, and P. Pirouz, Appl. Phys. Lett. **56**, 1353 (1990).

[13] A. Fissel, U. Kaiser, E. Ducke, B. Schröter, and W. Richter, J. Cryst. Growth **154**, 72 (1995).

[14] J. A. Borders, S. T. Picraux, and W. Beezhold, Appl. Phys. Lett. **18**, 509 (1971).

[15] K. J. Reeson, P. L. F. Hemment, J. Stoemenos, J. Davis, and G. E. Celler, Appl. Phys. Lett. **51**, 2242 (1987).

[16] J. K. N. Lindner and B. Stritzker, Nucl. Instrum. Methods Phys. Res. B **147**, 249 (1999).

[17] J. K. N. Lindner and B. Stritzker, Nucl. Instrum. Methods Phys. Res. B **148**, 528 (1999).

[18] J. K. N. Lindner, Nucl. Instrum. Methods Phys. Res. B **178**, 44 (2001).

[19] J. K. N. Lindner, Appl. Phys. A **77**, 27 (2003).

[20] P. Werner, S. Eichler, G. Mariani, R. Kögler, and W. Skorupa, Appl. Phys. Lett. **70**, 252 (1997).

[21] J. W. Strane, H. J. Stein, S. R. Lee, S. T. Picraux, J. K. Watanabe, and J. W. Mayer, J. Appl. Phys. **76**, 3656 (1994).

[22] C. Guedj, M. W. Dashiell, L. Kulik, J. Kolodzey, and A. Hairie, J. Appl. Phys. **84**, 4631 (1998).

[23] A. Nejim, P. L. F. Hemment, and J. Stoemenos, Appl. Phys. Lett. **66**, 2646 (1995).

[24] N. E. B. Cowern, A. Cacciato, J. S. Custer, F. W. Saris, and W. Vandervorst, Appl. Phys. Lett. **68**, 1150 (1996).

[25] P. M. Fahey, P. B. Griffin, and J. D. Plummer, Rev. Mod. Phys. **61**, 289 (1989).

[26] P. A. Stolk, H. J. Gossmann, D. J. Eaglesham, and J. M. Poate, Nucl. Instrum. Methods Phys. Res. B **96**, 187 (1995).

[27] P. A. Stolk, H.-J. Gossmann, D. J. Eaglesham, D. C. Jacobson, C. S. Rafferty, G. H. Gilmer, M. Jaraíz, J. M. Poate, H. S. Luftman, and T. E. Haynes, J. Appl. Phys. **81**, 6031 (1997).

[28] J. W. Strane, S. R. Lee, H. J. Stein, S. T. Picraux, J. K. Watanabe, and J. W. Mayer, J. Appl. Phys. **79**, 637 (1996).

[29] H. J. Osten, J. Griesche, and S. Scalese, Appl. Phys. Lett. **74**, 836 (1999).

[30] S.-T. Chang and C.-Y. Lin, Japanese J. Appl. Phys. **44**, 2257 (2005).

[31] H. J. Osten and P. Gaworzewski, J. Appl. Phys. **82**, 4977 (1997).

[32] R. A. Soref, J. Appl. Phys. **70**, 2470 (1991).

[33] E. Kasper, Phys. Scr. **T35**, 232 (1991).

[34] R. I. Scace and G. A. Slack, J. Chem. Phys. **30**, 1551 (1959).

[35] H. Moissan, C. R. Acad. Sci. **139**, 773 (1904).

[36] G. R. Fisher and P. Barnes, Philos. Mag. B **61**, 217 (1990).

[37] J. H. Edgar, J. Mater. Res. **7**, 235 (1992).

[38] O. V. Lossev, Telegrafiya i Telefoniya bez Provodov **44**, 485 (1927).

[39] H. J. Round, Electrical World **49**, 308 (1907).

[40] O. V. Lossev, Philos. Mag. Series 7 **6**, 1024 (1928).

[41] O. V. Lossev, Physik. Zeitschr. **30**, 920 (1929).

[42] O. V. Lossev, Physik. Zeitschr. **32**, 692 (1931).

[43] O. V. Lossev, Physik. Zeitschr. **34**, 397 (1933).

[44] L. Liu and J. H. Edgar, Mater. Sci. Eng., R **37**, 61 (2002).

[45] T. Takeuchi, H. Amano, K. Hiramatsu, N. Sawaki, and I. Akasaki, J. Cryst. Growth **115**, 634 (1991).

[46] A. Yamamoto, T. Yamauchi, T. Tanikawa, M. Sasase, B. K. Ghosh, A. Hashimoto, and Y. Ito, J. Cryst. Growth **261**, 266 (2004).

[47] Y. Ito, T. Yamauchi, A. Yamamoto, M. Sasase, S. Nishio, K. Yasuda, and Y. Ishigami, Appl. Surf. Sci. **238**, 159 (2004).

[48] M. Häberlen, J. W. Gerlach, B. Murphy, J. K. N. Lindner, and B. Stritzker, Journal of Crystal Growth **312**, 762 (2010).

[49] D. M. Brown, E. T. Downey, M. Ghezzo, J. W. Kretchmer, R. J. Saia, Y. S. Liu, J. A. Edmond, G. Gati, J. M. Pimbley, and W. E. Schneider, IEEE Trans. Electron Devices **40**, 325 (1993).

[50] F. Yan, X. Xin, S. Aslam, Y. Zhao, D. Franz, J. H. Zhao, and M. Weiner, IEEE J. Quantum Electron. **40**, 1315 (2004).

[51] W. L. Pribble, J. W. Palmour, S. T. Sheppard, R. P. Smith, S. T. Allen, T. J. Smith, Z. Ring, J. J. Sumakeris, A. W. Saxler, and J. W. Milligan, in *2002 IEEE MTT-S International Microwave Symposium Digest*, pp. 1819–1822, 2002.

[52] B. J. Baliga, IEEE Trans. Electron Devices **43**, 1717 (1996).

[53] C. E. Weitzel, J. W. Palmour, J. Carter, C.H., K. Moore, K. K. Nordquist, S. Allen, C. Thero, and M. Bhatnagar, IEEE Trans. Electron Devices **43**, 1732 (1996).

[54] L. Zhu and T. P. Chow, IEEE Trans. Electron Devices **55**, 1871 (2008).

[55] M. Bhatnagar, P. K. McLarty, and B. J. Baliga, IEEE Electron Device Lett. **13**, 501 (1992).

[56] M. Bhatnagar and B. J. Baliga, IEEE Trans. Electron Devices **40**, 645 (1993).

[57] S.-H. Ryu, A. K. Agarwal, R. Singh, and J. W. Palmour, IEEE Electron Device Lett. **22**, 124 (2001).

[58] F. Temcamani, P. Pouvil, O. Noblanc, C. Brylinski, P. Bannelier, B. Darges, and J. P. Prigent, in *2001 IEEE MTT-S International Microwave Symposium Digest*, pp. 641–644, 2001.

[59] P. Neudeck, J. Electron. Mater. **24**, 283 (1995).

[60] G. Pensl, M. Bassler, F. Ciobanu, V. Afanas'ev, H. Yano, T. Kimoto, and H. Matsunami, MRS Proc. **640** (2000).

[61] W. E. Nelson, F. A. Halden, and A. Rosengreen, J. Appl. Phys. **37**, 333 (1966).

[62] R. F. Davis, G. Kelner, M. Shur, J. W. Palmour, and J. A. Edmond, Proc. IEEE **79**, 677 (1991).

[63] W. F. Knippenberg, Philips Res. Repts. **18**, 161 (1963).

[64] A. E. van Arkel and J. H. de Boer, Z. Anorg. Chem. **148**, 345 (1925).

[65] K. Moers, Z. Anorg. Chem. **198**, 293 (1931).

[66] J. T. Kendall, J. Chem. Phys. **21**, 821 (1953).

[67] J. A. Lely, Ber. Deut. Keram. Ges. **32**, 229 (1955).

[68] Y. Tairov and V. F. Tsvetkov, J. Cryst. Growth **52**, 146 (1981).

[69] D. L. Barrett, R. G. Seidensticker, W. Gaida, R. H. Hopkins, and W. J. Choyke, J. Cryst. Growth **109**, 17 (1991).

[70] D. L. Barrett, J. P. McHugh, H. M. Hobgood, R. H. Hopkins, P. G. McMullin, R. C. Clarke, and W. J. Choyke, J. Cryst. Growth **128**, 358 (1993).

[71] R. A. Stein and P. Lanig, J. Cryst. Growth **131**, 71 (1993).

[72] L. Hoffmann, G. Ziegler, D. Theis, and C. Weyrich, J. Appl. Phys. **53**, 6962 (1982).

[73] F. C. Frank, Acta Crystallogr. **4**, 497 (1951).

[74] J. Heindl, H. P. Strunk, V. D. Heydemann, and G. Pensl, phys. status solidi (a) **162**, 251 (1997).

[75] N. Schulze, D. L. Barrett, and G. Pensl, Appl. Phys. Lett. **72**, 1632 (1998).

[76] S. Nishino, J. A. Powell, and H. A. Will, Appl. Phys. Lett. **42**, 460 (1983).

[77] K. Shibahara, S. Nishino, and H. Matsunami, J. Cryst. Growth **78**, 538 (1986).

[78] P. Pirouz, C. M. Chorey, and J. A. Powell, Appl. Phys. Lett. **50**, 221 (1987).

[79] P. Desjardins and J. E. Greene, J. Appl. Phys. **79**, 1423 (1996).

[80] M. Kitabatake, phys. status solidi (b) **202**, 405 (1997).

[81] J. A. Powell, L. G. Matus, M. A. Kuczmarski, C. M. Chorey, T. T. Cheng, and P. Pirouz, Appl. Phys. Lett. **51**, 823 (1987).

[82] H. Nagasawa, K. Yagi, T. Kawahara, and N. Hatta, Chemical Vapor Deposition **12**, 502 (2006).

[83] T. Hatayama, Y. Tarui, T. Fuyuki, and H. Matsunami, J. Cryst. Growth **150**, 934 (1995).

[84] S. Henke, B. Stritzker, and B. Rauschenbach, J. Appl. Phys. **78**, 2070 (1995).

[85] T. Fuyuki, T. Hatayama, and H. Matsunami, phys. status solidi (b) **202**, 359 (1997).

[86] T. Takaoka, H. Saito, Y. Igari, and I. Kusunoki, J. Cryst. Growth **183**, 175 (1998).

[87] H. S. Kong, B. L. Jiang, J. T. Glass, G. A. Rozgonyi, and K. L. More, J. Appl. Phys. **63**, 2645 (1988).

[88] H. S. Kong, J. T. Glass, and R. F. Davis, J. Appl. Phys. **64**, 2672 (1988).

[89] J. A. Powell, D. J. Larkin, L. G. Matus, W. J. Choyke, J. L. Bradshaw, L. Henderson, M. Yoganathan, J. Yang, and P. Pirouz, Appl. Phys. Lett. **56**, 1442 (1990).

[90] J. A. Powell, J. B. Petit, J. H. Edgar, I. G. Jenkins, L. G. Matus, J. W. Yang, P. Pirouz, W. J. Choyke, L. Clemen, and M. Yoganathan, Appl. Phys. Lett. **59**, 333 (1991).

[91] T. Ueda, H. Nishino, and H. Matsunami, J. Cryst. Growth **104**, 695 (1990).

[92] T. Yoshinobu, H. Mitsui, I. Izumikawa, T. Fuyuki, and H. Matsunami, Appl. Phys. Lett. **60**, 824 (1992).

[93] T. Fuyuki, M. Nakayama, T. Yoshinobu, H. Shiomi, and H. Matsunami, J. Cryst. Growth **95**, 461 (1989).

[94] T. Yoshinobu, M. Nakayama, H. Shiomi, T. Fuyuki, and H. Matsunami, J. Cryst. Growth **99**, 520 (1990).

[95] T. Fuyuki, T. Yoshinobu, and H. Matsunami, Thin Solid Films **225**, 225 (1993).

[96] S. Hara, T. Meguro, Y. Aoyagi, M. Kawai, S. Misawa, E. Sakuma, and S. Yoshida, Thin Solid Films **225**, 240 (1993).

[97] S. Tanaka, R. S. Kern, and R. F. Davis, Appl. Phys. Lett. **65**, 2851 (1994).

[98] M. D. Allendorf and D. A. Outka, Surf. Sci. **258**, 177 (1991).

[99] D. J. Eaglesham, F. C. Unterwald, H. Luftman, D. P. Adams, and S. M. Yalisove, J. Appl. Phys. **74**, 6615 (1993).

[100] S. Kaneda, Y. Sakamoto, T. Mihara, and T. Tanaka, J. Cryst. Growth **81**, 536 (1987).

[101] A. Fissel, B. Schröter, and W. Richter, Appl. Phys. Lett. **66**, 3182 (1995).

[102] A. Fissel, U. Kaiser, K. Pfennighaus, B. Schröter, and W. Richter, Appl. Phys. Lett. **68**, 1204 (1996).

[103] M. C. Righi, C. A. Pignedoli, R. D. Felice, C. M. Bertoni, and A. Catellani, Phys. Rev. Lett. **91**, 136101 (2003).

[104] F. L. Edelman, O. N. Kuznetsov, L. V. Lezheiko, and E. V. Lubopytova, Radiat. Eff. **29**, 13 (1976).

[105] T. Kimura, S. Kagiyama, and S. Yugo, Thin Solid Films **81**, 319 (1981).

[106] T. Kimura, S. Kagiyama, and S. Yugo, Thin Solid Films **94**, 191 (1982).

[107] K. J. Reeson, P. L. F. Hemment, R. F. Peart, C. D. Meekison, C. Marsh, G. R. Booker, R. J. Chater, J. A. Iulner, and J. Davis, Radiat. Eff. **99**, 71 (1986).

[108] P. Martin, B. Daudin, M. Dupuy, A. Ermolieff, M. Olivier, A. M. Papon, and G. Rolland, J. Appl. Phys. **67**, 2908 (1990).

[109] J. K. N. Lindner, M. Häberlen, G. Thorwarth, and B. Stritzker, Mater. Sci. Eng., C **26**, 857 (2006).

[110] J. K. N. Lindner, A. Frohnwieser, B. Rauschenbach, and B. Stritzker, MRS Proc. **354**, 171 (1994).

[111] J. K. N. Lindner, K. Volz, U. Preckwinkel, B. Götz, A. Frohnwieser, B. Rauschenbach, and B. Stritzker, Mater. Chem. Phys. **46**, 147 (1996).

[112] L. Calcagno, G. Compagnini, G. Foti, M. G. Grimaldi, and P. Musumeci, Nucl. Instrum. Methods Phys. Res. B **120**, 121 (1996).

[113] C. Serre, A. Pérez-Rodríguez, A. Romano-Rodríguez, J. R. Morante, R. Kögler, and W. Skorupa, J. Appl. Phys. **77**, 2978 (1995).

[114] J. K. N. Lindner, W. Reiber, and B. Stritzker, Mater. Sci. Forum **264-268**, 215 (1998).

[115] W. Attenberger, J. Lindner, and B. Stritzker, A method for forming a layered semiconductor structure and corresponding structure, Patent Application, 2003, WO 2003/034484 A3R4.

[116] W. Skorupa and R. A. Yankov, Mater. Chem. Phys. **44**, 101 (1996).

[117] R. C. Newman and J. B. Willis, J. Phys. Chem. Solids **26**, 373 (1965).

[118] J. A. Baker, T. N. Tucker, N. E. Moyer, and R. C. Buschert, J. Appl. Phys. **39**, 4365 (1968).

[119] A. R. Bean and R. C. Newman, J. Phys. Chem. Solids **32**, 1211 (1971).

[120] R. C. Newman and J. Wakefield, J. Phys. Chem. Solids **19**, 230 (1961).

[121] J. P. Kalejs, L. A. Ladd, and U. Gösele, Appl. Phys. Lett. **45**, 268 (1984).

[122] A. R. Bean and R. C. Newman, Solid State Commun. **8**, 175 (1970).

[123] G. D. Watkins and K. L. Brower, Phys. Rev. Lett. **36**, 1329 (1976).

[124] L. W. Song and G. D. Watkins, Phys. Rev. B **42**, 5759 (1990).

[125] A. K. Tipping and R. C. Newman, Semicond. Sci. Technol. **2**, 315 (1987).

[126] W. Hofker, H. Werner, D. Oosthoek, and N. Koeman, Appl. Phys. A **4**, 125 (1974).

[127] A. E. Michel, W. Rausch, P. A. Ronsheim, and R. H. Kastl, Appl. Phys. Lett. **50**, 416 (1987).

[128] N. E. B. Cowern, K. T. F. Janssen, and H. F. F. Jos, J. Appl. Phys. **68**, 6191 (1990).

[129] J. Zhu, Comput. Mater. Sci. **12**, 309 (1998).

[130] S. Isomae, T. Ishiba, T. Ando, and M. Tamura, J. Appl. Phys. **74**, 3815 (1993).

[131] S. Yagi, K. Abe, T. Okabayashi, Y. Yoneyama, A. Yamada, and M. Konagai, Japanese J. Appl. Phys. **41**, 2472 (2002).

[132] W. Kissinger, M. Weidner, H. J. Osten, and M. Eichler, Appl. Phys. Lett. **65**, 3356 (1994).

[133] J. W. Strane, H. J. Stein, S. R. Lee, B. L. Doyle, S. T. Picraux, and J. W. Mayer, Appl. Phys. Lett. **63**, 2786 (1993).

[134] S. S. Iyer, K. Eberl, M. S. Goorsky, F. K. LeGoues, J. C. Tsang, and F. Cardone, Appl. Phys. Lett. **60**, 356 (1992).

[135] G. G. Fischer, P. Zaumseil, E. Bugiel, and H. J. Osten, J. Appl. Phys. **77**, 1934 (1995).

[136] A. R. Powell, K. Eberl, F. E. LeGoues, B. A. Ek, and S. S. Iyer, J. Vac. Sci. Technol. B **11**, 1064 (1993).

[137] H. J. Osten, M. Kim, K. Pressel, and P. Zaumseil, J. Appl. Phys. **80**, 6711 (1996).

[138] P. Lavéant, G. Gerth, P. Werner, and U. Gösele, Mater. Sci. Eng., B **89**, 241 (2002).

[139] H. J. Osten, E. Bugiel, and P. Zaumseil, Appl. Phys. Lett. **64**, 3440 (1994).

[140] K. Eberl, S. S. Iyer, S. Zollner, J. C. Tsang, and F. K. LeGoues, Appl. Phys. Lett. **60**, 3033 (1992).

[141] A. R. Powell, K. Eberl, B. A. Ek, and S. S. Iyer, J. Cryst. Growth **127**, 425 (1993).

[142] H. J. Osten, phys. status solidi (a) **145**, 235 (1994).

[143] B. Dietrich, H. J. Osten, H. Rücker, M. Methfessel, and P. Zaumseil, Phys. Rev. B **49**, 17185 (1994).

[144] P. Werner, R. Kögler, W. Skorupa, and D. Eichler, in *Proceedings of the 11th International Conference on Ion Implantation Technology.*, pp. 675–678, 1996.

[145] F. Eichhorn, N. Schell, W. Matz, and R. Kögler, J. Appl. Phys. **86**, 4184 (1999).

[146] W. J. Taylor, T. Y. Tan, and U. Gösele, Appl. Phys. Lett. **62**, 3336 (1993).

[147] P. Erhart and K. Albe, Phys. Rev. B **71**, 035211 (2005).

[148] G. Kresse and J. Furthmüller, Comput. Mater. Sci. **6**, 15 (1996).

[149] P. S. de Laplace, *Théorie analytique des probabilités*, Oeuvres Complètes de Laplace Vol. VII (Gauthier-Villars, 1820).

[150] B. J. Alder and T. E. Wainwright, J. Chem. Phys. **27**, 1208 (1957).

[151] B. J. Alder and T. E. Wainwright, J. Chem. Phys. **31**, 459 (1959).

[152] J. Tersoff, Phys. Rev. Lett. **56**, 632 (1986).

[153] J. Tersoff, Phys. Rev. B **37**, 6991 (1988).

[154] J. Tersoff, Phys. Rev. B **38**, 9902 (1988).

[155] J. Tersoff, Phys. Rev. Lett. **61**, 2879 (1988).

[156] J. Tersoff, Phys. Rev. B **39**, 5566 (1989).

[157] G. C. Abell, Phys. Rev. B **31**, 6184 (1985).

[158] A. P. Horsfield, A. M. Bratkovsky, M. Fearn, D. G. Pettifor, and M. Aoki, Phys. Rev. B **53**, 12694 (1996).

[159] B. W. Dodson, Phys. Rev. B **35**, 2795 (1987).

[160] P. Erhart and K. Albe, Appl. Surf. Sci. **226**, 12 (2004).

[161] L. Verlet, Phys. Rev. **159**, 98 (1967).

[162] H. J. C. Berendsen, J. P. M. Postma, W. F. van Gunsteren, A. DiNola, and J. R. Haak, J. Chem. Phys. **81**, 3684 (1984).

[163] E. Schrödinger, Ann. Phys. (Leipzig) **384**, 361 (1926).

[164] L. H. Thomas, Proc. Cambridge Philos. Soc. **23**, 542 (1927).

[165] E. Fermi, Atti Accad. Naz. Lincei, Cl. Sci. Fis. Mat. Nat. Rend. **6**, 602 (1927).

[166] D. R. Hartree, Proc. Cambridge Philos. Soc. **24**, 89 (1928).

[167] W. Kohn, Rev. Mod. Phys. **71**, 1253 (1999).

[168] M. Born and R. Oppenheimer, Ann. Phys. (Leipzig) **389**, 457 (1927).

[169] P. Hohenberg and W. Kohn, Phys. Rev. **136**, B864 (1964).

[170] M. Levy, Phys. Rev. A **26**, 1200 (1982).

[171] W. Kohn and L. J. Sham, Phys. Rev. **140**, A1133 (1965).

[172] D. M. Ceperley and B. J. Alder, Phys. Rev. Lett. **45**, 566 (1980).

[173] J. P. Perdew and A. Zunger, Phys. Rev. B **23**, 5048 (1981).

[174] W. Kohn, Phys. Rev. Lett. **76**, 3168 (1996).

[175] W. Kohn and A. E. Mattsson, Phys. Rev. Lett. **81**, 3487 (1998).

[176] F. Bloch, Z. Phys. **52**, 555 (1929).

[177] M. L. Cohen and V. Heine, The fitting of pseudopotentials to experimental data and their subsequent application, Solid State Physics Vol. 24, pp. 37–248, Academic Press, 1970.

[178] D. R. Hamann, M. Schlüter, and C. Chiang, Phys. Rev. Lett. **43**, 1494 (1979).

[179] D. Vanderbilt, Phys. Rev. B **41**, 7892 (1990).

[180] N. Troullier and J. L. Martins, Phys. Rev. B **43**, 1993 (1991).

[181] A. Baldereschi, Phys. Rev. B **7**, 5212 (1973).

[182] D. J. Chadi and M. L. Cohen, Phys. Rev. B **8**, 5747 (1973).

[183] H. J. Monkhorst and J. D. Pack, Phys. Rev. B **13**, 5188 (1976).

[184] R. P. Feynman, Phys. Rev. **56**, 340 (1939).

[185] M. Kaukonen, P. K. Sitch, G. Jungnickel, R. M. Nieminen, S. Pöykkö, D. Porezag, and T. Frauenheim, Phys. Rev. B **57**, 9965 (1998).

[186] J. P. Perdew and Y. Wang, Phys. Rev. B **33**, 8800 (1986).

[187] J. P. Perdew, J. A. Chevary, S. H. Vosko, K. A. Jackson, M. R. Pederson, D. J. Singh, and C. Fiolhais, Phys. Rev. B **46**, 6671 (1992).

[188] E. R. Davidson, J. Comput. Phys. **17**, 87 (1975).

[189] M. Parrinello and A. Rahman, J. Appl. Phys. **52**, 7182 (1981).

[190] A. Dal Pino, A. M. Rappe, and J. D. Joannopoulos, Phys. Rev. B **47**, 12554 (1993).

[191] P. E. Blöchl, Phys. Rev. B **50**, 17953 (1994).

[192] O. K. Al-Mushadani and R. J. Needs, Phys. Rev. B **68**, 235205 (2003).

[193] W.-K. Leung, R. J. Needs, G. Rajagopal, S. Itoh, and S. Ihara, Phys. Rev. Lett. **83**, 2351 (1999).

[194] M. Z. Bazant, E. Kaxiras, and J. F. Justo, Phys. Rev. B **56**, 8542 (1997).

[195] J. F. Justo, M. Z. Bazant, E. Kaxiras, V. V. Bulatov, and S. Yip, Phys. Rev. B **58**, 2539 (1998).

[196] F. H. Stillinger and T. A. Weber, Phys. Rev. B **31**, 5262 (1985).

[197] J. Tersoff, Phys. Rev. Lett. **64**, 1757 (1990).

[198] K. Nordlund, PARCAS molecular dynamics code (2008).

[199] R. B. Capaz, A. Dal Pino, and J. D. Joannopoulos, Phys. Rev. B **50**, 7439 (1994).

[200] M. J. Burnard and G. G. DeLeo, Phys. Rev. B **47**, 10217 (1993).

[201] P. Leary, R. Jones, S. Öberg, and V. J. B. Torres, Phys. Rev. B **55**, 2188 (1997).

[202] R. Jones, B. J. Coomer, and P. R. Briddon, J. Phys.: Condens. Matter **16**, S2643 (2004).

[203] A. Mattoni, M. Ippolito, and L. Colombo, Phys. Rev. B **76**, 224103 (2007).

[204] A. Mattoni, F. Bernardini, and L. Colombo, Phys. Rev. B **66**, 195214 (2002).

[205] L. W. Song, X. D. Zhan, B. W. Benson, and G. D. Watkins, Phys. Rev. B **42**, 5765 (1990).

[206] R. B. Capaz, A. Dal Pino, and J. D. Joannopoulos, Phys. Rev. B **58**, 9845 (1998).

[207] C.-L. Liu, W. Windl, L. Borucki, S. Lu, and X.-Y. Liu, Appl. Phys. Lett. **80**, 52 (2002).

[208] P. E. Blöchl, E. Smargiassi, R. Car, D. B. Laks, W. Andreoni, and S. T. Pantelides, Phys. Rev. Lett. **70**, 2435 (1993).

[209] B. Sahli and W. Fichtner, Phys. Rev. B **72**, 245210 (2005).

[210] R. Kögler, F. Eichhorn, J. R. Kaschny, A. Mücklich, H. Reuther, W. Skorupa, C. Serre, and A. Perez-Rodriguez, Appl. Phys. A **76**, 827 (2003).

[211] F. Gao and W. J. Weber, Nucl. Instrum. Methods Phys. Res. B **191**, 487 (2002).

[212] A. F. Voter, Phys. Rev. Lett. **78**, 3908 (1997).

[213] A. F. Voter, J. Chem. Phys. **106**, 4665 (1997).

[214] A. F. Voter, Phys. Rev. B **57**, R13985 (1998).

[215] M. R. Sørensen and A. F. Voter, J. Chem. Phys. **112**, 9599 (2000).

[216] X. Wu and S. Wang, J. Chem. Phys. **110**, 9401 (1999).

[217] M. Tang and S. Yip, Phys. Rev. B **52**, 15150 (1995).

[218] F. Eichhorn, N. Schell, A. Mücklich, H. Metzger, W. Matz, and R. Kögler, J. Appl. Phys. **91**, 1287 (2002).

[219] M. Deguchi, M. Kitabatake, T. Hirao, N. Arai, and T. Izumi, Japanese J. Appl. Phys. **31**, 343 (1992).

Curriculum vitae

Personal data

Place and date of birth: Berlin, Germany | 17 November 1977

Basic education

Sep 1988 – Jul 1998	**Grammar school** Justus-von-Liebig-Gymnasium, Neusäß Holbein-Gymnasium, Augsburg
Sep 1984 – Jul 1988	**Elementary school** Ernst-Habermann-Grundschule, Berlin, Wilmersdorf

Conscription

Aug 1998 – Sep 1999	**Alternative civilian service** Hessing-Klinik, Augsburg

Scientific education

Jan 2006 – Present	**Doctoral studies in physics** Physics Department, University of Augsburg Thesis: *Atomistic simulation study on silicon carbide precipitation in silicon*
Jul 2009 – Present	**Collaboration with the University of Paderborn** Theoretical Physics, Physics Department
Jan 2006 – Dec 2008	**Scholarship student** Bayerische Forschungsstiftung
Oct/Nov 2007 Aug/Sep 2008	**Research period at the University of Helsinki** Division of Materials Physics, Department of Physics
Oct 1999 – Dec 2005	**Studies in physics** Physics Department, University of Augsburg Thesis: *Monte-Carlo-Simulation von selbstorganisierten nanometrischen* SiC_x*-Ausscheidungen in* C^+*-implantierten Silizium*

List of publications

F. Zirkelbach, B. Stritzker, K. Nordlund, J. K. N. Lindner, W. G. Schmidt, and E. Rauls
Combined *ab initio* and classical potential simulation study on silicon carbide precipitation in silicon
Phys. Rev. B **84**, 064126 (2011).

F. Zirkelbach, B. Stritzker, K. Nordlund, J. K. N. Lindner, W. G. Schmidt, and E. Rauls
Defects in carbon implanted silicon calculated by classical potentials and first-principles methods
Phys. Rev. B **82**, 094110 (2010).

F. Zirkelbach, J. K. N. Lindner, K. Nordlund, and B. Stritzker
Molecular dynamics simulation of defect formation and precipitation in heavily carbon doped silicon
Mater. Sci. Eng., B **159-160**, 149 (2009).

F. Zirkelbach, M. Häberlen, J. K. N. Lindner, and B. Stritzker
Monte carlo simulation study of a selforganisation process leading to ordered precipitate structures
Nucl. Instr. and Meth. B **257**, 75 (2007).

F. Zirkelbach, M. Häberlen, J. K. N. Lindner, and B. Stritzker
Monte-carlo simulation study of the self-organization of nanometric amorphous precipitates in regular arrays during ion irradiation
Nucl. Instr. and Meth. B **242**, 679 (2006).

F. Zirkelbach, M. Häberlen, J. K. N. Lindner, and B. Stritzker
Modelling of a selforganization process leading to periodic arrays of nanometric amorphous precipitates by ion irradiation
Comp. Mater. Sci. **33**, 310 (2005).

Acknowledgment

First of all, I would like to thank my official advisers Prof. Dr. Bernd Stritzker and Prof. Dr. Kai Nordlund for accepting me as a doctoral candidate at their chairs at the University of Augsburg and the University of Helsinki. I am grateful to Prof. Dr. Bernd Stritzker who, although being an experimental scientist, gave me the opportunity to work on a rather theoretical field. The working environment providing insight on problems dealt with in this thesis from the point of view of an experimentalist were of great importance contributing to the success of this work. Furthermore, I would like to thank Prof. Dr. Kai Nordlund for his expertise in the field of atomistic simulations and the possibility to repeatedly visit his group in Helsinki. Much progress of this study is owed to the regrettably few but fruitful discussions and explanations by electronic mail, within short meetings on conferences and, of course, during my long-term stays in the nice capital of Finland.

Due to the official supervising of both of them, participation in a special research fellowship of the Bayerische Forschungsstiftung was enabled providing financial support for the first three years. Next to living costs, travel expenses for scientific conferences as well as my stays in Helsinki were unbureaucratically taken over by the research foundation.

I owe my deepest gratitude to Prof. Dr. Jörg K. N. Lindner guiding me through my first time of scientific working already beginning with the diploma thesis. I am heartily thankful for his frequent encouragements and the confidence he has shown enabling a greatly independent research and the improvement of respective skills. Furthermore, his experiences in the materials system covered in this study and fine grasp with regard to scientific routines were of great help for this work.

Getting appointed to a professorship at the University of Paderborn, it was also him, who initiated a collaboration with the local theory group under the direction of Prof. Dr. Wolf Gero Schmidt. I would like to thank him for six month of financial support, which allowed me to extend my research period, as well as for his helpful contributions to common articles and respective publishing procedures. More importantly, the collaboration involved further investigations based on first-principles calculations, which improved the quality of this work to a great extent. At this point, I would like to express special thanks to Dr. Eva Rauls. The present thesis would not have been possible without her assistance and mentoring with respect to the utilized methods required by the new approach of investigation as well as her expertise in the materials system. I am greatly thankful for the possibility to repeatedly visit the theory group in Paderborn. In this context, Dr. Simone Sanna is acknowledged for respective technical support and Michael Weinl, doctoral student of Prof. Jörg K. N. Lindner back then, for accommodation.

I am grateful to Priv.-Doz. Dr. habil. Volker Eyert for writing one of the certificates of this work. Furthermore, his lectures on computational physics and the electronic structure of materials, which I attended during my academic studies, influenced me to pursue scientific research in the field of computational physics.

One more time, I would like to thank Prof. Dr. Bernd Stritzker for another two-month position as a member of his research staff and various long-term employments as a research assistant, which not only ensured a minimum of financial supply but also involved tutorships in the field of solid state physics that could be carried out in a more or less free and autonomous way.

I am grateful to Ralf Utermann, responsible for the computing infrastructure in the physics department, for providing access and support with the excellently maintained high performance units available in the Augsburg Linux Compute Cluster. Furthermore, being employed as an assistant under his direction during the first times of my studies, he provided insight into modern computing technology and, in doing so, sparked my interest in computational physics.

I would like to show my gratitude to Rolf Anders. Similarly situated, performing numerical investigations at another experimental physics division, he was always interested in discussing, both, specific and general problems related to physics as well as to scientific computing.

Residing in the office of the undergraduates, I would like to thank all of the many fellow students I met during this time. Interesting and not necessarily scientific discussions appeared on the daily agenda. It was a great time of lively exchange of ideas and excellent coffee that I will keep in good memory. I am likewise thankful to all the other members of the division for the distinctive and pleasant working environment and the permanent willingness to discuss, which very often happened on Fridays burning the midnight oil.

For discussions aside from natural science, I am grateful to the small but fine reading group formed on the fringes of the temporary student protests in 2009. I would like to thank Meta Schnell, Berthold Arlt, Michael Lippok, Erika Rempel, Leo Sellinger, Michaela Strattner, Katja Teich and Matthias Link for the numerous sessions reviewing elements of the critical theory of society.

I am grateful to Melanie Lenk for moral support during my time as a diploma and doctoral student. For the nice time we had and, in particular, for her patience and care in stressful times as well as for encouraging internet telephony calls during my stays abroad, I will always be thankful.

I would like to thank Stefanie Rajkay accompanying me during the last stages of this work. Although there cannot be a right life amidst wrongs[1], I am glad for our joint effort trying to organize and anticipate a way of (private) life that would be the actual right one in a free society.

Last but not least, I would like to express my gratitude to my parents Wilfriede and Karl Zirkelbach, who contributed to a great extent to pursue a scientific career without major difficulties. My brother Till Zirkelbach is greatly acknowledged for backup of any kind of concern.

Thanks!

---

[1] Theodor W. Adorno, *Minima Moralia: Reflexionen aus dem beschädigten Leben*, Suhrkamp 1994, p. 19.